A NOVEL PHOTOCATALYTIC PLASMA REACTOR FOR REFORMING OF WASTE GASES

S C CAPP

PHD 2021

A Novel Photocatalytic Plasma Reactor for Reforming of Waste Gases

SAMUEL CHARLES CAPP

A thesis submitted in partial fulfilment of the requirements of Manchester Metropolitan University for the degree of Doctor of Philosophy

Department of Engineering

Manchester Metropolitan University

2021

ACKNOWLEDGEMENTS

Firstly, I would like to thank my supervisors Dr. Zaenab Abd-Allah and Dr David Sawtell for their continuous support and patience throughout the whole 4 years, it would not have been possible without your expertise and dedication. Also, thank you for giving me the opportunity to work with you on this research, I am very grateful. Secondly, I would like to thank Professor Peter Kelly for his help, guidance and welcoming me into the surface engineering laboratory.

Personally, I would like to thank all the technicians at Manchester Metropolitan University, in particular Dr. Gary Miller and Mrs Hayley Andrews for their help and time with the analytical equipment, your tireless efforts never go unnoticed.

A huge thanks also go to the whole surface engineering group from 2016-2020; Justyna, Adele, Marina, Brice, Tiziana and Glen, teamwork makes the dream work.

As mentioned previously having a great team to support and help you is paramount to achieve your goals. Fellow PhD students within the university were always there to help, whether technically or socially, therefore, a huge thank you to Matt, Isablella, Hadi, AJ, Antoine, Niall and Dave.

Finally, a huge thanks to all my family and friends for baring with me and advising me throughout the whole 4 years.

ABSTRACT

Non-thermal plasma (NTP) is an area of research that is receiving ever more attention. The unique properties of NTP make it useful in many applications. One such application is combining NTP with catalysts known as plasma catalysis. Plasma catalysis can allow chemical reactions to occur at temperatures otherwise insufficient when using catalysts alone. A specific type of catalyst was employed termed photocatalysts. This is due to their unique property by which they can be activated by ultraviolet light or even visible light, both of which are naturally produced by plasma. This has the ability to further enhance the synergistic effect of NTP and catalyst. Therefore, investigation into the effects of combining photocatalysts and NTP plasma was studied. The research focused on using a physical deposition technique, magnetron sputtering, to introduce the photocatalysts in a novel way, into the NTP reactor for plasma catalysis. Specifically, the photocatalytic coatings were produced on dielectric particulates which are used within the NTP reactor.

Titanium dioxide based photocatalytic coatings, produced by magnetron sputtering onto particulates, were characterised by various characterisation techniques such as Raman spectroscopy, scanning electron microscopy and X-ray photoelectron microscopy and subsequently tested for photocatalytic activity through methylene blue degradation, which is a common method to determine photocatalytic activity, and showed an increase in degradation of methylene blue by up to 12.5 times. In order to understand the mechanisms involved between photocatalytic coatings and NTP, their effect on the reforming of oxygen and nitrogen gas mixtures and the dry reforming of methane was investigated. The presence of titanium dioxide was observed to affect the plasma chemistry in the NTP by acting as a sink for atomic oxygen, through photocatalytic formation of superoxide anion radical (O_2^-), and alteration of the dielectric constant of the dielectric particulates. The titanium dioxide coatings had a significant effect on the oxygen and nitrogen plasma chemistry, it was measured that the coatings enhanced ozone production by up to 80 times for a residence time of 0.011 s and up to 10 times for 0.0037 s compared to without any coatings and significantly decreased the formation of harmful nitrogen dioxide (NO_2) and nitrous oxide (N_2O) at a residence time of 0.011 s. In the dry reforming of methane experiments, it was found that the photocatalytic coatings enhanced the conversion of methane by 1.6 times and enhanced the conversion of CO_2 by 1.35 times. However, it was also observed that some photocatalysts, such as the tungsten doped titanium dioxide coatings can reduce the performance by effecting the plasma discharge.

The finding of this study shows that with careful understanding of the plasma-photocatalyst surface interaction, chemical processes could be tailored towards improving the production of desired product and limiting the formation of undesired by-products. Moreover, the photocatalysts produced by magnetron sputtering can enhance the surface interaction between plasma and photocatalysts with minimal disturbance to gas flow.

Table of Contents

LIST OF TABLES

LIST OF FIGURES

NOMENCLATURE

$BaTiO_3$ – Barium Titanate

BET - Brunauer–Emmett–Teller

CB – Conduction Band.

CH_4 – Methane

CO – Carbon Monoxide

CO_2 – Carbon Dioxide

DBD – Dielectric Barrier Discharge

EDX – Energy dispersive X-ray spectroscopy

H_2 - Hydrogen

hv – Photon

IR – Infrared

N_2 - Nitrogen

NTP – Non-Thermal Plasma

OES – Optical Emission Spectroscopy

O_2 - Oxygen

O_3 - Ozone

PBR – Packed Bed Reactor.

PVD – Physical Vapour Deposition

SEM – Scanning Electron Microscopy

TiO_2 – Titanium Dioxide

TiO_2-W – Titanium Dioxide doped with Tungsten

XPS – X-ray photoelectron spectroscopy

XRD – X-ray Diffraction

UV – Ultraviolet

VB – Valence Band.

THESIS STRUCTURE

Chapter 1 – Introduction to the premise behind the research, a background to the scope and content of the research and a list of research aims and objectives. This includes, but not limited to, a background information of the fourth state of matter, plasma, how it is generated and its treatment of waste gases. An introduction to photocatalysis and its combination with plasma and the methods/production of photocatalysts for use in this research.

Chapter 2 –Chapter 2 compromises of the methods used in this research varying from, materials production, using magnetron sputtering, materials characterisation including crystallinity, surface area and stoichiometry, experimental technique for evaluating the photocatalytic activity of deposited photocatalytic coatings, the design and operation of the dielectric barrier discharge closed system and power supply for the generation of non-thermal plasma used for the treatment of waste gases and the post processing of data obtained.

Chapter 3 – Deposition and optimisation of photocatalytic coatings using the physical vapour deposition technique, magnetron sputtering, onto glass particulates for evaluating photocatalytic activity of different coatings as prior optimisation of catalysts before implementing them into the dielectric barrier discharge used in consequential research regarding the treatment of waste gases.

Chapter 4 – Effect of developed photocatalysts coated onto dielectric particulates in the production of ozone from an oxygen and nitrogen gas mixture. The effects of these photocatalytic coatings on the plasma chemistry was investigated.

Chapter 5 – Effect of developed photocatalysts coated onto dielectric particulates in the remediation of methane and carbon dioxide. In this chapter the effects on the plasma chemistry and energy efficiency using different coated packing material compared to uncoated packing material was investigated along with the production of carbon monoxide.

Chapter 6 – Summary and conclusion of the work presented in this thesis and a description of further work to be carried out relating to this research.

CHAPTER 1 - BACKGROUND

In Chapter 1 an introduction to the fundamental reasoning and theory of non-thermal plasma reforming, photocatalysis and plasma catalysis is provided to give the reader an understanding to interpret the methodology, results and discussion of this report. The motivation and aims are explained to define the scope of the research and outline the importance and relevance to human knowledge. It begins with an introduction to the motivation behind the research followed by an outline of the current ways of producing hydrogen and syngas. Subsequently an introduction to plasma as an ionised gas, the different types of plasma, their properties, their usefulness and how it can be generated in the laboratory using several different methods including the method to generate plasma in this body of research. These methods are then characterised and reviewed according to literature and industry. Furthermore, the phenomenon of photocatalysis is explained to the reader, along with the interaction between photocatalysis and non-thermal plasma. It follows on with an introduction to photocatalysis preparation methods. Finally, an overview on how the photocatalysts were produced and coated through the physical vapour deposition technique named magnetron sputtering.

1.1 Introduction

The primary aim of this research was to further understand the role photocatalysts can play when combined with non-thermal plasma. At present there is still a gap in knowledge of the interaction between photocatalysts and non-thermal plasma. Part of this research was to gain more understanding of the interaction of the combination of photocatalysts and non-thermal plasma whilst trying to achieve a synergistic effect of them both. Non-thermal plasma and photocatalysts can change an undesirable reactant into a more valuable product, usually through treating waste gases. In this research the effect of photocatalyst and plasma on the effect of the production of ozone from a nitrogen-oxygen mix and the reforming of methane and carbon dioxide was investigated. The method of producing the catalyst for plasma catalysis was carried out through magnetron sputtering. This way of introducing the catalysts has not been investigated in this area of research. The desired advantage is that the catalyst can be in direct contact with the plasma whilst not being obstructive to the process and allow chemical reactions that would not be possible if using catalyst or plasma alone.

All work in this thesis was undertaken in the John Dalton Science and Engineering building at Manchester Metropolitan University as part of a project titled ‘A Novel Photocatalytic Plasma Reactor for Reforming of Waste Gases’. The project was funded by the Faculty of Science and Engineering at Manchester Metropolitan University. Part of this work was carried out in the Manchester Fuel Cell Innovation Centre part funded by the European Union.

The next section describes the background to the project, the premise and reasons why this work was initiated. It also describes the aims, general and specific, of the project.

1.1.1 Background and motivation

The demand for energy has increased from 1990 to 2015 by 60% from 346408 petajoules to 551688 petajoules [1]. The sources from which electrical energy have been obtained varies from region to region and has changed over time. In quarter one 2017 the United Kingdom obtained its electricity in the form of; gas 39.9 %, nuclear 18.9 %, renewables 26.6 %, coal 11.3 % and oil & other at 3.3 % [2]. Countries such as the United Kingdom face an energy trilemma which requires balancing energy security, energy costs and environmental impact. The environmental impact on our planet is one of the most imperative challenges that humankind faces. Carbon dioxide released by human activity traps infrared radiation within the atmosphere accelerating global warming. Global carbon emissions equivalent from the energy sector stood at 32.1 gigatonnes in 2016 [3]. Since 1958 the amount of carbon dioxide carbon dioxide in the earth's atmosphere was averaged at about 315 ppmv, worryingly the concentration of carbon dioxide as of 2017 is 407 ppmv [4] and as of May 2020 the carbon dioxide concentration reached 417 ppmv [5]. The increase in methane, carbon dioxide and nitrogen dioxide in the atmosphere is 7 %, 13 % and 6 % respectively in from 1958 to 2017 [6]. Countries around the world recognise the immediate need to protect our environment and are beginning to act. The Paris agreement in 2016 has been ratified by 147 countries and aims to hold the increase in average temperature to well below 2°C [7]. Therefore, the methods of energy production need to be reformed for a more environmentally sustainable future whilst remaining economically viable and secure. On top of this a more robust approach to what is released into the atmosphere and oceans should be more widely adopted. Consequently, countries must lower their greenhouse gas emissions and lessen their consumption of fossil fuels. Along with this, new technologies which can aid in contributing to a clean environment are of increasing importance.

To achieve this, one of the immediate and important steps is to reduce the reliance on fossil fuels such as their use in common processes regardless of their position in the system e.g. for energy production or in chemical processing. The energy and chemical industry are one of the main users of fossil fuels and in turn require diversification of their processes. Emerging technologies such as hydrogen fuel cells and the improvement in the technology of renewable energy methods provide promise. Hydrogen fuel cells provide a one-step chemical to electrical energy process and can reach electrical efficiencies of 90 % [8]. Another benefit of hydrogen fuel cells is that they produce no waste products. The basic components of a hydrogen fuel cell are an anode and a cathode with an electrolyte in-between [9]. The overall chemical reaction which occurs can be seen in [Eq. 1] [8]. Different approaches to obtaining chemicals for energy applications such as hydrogen are also being improved with constant innovation and research. Unlike other fuels such as oil, hydrogen has to be produced first before it can be used as a fuel. However, at present 95% of hydrogen is produced with the burning of fossil fuels.

$$H_2 + \frac{1}{2}O_2 \leftrightarrow H_2O \qquad \Delta G_f = -229 kJmol^{-1} \qquad [Eq.\ 1]$$

Alternative fuels such as biogas, biomass and syngas have received significant investment as a greener alternative to fossil fuels. Syngas also known as synthesis gas is primarily a mixture of hydrogen and carbon monoxide, although it can contain other gases such as methane, carbon dioxide and nitrogen. Syngas has received a great amount of attention as a direct fuel in combustion or as an intermediate product in the fuel and chemical industry. More than this syngas has applications in stationary power plants, in fact General Electric has led in the technology development of syngas gas turbine technology in the last 20 years. Up to 2007, general electric was operating gas turbines with a total capacity of more than 3 GW in 15 plants installed in USA, Canada, Singapore, Germany, Italy, The Netherlands, and Czech Republic [10].

Non-thermal plasma reactors (NTPs) are one such technology which can produce hydrogen or syngas, this can be done through the dry reforming of methane. Non-thermal plasma reactors only require a high voltage power supply from which can be powered by environmentally friendly methods. Research on obtaining the optimum conditions and setups of NTPs is required to overcome obstacles such as cost per mass of product and product yield per unit time and be attractive to industry for certain processes. Optimising the design of the reactors, gas flow rates, dielectric material, catalysts, gas ratios and power parameters among others need to be looked at. Due to the unique property of non-thermal plasma emitting both light and UV light introducing photocatalysts into the reactor could allow for activation by the plasma, this can cause an enhancement in the yield of desirable products hence, energy efficiency can be increased. The effects of combining photocatalysts and plasma requires research to understand the mechanisms and interactions between the two. Photocatalysts can affect the plasma characteristics and similarly plasma can affect the photocatalyst. It has been stated that although it is true that plasma reactors can produce UV photons it is suggested that the photon flux is too low to make any significant contribution to the catalytic effect [11]. However in many research publications investigating the combination of non-thermal plasma and photocatalysis there have been positive effects [12-15], even so the role that photocatalysts play still requires thorough investigation. The introduction of catalysts into non-thermal dielectric barrier discharges within literature has been mainly carried out through direct addition of catalyst into the discharge zone [16, 17] or downline of the plasma [18, 19] but until recently has been inserted through coating components of the reactor through methods such as sol-gel or PCVD [14, 20].

The use of magnetron sputtering, commonly used for photocatalyst deposition [21-24], has not been utilised for the introduction of catalysts in combination with non-thermal plasma. This unique and novel way of introducing photocatalysts to a non-thermal plasma dielectric barrier discharge setup will allow for the investigation into the effect of introducing photocatalytic materials in combination with non-thermal plasma and provide an insight to the interaction of the two. It is hoped that introducing the photocatalyst in this way can benefit the photocatalyst by it being directly in the discharge zone whilst having limited negative effects on the plasma discharge. Magnetron sputtering offers many advantages

as a physical vapour deposition technique (PVD) technique such as the ability to coat metals, metal oxides and alloys. Coatings produced by this technique can be tailored by thickness, crystallinity, stoichiometry and structural characteristics. This means that the photocatalysts can be optimised for production and subsequent utilisation in combination with non-thermal plasma can be completed. Using this technique to introduce catalysts for combination with non-thermal plasma can enhance the energy efficiency, conversion and product yields from waste gases such as methane and carbon dioxide and can provide a clearer picture to the interaction of photocatalysts and non-thermal plasma.

1.1.2 Aim

The aim is to investigate whether photocatalysts can improve the ability of atmospheric pressure plasma to convert waste gases into more valuable products. The aim is to also investigate whether magnetron sputtered photocatalytic coatings are an effective way to produce and incorporate the catalyst for the use in a non-thermal plasma dielectric barrier discharge. Finally, it is to open the door to using non-thermal plasma reactors for use in industry as a green option to treat waste gases.

1.1.3 Objectives

The aim of this project will be achieved by the following objectives:

Objective one: The design and build of a non-thermal packed bed plasma reactor to investigate the effect of photocatalysts on the production of ozone and syngas from waste gases. The reactor must have a suitable gas delivery system and be flexible to introduce photocatalysts with ease and efficiency.

Objective two: Coating of photocatalytic materials such as titanium oxide, onto dielectric materials using the physical vapour deposition (PVD) technique magnetron sputtering. Optimise the coating parameters and techniques such as time of deposition, elemental composition, pre-treatment of samples and power conditions.

Objective three: Characterisation of photocatalysts using several advanced analytical techniques such as Scanning Electron Microscopy (SEM), X-ray Powder Diffraction (XRD) and X-ray Photoelectron Spectroscopy (XRD) in order to identify the materials phase, the external morphology, chemical composition, crystalline structure and orientation, enabling the understanding of the performance of these materials in plasma catalysis processes.

Objective four: Investigate the effect of photocatalysts addition on the plasma chemistry for the formation of ozone and hydrogen. Use analytical techniques such as Fourier Transform Infrared Spectroscopy (FTIR), to characterise the produced chemicals and in-situ Optical Emission Spectroscopy (OES) to analyse the active species within the plasma.

Optimise the operating parameters, catalytic material and reactor design. Investigation into the effect of the applied power, gas residence time, molar ratio of feed gases, frequency, flow rate and packing volume.

1.2 Current processes for hydrogen and syngas production

This section provides an overview of current methods of producing hydrogen and syngas in industry.

1.2.1 Hydrogen

Presently, 95 % of hydrogen is obtained through the burning of fossil fuels without carbon capture, defeating the objective of clean energy [25]. In principle hydrogen can be produced from any hydrocarbon source. At present steam reforming is by far the most common means of hydrogen production which require the use of fossil fuels. Steam reforming uses fossil fuels, normally in the form of natural gas to produce synthesis gas, a combination of hydrogen, carbon monoxide and carbon dioxide. Steam reforming involves the reaction of steam with natural gas, the reaction is endothermic and so an external heat source is needed. Normal operation requires the use of catalysts and temperatures in the range of 450 ^{o}C-950 ^{o}C are used for this process. As stated the major disadvantage of steam reforming is the use of natural gas and the production of carbon dioxide, in fact for each mole of methane reformed more than one mole of carbon dioxide is produced [26]. Therefore, the way in which hydrogen is produced for utilisation needs to change in order for a hydrogen economy to become a clean source of energy.

A potential hydrogen production method is plasma catalysis. Plasma catalysis can allow reactions to take place at lower energies than using plasma or catalyst alone [11]. Research on plasma catalysis has been conducted on numerous occasions supporting the fact that this can allow chemical reactions to occur at much lower temperatures and pressures. Nguyen et al. [27] found the combination of non-thermal plasma (NTP) with zeolite catalysts improved the conversion of methane and carbon dioxide to 49.98 % and 52.15 % respectively from 17.98 % and 22.35 %. Another study by Mei et al. shows that the dissociation of carbon dioxide into carbon monoxide and oxygen and shows that the carbon dioxide conversion and energy efficiency were enhanced by up to 2.5 times with the addition of catalysts $BaTiO_3$ and TiO_2 [28].

1.2.2 Syngas

Production of syngas is primarily done via the gasification method whereby organic and fossil fuel based carbonaceous materials are converted, usually requiring high temperatures in excess of 700^{o}C, without combustion of the materials, in oxygen and/or steam. Gasification is a thermochemical process and can require complex equipment and skill to operate, more to this it is also rather expensive. Alternative techniques such as catalysis, photocatalysis and non-thermal plasma are promising techniques which could alleviate the complexity and cost of gasification. Catalytic reforming for syngas production mainly uses noble metal catalysts or nickel based catalysts. Using the catalytic method can produce conversions around 90 % [29]. However, disadvantages include high temperatures and deactivation of the catalysts. Photocatalysis is a promising way to generate syngas, as photocatalysis can be operated at a mild condition and with a lower energy input, however the syngas

generation efficiency is rather low. Plasma photocatalysis could provide a promising solution for syngas production.

1.3 Plasma

Plasma, the fourth state of matter, is defined as an ionised gas and is utilised in industry for various applications such as in fusion energy, water treatment, food storage and ventilation systems. In fact it is the most abundant form of matter in the universe occurring naturally in space such as in stars, nebulas and most things in-between. Plasma has a unique set of characteristics which can be harnessed in ways which can be beneficial to many processes. Gas, which is not ionised, is in the state of thermal equilibrium and assumes the Boltzmann distribution over kinetic and potential energy with the average kinetic energy of a gaseous particle at room temperature being about 0.04 eV [30]. If gaseous particles are subjected to a strong enough electric field, electrons can be removed from their orbit, ionising the parent atom and leaving behind a positive ion. This 'soup' of negative electrons and positive ions, is plasma. The charged particles then can interact with neutral particles and can cause further excitation and ionisation. Charged gaseous particles behave like a conductive media. Plasmas are generally neutral, in that in the body of the plasma there exists roughly equal numbers of negatively charged electrons and positively charged ions. Often this concept is called quasi neutrality [31]. Perturbations from this neutrality can occur within the plasma on a small scale, or at the edge of the plasma on a major scale.

An ionised gas can be weakly or strongly ionised. The degree to which the plasma is ionised is a matter of discussion. The main properties which are unique to plasma are:

- Response to magnetic fields.
- Response to electrical fields.
- Large number of high energy electron collisions.
- High density of ionic species.

Plasma is also made in the laboratory in order to provide benefits to many processes such as:

- Nuclear fusion
- Material and surface modification
- Gas reforming
- Deposition processes
- Plasma cleaning
- TVs
- Lighting

Plasma is normally split into two types due to the different properties they exhibit. These are 'cold' plasmas and 'hot' plasmas, often also termed non-thermal plasmas and thermal plasmas respectively. Thermal plasmas are in thermal equilibrium meaning that all plasma particles, electrons and ions, have

the same kinetic energy. Non-thermal plasma exists where the positive and negative ions are not in thermal equilibrium, in these plasmas electrons have highest temperature and kinetic energy.

1.3.1 Thermal plasma

Thermal plasma is produced using an excitation method such as direct current (DC), alternating current (AC), radio frequency or microwave and usually exists in the temperature range of 2000-20,000 K [32]. Thermal plasma exists in thermal equilibrium such that heavy particles, for example nuclei, are the same temperature as the electrons. These 'hot' plasmas exhibit a high energy density compared to 'cold' plasmas.

Applications of thermal plasma include:

- Metal melting and remelting.
- Plasma cutting and welding.
- Plasma in wire arc spraying.
- Thermal plasma CVD.
- Plasma waste treatment.
- Fusion energy.

1.3.2 Non-thermal plasma

Non-thermal plasmas, often referred to as 'cold' plasmas are normally produced at low or atmospheric pressure where the bulk gas is close to room temperature. The supplied electrical field and corresponding field energy generates free electrons, these electrons accelerate in the electrical field and can in turn provoke new ionisations. In regards to waste gas treatment, the main focus of this research, the temperature of the bulk gas does not need to be high to easily produce chemically active species. In non-thermal plasma the temperature of the gas T_g is proportional to the mean discharge power density, P, and the average reduced energy density deposited into the gas, [Eq. 2], where V is the discharge volume and Q is the gas flow rate [33].

$$T_g = \frac{PV}{Q} \qquad \text{[Eq. 2]}$$

However, generating non-thermal plasma at atmospheric pressure, in comparison to high pressure, the electric field needs to be higher in order to cause a breakdown of the gas. This high electric field can lead to an arc. Arc plasmas are high current (30 A-30 kA), low voltage (10 V-100 V) discharges that can have very high gas temperatures (10,000-100,000 K). Arcs can cause evaporation and erosion of electrodes [34]. Furthermore, arcs are detrimental to syngas production. Other than arcs there are two main breakdowns mechanisms which occur in non-thermal plasma these are Townsend breakdown and streamer breakdown. The Townsend breakdown, also known as the electron avalanche, was first studied by Townsend in 1910. This describes the movement of electrons towards the anode, colliding with various molecules, in turn ionising them. This creates positive ions which move towards the cathode

colliding with molecules and ionising them also. The positive ions collide with the cathode producing secondary electrons [35]. Streamer breakdown theory was first developed by Raether, Loeb and Meek, this is represented in figure 1 [36-38]. This type of breakdown is often found in the DBD and lightening in the atmosphere. Streamer discharges are responsible for ozone generation, pollutant control and are useful in medical applications. In the case of a streamer, electrons travel towards the anode ionising molecules and leaving behind a cloud of positive ions. This leads to a build-up of space charge. Photons are produced with this and in turn, photoelectric ionisation occurs, this phenomenon is more intense near the cathode and anode. Some electrons are produced from the cathode, the amount is proportional to the proximity of the avalanche to the cathode. The effect of this is that at the intercept of the cathode and avalanche, electrons are produced which cause other avalanches. This starts avalanches towards the space charge and electrons will stream into it [39].

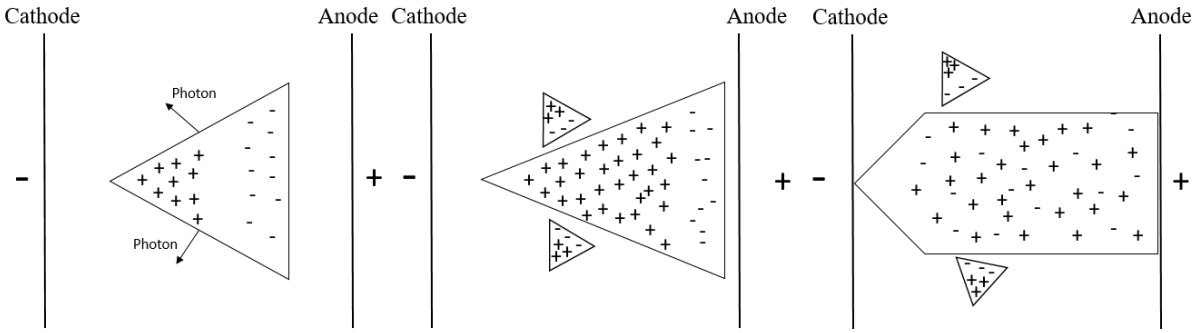

Figure 1 – Representation of a plasma streamer between anode and cathode. Adapted from [39].

1.4. Current dielectric barrier discharges used in research for gas treatment

This section focuses on non-thermal plasma and its generation and its role in gas treatment. It gives an overview of the various methods of producing non-thermal plasma in the laboratory and gives an in-depth description of the characteristics of each type of method.

1.4.1 Types of non-thermal plasma discharge devices

There are various methods of generating non-thermal plasma within a laboratory setting such as, the dielectric barrier discharge, corona discharge, surface discharge and using radio frequency or microwaves. Some principal approaches used in plasma science for the effective generation of atmospheric plasma are:

- Using sharp electrodes for increased electric field strength.
- Introducing dielectric material to limit the current transfer.
- Preventing increased thermalisation using a pulsed electrical signal.

- Using high flow rates to increase heat transfer.

Radio frequency and microwave discharges

Plasma discharges can be created through providing energy by the means of electromagnetic waves such as radio frequency and microwave frequency. A unique property of plasma generated via this method is the way the plasma does not have to be in contact with any electrodes. The generation of the high frequency needed for this method usually requires complex systems. In the case of radio frequency plasmas for non-thermal operation, a coupling of the electromagnetic field to the plasma discharges is important in order to increase energy efficiency. Some advantages of microwave generated plasmas are its high energy efficiency, potential scaling up of the technology, and high density plasma [40].

Corona discharge reactor

Corona discharges exist in several forms, depending on the polarity of the field and the electrode configurations. The corona discharge consists of an electrode in a point geometry which is surrounded by atmospheric air. A secondary plane electrode is present and the strong electric field between the two is the source of ionisation of the surrounding gas. The corona discharge can be generated by direct current, alternating current or pulsed direct current. The power input of a corona discharge is limited due to the ignition of a spark if the electric field is too high, using a pulsed signal is one way to increase the power before a spark transition could occur. The main type of discharge is in the form of a discharge streamer which can make it useful for pollutant removal [41]. The streamer corona is a relatively low temperature plasma with ion/neutral temperatures of the order of a few 100 K [42].

Gliding arc discharges

Gliding arc discharges consist of two diverging electrodes which is accompanied by a laminar or turbulent gas flow passing through the electrode gap. The gliding discharges begin with a plasma column at the minimum distance between electrodes, as the gas carries on further downstream the discharge is pulled along by the gas flow as the electrode gap increases. The gliding discharge will reach a point where the electrode gap is too large and so the discharge will extinguish. The gliding arc is a transitional type of atmospheric pressure arc discharge. It can provide relatively high levels of electron density, current and power, typical for thermal plasmas, together with relatively low temperature and elevated electric field, typical for cold non-equilibrium plasmas [43]. The gas temperature in a gliding arc can be significantly higher than in other types of NTP, up to 10,000 K [44]. Similar to corona discharge, the gliding arc discharge can be produced using direct current, alternating current or pulsed direct current.

Surface Discharge

The surface discharge comprises of a dielectric material on the surface of an electrode with another partial electrode on top. This allows the surface discharge, consisting of a large number of mini

nanosecond pulse streamers starting at the edge of the discharge electrode and developing in the vicinity of the discharge surface [45].

Dielectric barrier discharges

Dielectric barrier discharges (DBD) have been a useful device for generating non-thermal plasma since its discovery by W. Siemans in 1857 [46]. Characterised by insulating material in-between the current path of electrodes along with an air space, see figure 2, they offer many advantages when generating non-thermal plasma, such as: Atmospheric pressure operation, low cost, ease of scalability, and low power consumption.

Dielectric barrier discharges are used in industry for different purposes. Common uses are ozone production, bacterial inactivation [47], Plasma enhanced chemical vapour deposition [48], pollutant removal [49] and gas reforming [27]. Dielectric material is employed in order to limit current flow and distributes the discharge almost uniformly over the entire discharge area to avoid spark or arc discharges. The dielectric barrier discharge requires an alternating current for successful operation due to the fact that the insulating dielectric cannot pass a DC current, however operation through pulsed DC is possible. The DBD usually generates gas temperatures in the order of a few 100 K. The dielectric constant of the material has a significant impact on the performance of a DBD, this is because the dielectric constant is inversely proportional to the breakdown voltage and this means the higher the dielectric constant of the material the lower the breakdown voltage. The relationship between breakdown voltage (V_B) and dielectric constant of a parallel plate DBD is shown in the following equations, where k is the dielectric constant, A is the area of electrode, d is the thickness of the dielectric layer, C_g is the capacitance of the gap and C_d is the capacitance of the dielectric layers [50].

$$C_{cell} = \frac{C_g C_d}{C_g + C_d} \qquad \text{[Eq. 3]}$$

$$C_d = \frac{k \varepsilon_o A}{d} \qquad \text{[Eq. 4]}$$

$$V_B = \frac{1 - C_{cell}/C_{diel}}{1 - C_{cell}/\zeta_{diel}} \qquad V_B \text{ is inversely proportional to k.}$$

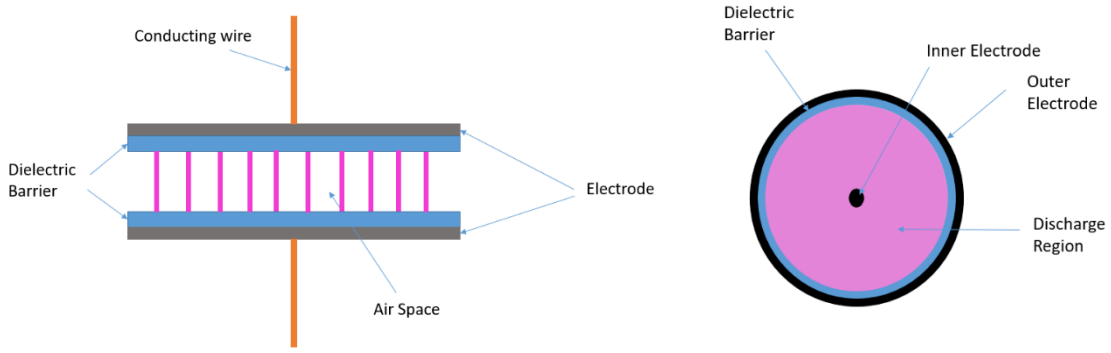

Figure 2 – Typical planar DBD (left) and cylindrical DBD (right)

Dielectric barrier discharges are commonly used in research studies due to their ability to ionise gases and produce plasma combined with their ease of construction and operation. The arrangements depend on various parameters such as, gas compositions and pressure, discharge configuration, the frequency of the applied voltage and field polarity [51]. Types of DBD are the parallel plate reactor, coaxial and packed bed reactor (PBR).

Packed bed dielectric barrier discharges

PBR's are one of the most widely investigated plasma based devices for industrial gas reforming [52]. PBR's are a type of dielectric barrier discharge where dielectric pellets or beads are 'packed' in between the electrodes within the air space. The common packing materials are barium titanate ($BaTiO_3$) and aluminium oxide (Al_2O_3). The higher the dielectric constant of the material the lower the breakdown voltage, this is due to the effects that the dielectric constant has on the electric field produced around the contact points of the beads [53]. The higher electric field strength rises to less power being used in order to produce the same energy density in the plasma discharges.

Packed bed packing materials

The size of the packing material and the gap between the electrodes has an effect on the plasma properties and therefore the desired process. Many investigations have been published on the effect of the packing materials geometry on DBD properties Montoro-Damas et al 2015, found that the smaller the particles size the higher the breakdown voltage and higher the occurrence of partial discharging. This causes a decrease in the fraction of the reactor where plasma formation occurs and is caused by insufficient local electric field strength [52]. However, the smaller the particle size the larger the surface area for catalysis to occur, increased number density of contact points and improved gas-plasma contacting [54], Reducing particle size can also change the nature of the discharge and increase the pressure drop within the reactor Ergun et al 1949, found that the pressure drop is effected by the particulate sizes and void fraction [55]. Furthermore, the larger the particle size the lower the breakdown

voltage which can lead to greater power efficiencies. Not only does the particle size matter, the geometry of the packing material can have an effect on the discharge characteristics [56].

Electrical characteristics

In order for a DBD to operate, an electrical circuit must be in place requiring a high voltage and an alternating current. An electrical discharge occurs in the air space when a high enough potential difference is present from one electrode to the other, this critical potential difference is also known as the breakdown voltage. At or above the breakdown voltage, free electrons, generated due to the applied electric field, accumulate in front of the anode, leaving behind a positive space charge of ions. Once this local electric field produced by the space charges is high enough, a streamer occurs, usually moving form anode to cathode. As a result, charge builds up on the dielectric surface reducing the electric field and extinguishing any further discharges, until reversal of the AC current. The electric discharge occurring in a DBD is terminated at the surface of the dielectrics. During each cycle of alternating voltage there are two plasma discharges and two 'dark' periods. During the discharge the potential drop across the air space has a constant magnitude with either a positive or negative value depending on the direction of current. The quenching of the discharge coincides with the maximum voltage. The dark period relates to the absence of charge transport across the air space. A current monitor and a voltage probe within the circuit measures current and voltage which can be displayed on an oscilloscope. At low voltages the current wave is out of phase by 90° and with increasing voltage the current wave increases peak to peak. The discharge period coincides with the maximum current and the ending of the discharge coincides with the maximum voltage [57]. The power dissipated within the DBD is almost exclusively during the discharge period. The average power dissipated within a DBD can be calculated by multiplying the voltage and current over one time period, as seen in [Eq. 5], where P is the power, V_t is the absolute mean voltage and I_t is the absolute mean current, within one wavelength.

$$P = \int_0^t \sqrt{V_t \times I_t} \qquad \text{[Eq. 5]}$$

Power can also be calculated by the area of a Lissajous figure of charge against potential difference between electrodes. The charge can be measured by a capacitor in series with the DBD by the product of the potential difference across the capacitor and the capacitance of the capacitor. However, the capacitance of the capacitor must be large enough so that the voltage difference between the two electrodes of the DBD is as close to the voltage applied to the capacitor. This ensures that the capacitance probe is not intrusive and does not require a high voltage probe. The equation for capacitors in series is shown in [Eq. 6].

$$C_{total} = \frac{1}{\frac{1}{C_1}+\frac{1}{C_2}+\frac{1}{C_3}} \qquad \text{[Eq. 6]}$$

1.5 Catalysis, photocatalysis and plasma catalysis

Catalysis is a process which allows chemical reactions to take place at temperatures or via reaction routes not possible without a catalyst. Catalysis can be split up into two main sub groups, homogenous catalysis and heterogeneous catalysis. Homogeneous catalysis refers to the reactants and catalyst being in the same state, such as liquid and liquid, and heterogeneous catalysis is where the reactants and catalyst are is different states, such as gas and solid or liquid and solid. There are several examples of catalysis used in everyday processes such as fluidic catalytic cracking and the Haber process [58, 59].

The word 'Photocatalysis' is of Greek origin, 'photo' coming from 'phos' being light and catalysis coming from 'katalyo' meaning decompose. The difference of a photocatalyst and a catalyst is in the method of activation, the former being photons of high enough energy and the latter being thermal energy. In photocatalysis photons transfer their energy to electrons resulting in the energy of the electron to be high enough to transfer from the valence band to the conduction band. This results in electron and hole pairs to be formed. The valence band is outer most electron orbital that electrons can occupy whereas the conductance band is the band in which electrons exist with enough energy and mobility to move freely [60].

1.5.1 Photocatalysis

A particular attention to heterogeneous photocatalysis is focused upon throughout this research, heterogeneous catalysis receives a large amount of emphasis due to its potential in environmental and energy related applications [61, 62]. Semiconductors make good candidates for photocatalysts due to their useful properties in electronic structure, photon absorption properties, charge transport characteristics and excited state lifetimes. Semiconductors in their non-conductive ground state require energy in order to be conductive, the amount of energy has to overcome the energy gap in order to transport an electron from the valence band to the conduction band and this energy gap is referred to as the bandgap. The resulting gap left by the electron is a positively charge hole and together reduction and oxidation can happen at the electron-hole pair. The electron-hole pairs can easily recombine due to the low kinetic barrier for the recombination process and release energy.

The electron hole pairs can initiate the direct oxidation of adsorbed species. At the positive holes, hydroxyl radicals such as $OH^{\cdot}$ can be formed through the oxidation of hydroxyl groups at the catalyst surface. At the conduction band electrons present can cause the reduction of electron-accepting species for example the molecules adsorbed on the surface. It is also possible to promote the formation of superoxide radicals $O_2^{\cdot -}$ and subsequent formation of $OH^{\cdot}$. For example, photocatalysis has the possibility of hydrogen generation and conversion of carbon dioxide to methane, methanol, and formaldehyde [63-66] Along with this, photocatalysis has the ability to produce carbon monoxide from methane [67]. Suitable characteristics which make a material a good photocatalyst are good photoactive properties, its band gap, morphology, particle size, porosity, surface area, surface hydroxyl density,

activation by UV and/or visible irradiation, chemical and biological inertness, photostability, low cost and nontoxicity [68, 69].

1.5.2 Titanium dioxide

Titanium dioxide (TiO_2) is a well-known photocatalyst and has been one of the most investigated semiconductors since its discovery of water splitting properties in the 1970s by Fujishima [70]. Ever since then there has been extensive research into its properties and to find beneficial applications. Titanium dioxide was initially industrially produced to replace the toxic lead oxide as the pigment in white paint. The advantageous properties of TiO_2 is its chemical stability, biocompatibility, physical, optical, electrical properties, its relative low cost and high oxidizing power [71]. A lot of research has been conducted to obtain titanium dioxide in a form in which it can be activated by visible light. This is due to the fact that titanium dioxide has a band gap of 3.2 eV which needs ultraviolet radiation with a wavelength less than 385nm in order to activate its photocatalyst properties. TiO_2 is a semiconductor, so the UV radiation is absorbed by electrons raising their energy levels from the valence band to the conductive band. The valence band edge of TiO_2 primarily derives from oxygen 2p orbitals and the conduction band edge from titanium 3d orbitals. For non-metal light-element dopants, the modified optical properties are in general due to the electronic transitions from the dopant 2p or 3p orbitals to Ti 3d orbitals. This formation of electron and hole pairs, as seen in [Eq. 7] allows oxidation and reduction reactions to occur at the surface.

$$TiO_2 + e^-(> 3.2eV) \rightarrow h^+ + e^- \qquad \text{[Eq. 7]}$$

TiO_2 has 3 main phases, amorphous, anatase, rutile and brookite. Different annealing temperatures can alter the crystalline phase of TiO_2. Anatase exhibits a tetragonal structure formed from octahedrals connected by their vertices. The structure of the rutile phase is also arranged as a tetrahedral structure but with the octahedrals connected by the edges. Brookite has an orthorhombic structure, where both the edges and vertices are connected. It has been observed that anatase and rutile has effective photocatalytic activity [72]. Annealing TiO_2 thin films at temperature up to 700°C for 1 hour in air formed anatase [73]. Temperatures from 900°C and above form the rutile crystalline phase [72].

Despite the lower value of band gap for the rutile titania phase (3.0 eV) compared to anatase (3.2 eV), anatase exhibits better photocatalytic properties. The mechanism of high photocatalytic activity of anatase is still a debated subject. There are several reasons proposed to explain the higher anatase photoactivity compared to rutile. Firstly, the crystal size, surface area and porosity difference between anatase and rutile. This effects the recombination of electrons and holes, thus modifying photocatalytic properties. Secondly the higher Fermi level; the Fermi level of anatase is higher than the one of rutile by 0.1eV. This results in higher level of hydroxyl groups on the surface and therefore higher photocatalytic activity. Finally the indirect band gap of anatase; anatase has an indirect band gap

compared to a direct band gap of rutile, which means that the conduction band is located away from the maximum in the valence band. This results in the ability of electrons to stabilize at the lower level of the conduction band itself, consequently giving a longer life time and greater mobility [74].

The brookite phase of titania has an orthorhombic crystal structure, and is more rare and difficult to obtain than anatase and rutile. In some recent work brookite titania was shown to have photocatalytic properties.

1.5.3 Black titanium dioxide

Black titanium dioxide also known as reduced titanium dioxide is the removal or incorporation of oxygen or hydrogen respectively improving photocatalytic performance. This results in a reduction of the bandgap allowing increased solar adsorption for photocatalysis. Black titania can be produced by a novel hydrogenation method [75], it is also possible to produce black titania via coating deposition processes such as magnetron sputtering [76] this can have the effect of disordering the surface, generating Ti^{3+} , oxygen vacancies and improving Ti-H and Ti-OH species resulting in an increased shift in the valence band. Ti^{3+} ions and oxygen vacancies can be detected by various methods such as XPS and Raman spectroscopy in the case of a shift in peaks and reduction in peak intensity.

1.6 Doping

Doping is the introduction of atoms in order to produce additional energy levels into the band structure of a catalyst which can be used to trap electrons or holes to separate carriers from the bands, thus allowing more carriers to successfully diffuse to the surface. A schematic representation of the effects of doping can be seen in figure 3. The purpose of doping is modifying a catalysts bandgap and electronic structure to optimize its optical properties for visible light harvest and to improve the charge kinetics to reduce the recombination of photogenerated carriers, and hence improve the interface and surface characteristics for more efficient catalysis [77].

1.6.1 Metal dopants

Metal dopants can alter the band gap of photocatalytic materials. The photoactivity of metal-doped TiO_2 can be explained by a new energy level produced in the band gap of TiO_2 by the dispersion of metal nanoparticles in the TiO_2 matrix [78]. With the introduction of a new energy level, as seen in figure 3, an electron from the valence band can be excited from the defect state to the TiO_2 conduction band by a lower energy photon. Additional benefit of transition metal doping is the improved trapping of electrons to inhibit electron-hole recombination which would otherwise reduce photocatalytic activity [78]. The transition metal-ion doping can act as recombination centres for electrons and holes of TiO_2, thus reduces the overall activity of the photocatalyst [79]. Some typical metal dopants are tungsten, copper, iron and chromium among others [80, 81], the effect of doping a TiO_2 photocatalyst with tungsten can be seen in figure 4.

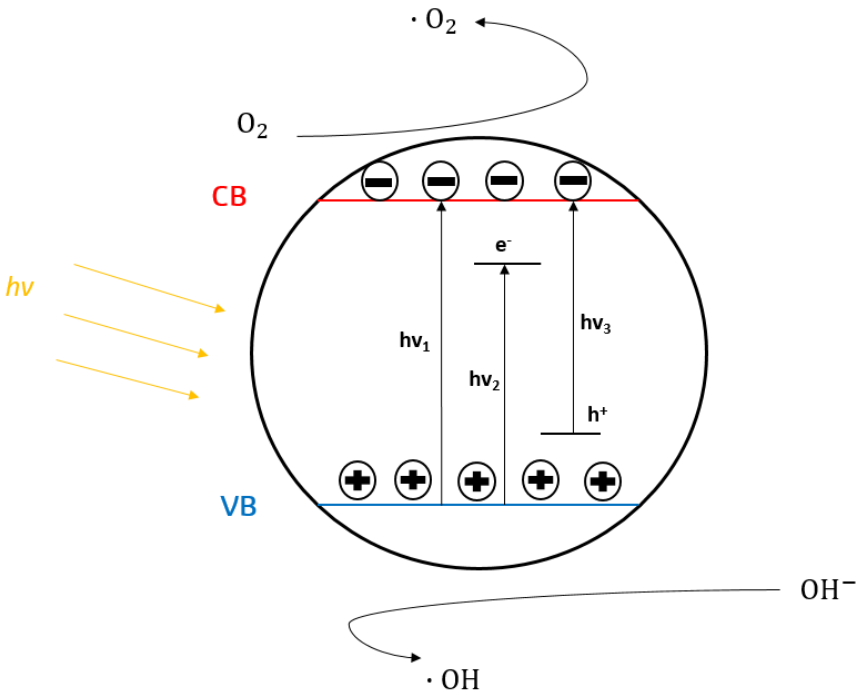

Figure 3 – Schematic representation of the effect of types of doping in a semiconductor where hv is the required photon energy to raise electron form the valence band (VB) to the conduction band (CB). Adapted from [78].

1.6.2 Non-metal dopants

Non-metal dopants can also change the semiconductor properties of TiO_2. TiO_2 is reported as the most promising photocatalyst candidate [82]. Non-metal doping using nitrogen is the most studied [83] due to its comparable atomic size with oxygen, and its low ionization energy Other studied non-metal dopants are carbon, fluorine and sulphur. Zinc oxide doped with nitrogen, carbon and sulphur all improved the photocatalytic efficiency by enhancement of light absorption and more efficient electron-holes pairs [84]. Non-metal dopants such as nitrogen can decrease the electronegativity of the catalyst by introducing an energy level just above the valence band of TiO_2 [85], represented in figure 3, requiring a lower energy photon to induce conductivity. Furthermore, it can act as a trapping centre for the photogenerated electrons and decrease the rate of recombination of photogenerated species. There are other ways in which a non-metal dopant can alter the photocatalytic activity of TiO_2 apart from band gap narrowing. Oxygen vacancies can become traps for photogenerated electrons it has been reported that the higher the amount of oxygen vacancies the better the photocatalytic efficiency [86] [87]. Ihara, et al. [88] concluded that oxygen vacancies formed in the grain boundaries are important and nitrogen doped in part of oxygen are important as a blocker for reoxidation.

1.6.3 Other dopants

Rare earth dopants added to metal oxide photocatalysts have also received much attention due to their improvements to photocatalytic activity. This also affects the electron transfer activity from valence band to conduction band. Another method to improve the photocatalytic activity can be to couple semiconductors. This can enhance certain characteristics, similarly like the addition of dopants, which improve photocatalytic activity such as increasing the lifetime of the charge carrier, reducing the recombination of electron hole pairs. Upon light irradiation, the photo generated electrons can flow from one semiconductor with a higher conduction band to the other with a lower conduction band.

Moreover, the irradiation intensity and photoreactor design also play a crucial role in determining the performance of a photocatalyst [89]. Photocatalyst activation by wavelengths corresponding to plasma emissions makes photocatalysts of interest for enhancing conversion efficiencies of a given plasma process.

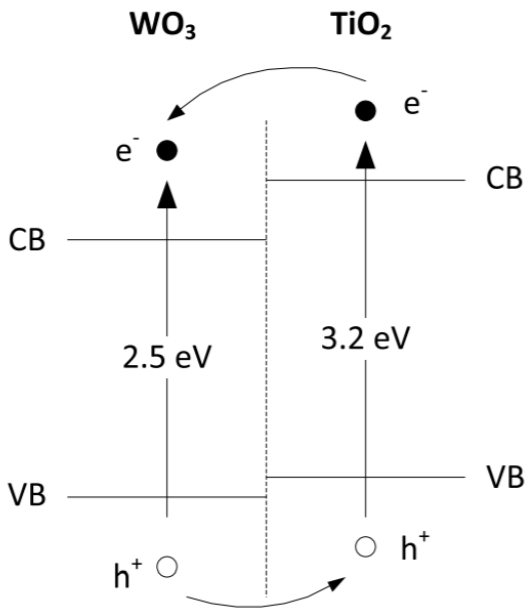

Figure 4 – Schematic diagram representing the effect of W doping on TiO_2. Taken from [23].

1.7 Plasma catalysis

Non-thermal plasma is another promising technique to generate syngas via the dry reforming of methane with relatively lower operating temperatures compared to catalysis [90]. However the energy efficiency of the process needs to be improved for it to be a competitive process [91]. Therefore combining photocatalyst with plasma to form a hybrid system could provide advantages compared to using catalysis, plasma reforming or photocatalysis reforming. A synergy between plasma and photocatalyst can be achieved. Plasma can modify the properties of catalysts such as specific surface area, pore size and surface energy, whereas the catalyst can affect the plasma by changing the discharge behaviour, electron energy density and temperature [20, 92, 93]. Moreover, photocatalysis can be induced since photons and electrons generated by the plasma can be absorbed by the photocatalyst to form electron-hole pairs which facilitate oxidation-reduction reactions [29] [30].

Along with the addition of catalyst, the conversion and efficiencies of using NTP are affected by the design and operational parameters of the plasma reactor itself, including reactor type, dielectric material, packing of dielectric material and volume. The electrical parameters also have an effect such as pulsing of the electrical signal, peak to peak voltage and the frequency applied. The flow rate, composition of gases, temperature and pressure of gas flowing into the reactor also affect the conversion, yield and selectivity [94-97].

As previously mentioned the dielectric barrier discharge, allows us to combine the advantageous properties of non-equilibrium plasma with the ease of atmospheric operation [46].

Plasma as mentioned previously is useful for the reforming of compounds or the production of products however the combination with heterogeneous catalysts can work in harmony with the plasma. The plasma discharge breaks down the gases to form a cocktail of reactive species, such as ions, electrons and vibrationally excited particles which are highly reactive. Combining the catalysts with the plasma means reactions can take place at temperatures lower than using catalysts or plasma alone. Abedi et al 2015, studied that combining non-thermal plasma and TiO_2-ZnO/GAC. They found that the removal efficiency of harmful chlorinated by-products was decreased significantly along with the NO, NO_2, O_3, $COCl_2$, trichlorobenzaldehyde [98]. Metal catalysts nickel, cobalt, copper and manganese supported on γ-Al_2O_3 were investigated by Zeng et al 2015 in a coaxial DBD reactor for the dry reforming of methane [99]. The nickel and manganese catalysts significantly increased the conversion of methane confirming a plasma catalytic effect. The optimum parameters achieved a 19.6 % conversion of methane at a discharge power of 7.5 W and a gas flow rate of 50mlmin^{-1} with the /Ni/γ-Al_2O_3. The molar ratio of carbon dioxide and methane significantly affected the conversion of reactants, the selectivity and yield of products. $LaFeO_3$ catalysts improved the efficiency and degradation of carbon dioxide and methane in a spark discharge reactor [13].

However, as the plasma itself can have an effect on the catalyst the opposite is also true. The plasma could activate the catalyst, change the surface energy or alter the catalysts physical properties such as the lifetime of electron hole pairs can be increased in the presence of an electric field [100, 101]. In turn the catalyst can affect the discharge behaviour, breakdown voltage or number of microdischarges. However, the underlying mechanisms of combining catalysts and plasma are not yet completely understood. Due to the effects of combining the two phenomena, traditional thermal catalysts are not necessarily the most suitable. Finding a synergistic outcome of this combination is required for this to be a viable technique. In order for plasma catalysis to play a bigger role for processes such as synthesis of products such as methanol and syngas, the energy efficiency needs to be improved.

1.8 Plasma catalysis with dielectric barrier discharges

Plasma catalysis is receiving greater attention in research for its ability to overcome the disadvantages observed when plasma or catalysts are used alone. There are two main ways of combining plasma and catalyst and are usually defined as either one-stage configuration or two-stage configuration, see figure 5. One-stage configuration is where the catalyst is placed within the discharge area meaning the catalyst is in direct contact with the plasma. A benefit of this is the short-lived species can interact with the catalyst. With the one-stage configuration the addition of catalysts packed into the reactor can have an effect on the electrical properties of the plasma such as the electric field and the nature of discharge, as a result the plasma chemistry could differ in comparison to plasma alone.

A two stage configuration incorporates the catalyst at the end of the discharge zone meaning only excited, intermediate or long lived species will come into contact with the catalyst. For example, introducing powdered titanium dioxide TiO_2 catalyst in a packed bed plasma reactor with barium titanate dielectrics increased the destruction of CFC-12 from 12 % to 27 % [102].

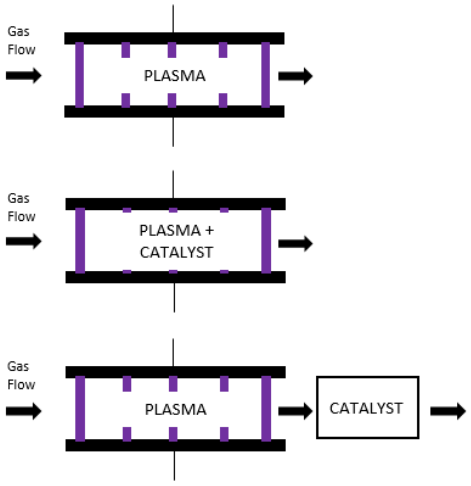

Figure 5 – Plasma alone (top), one stage plasma catalysis configuration (middle), two stage plasma catalysis (bottom).

1.9 Operating parameters for current plasma reactors for dry reforming of methane

This section reviews the current literature on the effects of operational parameters in non-thermal plasma reactors which have been developed for the dry reforming of methane. This includes the type of plasma reactor, the flow rate, feed gas ratio, carrier gas, voltage, frequency and packing material for packed bed reactors.

1.9.1 Flow rate

The total flow rate of gases fed into the reactor can have a significant effect on the conversion of reactants and selectivity of products. A higher flow rate reduces the residence time which lowers the probability of dissociation and consequently the conversion efficiency [96]. However, with a higher flow rate it is found that the energy efficiency is increased due to increased products per unit time. The effect of flow rate on the H_2:CO selectivity and carbon balance was found to be negligible [103]. Table 1 shows the effects of flow rate in various DBD's on the conversion of methane and carbon dioxide and the energy efficiency, if stated.

Table 1 – Effect of flow rate on the dry reforming of methane in DBDs

Plasma Reactor	CH_4:CO_2 Ratio	Total Flow Rate (CH_4/CO_2)	Effect of Flow Rate On Conversion % (Low Flow:High Flow)	Effect of Flow Rate On Energy Efficiency	Reference
Packed bed	1:1	40sccm-120sccm	CH_4 – (53.4%:36.2%) CO_2 – (59.2%:43.4%)	↑ 2.66	[96]
Packed bed	1:1	300sccm – 1600sccm	CH_4 – (65%:35%) CO_2 – (60%:40%)	-	[27]
Coaxial DBD	1:1.25	50sccm – 100sccm	CH_4 – (46%:30.5%) CO_2 – (25.8%:14.8%)	-	[104]

1.9.2 CH_4:CO_2 ratio

The molar ratio of CH_4:CO_2 could affect the relative conversions of each reactant. Studies showed that with a decreased CH_4:CO_2 ratio the conversion of methane increased but inversely the carbon dioxide conversion decreases. This is ascribed due to the increased reverse water gas shift reactions (RWGS), see [Eq. 8], due to the increased carbon dioxide content in carbon dioxide rich feeds, whereas in methane rich feeds the increased methane content suppresses the RWGS reactions.

$$H_2 + CO_2 \leftrightarrow CO + H_2O \qquad \text{[Eq. 8]}$$

The ratio of CO:H_2 is highly dependent on the feed ratio of CH_4:CO_2 in the gas stream. An increase in carbon dioxide results in more carbon monoxide whereas an increased methane content increases hydrogen production. It has been suggested that a higher ratio of methane to carbon dioxide is more favourable in the dry reforming of methane as it leads to higher conversions, hydrogen selectivity and energy efficiency [96], however, some studies suggests that an excess of carbon dioxide increases hydrogen selectivity and conversion [99], due to an excess of oxygen radicals [105]. Some studies suggest that a ratio of 1:1 is the most suitable for hydrogen selectivity [106]. Increasing the methane also increases the abundance of higher hydrocarbons such as C_2H_6, C_2H_4 and C_3H_8 [107]. The highest selectivity of CO:H_2 could perhaps be a combination of multiple conditions such as, power, packing material, catalysts and frequency among others. Table 2 shows the effect of the ratio of CH_4:CO_2 on the methane and carbon dioxide conversions and the CO:H_2 selectivity.

Table 2 – Effects of CH_4:CO_2 ratio on the respective conversion and CO:H_2 selectivity.

Plasma Reactor	Ratio (CH_4:CO_2)	CH_4 Conversion %	CO_2 Conversion %	CO/H_2 Selectivity	Reference
Packed bed	1:1 to 1:4	60%:90%	60%:30%	1.26:1 to 3.13:1	[106]
Coaxial packed-bed	1:0.4 to 1:2.3	11.5%:19%	9%:9%	N/A	[108]
Packed bed.	0.25:1 to 4:1	25%:40%	25%:52%	1:1.12 to 1:1.24	[27]
Packed bed	0.3:1 to 3:1	50%:60%	40%:42%	1:0.5 to 1:2.4	[96]
Coaxial DBD	1:0.5 – 1:1.5	20.2%:37.2%	23.1%:16.3%	1.23:1 to 1.22:1	[104]

1.9.3 Carrier gas

Adding an inert carrier gas such as argon or helium can increase conversion and energy efficiency whilst also maintaining and initiating the discharge. Carrier gases can improve conversion, selectivity and yields, reasons for this can be attributed by its low breakdown voltage, discharge characteristics and reaction pathways. Carrier gases can affect the electron energy distribution function (EEDF) [109], which as a result affects the discharge characteristics and reaction pathways. The lower breakdown voltage brings about an increased number of ionized and excited species which can interact with gases within the plasma to form radicals [107]. Reaction mechanisms with a carrier gas of argon are as follows:

$$e^- + Ar \rightarrow e^- + Ar^* \quad \text{[Eq. 9]}$$

$$e^- + CH_4 \rightarrow CH_3 + H + e^- \quad \text{[Eq. 10]}$$

$$Ar^* + CH_4 \rightarrow CH_3 + H + Ar \quad \text{[Eq. 11]}$$

Helium as a carrier gas can also lead to improved conversion and energy efficiency due to excited He^+, He_2^+ and e^- interacting with CH_4 and CO_2 generating CH_4^+ and CO_2^+ [108]. Other gases such as neon can be used however, it was found that for the same conditions, using argon as a carrier gas achieved the highest methane conversion compared to helium and neon in a planar type DBD reactor [110]. This was because argon shows a higher electron temperature and electron density hence, the numbers of

excited and ionized atoms are expected to be higher. Moreover, the density of active atoms is expected to additionally increase, because the energies of the excitation and ionization of argon are lower, therefore, argon can be expected to generate a larger number of excited and ionized atoms compared to helium and neon [110].

1.9.4 Voltage

The peak to peak voltage has a significant impact with regards to conversion and yields of products. Increasing the voltage has a proportional effect on discharge energy and results in a higher energy density of electrons. Chemical reactions or conversions are directly affected by excited or ionized species as are electron impact collisions. This can trigger the dissociation of reactants into their fragments for consequent reactions with other species, either in the plasma or on the surface of catalysts. For example it was found that increasing the voltage from 8 kV to 11 kV increased the production of hydrogen from methane and hexadecane from a total of 6.83 ml/min to 169.08 ml/min [95].

1.9.5 Frequency

In a DBD an alternating current with a high enough voltage is supplied to ionise the gases, generating a plasma, hence a suitable driving frequency must be chosen. At very high frequencies the limitation of current by the dielectric becomes less effective, DBD'S can operate in a frequency range of about 1 kHz to 10000 kHz [46], however in gas processing it is recommended that a frequency no more than 20 kHz is used [111]. At higher frequencies a higher energy consumption is experienced, this has to be taken into consideration for industrialisation and energy efficiency. A higher frequency can introduce more discharges per unit time, increasing conversion however only to a certain extent.

1.9.6 Packing material

For PBR's the type of packing material is an important parameter in all gas processing. Everything from packing size, material type and the gap between the electrodes has an effect on the plasma properties and therefore the desired process. Many investigations have been published on the effect of the packing materials geometry and yet an overall acceptance for ideal conditions has yet to be found due to the fact that the effect of particle size can depend on reactor type and geometry, processing gas and packing material. Butterworth et al found that the smaller the particles size the higher the breakdown voltage and the occurrence of partial discharging which has a negative effect. However, smaller size can increase the surface area for heterogeneous catalytic reactions and increase the contact points where plasma can form. This results in increased discharges leading to a higher quantity of radical species [54] Ergun et al found that the pressure drop is greater with increased packing volume and smaller particle size [55]. Adversely larger particle size result in a lower breakdown voltage and a decrease in the amount of partial discharges.

It is found that the effect of the particle size is different depending on the material, mainly due to shape, dielectric constant and porosity. Barium titanate ($BaTiO_3$) has a dielectric constant (ε) between 3000

and 12000 making it a perfect fit for use as a dielectric material in a PBR [53, 112]. Careful consideration into the material itself is not enough. The pellet size also has a key role in the plasma properties. The shape and size of the pellets affects the maximum discharge current peak, pressure drop in the reactor, breakdown voltage and the breakdown or formation of compounds [56]. Research was conducted by Butterworth et al. found that larger particles typically lead to lower conversion, while smaller particle size leads to higher breakdown voltage and leads to partial discharging which decreases the reactor performance [54]. The presence of $BaTiO_3$ or TiO_2, for example as the packing material, with a carrier gas of argon or nitrogen in a DBD, can change the nature of the discharge. Instead of the discharge being primarily formed of filamentary discharges without packing material a transition to surface discharges as well as filamentary on the catalyst has been reported. As a result there is an increase in electron energy, this enhances the concentration of higher energy electrons and increases the vibrational temperature of carrier gas leading to an effect on the plasma chemical reactions [113].

1.10 Surface engineering and coating methods.

Surface engineering is the changing of a materials surface either through changing the properties of the bulk material or by adding a material on the bulk substrate in order to change or enhance the surface characteristics. The three main ways in which a surface can be modified are:

- Alteration of a surface without changing the composition of the surface such as plasma treatment, hardening or heat treatment.
- A change in the surface composition but without adding an additional layer of another material.
- Surface coating through a deposition technique such as sol-gel, PECVD, magnetron sputtering or painting.

Surface properties have a significant influence on the behaviour and performance of a material as it is in direct contact with the surrounding environment. With surface engineering, the surface and substrate can be designed in order to enhance the performance in which neither is capable to produce on its own.

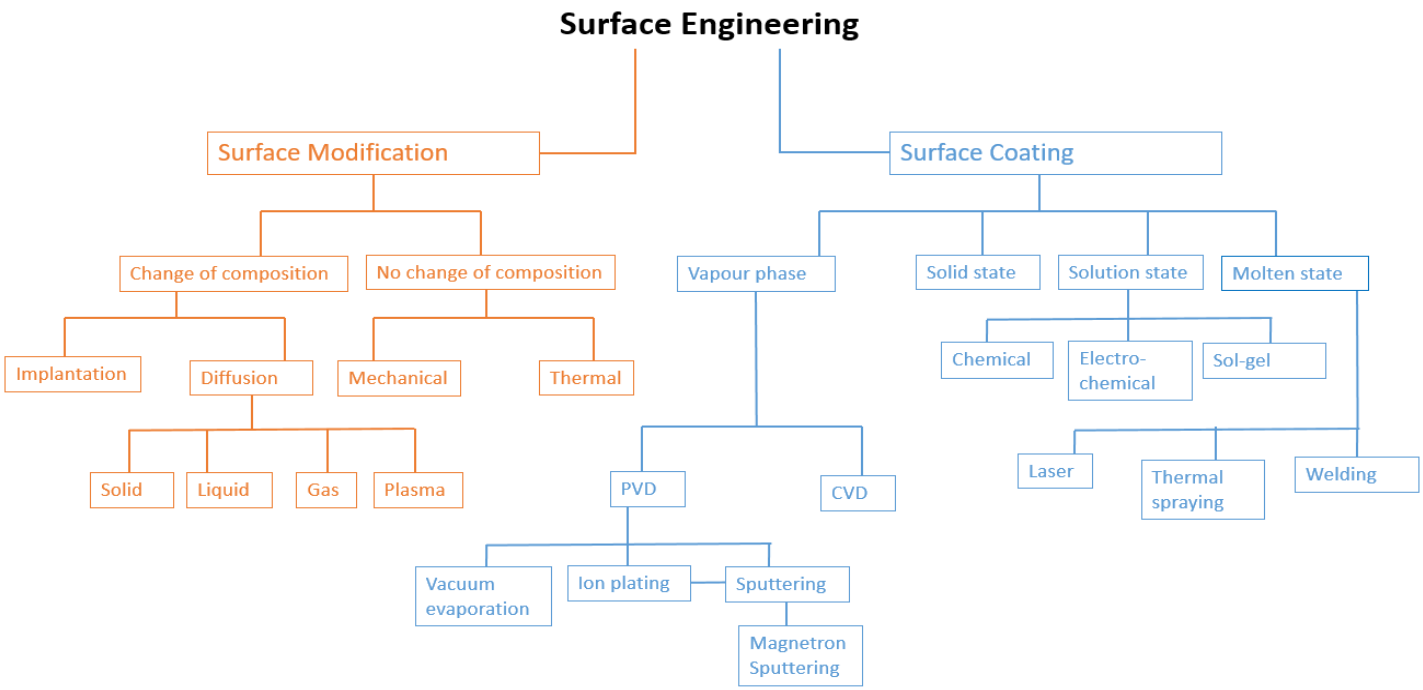

Figure 6 – Surface engineering tree and its sub components.

Thin films are a type of surface coating that can be defined as a low dimensional material coating that are made through the addition of a new layer of material onto a substrate through a deposition process. Thin films are in the range of nanometers to micrometers in thickness and can even be atomic monolayers. Thin films are currently used in a wide variety of applications for example as protective layers [114], photoactive layers [115], dry lubricants [116], catalysts and gas separating layers [117-119]. Thin film deposition were chosen for this work as they can exhibit good photocatalytic properties as demonstrated in previous studies [117, 120-122].

1.10.1 Coating processes

Thin films can be deposited through a variety of coating methods, as seen in figure 6. Surface properties which can be altered by thin film coatings are morphology, composition, structure, cohesion and adhesion. Thin film coatings are developed to achieve and improve the performance which neither can substrate nor coating material can achieve on its own. In this work when coatings are mentioned it refers to thin film coatings. Coating processes can be categorised as gaseous, solution, molten or semi-molten and solid-state processes.

Solid state processes generally produce thicker coatings which are greater than the scope of the work and types of coatings discussed. Solution state processes usually involve an aqueous solution followed by drying, deposits can be produced on metallic or non-metallic substrates. Gaseous state processes involve the coating material passing through a gaseous or vapour phase before deposition, chemical vapour deposition (CVD), and physical vapour deposition (PVD) are two prominent gaseous state process techniques.

Chemical vapour deposition

Chemical vapour deposition introduces the coating material in a gas flow, normally requires temperatures in the range of 150-12,000°C and deposits thicknesses in the range of 0.5-2000 μm. The pressure can be in the region of atmospheric pressure to 1 Pa or less. Use of lasers, electron beams, non-thermal plasma or ion bombardment is used to coat at lower temperatures. Well-adhered, uniform and dense coatings can be formed by this method [48, 123, 124].

PECVD

Plasma Enhanced Chemical Vapour Deposition (PECVD) is a widely accepted technique for thin-film production. PECVD has the capability to operate at lower temperatures than thermally driven CVD. The energetic conditions in a PECVD reactor allow for the creation of high-energy, relatively unstable bonding states as compared to more traditional thin-film techniques [125]. PECVD can be used to develop photocatalytic thin films [126, 127].

Solution state processes

One solution state process is the sol-gel process. Sol-gel generally follows three steps, those are hydrolysis, condensation and drying. Film thicknesses up to 1 µm can be deposited. Sol-gel is commonly used in catalyst coatings [128-130].

Wetness impregnation is a technique that can be used for the synthesis of catalyst thin films on a support and is a very common method due to its technical simplicity, low cost and low waste. The general method is the combination of support and a precursor containing solution. The catalyst can then be dried and calcined to obtain the desired catalyst. It is fundamental to find the optimum parameters for this technique as the effectiveness of the catalyst relies on their size and distribution over the support.

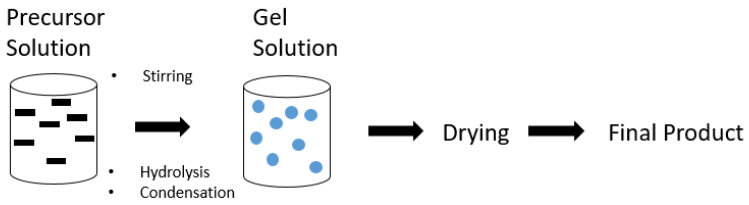

Figure 7 –The sol gel process, adapted from [129, 131].

Physical vapour deposition

Physical vapour deposition (PVD) involves the atomisation or vaporisation of the coating material from a solid state for deposition onto a substrate [132]. There are many types of PVD and usually differ by their means of atomisation of the target material. This is often divided into evaporation and sputtering where evaporation is achieved by thermal processes and sputtering is the kinetic atomisation of coating material. PVD processes can deposit films of elements, molecules and compound by the reaction of the depositing material and the ambient gas environment. In PVD several factors can affect the film properties:

- Substrate surface condition.
    - The substrate surface includes surface morphology, chemistry, crystallography, mechanical properties surface defects, outgassing and stability of the surface.
- System and fixture geometry
    - Angle of incidence, uniformity of the deposition and deposition rate.
- Deposition parameters
    - Substrate temperature, deposition rate, energy input to the growing surface, gaseous contamination, presence of concurrent energetic particle bombardment during growth.
- Film growth
    - Nucleation density, surface mobility, type and extent of the interface, growth morphology, reaction with ambient gases, gas entrapment, residual film stress, lattice defect generation, and momentum input to the growing surface.

- Postdeposition processing and reactions.
    - Reaction of film surface with ambient gases, adsorption onto film surface, reaction of film with storage environment.

Vacuum evaporation

Vacuum evaporation is a PVD process in which material is evaporated via a thermal vaporisation source and reaches the substrate without collision with gas molecules.

Advantages include:

- High purity films.
- Solid source material.
- Line of sight deposition.
- Monitoring and control of film deposition.
- Relatively cheap.

Disadvantages include:

- Alloy or compound films are difficult to produce.
- Complex shapes are difficult to coat due to line of sight.
- Poor films thickness uniformity over large area.

Sputter deposition

Sputter deposition is the deposition of materials vaporised from a surface also known as the target. The target material is physically ejected by momentum transfer from an energetic bombarding particle in a non-thermal process. This is generally done by a gaseous ion accelerated from a plasma and takes place in a vacuum.

Advantages include:

- Elements, alloys and compounds can be deposited relatively easily.
- The target provides a stable, long lived vapourisation source.
- Reactive deposition is relatively straight forward.

Disadvantages include:

- Low sputtering rates.
- Film properties depend on angle of incidence.
- Targets can be expensive.
- Possible film contamination.

Ion plating

Ion plating uses concurrent or periodic energetic particle bombardment of the depositing film to modify and control the composition and properties of the depositing film. The depositing material can be vaporised by evaporation or sputtering. The energetic particles used for bombardment are an inert gas or reactive gas similar to sputter deposition.

Advantages include:

- Controlled bombardment can be used to modify film properties.
- Film properties are less dependent on the angle of incidence.
- Bombardment can be used to improve the chemical composition of the film.

Disadvantages include:

- Many variables to control such as mass, energy and flux of depositing particles.
- Difficult to obtain uniform ion bombardment.
- Substrate heating can be excessive.
- Bombarding gas can be incorporated into growing film.

1.10.2 Magnetron sputtering

Magnetron sputtering is a PVD process, which is the most widely used sputter deposition technique [22]. Argon is supplied to the vacuum chamber and a high voltage is applied between the cathode – commonly located behind the sputtering target and the anode – commonly connected to the chamber as electrical ground. The magnetic field produced by the magnetron form electron traps which are configured that the $E \times B$ electron drift (the cyclotron motion of a charged particles around magnetic field lines), where B is the magnetic field strength and E is the electric field, currents close on themselves [133]. This enables a dense plasma to concentrate around the target causing more high energy collisions and in turn increasing the sputtering rate. This is schematically shown in Figure 8.

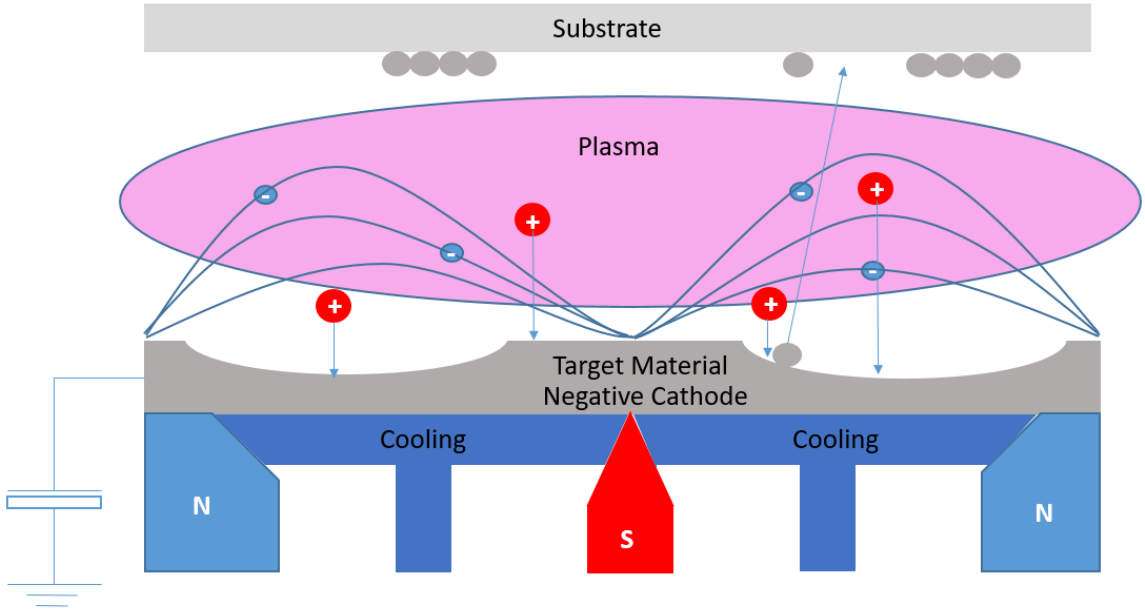

Figure 8 – General process of magnetron sputtering, adapted from [134].

The reason magnetron sputtering is the chosen technique for photocatalyst deposition onto dielectric material is due to its ease of forming high quality compound films such as nitrides, oxides, carbides or combinations [135]. This makes it ideal for the TiO_2 or doped TiO_2 films to be formed due to the ability of using more than one target material at the same time. Electrons from the target accelerate away from the surface by the electric field but spirals back around the magnetic field lines and returns to the surface. The $E \times B$ force traps the electrons and causes the electrons to also move normal to the $E \times B$ plane and form a circulating pattern. Due to the arrangement of the magnets the path of the electrons form a characteristic 'racetrack' shape and cause non-uniform erosion of the target surface.

The arrangement of the magnetics of the magnetron can be altered in order to achieve different properties. They are usually defined as balanced and unbalanced magnetrons. Balanced magnetrons keep the electrons close to the surface of the target due to the equal strengths of the north and south magnets whereas the unbalanced configuration has unequal strengths of magnets and can alter the

magnetic field by increasing or decreasing the plasma region, as seen in figure 9, this can be useful in reactive sputtering.

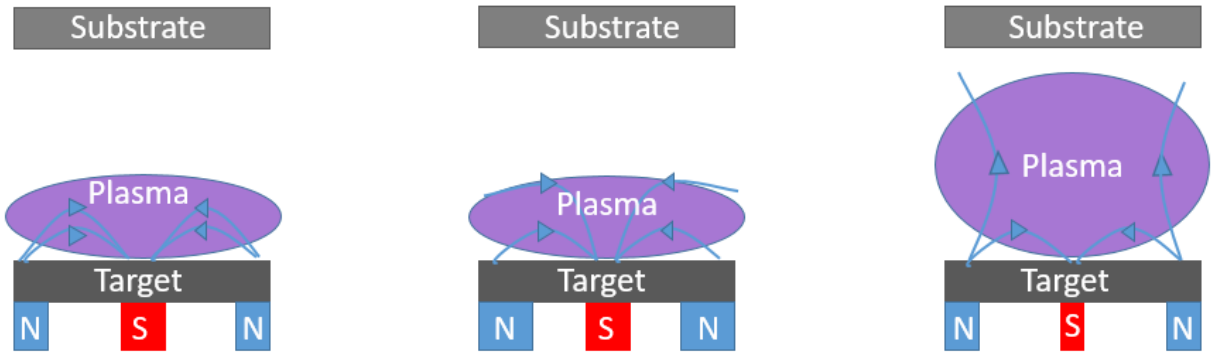

Figure 9 – Different configurations of the magnetron. Balanced magnetron sputtering (left), unbalanced type 1 (middle), unbalanced type 2 (right).

Reactive sputter deposition is the process whereby the depositing material reacts with the ambient gas to form a compound film material. The disadvantage of this is the poisoning of the target with the reactive gas which reduces sputtering rate and efficiency. In reactive sputtering the reactive gas can be mixed with an inert gas resulting in increased dissociation, ionisation and excitation of the reactive gas in the plasma region. The type of discharge used in magnetron sputtering is the glow discharge plasma. This type of plasma is again formed by partially ionizing a gas, for this process it is formed at a pressure well below atmospheric pressure.

1.10.3 Surface Characterisation

Characterisation of film properties and the bulk substrate is important to ensure the substrate/film properties are what is desired. It is also important to ensure reproducibility and confirmation of the physical properties. Characterisation can involve analysing surface and bulk morphology such as crystallinity, stoichiometry, optical properties such as optical adsorption and colour, chemical properties, corrosion and catalytic activity. Moreover, mechanical properties such as hardness, toughness and electrical properties such as dielectric constant, conductivity can be measured.

Surface measurements can involve testing to the whole film for example, of catalytic activity. However, some measurements such as stoichiometry and crystallinity are conducted on a specific area and are usually applied to the whole film which can be an assumption.

Certain techniques used to characterise the individual properties of the surface and film are, surface profilometers, atomic force microscope (AFM), scanning tunnelling microscope (STM), magnetic force microscope, white light interferometry and scanning electron microscopy (SEM).

Techniques used to analyse chemical properties are, Energy Dispersive X-Ray Spectroscopy (EDX), X-Ray Fluorescence (XRF), X-Ray Powder Diffraction (XRD), Raman Spectroscopy, X-Ray Photoelectron Spectroscopy (XPS), Infrared Spectroscopy and Rutherford Backscattering Spectrometry.

Finally, examples or surface techniques for physical properties are, tensile testing using the small punch technique and nano-indentation.

For the characterisation of the prepared photocatalysts in this report imaging techniques such as SEM and Raman spectroscopy were used, crystallography techniques such as XRD and Raman spectroscopy were used and elemental characterisation techniques such as EDX and XPS were used. These techniques are explained in further detail in chapter 2.

CHAPTER 2 - METHODOLOGY

In this chapter an extensive description of the methodologies used for the research carried out for this thesis is presented. This includes, in detail, a description of the magnetron sputtering rig used and the procedure used for preparation of the coatings, along with this the process of treatment of the particulates prior to coating and post coating is described. Furthermore, the equipment and techniques used for characterisation of the coated particulates is described, this includes scanning electron microscopy (SEM), elemental mapping, x-ray diffraction (XRD), x-ray photoelectron spectroscopy (XPS), Brunauer-Emmett-Teller (BET) surface area analysis and Raman spectroscopy. In regard to the evaluation of the performance of the photocatalytic coated particulates, the degradation of methylene blue dye solution was used, the methodology will outline the procedure of this test and subsequent analysis. A non-thermal dielectric barrier discharge was designed and developed for this research, an in depth overview of the system and its operation is presented in the methodology along with the post processing and evaluation of various parameters and outputs, this includes the measurement and calculation of the applied power control of input gases and the post processing of the output gases, which were analysed by Fourier transform infrared spectroscopy (FTIR). Finally, the method for measuring the optical characteristics produced by the plasma by optical emission spectroscopy (OES) is described.

2.1 Magnetron Sputtering of Titanium Dioxide and Titanium Dioxide Doped with Tungsten

Magnetron sputtering was used to coat glass and $BaTiO_3$ particulates with TiO_2 and TiO_2 doped with tungsten (TiO_2-W). A schematic diagram of the rig used for the coatings can be seen in figure 10, the oscillating bowl was directly underneath the two targets of titanium and tungsten. The tungsten target was covered up when only depositing titanium. For glass particulates, this allowed the coating to be characterised and optimised, whereas, the $BaTiO_3$ was the material of choice for the packed bed plasma reactor, due to its high dielectric constant (up to 12,000) [112]. Prior to sputtering a pre-treatment procedure was performed for the $BaTiO_3$. Finally, post-treatment was performed by annealing to obtain photocatalytic phases.

2.1.1 Pre-treatment of substrate

For the deposition of photocatalytic coatings onto glass beads, borosilicate glass beads from Sigma Aldrich were used. The nature of the substrate required no pre-treatment for preparation prior to coatings. $BaTiO_3$ particulates purchased from Catal International had a fragile surface therefore prior to coating, calcination at 1100°C in a Carbolite Gero furnace, in air, for 4 hours was performed in order to achieve a more robust surface.

2.1.2 Deposition of TiO_2

Magnetron sputtering of photocatalytic thin films was performed in a high vacuum with the presence of argon and a reactive gas of oxygen. The deposition technique was powered by a pulsed DC power supply. For the coatings of TiO_2 a 99.5% pure titanium target fitted on a Gencoa Ltd unbalanced type II magnetron was used within a sputtering rig which was pumped down to a minimum base pressure of 1×10^{-4} Pa, achieved through a combination of rotary and diffusion vacuum pumps, before argon and oxygen were introduced. For the coatings of TiO_2-W, a 99.5% pure titanium and a 99.5% pure tungsten target were used, the same base pressure as aforementioned coatings was achieved. The pulsed DC power was supplied to the magnetron by an Advanced Energy Pinnacle Plus, Fort Collins, CO, USA. The powers applied for the deposition of coatings varied from (80 – 1000 W), further details on operational parameters for individual coatings can be seen in Chapter 3. The base pressure was measured by an Edwards penning gauge, prior to the commencement of sputtering the penning gauge was switched off and a MKS baratron capacitance monometer was used to measure the pressure inside the chamber. The supply of argon and oxygen were controlled by MKS mass flow controllers.

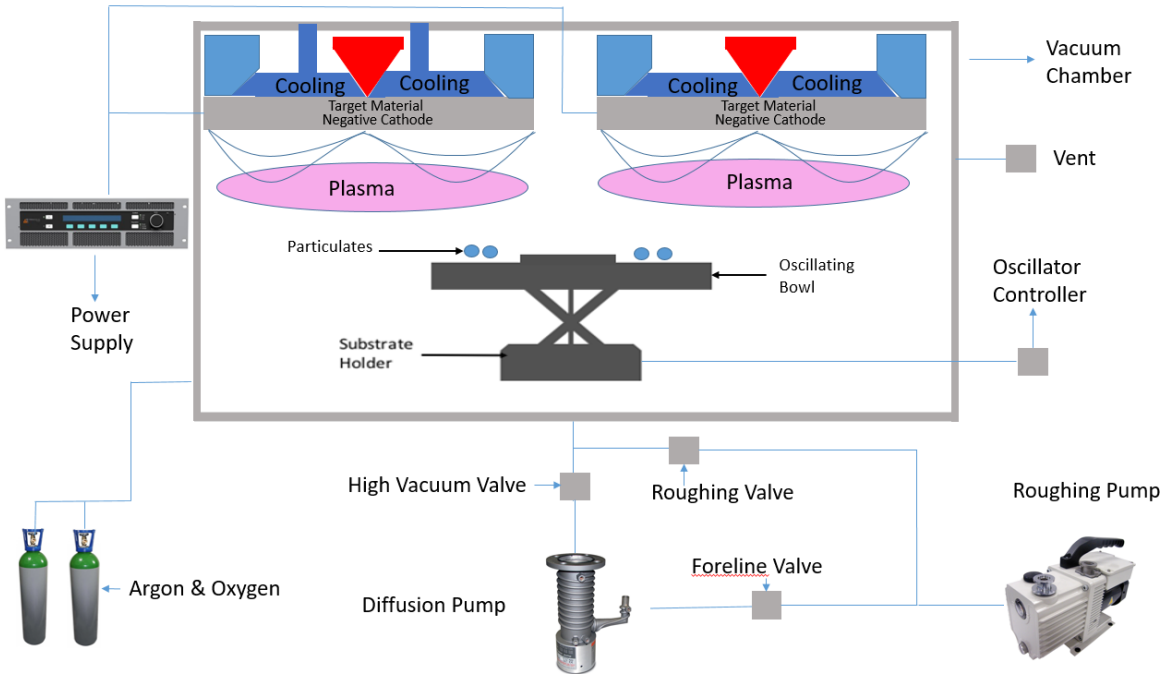

Figure 10 – Schematic of the vacuum system of the magnetron sputtering rig used for the coatings of titanium dioxide based photocatalysts.

The deposition process for the TiO_2 photocatalyst onto $BaTiO_3$ particulates was carried out using a bespoke oscillating bowl for the uniform coating of the particulates, as shown in figure 11. The bowl oscillates vertically with springs connected between the electromagnet and the base plate which also impart a lateral twisting moment to the oscillation. The resulting motion causes particles in the bowl to roll or hop in a circular path around the bottom of the bowl and, thus, over time all surfaces of the particles are exposed to the coating flux. The design of the oscillator is described in detail elsewhere by Ratova et al and has also been used for the coating of powders or particulates [136, 137]. The oscillating bowl is powered by an analog controller which allows the level of vibration to be varied, for clarity in this work, the term oscillating power describes this.

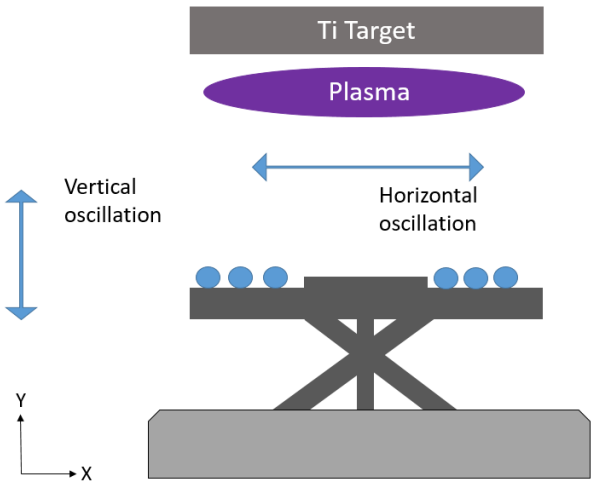

Figure 11 – Schematic of oscillating bowl mechanism for deposition of TiO_2 using magnetron sputtering.

2.1.3 Post-treatment of Substrate

Coated particulates were left to cool before venting the chamber and subsequent storage. Coated particulates were annealed in an air-filled muffle furnace, model Carbolite 3000. Once annealing was finished they were left to cool to room temperature.TiO_2 thin films were heated to 500 °C for an hour to obtain an anatase phase whereas, TiO_2-W thin films were annealed to 600 °C for 30 minutes in order to obtain an anatase phase. TiO_2-W is annealed at 600ºC for 30mins due to the effect of tungsten inhibiting the amorphous to anatase phase change by lowering the diffusivity of Ti and O ions and constraining the volume available for anatase lattice formation hence, requiring a higher annealing temperature to obtain an anatase phase [120, 138].

2.2 Surface characterisation

Surface characterisation of the coating properties and the bulk substrate is important to ensure the substrate/coating properties are what is desired. It is also important to ensure reproducibility and confirmation of the physical properties. In this work the surface characterisation techniques used were SEM/EDX, XPS and Raman spectroscopy and BET surface area analysis. SEM/EDX was used to look at the physical nature of the coating, to understand the topography of coating which was present on the substrate and to observe the coating's uniformity and dispersion. Raman spectroscopy was used to analyse the crystallinity of the coating as this is fundamental to the photocatalytic properties. XPS was used in order to understand the chemical bonds present and further characterise the coating and its properties, this can aid in the determination of the effect of the coatings on the plasma chemistry. BET surface area analysis was used in order to investigate the surface area of both the substrates prior to coating and after coating to give a greater understanding of the surface topography.

2.2.1 SEM/EDX

Scanning electron microscopy (SEM) is a physiochemical technique which involves firing a focused high energy beam of electrons with energies of between 5-30 kV at a sample. It is used as a method of visualising a surface at a high magnification and depth of field otherwise unachievable by optical microscopes giving a topographical view of a sample. It can also be used to detect the elemental composition at a samples surface via energy dispersive x-ray spectroscopy (EDX or EDS), the technique differs to an optical microscope, which detects light whereas scanning electron microscopy generates and detects electrons. Optical microscopes rely on lens technology to achieve high resolutions, (the limit of resolutions is defined as the minimum distances at which two things can be seen apart), however, this can only reach around a resolution of ~200nm. SEM, by using electrons can achieve a resolution of 0.9nm in comparison the human eye at maximum can achieve a resolution of 0.1mm. It can also analyse the elemental makeup by EDX. Electrons are fired at the surface of a material and subsequently interact in various ways, see figure 12. The result of this produces photons, electrons (back scattered electrons and secondary electrons) and x-rays which then hit different types of detectors eventually leading to the production of an image. The configuration of scanning electron microscopes harbour an electron gun, electron lenses, apertures, stigmator, electron detectors, a vacuum system, scanning coils, a specimen holder and specimen stage, see figure 13. The SEM requires a vacuum environment in order to function properly. Operating parameters of an SEM include: accelerating voltage, spot size, aperture size and working distance.

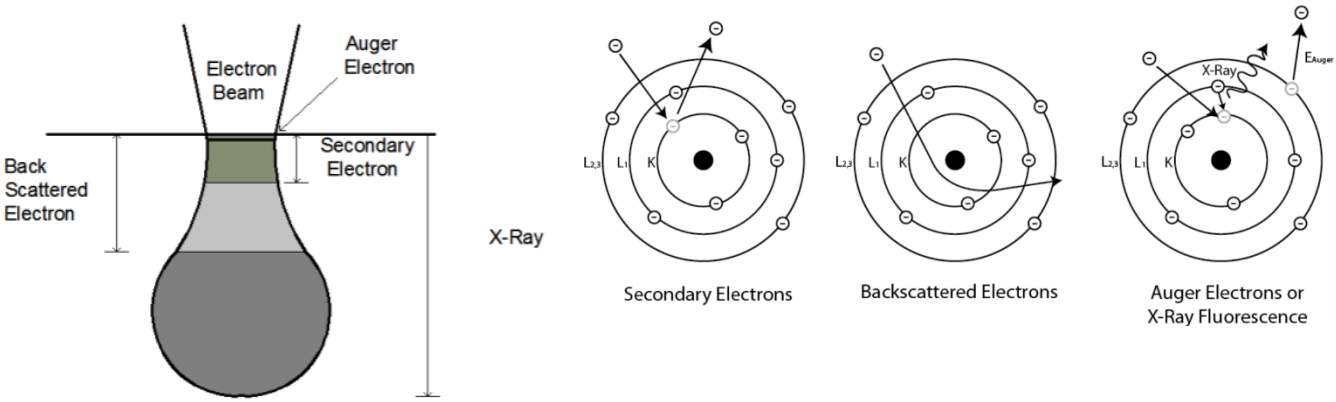

Figure 12 – Different interactions of incident electrons at the substrate of a sample in the scanning electron microscope [139, 140].

EDX spectroscopy is the detection of the elemental composition of a sample from boron upwards, by atomic number, due to lighter elements emitting either no characteristic x-rays or too low of an energy x-rays. The electrons interact with the substrate and cause the emission of characteristic x-rays which can be differentiated by energy and hence the element along with its concentration can be determined. The electron beam will excite the electron in the nucleus of the atom, causing it's ejection from the nucleus and creating an electron hole. An electron of higher energy will replace the missing ejected electron and in doing so releases a characteristic energy X-ray.

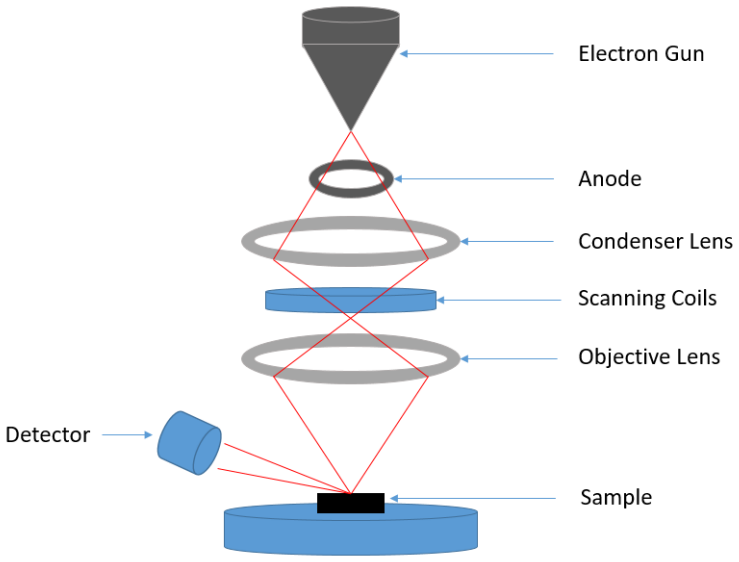

Figure 13 – Schematic representation of SEM microscope.

It can be seen in figure 12 that the previously evocated emissions are not the only ones that can be emitted from a surface, as other emissions are not measured in this work, they are therefore not explained here.

A JEOL JSM-5600LV SEM was used to collect the images in this report. The optical zoom was 13kX with a working distance of 6.2 mm and an acceleration voltage of 2 kV.

2.2.3 Raman spectroscopy

Raman spectroscopy is an analytical technique which can be applied to a wide range of materials encompassing most solid surfaces. Raman spectroscopy is known as a complementary technique to IR spectroscopy but is sensitive to the vibrational modes which are not as strongly shown via IR spectroscopy. Molecules can have vibrations which are not IR active (the net molecular dipole moment does not change) but have vibrations which are Raman active (the polarizability of the molecule changes), therefore the polarizability of a molecule is the parameter used in determining Raman intensities. Raman spectroscopy relies on a scattering process known as the Raman effect. The Raman effect was first predicted by Smekal in 1923 but first observed by Sir C V Raman in 1928 [141, 142]. The Raman effect is the process whereby incident radiation is absorbed into a virtual electronic state of the molecule followed by emission when going back to its lower excited vibrational state. The detection of photons is analysed in order to detect the molecular vibrations of the sample. Raman spectroscopy utilises a laser as an excitation source and therefore requires a high flux of photons. Raman spectroscopy is a technique that can be applied to most solid surfaces and is applicable to small areas of a sample.

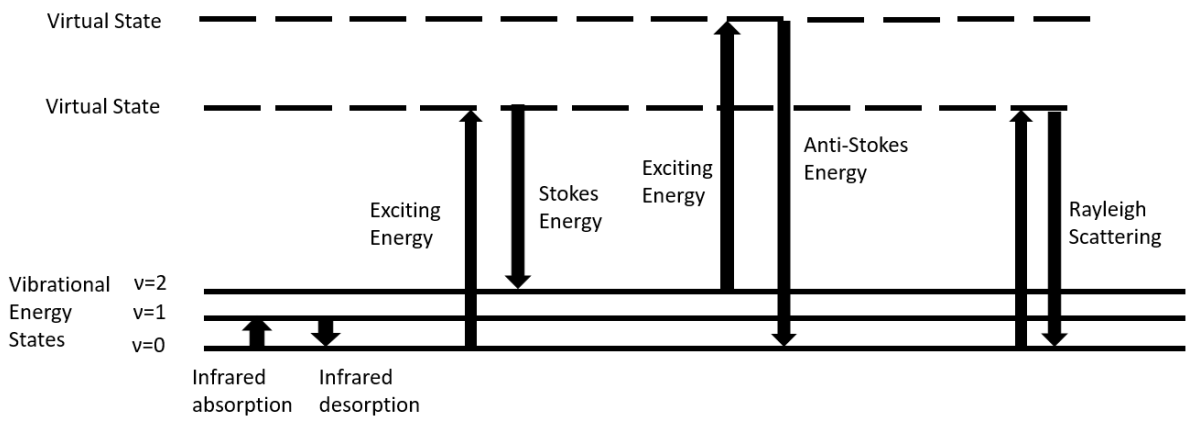

Figure 14 – Transitional energy levels of absorption and desorption of energy in Raman spectroscopy

There are two types of Raman scattering which can occur, these are Stokes and anti-stokes, as shown in figure 14. Most photons of light will experience Rayleigh scattering, which is a process where the photon is scattered by the electron cloud, resulting in minimal energy or frequency change. However, if the scattered photons cause nuclear motion, this will result in energy gain or loss by the photon in a transfer with the molecule, depending if it is stokes or anti-stokes. Stokes energy is where the photon causes a shift in energy of the electron from a lower state to a higher virtual state and a relaxation to an energy state higher than the original state, emitting a lower energy photon. Anti-stokes energy however occurs if the electron is already in a higher excited state and once excited to a virtual state relaxes to the ground state resulting in a higher energy photon being released.

Raman spectroscopy is a useful non-destructive analytical technique and requires no sample preparation. Due to its ability to analyse a small amount of sample it can be ideal for photocatalyst characterisation. Raman spectroscopy is therefore useful in this work to analyse the crystal structure of photocatalytic coatings.

Raman spectroscopy was performed using a ThermoFisher scientific DXR Raman microscope with a 532 nm laser at 1 mW, 50x LWD microscope, 900 line per mm grating, an estimated spot size of 1.1 μm and a 25 μm pinhole.

All spectra obtained were compared to a database of standard spectra provided by ThermoFisher scientific in order to analyse the crystallography of samples.

2.2.4 XPS

X-ray photoelectron spectroscopy (XPS), also called electron spectroscopy surface characterisation is a technique for investigating thin surface layers. In XPS the sample is bombarded with *x*-rays with a well-defined energy, usually from an Al Kα or Mg Kα source. The x-rays interact with core electrons around the nucleus of the different atoms present at the surface of the sample and cause an emission of a photoelectron. The kinetic energy (KE) of these emitted electrons is characteristic of the element from which the photoelectron originated. Each electron present in an atom has characteristic binding energies, it is this that is measured and analysed. The position and intensity of the peaks in the resulting energy spectrum provide the desired chemical state and quantitative information. In order to quantify the binding energy the photo emitted electrons are measured by their kinetic energy by a detector and electrons that are emitted from the top 1-10 nm of the material are analysed.

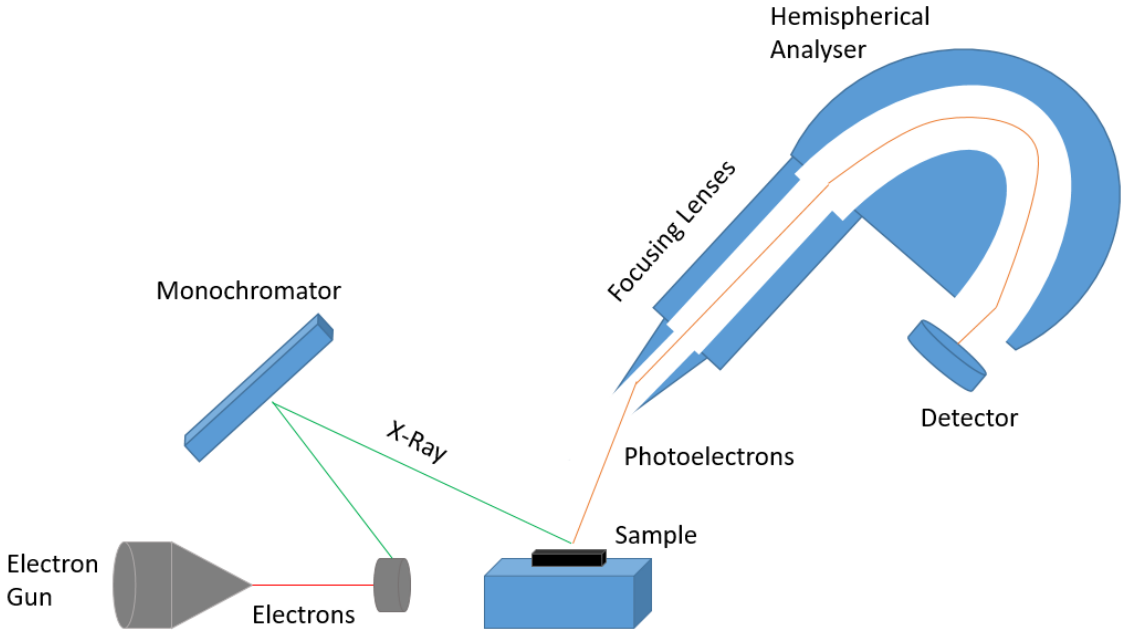

Figure 15 - Schematic representation of XPS spectroscopy. Adapted from [143].

The relationship between the measured KE of the photoelectron and the binding energy is shown in [Eq. 12].

$$BE = hv - KE \qquad \text{[Eq. 12]}$$

A photoelectron spectrum is recorded by counting ejected electrons over a range of electron kinetic energies. The energies and intensities of the photoelectron peaks enable identification and quantification of all surface elements, except hydrogen, as it has no inner shell electrons [144]. Instead, hydrogen has a 1s electron which is a valence electron, hence any signal from hydrogen would overlap with signals from excitation of valence electrons from other surface atoms, as binding energies of valence electrons

change significantly . XPS can measure the elemental composition, empirical formula, chemical state and electronic state of the elements within a material.

XPS analysis was performed with an AMICUS photoelectron spectrometer (Kratos analytical AXIS Supra^{+}) equipped with Mg K X-rays as the primary excitation source. The binding energy was referenced to the C 1s line at 284.8 eV for calibration. Curve fitting was performed applying a Gaussian function with a Shirley background. The detector was a hemispherical analyser coupled to a delay line detector, operating with a 110 μm aperture in the lens column with the lens operating in the FOV2 mode with a resolution of 40 eV.

2.2.5 Brunauer-Emmett-Teller Surface Area Analysis

Brunauer-Emmett-Teller (BET) measures the surface area of a sample based on the gas adsorption as per the BET method, seen [Eq.13]. At -196°C (boiling point of nitrogen) nitrogen gas is below the critical temperature and so condenses on the surface of a sample. It is assumed that the gas condenses onto the surface in a monolayer and so, as the atomic radius of nitrogen is known, the amount of adsorbed (condensed) gas is correlated to the total surface area of the sample including pores at the surface (inaccessible pores are not detected). Derived over sixty-five years ago, the application of the BET equation is one of the most popular approaches for the calculation of the specific surface area. The determination of surface areas from the BET theory is an application of the BET equation, see [Eq. 13], where X is the weight of the gas adsorbed, P/P_o is the relative pressure, X_m is the monolayer capacity and C is constant [145].

$$\frac{P/P_o}{X\left[1-\left(\frac{P}{P_0}\right)\right]} = \frac{1}{X_m C} + \frac{C-1}{X_m C}\left(\frac{P}{P_0}\right) \qquad \text{[Eq. 13]}$$

The general method of performing a BET surface area measurement is as follows, first a sample within a tube is degassed in order to remove the adsorbed species from the sample by heating and evacuating, or by adding nitrogen. Secondly the sample and reference tube are evacuated. At this stage most methods will perform a dead volume measurement using an inert gas such as He in order make sure both tubes have similar dead volumes. Subsequently the dead-volume gas is pumped out. Next the adsorbate gas is admitted into the two tubes, adsorption of the gas onto the sample occurs, in doing so the pressure in the confined volume falls until the adsorbate gas and adsorptive gas are in equilibrium. Therefore the amount of adsorbate gas at the equilibrium pressure is the difference between the amount admitted and amount remaining in gas phase.

A number of data points should be collected. The P/P_o should range from 0.025 to 0.30 to successfully determine the surface area using the BET equation. At relative pressures higher than 0.5, there is the onset of capillary condensation, and at relative pressures that are too low, only monolayer formation is occurring. When the BET equation is plotted, the graph should have a positive gradient. If such a graph is not obtained, then the BET method was unsuccessful in obtaining the surface area. The slope and y-intercept can be obtained using least squares regression. The monolayer capacity X_m can be calculated with [Eq. 14] [145].

$$S_t = \frac{X_m L_{av} A_m}{M_v} \qquad \text{[Eq. 14]}$$

Once X_m is determined, the total surface area S_t can be calculated with the following equation, where L_{av} is Avogadro's number, A_m is the cross sectional area of the adsorbate and equals 0.162 nm^2 for an absorbed nitrogen molecule, and M_v is the molar volume and equals 22414 mL.

BET surface areas of the samples were calculated in the relative pressure range 0.05–0.30 by nitrogen adsorption / desorption measurements using a Micromeritics ASAP 2020 surface area analyser at −196 °C. Samples were degassed under vacuum ($p < 10^{-5}$ mbar) for 12 h at 300 °C prior to analysis.

2.3 Photocatalytic Activity through the Methylene Blue Degradation Method

The photocatalytic activity of the coated particulates were analysed using dye degradation. Methylene blue was chosen due to its frequent use in testing for photocatalytic activity [146-149]. ISO standard 10678 confirms the use of methylene blue as a model organic dye for the determination of photocatalytic activity of surfaces in an aqueous medium [150]. 3.0 g of glass particulates and 1.5 g of $BaTiO_3$ particulates were used per test due to the different densities of the particulates. An Ocean Optics DH-2000-BAL UV-VIS-NIR spectrometer, UV-A source (2 × 15 W Sankyo Denki black light blue lamps, peaked at 365 nm) and Spectrasuite software, which measures and displays the absorption of light passing through the cuvette dye solution was used. Particulates were placed within a covered cuvette (40 x 40 mm) with 50mL of methylene blue solution (2 µmol/L) and left until the absorption of methylene blue on the surface of the particulates was in equilibrium with the methylene blue in solution. Subsequently the UV light was radiated upon the sample, and the degradation of methylene blue was measured for 2 hours. The degradation takes place according to [Eq. 15] with the colour change from blue to colourless [151].

$$C_{16}H_{18}N_3SCl + 25.5O_2 \xrightarrow{hv>bandgap,\ TiO_2} HCl + H_2SO_4 + 3HNO_3 + 16CO_2 + 6H_2O \qquad \text{[Eq. 15]}$$

The characteristic wavelength of absorption of methylene blue dye, which was measured, is 664.11 nm. The increase in light passing through the solution is proportional to the degradation of the methylene blue dye. The reaction rate constant, k_a, of methylene blue degradation is taken as a measure of the photocatalytic activity of the coated particulates, and was calculated using [Eq. 16] where A_o is the absorbance at the start, 0 and A_t is the absorbance at time, t [120, 152].

$$\ln\left(\frac{A_o}{A_t}\right) = k_a t \qquad \text{[Eq. 16]}$$

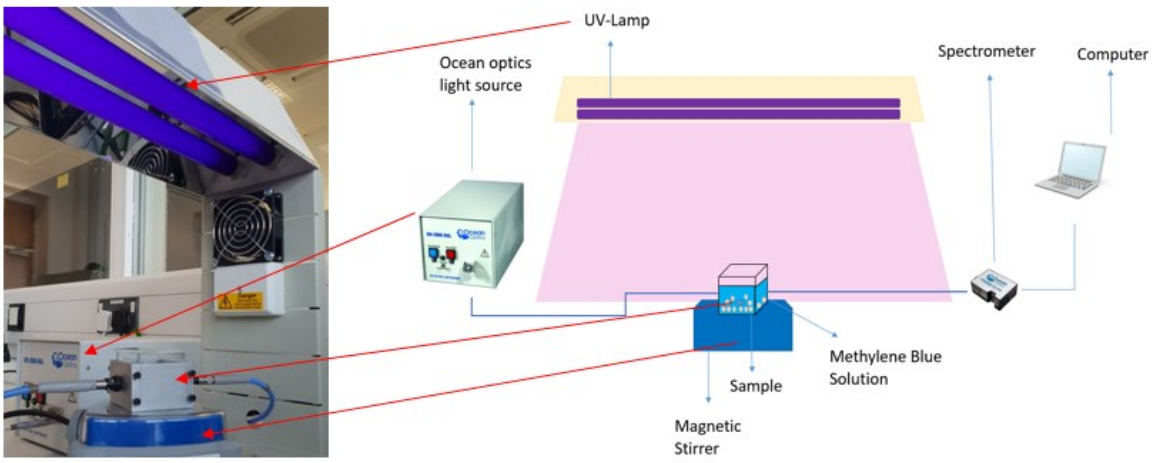

Figure 16 – Methylene blue degradation experimental setup for the measurement of photocatalytic activity of coated particulates.

2.4 Overview of the dielectric barrier discharge closed system and power supply for the generation of non-thermal plasma.

2.4.1 Packed bed reactor

A one-stage configuration packed bed reactor with $BaTiO_3$ dielectric bead packing material, sourced from CATAL International, has been constructed for the research carried out in this thesis. Barium titanate beads can be produced by heating barium carbonate ($BaCO_3$) and titanium dioxide (TiO_2) to around 1000ºC [153]. $BaTiO_3$ has a dielectric constant between up to 12,000 and is commonly used as a dielectric material for gaseous pollutant remediation with scientific literature [53]. The dielectric constant is affected by the operating conditions, such as temperature, applied frequency and applied electric field strength. The packed bed reactor, shown in figure 17 and 18, was designed using computer aided design software and manufactured in house. It consists of: two replaceable electrodes, a funnel (machined inside a stainless-steel cylinder), electric wire attachment, 'cork' and a gas pipe welded to the funnel. A quarter inch stainless steel tube with wall thickness of 1 mm was welded onto a 27 mm outer diameter stainless steel funnel which was manufactured using computer numerical controlled (CNC) machines. On the end of the funnel a flat metal end with 87 holes of 1 mm diameter and a surface area of 1253.37 mm^2, was cut by water jet from sheet metal, for gas transfer through the packed bed reactor. A removable acrylonitrile butadiene styrene (ABS) plastic cork was 3D printed using an Ultimaker 2+ 3D printer. The cork has a groove for an O-ring in order to provide a seal between the inside of the reactor and the external atmosphere. The encapsulating borosilicate glass tube had an inner diameter of 28 mm and a 2 mm wall thickness. Dielectric beads of $BaTiO_3$ are sandwiched between the two electrodes. The mass of the $BaTiO_3$ packing material for various separation of the electrodes was measured and recorded. The specific mass was then used and kept constant to ensure the amount of beads in the reactor is fixed when experiments are run.

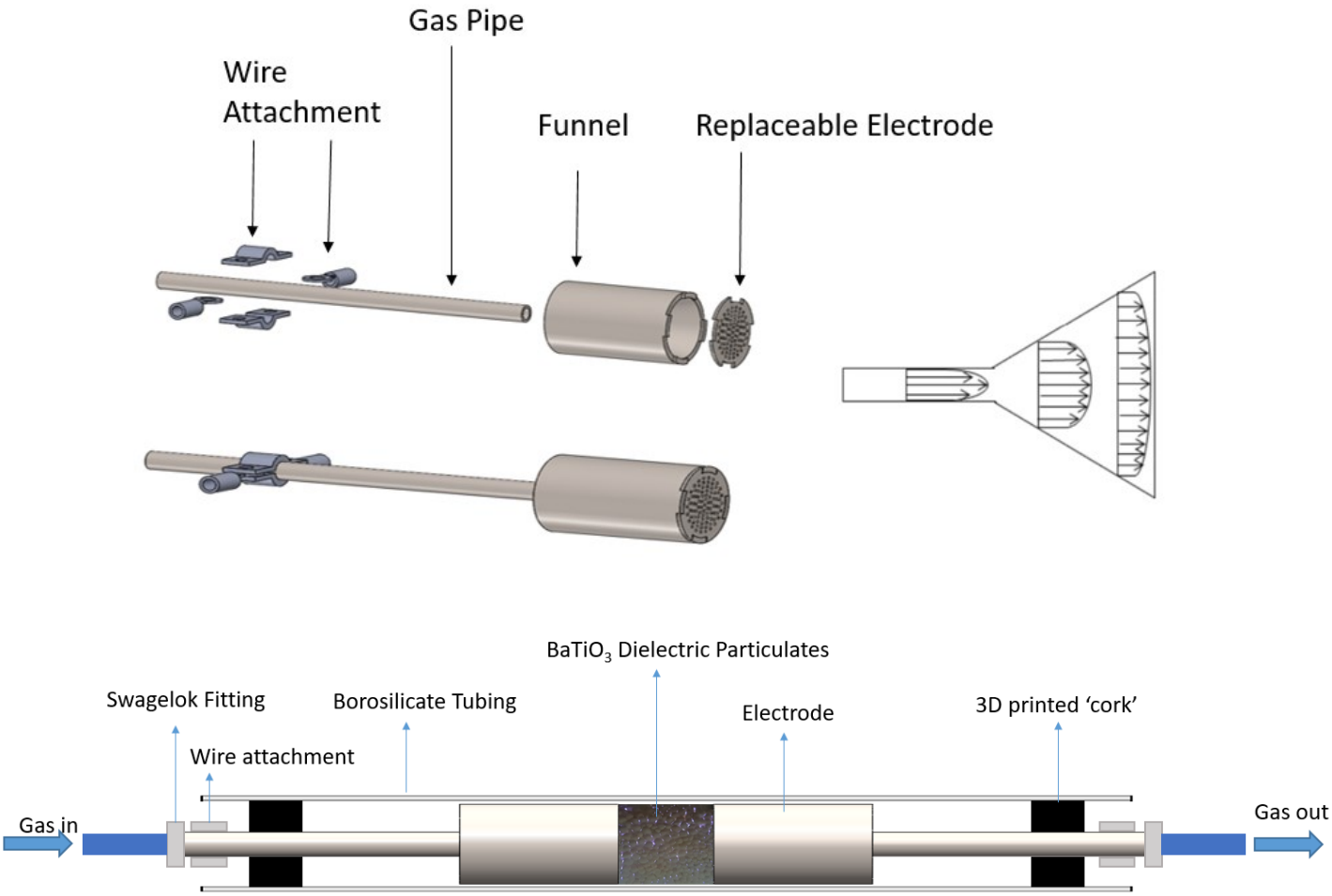

Figure 17– Packed bed reactor in exploded view and assembled view, velocity profile of a gas flowing out of a funnel (top). Full schematic of the PBR setup (bottom).

Figure 18 – Packed bed reactor in operation with $BaTiO_3$ packing material.

2.4.2 Power supply

In order to provide the required electric field for generating plasma, a bespoke power supply was used. The power supply consists of a signal generator (TTI TG2000), audio amplifier (ProSound 1600) and a custom-built high voltage transformer (Amethyst Designs). Current and voltage measurements were made with a Pearson 4100 current monitor and a Tektroniks 1000:1 voltage probe, recorded on a Tektronix DPO 3014 digital oscilloscope. Applied power was calculated from the current and voltage measurements, see appendix CODE 3 for MatLab code used.

2.4.3 Closed system/gas control

A MKS multi gas controller 647C controlled the mass flow controllers which supplied the gases. The mass flow controllers were MKS G Series with an upper limit of 5 SLM and lower limit of 0.5 sccm. The methane and carbon dioxide was mixed with argon at a flow rate of between 200 sccm and 2 SLM to ensure the gas mixture was well below the lower explosive limit of 5 % of methane in air. Regular checks to the system was performed to ensure there was no leaks in the system.

2.4.4 Dry reforming of methane using a packed bed plasma reactor

Prior to beginning the experiments the closed system was flushed through with inert argon gas to purge the impurities such as water vapour or the residual process gases from previous experiments, and a background for the FTIR was taken. Methane and carbon dioxide were then switched on. The gases were allowed to flow for 30 minutes before recording three FTIR scans, each 15 minutes apart, to ensure the gases were at steady state and the intensity of the characteristic peaks showed no deviation. After the gases were at steady state plasma was initiated by increasing the voltage to the required level. At the time of 10, 15 and 20 minutes an FTIR scan and the electrical characteristics were recorded.

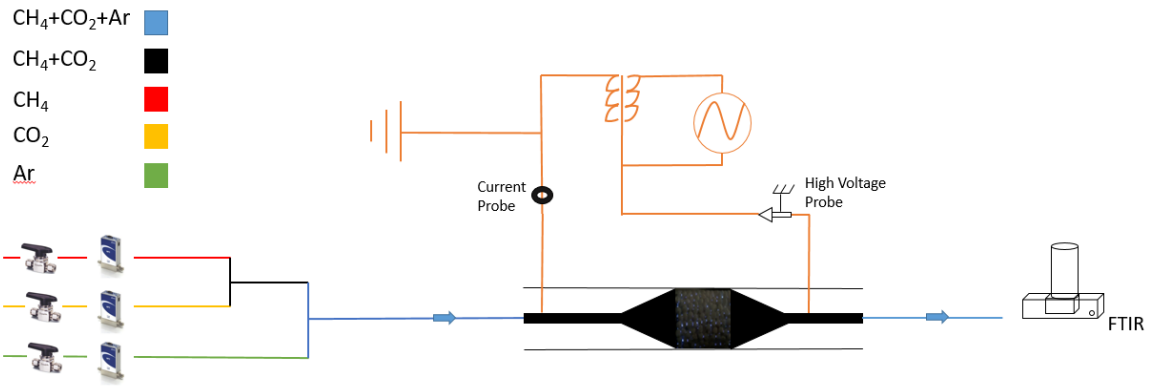

Figure 19 – Schematic of the PBR setup used for the dry reforming of methane.

2.4.5 Post processing of electrical data

The instantaneous current properties were measured by a Pearson™ wide band current monitor and the instantaneous voltage was recorded via a FLDITEST GE 3830 30kV AC+AC peak CAT II voltage

probe. Three readings at separate intervals were taken in order to measure the power supplied to the plasma. The power must remain constant for all tests in order to be comparable to each other as the input power has a significant effect on the plasma properties and therefore on the chemistry occurring [99]. The power was calculated through [Eq. 17], where P_t is the deposited power to the whole DBD over one period in watts, t is the period in seconds, V_t is the applied voltage measured in volts and I_t is the input current measured in amperes [13]. The measurement interval is 2E-8 s whereas the microdischarge pulse durations range from 1 x 10^{-8} and 15 x 10^{-8} s [54], therefore this measurement is expected to miss a small number of electrical discharges.

$$P_t = \int_0^t \sqrt{V_t^2 \times I_t^2}\, dt \qquad \text{[Eq. 16]}$$

This approach is sometimes not easy to practically implement due to heavy distortion of the current waveform. Furthermore, it does not take into consideration any losses in the system, such as heat or due to the resolution of measuring current and voltage being too large, resulting in the failure to capture all filamentary discharges [154]. This equation was implemented into code on MatLab which processes the raw data recorded by the equipment. The code can be seen in the appendix as CODE 3.

2.4.6 FTIR

Fourier Transform Infrared Spectroscopy (FTIR) is an analytical technique which aids classification of samples and their abundance. Infrared spectroscopy is a key technique for materials analysis partly due to its large versatility and its ability to be applicable to almost any surface. The advantage of FTIR spectroscopy is the low signal to noise ratio, providing improved spectra, and its quick and simple analysis of samples. The FTIR has the ability to analyse solid, liquid and gas samples.

A criterion for IR absorption is a net change in dipole moment in a molecule as it vibrates or rotates. Absorption of IR radiation is typical of molecular species that have a small energy difference between the rotational and vibrational states. A molecule where the charge distribution between its elements is not evenly distributed, such as where molecules have different electronegativity causes the molecule to have a dipole moment. The dipole moment is determined by the magnitude of the charge difference and the distance between the two centres of charge. IR spectroscopy relies on the absorption of infrared wavelengths to change the molecules vibrational energy levels. This interaction is a resonance condition involving the electric dipole mediated transition between vibrational energy levels [155]. Therefore for the vibration of a molecule to be infra-red active it should produce a change in the dipole moment. As different materials have a different yet unique combination of atoms and as a consequence no two compounds produce the exact same infrared spectrum. Examples of molecules which do not have diploe moment are hydrogen, oxygen, nitrogen and argon therefore it was not possible to measure any hydrogen produced in this work.

As a result the IR spectrum represents a molecular ‘fingerprint’ of a sample with absorption peaks which correspond to the frequencies of vibrations between the bonds of the atoms. Therefore, infrared spectroscopy can result in a positive identification (qualitative analysis) of every different kind of material. In addition, the size of the peaks in the spectrum is a direct indication of the amount of material present and so quantitative analysis can also be performed [156].

The basic components of an FTIR are an infrared source, an interferometer which uses a beam splitter and mirrors, detectors and computer software. Figure 20 shows a schematic of an interferometer, demonstrating the path of infrared light being split by the beam splitter. The two infrared beams hit a fixed mirror and hit a moving mirror, the two beams then recombine and interfere, which produces infrared across all of its frequencies. The infrared beam of all frequencies pass through the sample where the absorption and transmittance take place. The infrared frequencies then hit a detector and after which is decrypted by Fourier transform into quantitative data.

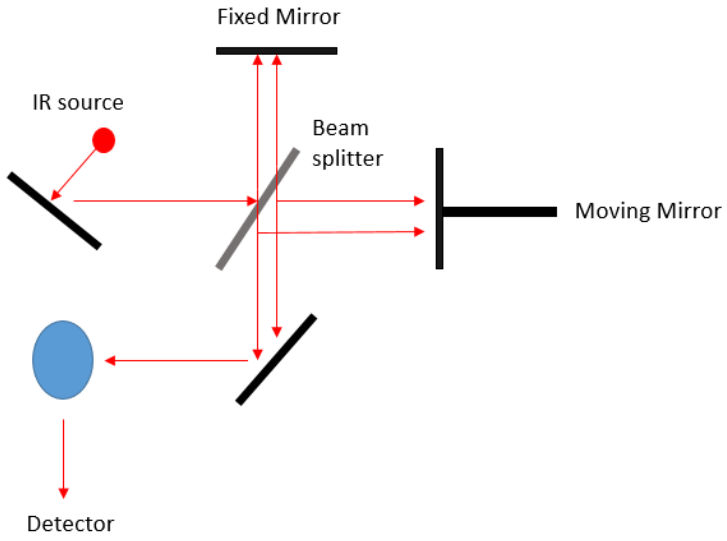

Figure 20 – Schematic representation of an FTIR interferometer.

The spectra obtained by FTIR can later be processed by the user giving the molecule or compound present and its abundance. The molecule or compound present is compared to reference standard spectra in which no compound will have the same, this can identify the molecule or compound. The absorbance intensity is proportional to the abundance of the specific compound which means it can be quantified. This is defined through the Beer Lambert law which is defined by [Eq. 18]. Further details on the method to calculate the concentration can be seen in Section 2.4.7. Table 3 shows the strongest IR vibrational modes for the gases which were detected within this report.

Table 3 – The strongest IR vibrational modes by number of modes and wavenumber.

Molecule	Number of Vibrational Modes	Wavenumber	References
Methane	4	1306 cm^{-1}	[157]
		1533 cm^{-1}	
		3018 cm^{-1}	
Carbon Dioxide	4	667 cm^{-1}	[157]
		1340 cm^{-1}	
		2350 cm^{-1}	
Carbon Monoxide	1	2143 cm^{-1}	
Ozone	3	717 cm^{-1}	[158]
		1089 cm^{-1}	
		1152 cm^{-1}	
NO_2	3	648 cm^{-1}	[159]
		1320 cm^{-1}	
		1621 cm^{-1}	
N_2O	3	589 cm^{-1}	[157]
		1285 cm^{-1}	
		2224 cm^{-1}	
N_2O_5	4	1243 cm^{-1}	[160]
		1339 cm^{-1}	
		1702 cm^{-1}	
		1742 cm^{-1}	

In this research the inlet gases travelled through a closed system through the packed bed reactor and entering the Specac Tornado 5 metre FTIR gas cell with a path length of 5m before exiting to extraction. Spectrum software was used in tandem with a Perkin Elmer Spectrum Two FTIR for data analysis and collection. Obtained spectra was uploaded to MatLab for peak area calculation. Referenced standard spectra was also uploaded to MatLab for peak area calculation. Using the Beer-Lambert law seen in [Eq. 18] the concentration in ppm was calculated, where ε is the molar attenuation coefficient or absorptivity of the attenuating species, c is the concentration of attenuating species, l is the path length, A is absorbance, I_o is the initial absorbance and I is the measured absorbance.

$$I = I_0 \exp \varepsilon c l \qquad \text{[Eq. 18]}$$

Since the spectra is measured with respect to absorbance the inverted function is seen in [Eq. 19]

$$A = -ln(I/I_0) = \varepsilon c l \qquad \text{[Eq. 19]}$$

For the production of ozone the resolution was 4 cm^{-1} and the number of scans performed was 4, in the dry reforming of methane a resolution of 1cm^{-1} was used, in order to increase the accuracy of the results, with number of scans also 4.

2.4.7 FTIR Measurement

The output of the gases from the packed bed plasma reactor feed directly into the FTIR gas cell and from there go directly to the extraction. Prior to any experiment the gas cell is flushed with inert and IR invisible gases to ensure there are no impurities within the closed gas loop and an experimental background is taken. A background spectrum is taken to eliminate the impurities within the gas flow such as H_2O or residual CO_2 and to account for impurities in the beam path. This is then subtracted from the recorded scan for a given measurement. Recorded FTIR measurements were analysed with MatLab software in order to find the concentration of the species produced after comparing to standard spectra information of which is displayed in table 4. The area of a peak is proportional to the concentration of the molecule responsible for that peak, and so calculating this area allows us to calculate the ppm of measured species. The code used in order to calculate the area is presented in the appendix under CODE 1 and 2, and figure 21 shows it in operation.

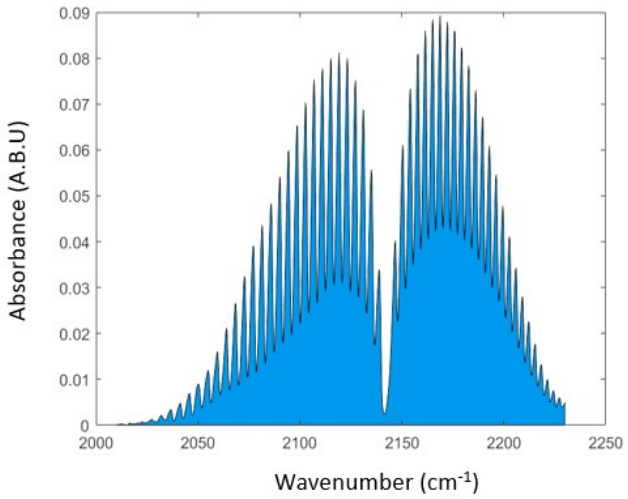

Figure 21 – Example of the area calculation using the MatLab code, the blue highlighted is the area which is calculated for carbon monoxide.

The area underneath the characteristic peaks is proportional to the concentration of the molecule. Using Mat Lab code as seen in the CODE 1 and 2 in the appendix, integration between two points which correspond to the wavenumbers of the characteristic peaks was performed. The concentration is calculated with respect to a standard spectra of known concentration. This can be done using [Eq. 20] where A_m is the area of the measured spectra and A_s is the area of the standard spectra, this is multiplied by the quotient of the measuring path length over the standard spectra path length.

$$c = \frac{A_m}{A_s} \times \frac{\text{standard path length}}{\text{measured path length}} \quad \text{[Eq. 20]}$$

Table 4 shows the parameters for each standard spectra which was used for concentration calculations, table 5 shows the wavenumbers used for each peak when calculating the area of the peak.

Table 4 – The parameters for each standard spectra which was used for concentration calculations for measured spectra.

Molecule	Path Length	Area	Concentration	Reference
Ozone	1	42.045	40ppm	[161]
NO_2	1	0.063424111	1ppm	[162]
N_2O	1	0.063571216	1ppm	[163]
N_2O_5	2.12	1.7794	72.61ppm	[164]
CH_4	1	0.0178	1ppm	[162]
CO_2	1	0.1122	1ppm	[162]
CO	1	0.0109	1ppm	[162]

Table 5 – Wavenumbers of species used to calculate the area of the measured spectra

Molecule	**Wavenumber cm^{-1}**
Ozone	970-1100
NO_2	1540-1660
N_2O	2150-2260
	2520-2600
	3420-3500
N_2O_5	1680-1760
CH_4	1175-1400
	2550-3200
CO_2*	3540-3660
	3660-3760
CO	2010-2230

*The CO_2 peak at 2230-2400 was disregarded as the absorbance was greater than 1.0.

Conversion of reactants were calculated through the percentage reduction in FTIR area which can be seen in [Eq. 21].

$$\frac{\text{Concentration of input} - \text{concentraation of output (ppm)}}{\text{Concentration of input (ppm)}} \times 100\% \qquad \text{[Eq. 21]}$$

The specific energy density was defined as seen in [Eq. 22]

$$SED\ (\frac{\text{kJ}}{\text{L}}) = \frac{\text{Discharge Power (kW)}}{\text{Total Flow Rate } (\frac{\text{L}}{\text{s}})} \qquad \text{[Eq. 22]}$$

Finally in order to compare the results obtained in this thesis to literature, the energy efficiency was calculated using [Eq. 23] [28]. In order to find the conversion of carbon dioxide and methane in mmol s^{-1}, the ppm per volume was calculated and multiplied by the flow rate and converted to mmol s^{-1} by the ideal gas law as seen in [Eq. 24].

$$E\left(\frac{mmol}{kJ}\right) = \frac{CO_2 + CH_4\ converted\ (mmol\ s^{-1})}{Discharge\ Power\ (kW)} \qquad \text{[Eq. 23]}$$

$$\text{PV} = \text{nRT} \qquad \text{[Eq. 24]}$$

2.4.8 OES Spectroscopy

Optical emission spectroscopy is used as a measurement technique in plasma processing to identify excited species present within the plasma. As electrons rise and fall in energy level, the atom will emit the difference in energy. The packet of energy released with a specific wavelength of between 200 to 800 nm can be detected by the optical emission spectrometer giving information about species present. The OES spectrometer used for the production of ozone experiments was an Ocean Optics USB4000 whereas an Ocean Optics HR2000+ was used for the dry reforming of methane experiments, both of which were connected to Ocean View software. A collimating lense attached to an optical fibre was placed directly over the packing material with a quartz glass tube acting as the separation barrier. The collection parameters can be seen in table 6. Before any readings were taken a dark background was taken to account for stray electrical signals and stray background light. The intensity of the peaks are measured in counts against the wavelength in nm.

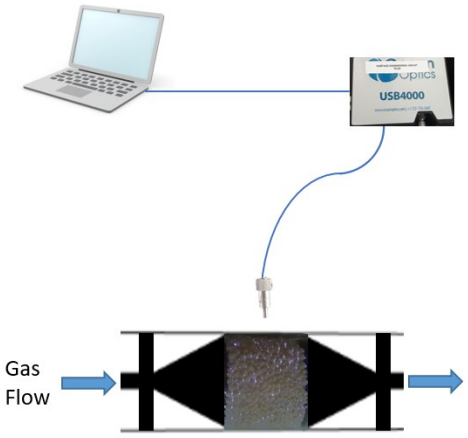

Figure 22 – Schematic of the Ocean Optics spectrometer and data acquisition during plasma processes.

Table 6 – OES data acquisition parameters used for the measurement of optical emissions of the plasma processes.

OES Parameter	Value
Integration Time	3000 µs
Scans to Average	4
Boxcar width	4
Data Collection Time	5 µs

CHAPTER 3 – DEPOSITION OF PHOTOCATALYTIC COATINGS ONTO PARTICULATES FOR USE IN A PACKED BED DIELECTRIC BARRIER DISCHARGE

The deposition of photocatalytic coatings onto glass particulates formed the primary work in order to establish a basis to characterise and evaluate the coatings, and then to refine the conditions for use in the plasma reactor. Glass particulates, of diameter 2 mm, were coated with TiO_2 and TiO_2-W through a bespoke magnetron sputtering process. Post coating heat treatment was performed in order to obtain the best crystallinity for photocatalytic activity. Subsequent characterisation and analysis of the coatings was carried out by Raman spectroscopy, SEM and XPS to determine the crystallinity, stoichiometry and uniformity of the photocatalytic coatings. An investigation into the photocatalytic activity of the prepared coatings was undertaken through the degradation of methylene blue. A factorial design of experiments was utilised in order to investigate the effect of various sputtering conditions in an efficient way for the optimisation of photocatalytic coatings. Thereupon photocatalytic TiO_2 and TiO_2-W coatings were deposited onto $BaTiO_3$ particulates and subsequently were characterised via SEM/EDX and XPS to again determine the crystallinity, stoichiometry and uniformity of the photocatalytic coatings. Photocatalytic activity through the degradation of methylene blue was also used to test the photocatalytic activity of the $BaTiO_3$ particulates. It was observed that for both the glass and $BaTiO_3$ the addition of TiO_2 coatings which were annealed increased the degradation of methylene blue under UV light. It was also observed that the unannealed TiO_2 coated glass or $BaTiO_3$ showed no photocatalytic activity, this was as a consequence of the presence of phototactically active anatase. Subsequent addition of W in the TiO_2 coating promoted increased degradation of methylene blue and hence increased photocatalytic activity.

3.1 Pulsed DC Magnetron Sputtering of Photocatalytic Coatings

Photocatalytic thin films were deposited by pulsed DC magnetron sputtering in a rig which contained two planar unbalanced type II magnetrons. Pulsed DC magnetron sputtering is required due to the inefficiency of DC magneton sputtering for reactive sputtering of oxides due to the build-up of positive charges at the cathode as the target surface becomes 'poisoned'. This can consequently lead to arcing and results in inhomogeneity and defects in the film and instabilities of the deposition process [165]. Furthermore arcing can damage equipment such as the power supply. Pulsed DC was chosen due to its ability to be readily controlled and has been proven to produce good coating uniformity, adhesion and reproducibility [152, 166]. All coatings were deposited in the magnetron sputtering rig which was pumped down to a base pressure of 1×10^{-3} Pa. A single 300 mm x 100 mm type II unbalanced planar magnetron was used along with a titanium target of 99.5 % purity for TiO_2 coatings. Two 300 mm x 100 mm type II unbalanced planar magnetrons were used along with a target of titanium and tungsten both of 99.5 % purity for TiO_2-W coatings. The reactive sputtering process was performed with the addition of oxygen. A dual channel Advanced Energy Pinnacle Plus power supply operated in pulsed DC mode was used to power the magnetrons. The flows of oxygen and argon were controlled using mass-flow controllers. The process of sputtering the TiO_2 photocatalyst onto glass and $BaTiO_3$ particulates was carried out using a bespoke oscillating bowl for the uniform coating of the particulates. This type of method has been used previously as it rotates the particulates around the bowl and induces a vibration, spinning the particulates on their axis in order to try and achieve a more uniform coating. [136, 137].

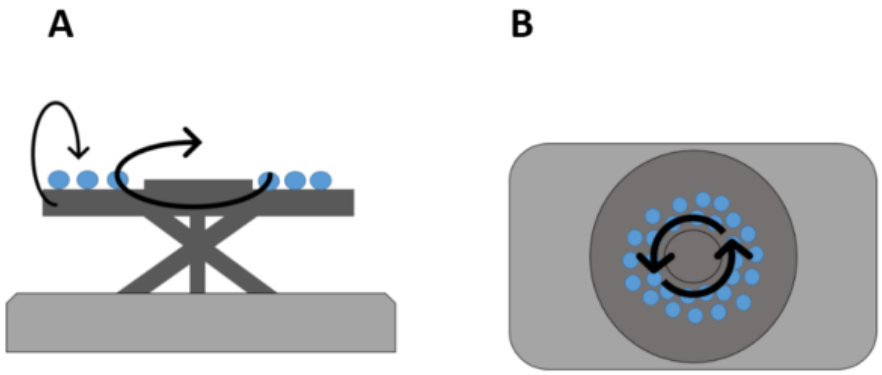

Figure 23 – Bespoke oscillating bowl used for deposition of photocatalysts onto particulates showing the rotational motion for uniform coating. A) Left side view, B) Top view.

3.2 Hysteresis of Reactive Gas Pressure and Voltage

Reactive gas sputtering forms reactive products on the target surface, which can affect the electrical properties of the target and the plasma discharge, which can in turn affect the deposition rate. If there is too much reactive gas present, such as oxygen, the target's surface can become 'poisoned' with a compound layer, for example a titanium target's surface can be covered in TiO_2. As a result of this the deposition rate can be significantly reduced [167]. A hysteresis behaviour occurs after increasing the reactive gas flow rate as, due to the reduced deposition rate, a lower amount of reactive gas is required to return the target to a metallic sputtering regime. A hysteresis experiment was carried out, which involves the steady increase of oxygen flow, from a specified minimum, into the magnetron sputtering chamber and allowing the voltage and pressure within the chamber to stabilise. Following the increase in oxygen flow and until a maximum flow is used the process is repeated but in the reverse direction (oxygen flow is progressively reduced from a maximum to a minimum). Hysteresis behaviour is typically observed for both chamber pressure and discharge voltage. Where the oxygen flow is kept low a high deposition rate and low reactive gas partial pressure is observed and the deposition mode is defined as metallic mode. Contrary to this, where oxygen flow is high, a low deposition rate and high partial pressure of reactive gas is observed. This deposition mode is defined as poisoned mode. Some materials show little or no hysteresis behaviour due to their absence of reactive gas poisoning, however deposition of titanium dioxide causes a strong hysteresis. In order to deposit stoichiometric films at high deposition rates, the system should be operated in the transition regime between metallic and poisoned modes. Hysteresis behaviour can be reduced by significant increases of the pumping speed, however this solution is not cost-effective.

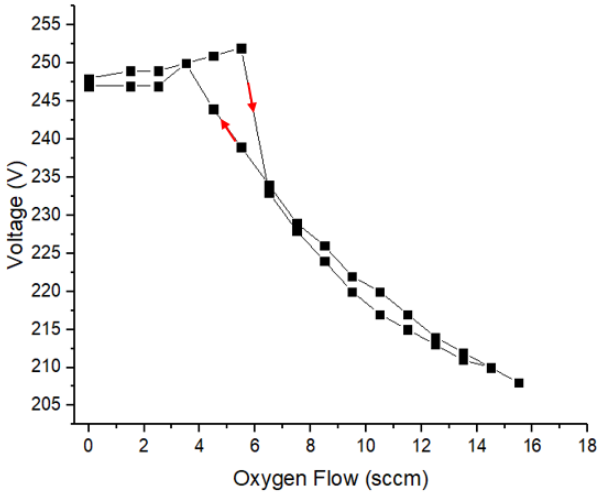

Figure 24 – Hysteresis of the sputtering of TiO_2 in the magnetron sputtering chamber used for the production of photocatalytic coatings

3.3 Initial Coating of Titanium Dioxide onto Glass Particulates

The magnetron sputtering of TiO_2 coatings onto glass particulates was initially carried out in order to determine the feasibility of coating TiO_2 using magnetron sputtering and obtaining a coating with good photocatalytic activity. One of the main concerns was obtaining a stoichiometric TiO_2 and whether the coating would be uniformly distributed around the whole of the glass particulates. For the initial coatings of TiO_2 onto glass a 1, 2 and 3 hour coating was produced, information on the parameters used during the sputtering process can be seen in table 7.

Table 7 – Magnetron sputtering parameters including deposition time, frequency, duty and oscillating bowl power (%) of (V_{max} delivered to the equipment) for the production of TiO_2 photocatalytic coatings on glass particulates.

Deposition Time (hr)	Power (W)	Frequency (kHz)	Duty (µs)	Oscillating Power (%)*	Pre Coating Treatment	Post Coating Treatment
1	1000	150	3.3	70	-	500°C for 1 hour
2	1000	150	3.3	70	-	500°C for 1 hour
3	1000	150	3.3	70	-	500°C for 1 hour

** Oscillating power refers to the power supplied to the electromagnet which imparts oscillating motion to the particulates.*

Figure 25 – Image of uncoated glass particulates (left,) as-deposited TiO_2 coated glass particulates (middle) and TiO_2 coated glass particulates annealed at 500°C (right).

3.3.1 Surface Characterisation

3.3.1.1 Raman Spectroscopy

Raman spectroscopy was used to verify the presence of anatase TiO_2 on the surface of the coated and annealed particulates. Anatase TiO_2 has been investigated by Ohsaka and found that characteristic peaks occur at wavenumbers 144 cm^{-1} (E_g), 197 cm^{-1} (E_g), 399 cm^{-1} (B_{1g}), 513 cm^{-1} (A_{1g}), 519 cm^{-1} (B_{1g}), and 639 cm^{-1} (E_g) [168]. Figure 26 shows a clear increase in the intensity of the characteristic anatase peak at 144cm^{-1} and shows that the surface coverage of TiO_2 increases from 1 to 3 hours, indicating that the 1 hour coating does not achieve maximum coverage of the glass particulate and that increasing the deposition time to 3 hours achieves a better distribution of TiO_2. Increase in deposition time increases the intensity of the anatase peaks, indicating a higher concentration, crystallinity or distribution of anatase upon the glass beads surface, since Raman intensity is directly linked to these parameters [169]. It is expected that the 3 hour coated glass particulates would then have more active sites for oxidation and reduction reactions to take place at the surface and hence have a higher photocatalytic activity. The estimated thickness of coatings from 1-3 hours is ~250-1500nm, based on coatings of titanium dioxide on flat substrates and measured with Detak profilometry [23].

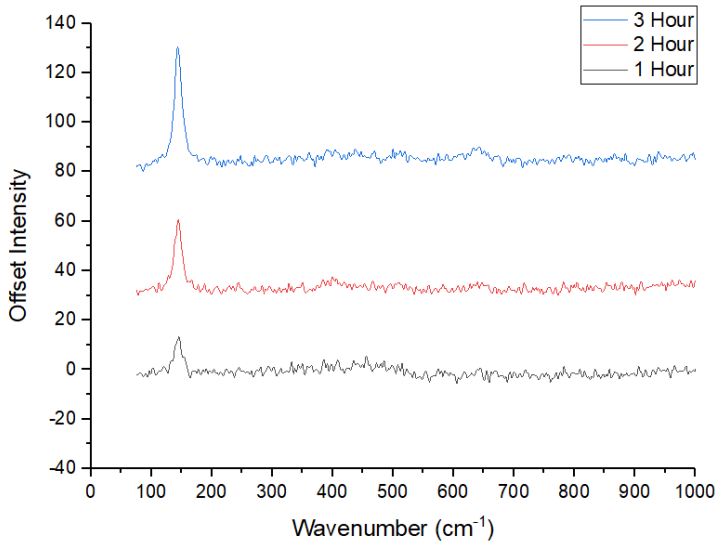

Figure 26 – Raman spectra of 1, 2 and 3 hour TiO_2 coated glass particulates with a frequency of 150 kHz, a duty of 3.3µs and oscillating power of 70%

3.3.1.2 SEM

SEM imaging was performed to ascertain the coatings characteristics, including surface topography, coating uniformity and coating coverage. The coating appears to cover the majority of the surface, however it seems that the coating uniformity is not totally consistent due to what seems to be patches where the coating is absent. This could be due to poor mechanical adhesion, wear from oscillation or insufficient sputtering.

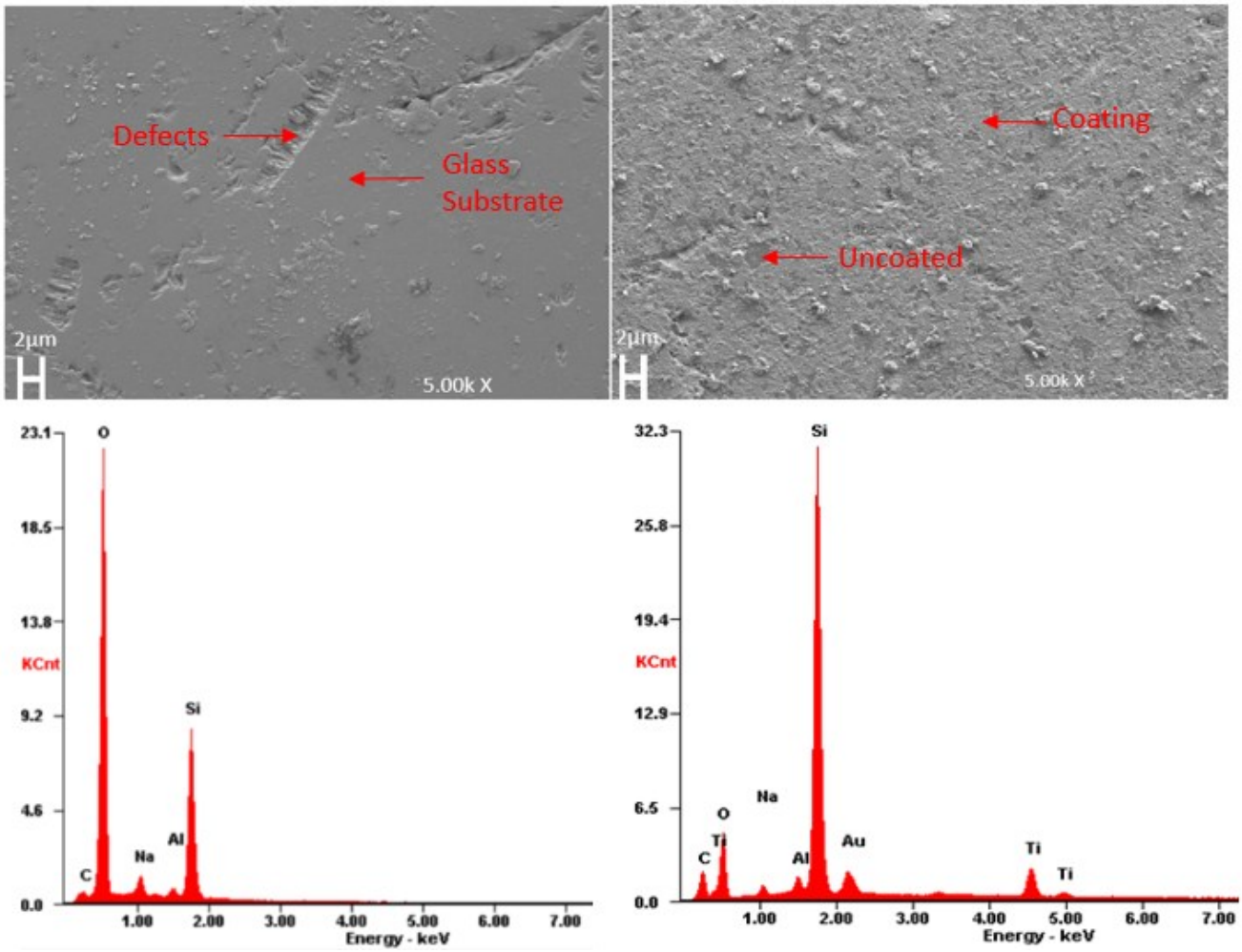

Figure 27 – SEM images of uncoated glass particulates (top left) and 3 hour TiO_2 coated glass particulates (top right). EDX spectra of uncoated glass particulates (bottom left) and EDX spectra of 3 hour TiO_2 coated glass particulates (bottom right)

3.3.1.3 XRD

Due to the large spherical nature of the particulates, XRD analysis proved to be unsuccessful in producing any successful spectra for titanium dioxide coatings onto glass particulates. This was also consistent for other coatings discussed in this chapter.

3.3.2 Photocatalytic Activity

The 1, 2 and 3 hours coatings were placed within the methylene blue solution, in the dark, and stirred until an equilibrium between absorption and desorption was achieved. The rate of degradation of methylene blue was calculated and photocatalytic activity was measured, as described in Chapter 2 – Methodology.

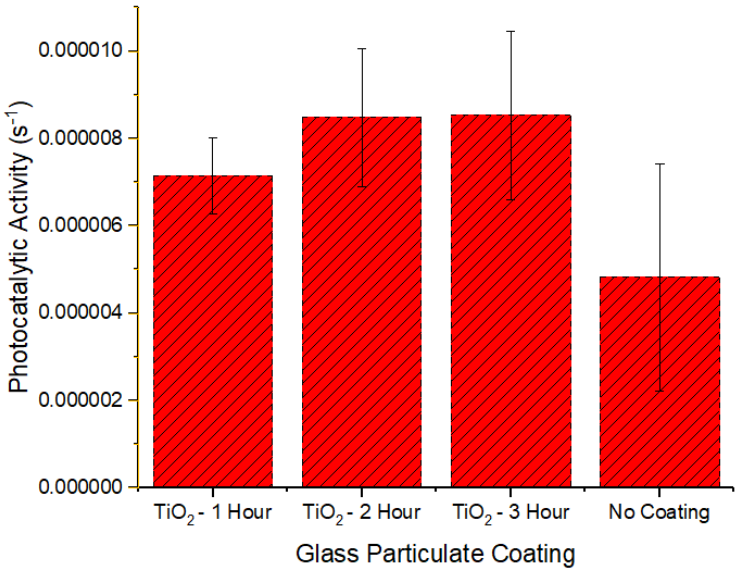

Figure 28 – Photocatalytic activity of 1, 2 and 3 hour TiO_2 coated glass particulates using the methylene blue degradation method.

Figure 28 shows the photocatalytic activity (rate of degradation of methylene blue) for non-coated glass particulates and TiO_2 coated glass particulates. Photocatalytic activity increased with the addition of an annealed TiO_2 coating and also increased with deposition time, from 1 to 3 hours. However, there is no apparent increase from 2 to 3 hours, this suggests the maximum coverage of photocatalytic sites after ~2 hours and a saturation of photocatalytic activity. The 3 hour TiO_2 coated thin film increased the photocatalytic activity by 76% compared to uncoated glass particulates. The existence of photocatalytic TiO_2 on the glass bead surfaces would produce $OH^{\cdot}$ and H^{+} radicals from the water in the methylene blue solution which reacts and decomposes the methylene blue dye. An increase in deposition time increases the TiO_2 coverage, hence providing more electron-hole pairs to produce $OH^{\cdot}$ and H^{+} which react with methylene blue and C–S+=C forms C–S(=O)–C which leads to the break-up of the aromatic ring causing the degradation of methylene blue [170].

Tests using non-coated glass particulates still cause degradation of methylene blue, due to irradiation by UV, however, this is not due to photocatalytic activity [171].

3.3.3 Summary

Deposition of 1, 2 and 3 hour TiO_2 coatings onto 2mm glass particulates was carried out to investigate the feasibility of magnetron sputtering for photocatalytic preparation. Post deposition annealing was carried out at 500^{o}C to obtain an anatase phase. Surface characterisation performed by Raman spectroscopy confirmed the presence of anatase on the 2 mm glass particulates. Increasing the deposition time from 1 to 3 hours increased the presence of anatase TiO_2 on the glass surface. Photocatalytic testing using the methylene blue method was carried out and showed an increase of photocatalytic activity by up to 76% compared to no coating.

3.4 Factorial Design of Experiments to Investigate Various Sputtering Parameters of Titanium Dioxide Coatings on Glass Particulates

A 4th order factorial design of experiments (DoE) was utilised in order to investigate the effect of pulse frequency (kHz) and pulse on time (µs) of the applied power, deposition time (hr) and oxygen flow (sccm) on the stoichiometry, and crystallinity and photocatalytic activity of sputtered samples and gain a further understanding of the magnetron sputtering process and its effect on photocatalytic coatings. Table 8 shows the coatings parameters chosen for investigation for the DoE. This offered the most efficient process in order to optimise photocatalytic coatings onto the particulates for use in the PBR. Depending on the type of factorial experiment, it can ensure that in each complete trial or replicate of the experiment all possible combinations of factors are investigated. The effect of each factor is estimated by the change in the measured response. The response in this case is the photocatalytic activity.

Table 8 – Coating parameters for the design of experiments of TiO_2 coated glass particulates.

Frequency (kHz)	Duty (µs)	Deposition Time (hr)	Oxygen Flow (sccm)
125	3.3	1	6.5
150	3.3	3	15
150	3.3	1	6.5
150	2.5	3	15
150	2.5	1	6.5
125	3.3	1	15
125	3.3	3	6.5
150	2.5	3	6.5
125	2.5	1	15
150	3.3	3	6.5
125	2.5	3	15
125	2.5	3	6.5
150	2.5	1	15
125	2.5	1	6.5
150	3.3	1	15
125	3.3	3	15

3.4.1 Surface Characterisation of Titanium Dioxide Coated Glass Particulates

3.4.1.1 Raman Spectroscopy

Raman spectroscopy showed the presence of anatase TiO_2 on the surface of the all coated and annealed particulates. A clear increase in the intensity of the characteristic anatase peak at 144 cm^{-1} shows that the surface coverage of TiO_2 increases from 1 to 3 hours, these results are in agreement with the initial TiO_2 coatings on glass particulates. There is no real effect on the intensity of anatase when changing frequency, duty or oxygen flow, see figure 29. Table 9 shows the intensity of the anatase peak at 144 cm^{-1}.

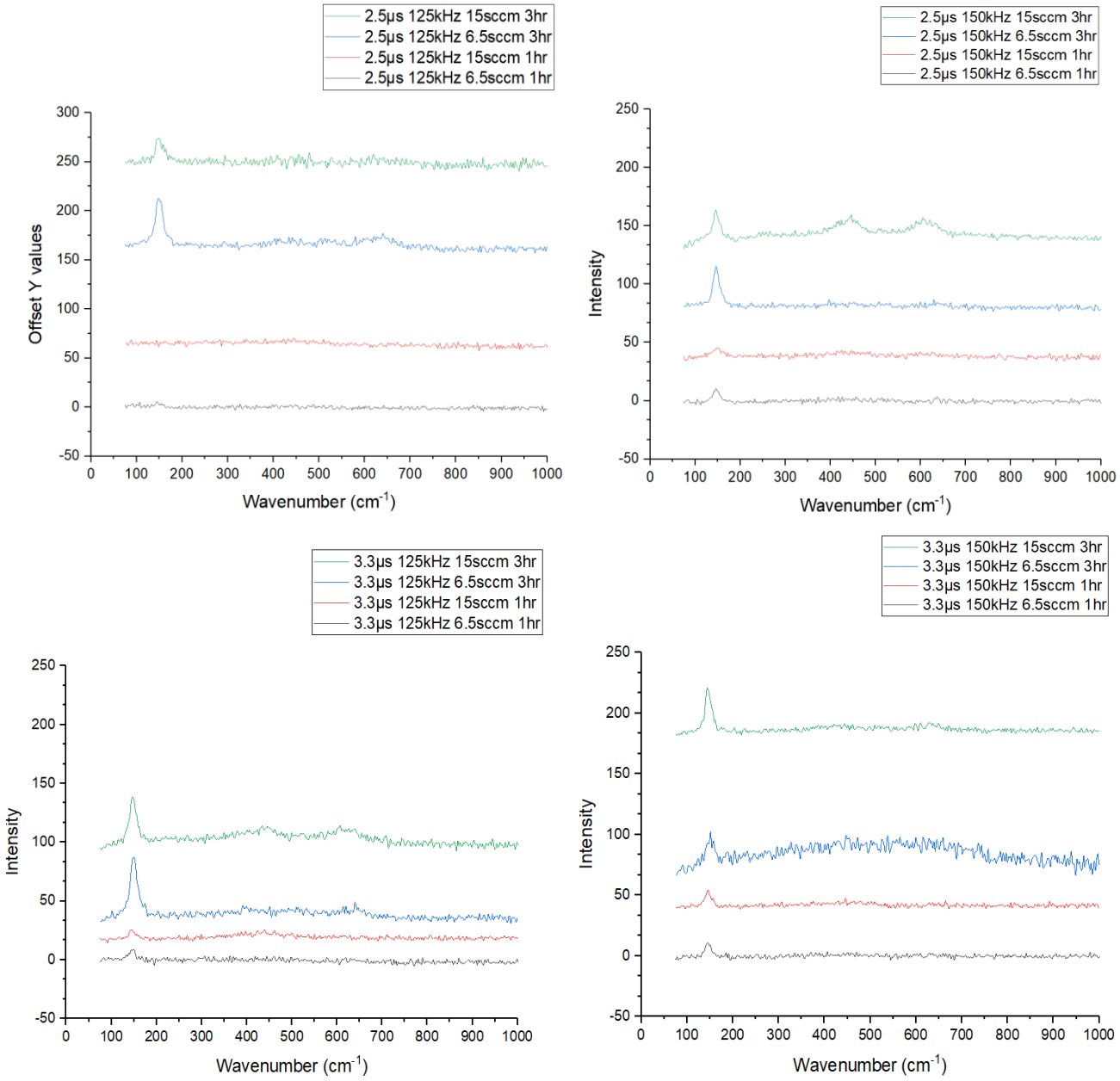

Figure 29 – Raman spectra of the DoE TiO_2 coated glass particulates

Table 9 – Intensity of 145cm^{-1} characteristic anatase peak of factorial design of experiments TiO_2 coatings on glass particulates

Coating Parameters	**Deposition Time**	**Intensity at 145cm^{-1} (A.B.U)**
125 kHz, 2.5 µs, 6.5 sccm	1	5.69
125 kHz, 2.5 µs, 6.5 sccm	3	45.56
125 kHz, 2.5 µs, 15 sccm	1	3.10
125 kHz, 2.5 µs, 15 sccm	3	23.92
125 kHz, 3.3 µs, 6.5 sccm	1	10.59
125 kHz, 3.3 µs, 6.5 sccm	3	33.71
125 kHz, 3.3 µs, 15 sccm	1	5.98
125 kHz, 3.3 µs, 15 sccm	3	21.04
150 kHz, 2.5 µs, 6.5 sccm	1	8.01
150 kHz, 2.5 µs, 6.5 sccm	3	47.38
150 kHz, 2.5 µs, 15 sccm	1	6.01
150 kHz, 2.5 µs, 15 sccm	3	34.27
150 kHz, 3.3 µs, 6.5 sccm	1	10.72
150 kHz, 3.3 µs, 6.5 sccm	3	20.08
150 kHz, 3.3 µs, 15 sccm	1	12.32
150 kHz, 3.3 µs, 15 sccm	3	33.83

3.4.1.2 SEM

SEM imaging shows an increase in coating coverage from the 1 hour to the 3 hour coatings, as demonstrated in figure 30, when comparing images B and D (1 hour deposition time) and images C and E (3 hour deposition time).The effect of the frequency, duty and oxygen flow does not seem to show any significant difference on the topography of the coatings. Cross sectional analysis was unable to be performed due to the nature of the spherical substrate and so further optical analysis could not be performed. Although the coatings showed relatively consistent coverage, the motion of the particulates constantly rotating and oscillating mean that the whole of the particulate would not always receive a consistent fluence of sputtered particles resulting in the rougher appearance.

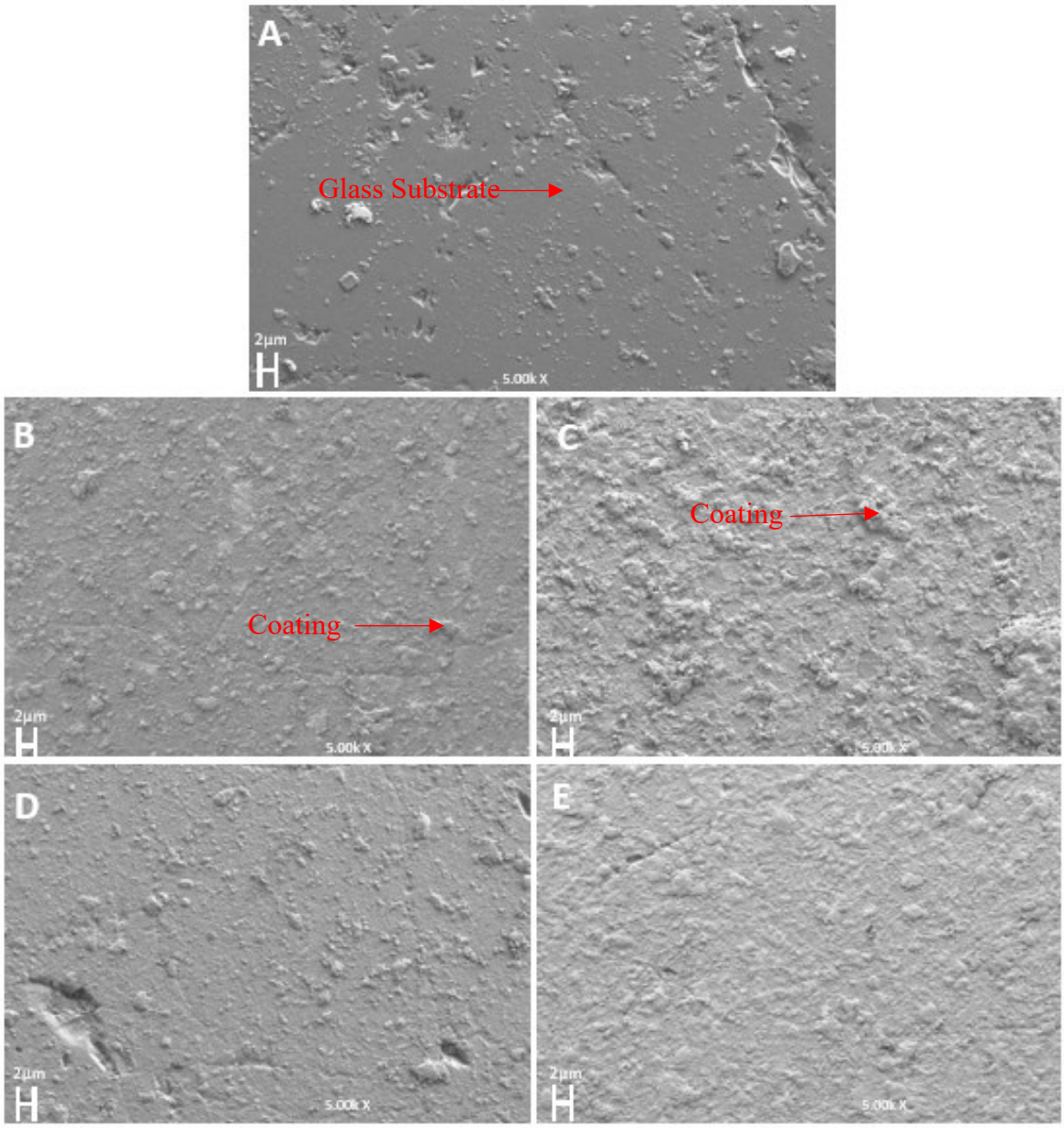

Figure 30 – SEM images of TiO_2 coated glass beads, (A) glass particulate no coating, (B) 3.3 µs, 150 kHz, 6.5 sccm, 1 hr (C) 3.3 µs, 150 kHz, 6.5 sccm, 3 hr (D) 3.3 µs, 150 kHz, 15 sccm, 1 hr (E) 3.3 µs, 150 kHz, 15 sccm, 3 hr.

3.4.1.3 XPS

XPS spectroscopy of 100 µm by 100 µm areas was carried out on select samples to analyse the stoichiometry of the surface of the particulates without coating and with coating and enable an understanding of the role that the surface coatings could play in non-thermal plasma experiments. The XPS spectroscopy of the glass particulates showed an absence of Ti 2p, 3s and 3p orbitals and showed strong peaks at Si 2s and Si 2p orbitals. After coating for 3 hours strong Ti 2p, 3s and 3p orbitals were present. As seen in Figure 31, Ti 2p peaks at 458, 464 and 471 eV, Ti 3s peaks at 62 eV and Ti 3p peaks at 36 eV. As seen in figure 32, the characteristic peak at 458 eV indicates a presence of TiO_2 due the Ti^{4+} state [172], whereas metallic Ti is usually at 454 eV [173, 174]. A large decrease in Si 2s and Si 2p orbitals at 154 and 103 eV respectively was observed after coating the glass particulates with TiO_2. This illustrates the coating method was successful in depositing TiO_2 c onto the glass particulates. A small increase in O 2s peak strength was observed however, this is not significant enough to discuss.

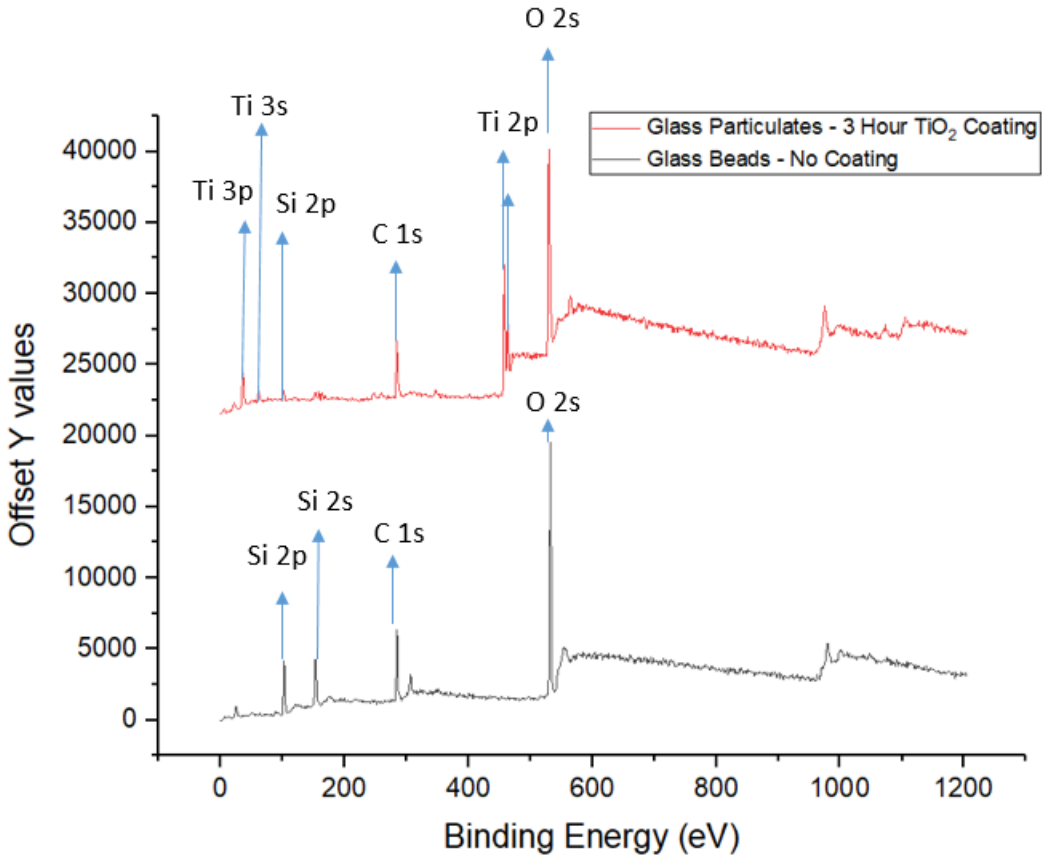

Figure 31 – XPS spectroscopy of glass particulates without coating and glass particulates with 3 hour TiO_2 coating. (frequency – 150 kHz, duty – 3.3 µs, oxygen – 6.5 sccm).

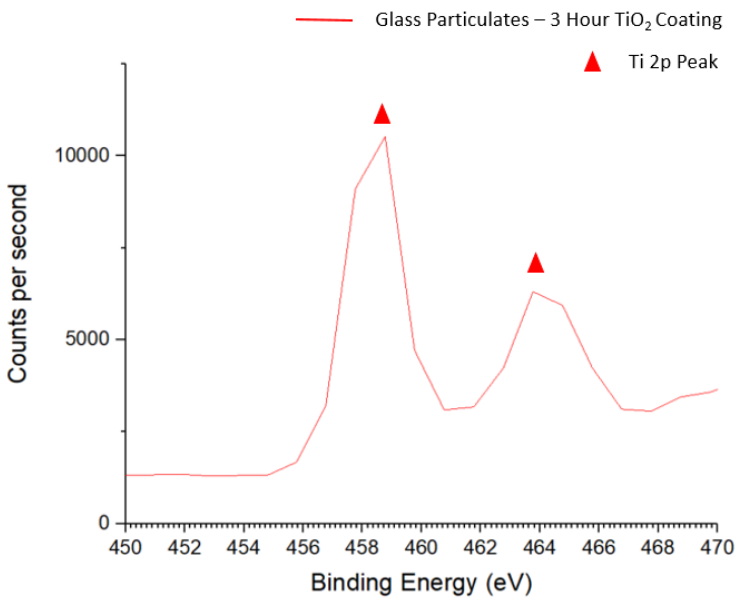

Figure 32– XPS spectroscopy of glass particulates with 3 hour TiO_2 coating (frequency – 150 kHz, duty – 3.3 µs, oxygen – 6.5 sccm), showing 458 Ti2p peak.

3.4.2 Photocatalytic Activity

All the experimental designs and results were statistically analysed using Minitab®. Figure 33 displays the main effect plot which shows the how the factors effect the mean response, in this case, the photocatalytic activity, for the factors of applied frequency, duty, deposition time and oxygen flow rate. Figure 34 is a Pareto chart of the standardised effects which shows the largest effect to the smallest effect. The vertical line at an absolute value of 2.04, indicates which effects are statistically significant, this is based on an alpha value of 0.05 which represents a confidence level of 95%. Finally, Figure 35 shows the interaction plot which shows the relationship between the factors and the response. A parallel line indicates that no interaction occurs whereas, non-parallel lines indicate the interaction.

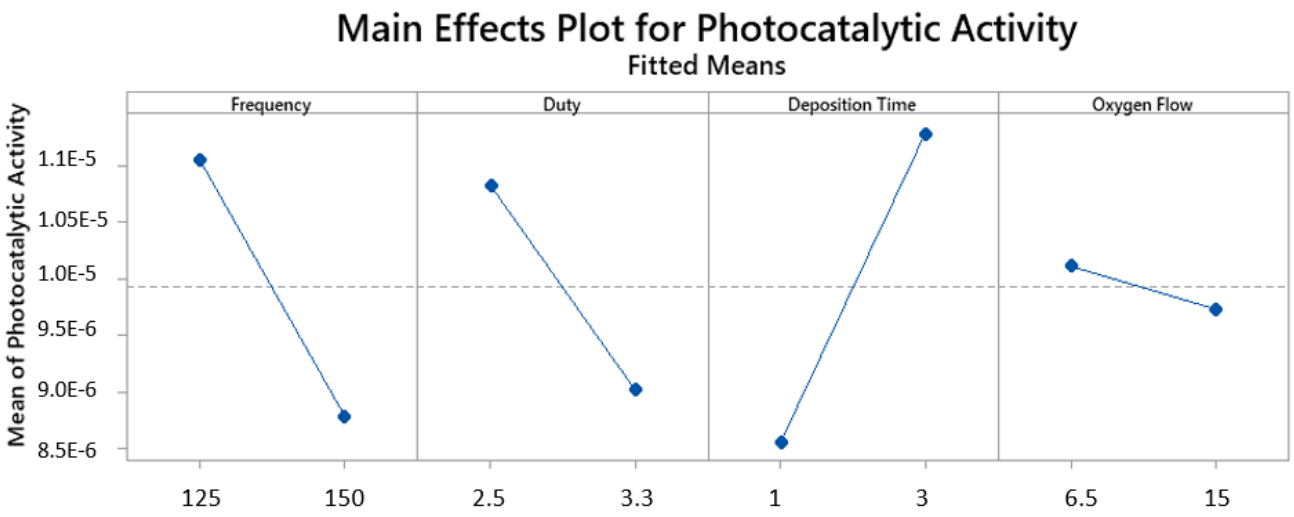

Figure 33 – Main effects plot of duty, deposition time, frequency and oxygen flow with a response of photocatalytic activity. Frequency (kHz), Duty (µs), Deposition time (hours), Oxygen flow (sccm).

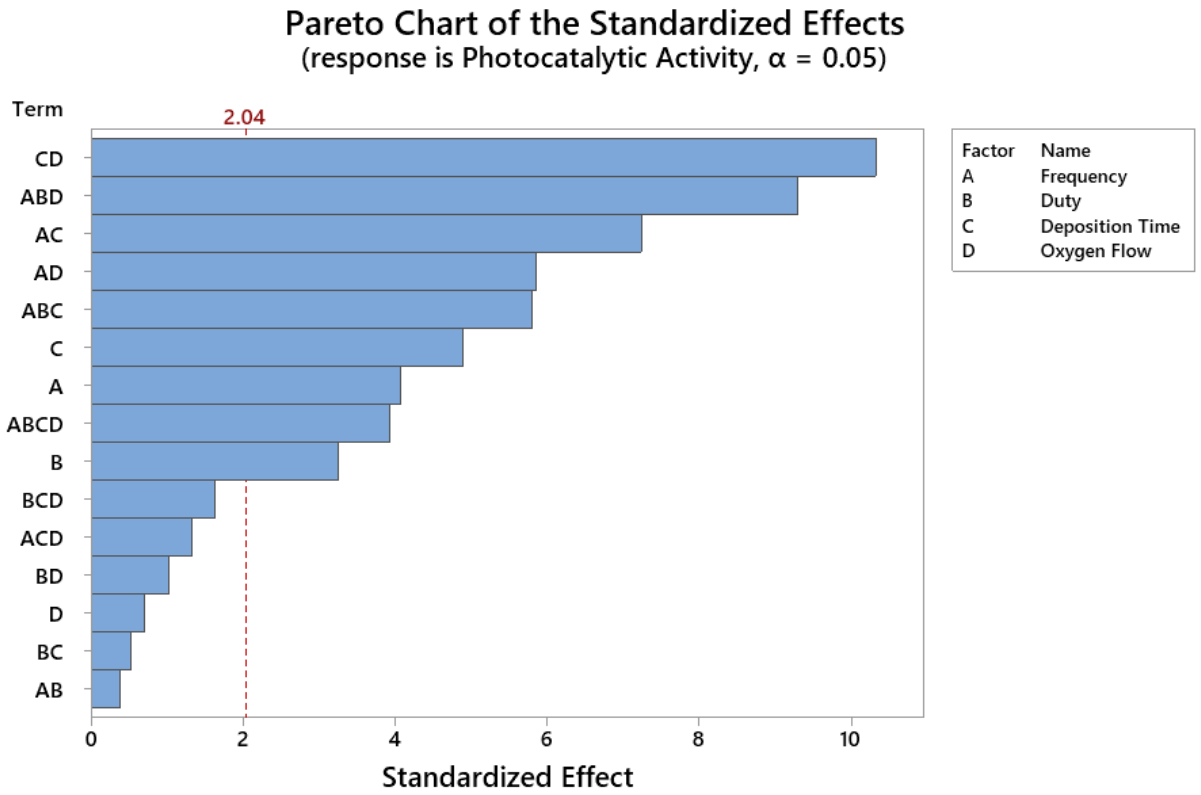

Figure 34 – Pareto chart of the standardised effects of duty, deposition time, frequency and oxygen flow with a response of photocatalytic activity

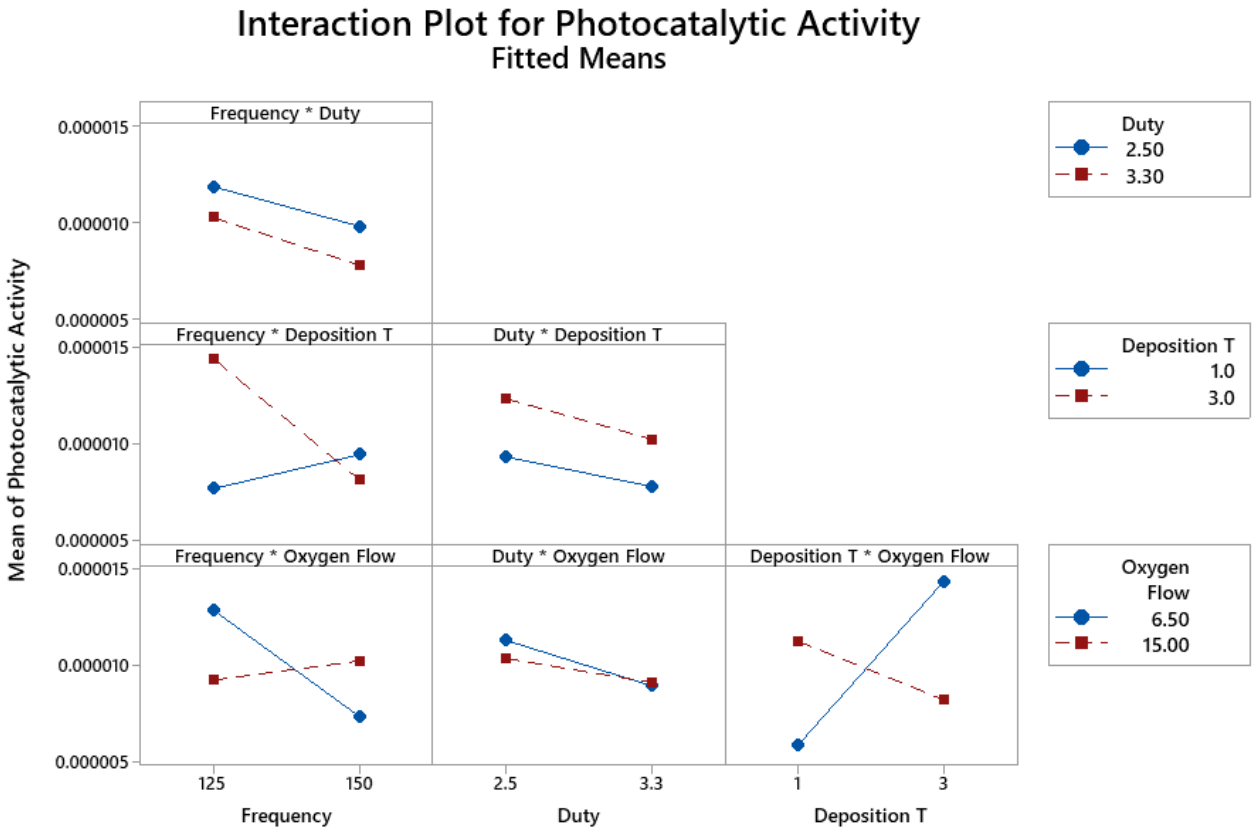

Figure 35 – Interaction plot of duty, deposition time, frequency and oxygen flow with a response of photocatalytic activity

Table 10 – Model summary of factorial design of experiments of TiO_2 coated glass particulates.

S	R-sq	R-sq (adjusted)	R-sq (predicted)
1.9E-6	92.34%	88.75%	82.77%

Table 11 – Voltage and current readings taken during the deposition of TiO_2 onto glass particulates using magneton sputtering.

Coating	Average Voltage (-V)	Standard Deviation (σ)	Average Current (A)	Standard Deviation (σ)
125 kHz 2.5 µs 6.5 sccm	279	2.22	3.59	0.025
125 kHz 3.3 µs 6.5 sccm	248	1.12	4.04	0.019
125 kHz 2.5 µs 15 sccm	266	2.14	3.76	0.028
125 kHz 3.3 µs 15 sccm	233	2.81	4.29	0.055
150 kHz 2.5 µs 6.5 sccm	261	1.50	3.84	0.020
150 kHz 3.3 µs 6.5 sccm	231	2.33	4.35	0.062
150 kHz 2.5 µs 15 sccm	248	4.41	4.03	0.075
150 kHz 3.3 µs 15 sccm	216	2.46	4.65	0.070

3.4.3. Effect of Operating Parameters

The effect of the frequency is a critical factor effecting the photocatalytic activity of the deposited coatings, according to figure 33 and figure 34. The mean photocatalytic activity was increased by 22% by decreasing the frequency of the DC pulse to 125 kHz from 150 kHz. Pareto analysis shows that frequency, when analysing individual parameters and not in combination, has the second largest effect on the photocatalytic activity. It has been proven that for mid-frequency pulsed dc magnetron sputtering, film structure is governed by the ion to atom ratio incident at the substrate [175, 176]. Ion energy flux to the substrate increases with frequency and decreases with duty. Ratova et al found the impact of the frequency is not as important as the impact of the duty [177], in the experiments shown the frequency had a bigger impact on the photocatalytic activity than of the duty, however, both had significant impact on the photocatalytic activity of the deposited film. There seems to be no significant interaction when

changing the frequency and duty together. According to the interaction plot analysis in figure 35, the frequency along with the deposition time and the oxygen flow had a significant impact of the photocatalytic activity. As the ion energy flux to the substrate increases with frequency. Altering the frequency and duty effects the current and voltage at the target. It is generally known that sputtering yields increase relatively slowly with increasing ion energy or applied voltage, at the same time the number of particles striking the cathode is proportional to the current density. Consequently, current is a significantly more important parameter for determining the deposition rate rather than voltage. However the voltage determines the energy of the argon ions as they collide with the target, this also has a significant impact on the coating process.

The duty or duty cycle had the least significant impact on the photocatalytic activity out of all the critical parameters. The time of the off period between two on periods was changed from 2.5μs to 3.3μs. The duty cycle has an important role on the argon magnetron plasma properties effecting the deposition process and thus the effectiveness of the photocatalyst coating. There are no significant interactions of duty on other parameters which effect the photocatalytic activity.

Increasing the deposition time from 1 to 3 hours increased the photocatalytic activity by 32% on average. It was found that the deposition time had the most significant impact on photocatalytic properties. The deposition time increases the weight percentage and surface coverage of photocatalyst on the substrate. This provides more active sites where photocatalytic reactions can occur and hence increases photocatalytic activity. However, the increasing of deposition time for enhanced photocatalytic activity eventually reaches a point where there is no significant increase due to over saturation and a ceiling in the number of activation sites [178].

3.4.4. Summary

A hysteresis test of reactive gas pressure and voltage was performed and found that the transition between metallic sputtering and poisoned mode was around 6-6.5sccm of oxygen flow. A factorial design of experiments was carried out to investigate the effect of various sputtering parameters on the photocatalytic TiO_2 glass beads. It was found that the deposition time, frequency and duty all had a significant effect on the photocatalytic activity of the produced TiO_2 photocatalysts. Optimum conditions were a frequency of 125 kHz, duty of 2.5 μs and a deposition time of 3 hours.

3.5 Coatings of Titanium Dioxide on Barium Titanate Particulates

The initial magnetron sputtering of TiO_2 coatings onto $BaTiO_3$ particulates was also carried out in order to determine the feasibility of depositing TiO_2 photocatalysts using magnetron sputtering and obtaining a coating with good photocatalytic activity. The main concerns were whether the coating would be uniformly distributed around the whole of the $BaTiO_3$ particulates to obtain a good stoichiometric TiO_2 coverage and the adhesion of the TiO_2 coating onto the $BaTiO_3$ particulates due to the different surface topography of the $BaTiO_3$ particulates in comparison to the smoothness of the glass particulates. The preparation of $BaTiO_3$ particulates by CATAL international was by the sintering of $BaTiO_3$ powders. This process made the $BaTiO_3$ particulates surface rather fragile. Due to the fragile nature of the $BaTiO_3$ particulates surface, CATAL international recommended annealing at high temperature for 4 hours. Therefore, annealing at 1100°C for 4 hours was carried out prior to any deposition, this managed to reinforce the robustness of the surface to allow better adhesion of the deposited coating. Along with changing the pre-treatment of the $BaTiO_3$ particulates it was decided that increasing the deposition time compared to the glass particulates was necessary due to an increased surface area of the $BaTiO_3$. Finally, upon coating of $BaTiO_3$ during the run of 125 kHz and 2.5µs arcing was experienced, however it was more stable at 150 kHz and 3.3µs hence, coatings using these parameters were chosen.

Table 12 – Deposition parameters for the initial magnetron sputtering coating of photocatalysts onto $BaTiO_3$ particulates.

Deposition Time (hr)	Power (W)	Frequency (kHz)	Duty (µs)	Oscillating Power (%)	Pre Coating Treatment	Post Coating Treatment
3	1000	150	3.3	70	1100°C for 4 hours	-
3	1000	150	3.3	70	1100°C for 4 hours	500°C for 1 hour
6	1000	150	3.3	70	1100°C for 4 hours	500°C for 1 hour
9	1000	150	3.3	70	1100°C for 4 hours	500°C for 1 hour

3.5.1 Surface Characterisation

3.5.1.1 Raman Spectroscopy

Surface characterisation of $BaTiO_3$ particulates was carried out to analyse the TiO_2 coating after deposition. As seen in graph B, figure 36, the analysis through Raman spectroscopy of the $BaTiO_3$ particulates confirmed an anatase presence on the $BaTiO_3$. The characteristic anatase peak at 144 cm^{-1} and 399 cm-1 was clearly visible along with the characteristic peaks of $BaTiO_3$, which can be seen on graph A, figure 36.

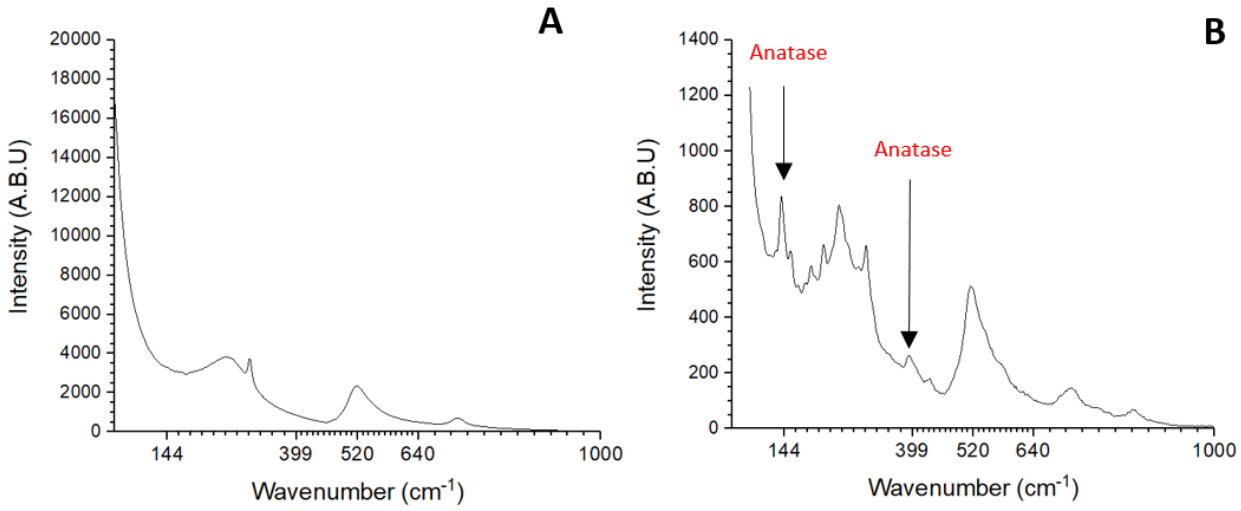

*Figure 36 – Raman spectra of – **(A)** $BaTiO_3$ particulates no coating **(B)** $BaTiO_3$ particulates with TiO_2 coating annealed at 500°C for 1 hour.*

3.5.1.2 SEM

Figure 37 and figure 38 show the surface of $BaTiO_3$ particulates after coating with TiO_2-W. The surface of the $BaTiO_3$ particulates compromises of small micro particles sintered together, this is due to the process of forming the particulates from powder when manufactured by CATAL international. As seen in figure 37 and figure 38 it appears that upon coating the gaps between the micro particles are 'filled in' by the sputtered TiO_2, this could have various effects on its average pore size and surface area.

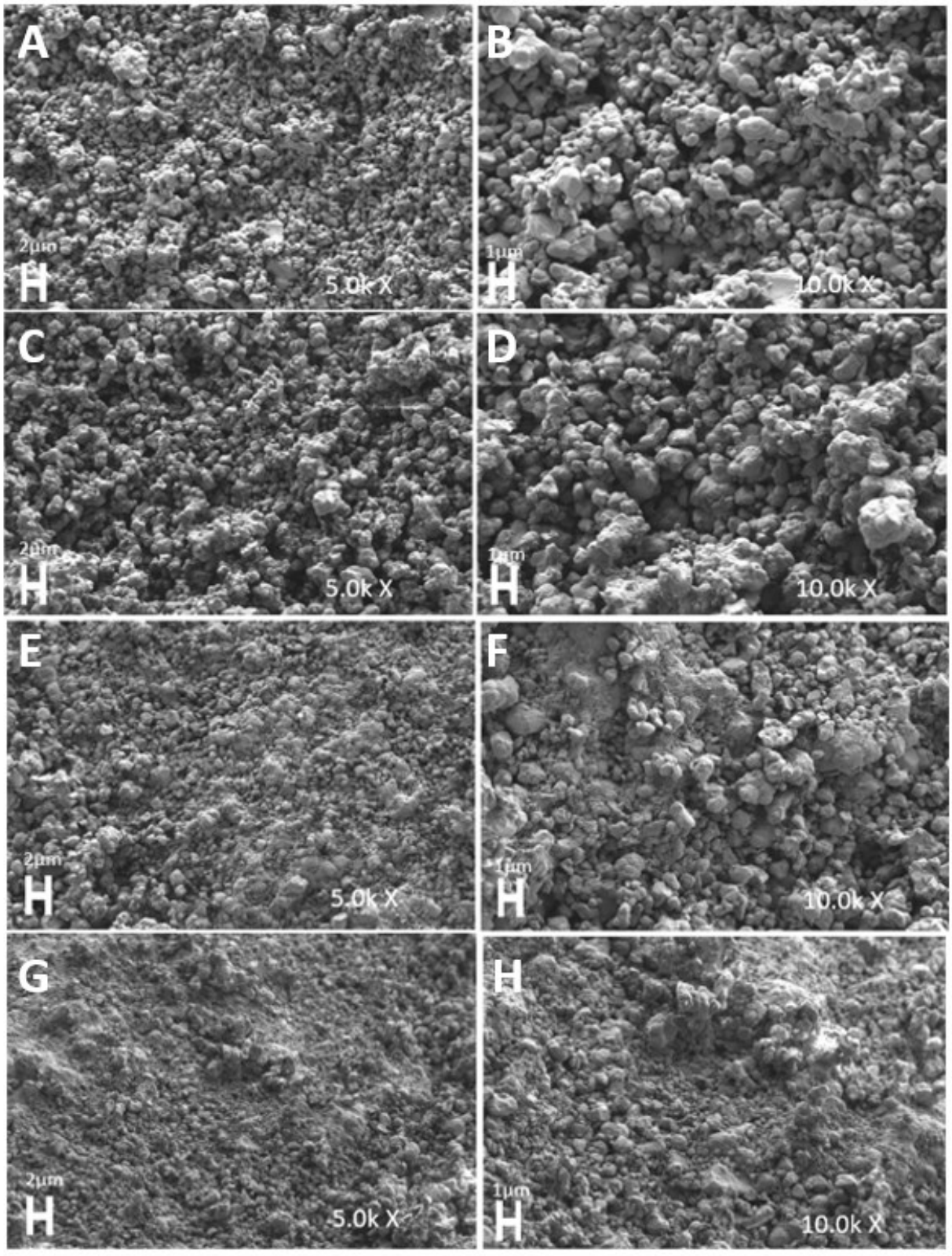

Figure 37 – (A and B) SEM images of non-coated $BaTiO_3$ surface, (C and D) $BaTiO_3$ coated with TiO_2 for 3 hours, (E and F) $BaTiO_3$ coated with TiO_2 for 6 hours, (G and H) $BaTiO_3$ coated with TiO_2 for 9 hours.

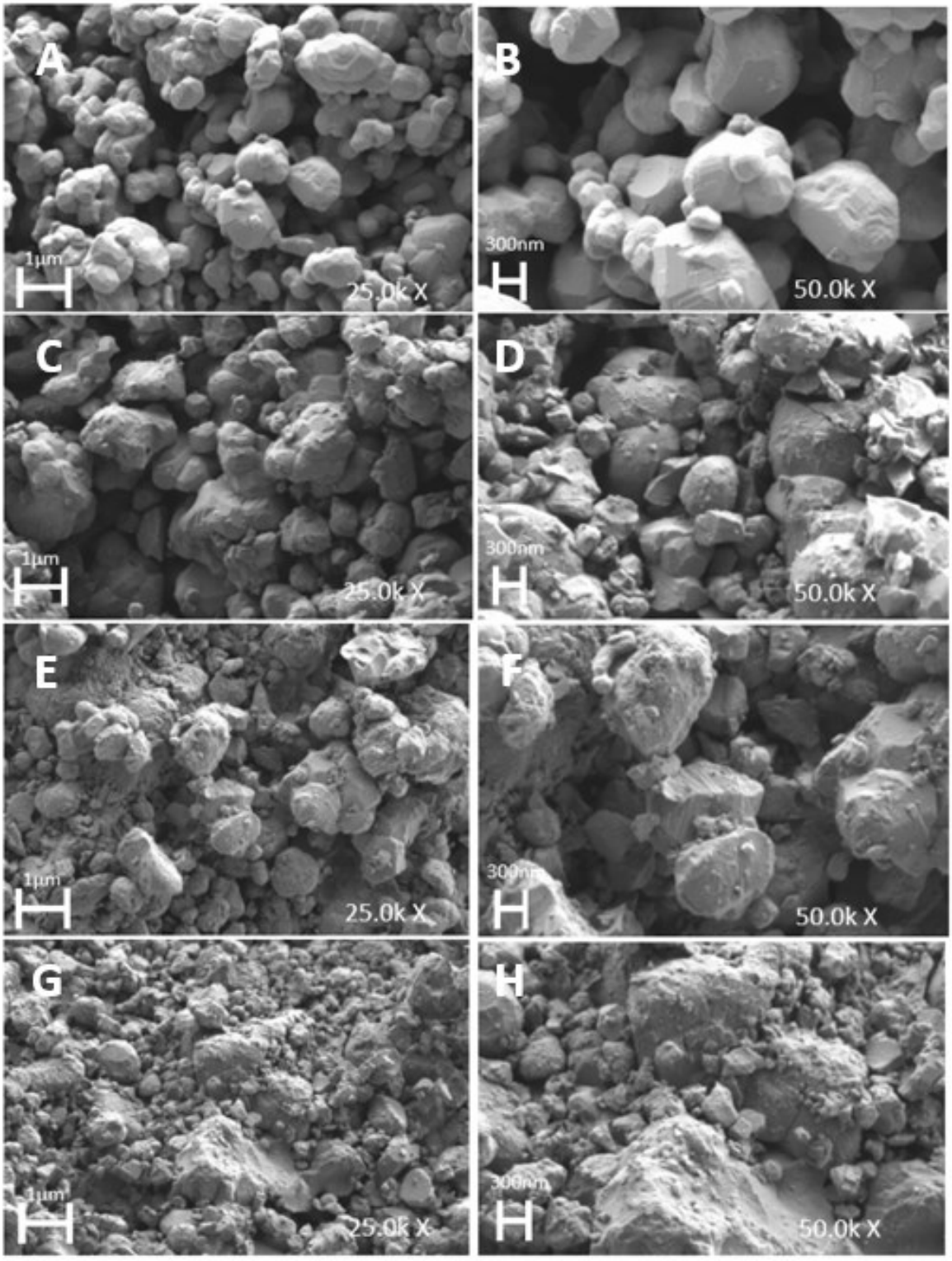

Figure 38 – (A and B) SEM images of non-coated $BaTiO_3$ surface, (C and D) $BaTiO_3$ coated with TiO_2 for 3 hours, (E and F) $BaTiO_3$ coated with TiO_2 for 6 hours, (G and H) $BaTiO_3$ coated with TiO_2 for 9 hours.

3.5.1.3 XPS

XPS spectroscopy of 100µm by 100µm areas was carried out to analyse the stoichiometry of the surface of the $BaTiO_3$ particulates and enable an understanding of the role that the surface coatings could play in non-thermal plasma experiments. Figure 39 shows the XPS spectroscopy of the TiO_2 coated $BaTiO_3$ particulates showed an increase of Ti 3p orbitals at 36eV and a strong decrease in Ba 3d, 4p and 4d orbitals. This illustrates an increased surface coverage of Ti compared to Ba due to the 3 hour TiO_2 coating.

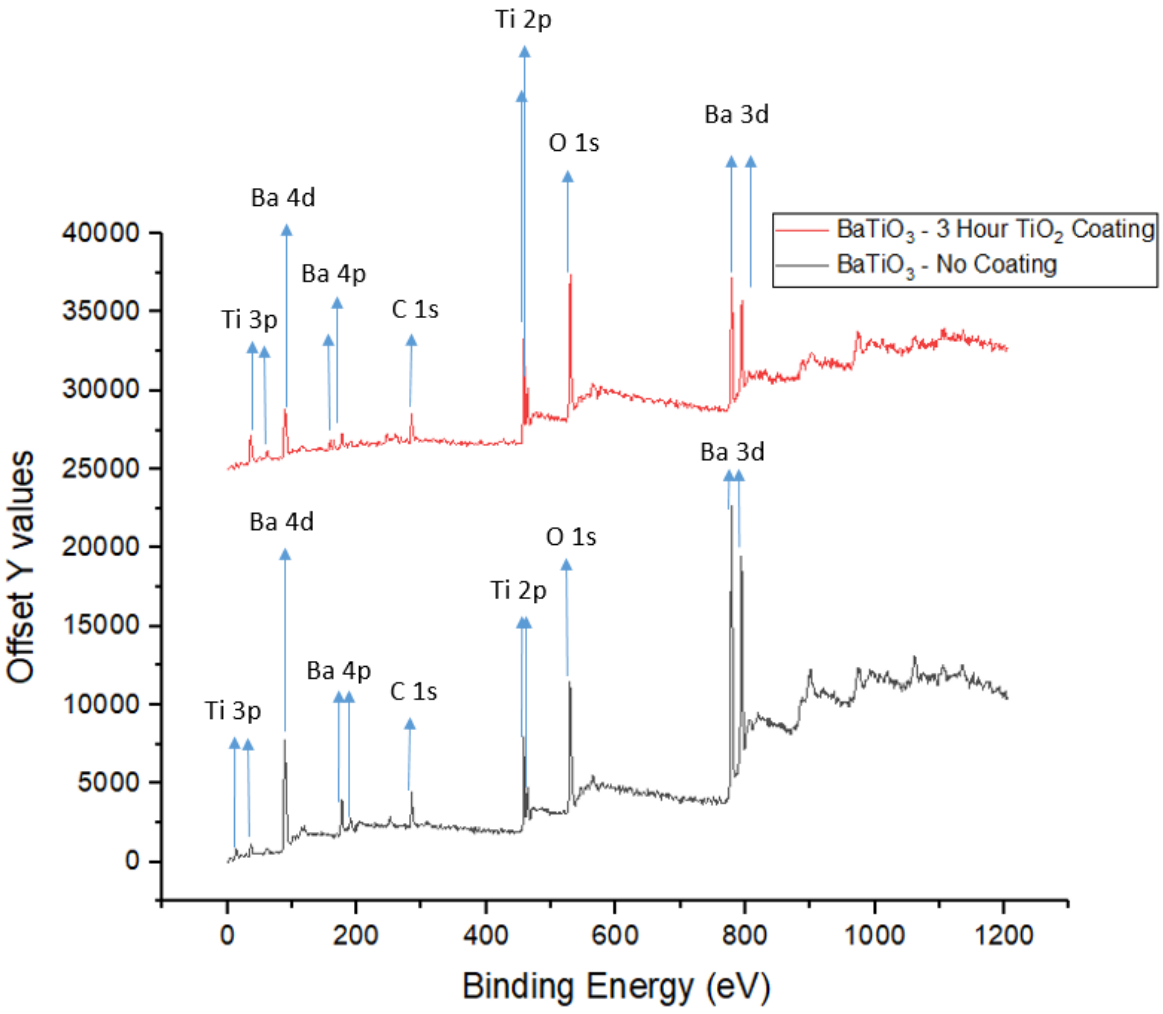

Figure 39 – XPS spectra of $BaTiO_3$ without coating and after coating with TiO_2 for 3 hours via magnetron sputtering.

3.5.2 Photocatalytic Activity

The photocatalytic activity was measured to see the effects of the coatings on the $BaTiO_3$ particulates and to see if the deposition of the photocatalytic coating was successful with the parameters used. It is unfair to compare these results to the glass beads as a lower amount of beads were used at 1.5g per 50ml of methylene blue solution. On top of this the $BaTiO_3$ particulates have a higher surface area than the glass particulates.

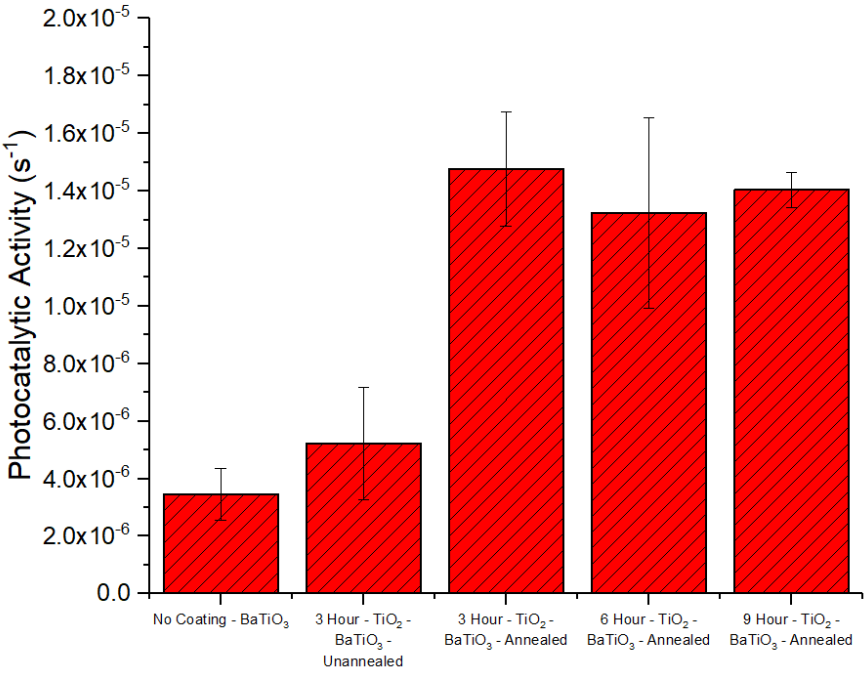

Figure 40 – Photocatalytic activity of 1, 2 and 3 hour TiO_2 coated $BaTiO_3$ particulates using the methylene blue degradation method.

Photocatalytic activity of the TiO_2 coated $BaTiO_3$ particulates in comparison to the uncoated $BaTiO_3$ once annealed showed an increase of 4 times to a photocatalytic activity of 1.48E-5. This proves that the annealing process is significant and supports the theory that the TiO_2, is amorphous upon deposition on the $BaTiO_3$. The annealing process clearly converts the amorphous TiO_2 coating into a photocatalytically active one, as seen by the enhancement of photocatalytic activity, the most likely crystalline phase obtained is the anatase TiO_2 structure as the annealing process was identical to that of the TiO_2 coated glass particulates. Evidence of this can be seen in the XPS results and confirmed by Raman spectroscopy, seen in figure 39 and figure 36 respectively. However, the increase of deposition time to 6 and 9 hours did not further increase the photocatalytic activity as expected. Maximum surface coverage could have been achieved with the 3 hours deposition and so could be the explanation behind the photocatalytic activity staying constant with increasing deposition time.

3.5.3. Summary

Coating of 3, 6 and 9 hour TiO_2 coatings were deposited onto $BaTiO_3$ particulates to investigate the feasibility of magnetron sputtering for photocatalytic preparation. Post deposition annealing was carried out at 500ºC to obtain an anatase phase. Maximum surface coverage and saturation of the substrate was achieved at 3 hours deposition. XPS analysis shows the presence of a TiO_2 coating on the $BaTiO_3$. Raman spectroscopy confirmed the presence of anatase TiO_2 on the $BaTiO_3$. TiO_2 coated $BaTiO_3$ which was as-deposited showed little photocatalytic activity eluding to an amorphous non-photocatalytic coating. Photocatalytic testing using the methylene blue method was carried out and showed an increase of photocatalytic activity with the annealed TiO_2 coated $BaTiO_3$ by up to 400% compared to uncoated $BaTiO_3$. Photocatalytic testing using the methylene blue method was carried out and showed an increase of photocatalytic activity with the annealed TiO_2 coated $BaTiO_3$ by up to 283% compared to the unannealed TiO_2 coated $BaTiO_3$.

3.6 Deposition of Tungsten-Doped Titanium Dioxide Coatings on Glass Particulates

TiO_2-W coatings have been deposited using two planar unbalanced type II magnetrons onto glass particulates as a precursor to depositing TiO_2-W onto $BaTiO_3$ particulates to investigate the effect of doping on the coatings properties including crystallinity and photocatalytic activity. All coatings were deposited in a two target magnetron sputtering rig which was pumped down to a base pressure of 1×10^{-3} Pa. Two 300 mm x 100 mm type II unbalanced planar magnetrons were used with targets of titanium and tungsten of 99.5% purity. The reactive sputtering process was carried out in an argon/oxygen atmosphere. A dual channel Advanced Energy Pinnacle Plus power supply operated in pulsed DC mode was used to power the magnetrons. Tungsten has been investigated as a dopant in TiO_2 photocatalysis due to effective reduction of the bandgap in previous literature [179-181] however, it has previously been found that excessive tungsten within the matrix can be ineffective in terms of photocatalytic activity. Sputtering conditions from previously optimised tungsten-doped coatings were used, this required to power to the tungsten target to be 80 W [23]. The titanium target parameters were kept the same as the previous coatings on $BaTiO_3$. Post deposition annealing to 600°C for 30 minutes to obtain an anatase TiO_2 phase due to previous work [23]. Conditions for the coatings can be seen below in table 13.

Table 13 – Deposition parameters for the initial magnetron sputtering coating of TiO_2-W photocatalysts onto glass particulates.

Deposition Time (hr)	Power Ti Target (W)	Power W Target (W)	Ti Target Frequency (kHz)	W Target Frequency (kHz)	Ti Target Duty (µs)	W Target Duty (µs)	Oscillating Power (%)	Pre Coating Treatment	Post Coating Treatment
1	1000	80	150	100	3.3	2.5	70	-	600°C for 30 mins
2	1000	80	150	100	3.3	2.5	70	-	600°C for 30 mins
3	1000	80	150	100	3.3	2.5	70	-	600°C for 30 mins

3.6.1 Surface Characterisation

3.6.1.1 Raman Spectroscopy

Raman surface characterisation of coated glass particulates were carried out in order to determine the crystallinity of the coating upon adding the tungsten dopant. TiO_2 coated particulates doped with tungsten showed an anatase phase along with a WO_3 phase. WO_3 has characteristic Raman peaks at 218, 253 274, 320, 711, 806 cm^{-1} [182, 183]. The peak at 926 cm^{-1} could be due to the bonding of tungsten to titanium and then forming a tungsten-titanium oxide similar to $BaWO_4$ or $Fe_2(WO_4)_3$ which has characteristic peaks at 940 cm^{-1} and 1036 cm^{-1} respectively [184].

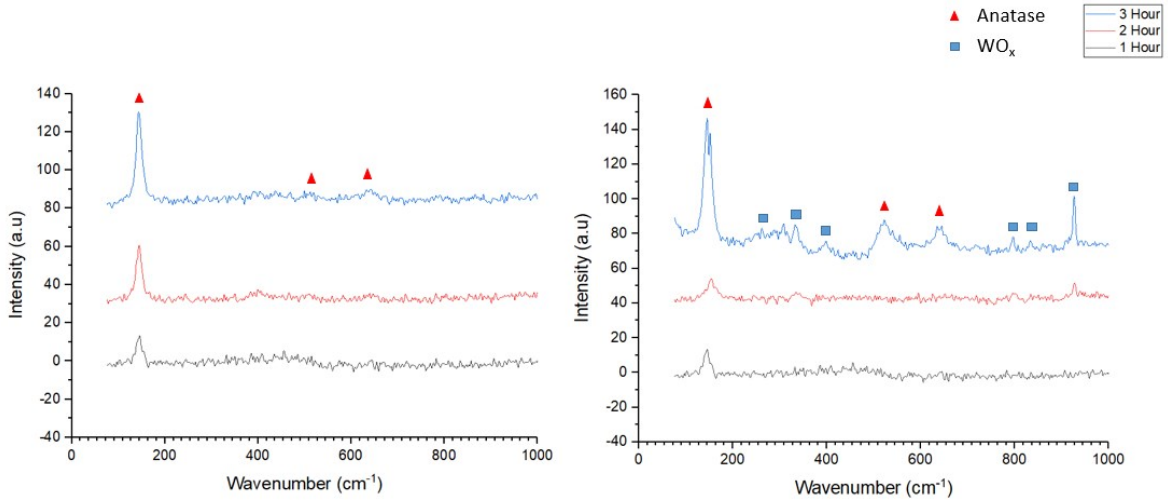

Figure 41 – Raman spectra of 1,2 and 3 hour TiO_2 coated glass particulates (left) and 1,2 and 3 hour TiO_2-W coated glass particulates (right)

3.6.1.2 SEM

Figure 42 shows SEM images of the glass particultes before and after coating of TiO_2-W. Glass particulates coated with TiO_2-W shows similar coating coverage as TiO_2 coatings presented in figure 30. .

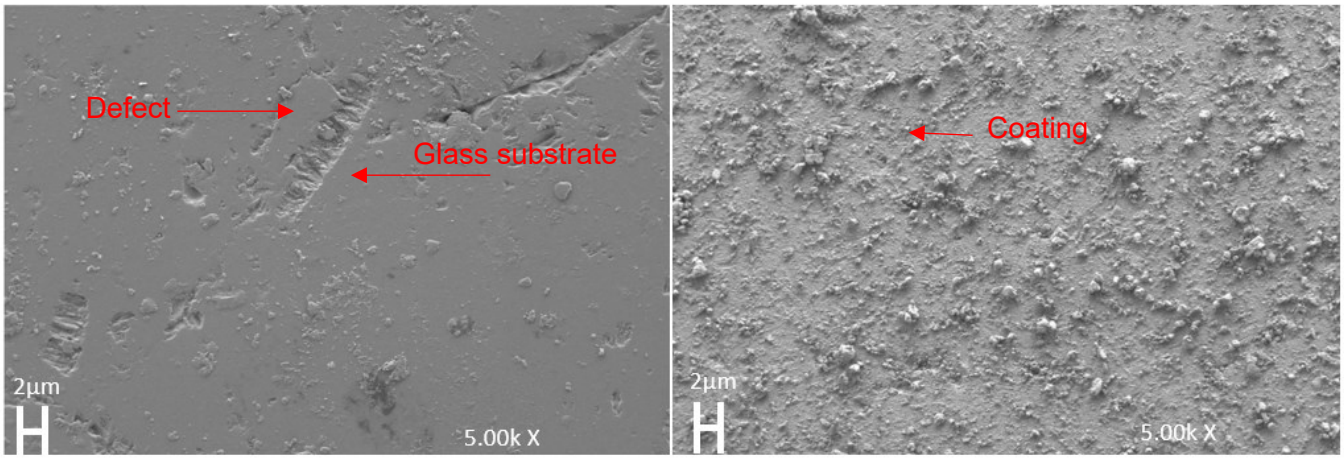

Figure 42 – SEM images of the glass particulate's surface without coating (left) and with TiO_2-W 3 hour coating (right).

Figure 43 shows EDX images of an uncoated glass particulate and TiO_2-W coated particulate. The image confirms that the dispersion of the coating is uniform, which allow maximum active sites for photocatalytic reactions.

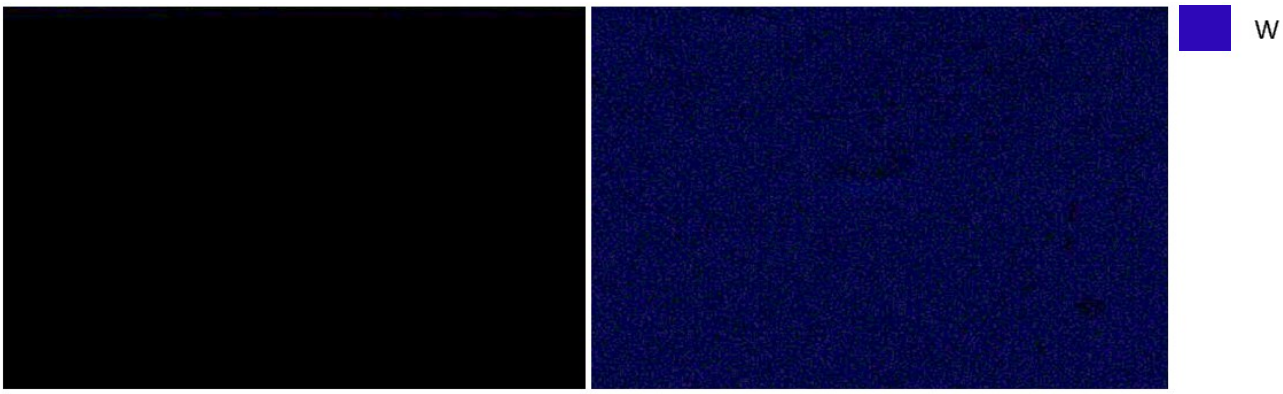

Figure 43 – EDX spectra of the glass particulate's surface without coating (left) and with TiO_2-W 3 hour coating (right).

3.6.1.3 XPS

XPS spectroscopy of 100 µm by 100 µm areas was carried out to analyse the stoichiometry of the surface of the glass particulates coated with TiO_2 and TiO_2-W and enable an understanding of the role that doped surface coatings could play in non-thermal plasma experiments. The XPS spectroscopy of the TiO_2-W glass particulates show peaks of W 4f at 35 and 37.2eV, W 4d at 248 eV and W 4p at 458 eV, which agree with literature [185]. Typical W 4f peaks of WO_3 appear at 38.1 and 36 eV according to thermo scientific whereas W metal is present at 33.7 eV and 31.6 eV. A W metal loss feature is also present at 37 eV [186]. Peaks corresponding to W 4f overlap with Ti 3s peaks in XPS, Sathasivam et al found that W $4f_{7/2}$ peaks at 35 eV corresponded to W^{6+} [180]. Impurities of Bi were detected on the non-coated glass particulates. This illustrates that the presence of WO_3 is present along with TiO_2 on the $BaTiO_3$ particulates.

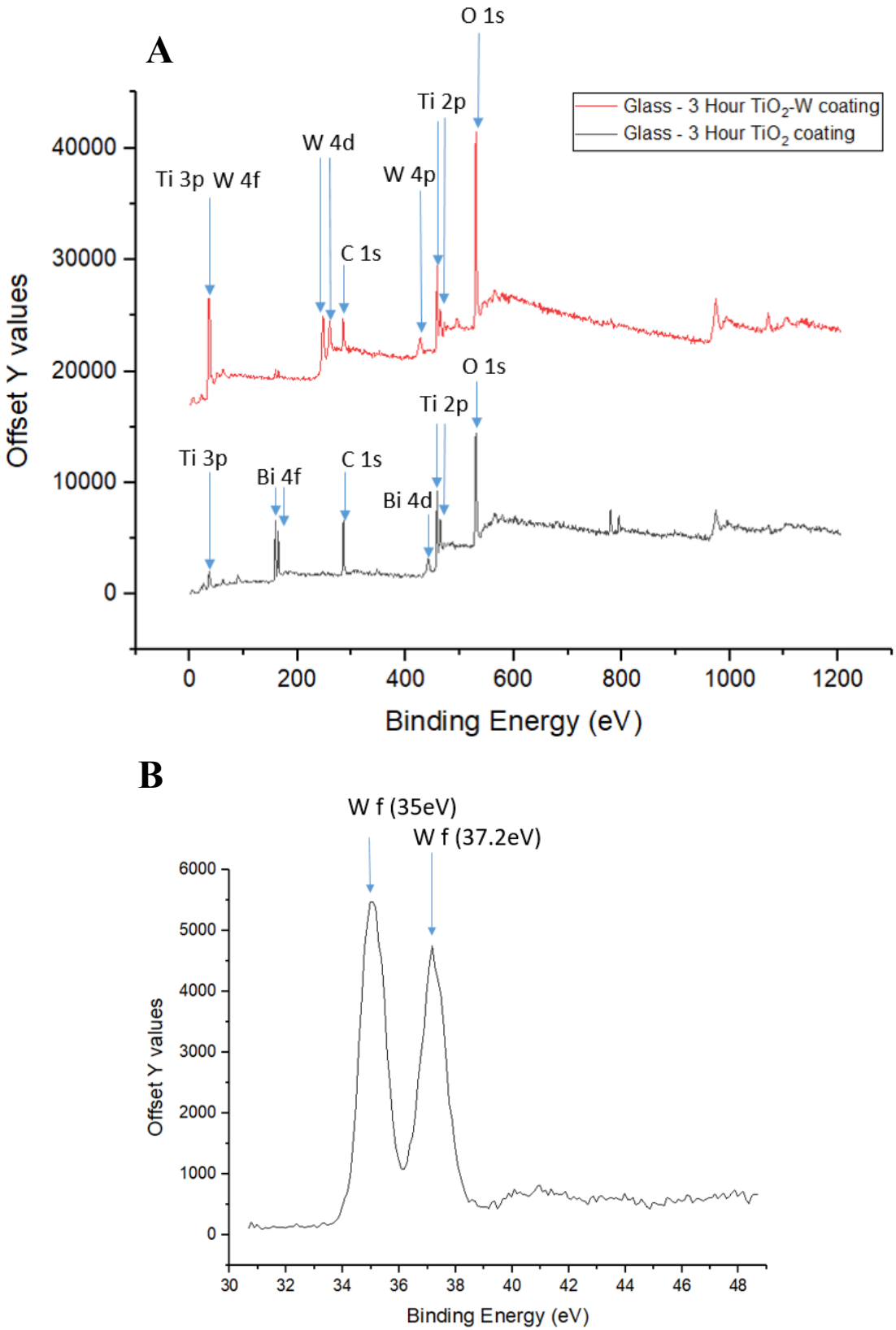

*Figure 44 – (**A**) XPS spectra of glass particulates with 3 hour coating of TiO_2 and glass particulates with 3 hour TiO_2-W coating. (**B**) Focussed XPS scan of glass particulates with 3 hour TiO_2-W coating showing Wf peaks.*

3.6.2 Photocatalytic Activity

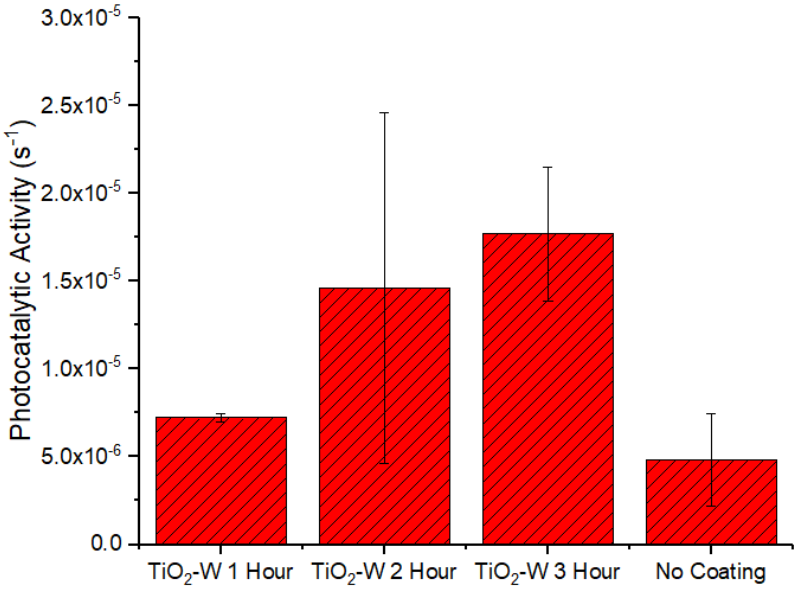

Figure 45 – Photocatalytic activity of 1, 2 and 3 hour TiO_2-W coated glass particulates using the methylene blue degradation method.

Photocatalytic testing, see figure 45, showed that the TiO_2-W glass coated samples showed higher photocatalytic activity than the TiO_2 coatings. The TiO_2-W coatings showed an increase in photocatalytic activity compared to non-coated glass particulates by up to 4 times with a photocatalytic activity of 1.78E-5 s^{-1}, this was achieved by the 3 hour coating. Increasing the deposition time from 1 to 3 hours increased the photocatalytic activity by 2.4 times from a photocatalytic activity of 7.4E-6 s^{-1} for the 1 hour coating. Increased surface coverage would provide more active sites for the degradation of methylene blue. TiO_2-W coatings showed an increase in photocatalytic activity compared to TiO_2 coated glass particulates by up to 2 times.

3.6.3. Summary

1,2 and 3 hour TiO_2-W coatings were deposited onto glass particulates to investigate the feasibility of magnetron sputtering for photocatalytic preparation and investigate the effect of doping on the photocatalytic performance. Post deposition annealing was carried out at 600°C, a mixture of anatase and tungsten oxide crystalline phases were present. XPS spectroscopy confirmed the presence of TiO_2 and WO_3 on the glass particulates. Increasing the deposition time from 1 to 3 hours increased the photocatalytic performance of the coating. Photocatalytic testing using the methylene blue method was carried out and showed an increase of photocatalytic activity with the annealed TiO_2-W by up to 200% compared to the TiO_2 coated glass particulates. This shows successful enhancement of photocatalytic activity due to W doping.

3.7 Deposition of Tungsten-Doped Titanium Dioxide Coatings on Barium Titanate Particulates

TiO_2-W coatings have been deposited onto $BaTiO_3$ particulates for use in the packed bed dielectric barrier discharge. Deposition was carried out with a pulse frequency of 150 kHz, a pulse on time of 3.3 µs and power of 1000 W. The flows of oxygen and argon were controlled using mass-flow controllers and fixed to 11.5sccm and 15sccm respectively. Heat treatment was performed in an air filled muffle furnace, model Carbolite 3000. TiO_2-W films were annealed to 600˚C for 30mins to obtain an anatase phase. Deposition parameters can be seen below in table 14.

Table 14 – Deposition parameters for the initial magnetron sputtering coating of TiO_2-W photocatalysts onto $BaTiO_3$ particulates.

Deposition Time (hr)	**Power Ti Target (W)**	**Power W Target (W)**	**Ti Target Frequency (kHz)**	**W Target Frequency (kHz)**	**Ti Target Duty (µs)**	**W Target Duty (µs)**	**Oscillating Power (%)**	**Pre Coating Treatment**	**Post Coating Treatment**
3	1000	80	150	100	3.3	2.5	70	-	600°C for 30 mins

3.7.1 Surface Characterisation

3.7.1.1 SEM

SEM imaging, see figure 46-48 was performed primarily in order to investigate the effect of deposition time on the coverage of TiO_2 on the glass particulates. SEM images taken at a magnification of 5,000x showed a visual image of the substrate pre and post coating. It can be seen that the surface roughness is significantly higher for the $BaTiO_3$ particulates than the glass particulates. The surface area of the $BaTiO_3$ was calculated to be 0.7091 m^2/g by BET surface area analysis whilst the glass particulates had a calculated surface of 0.0013 m^2/g. It can be seen that the surface of the $BaTiO_3$ particulates changes upon deposition, the addition of TiO_2 seems to fill in the 'gaps' and cover the $BaTiO_3$ particulates surface.

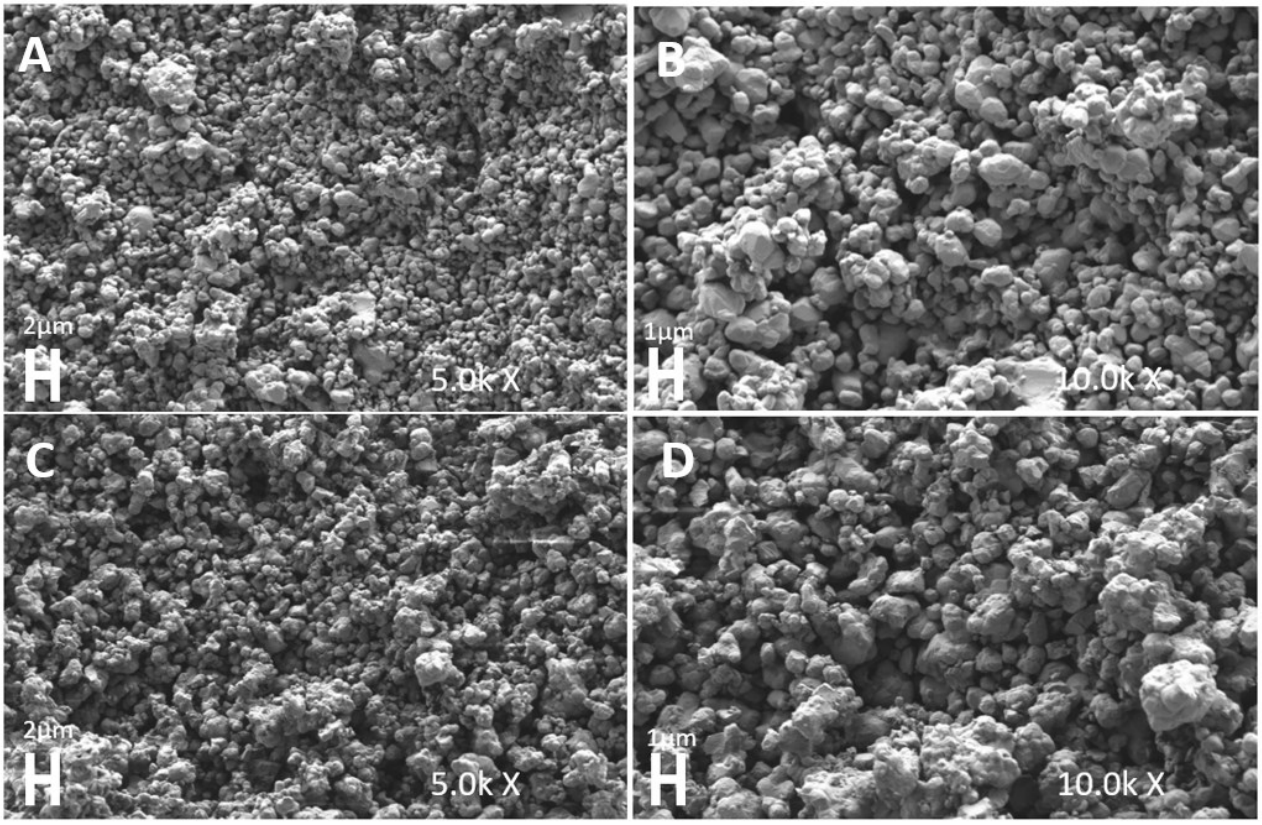

Figure 46 – (A and B) SEM images of non-coated $BaTiO_3$ surface and (C and D) $BaTiO_3$ coated with TiO_2-W for 3 hours.

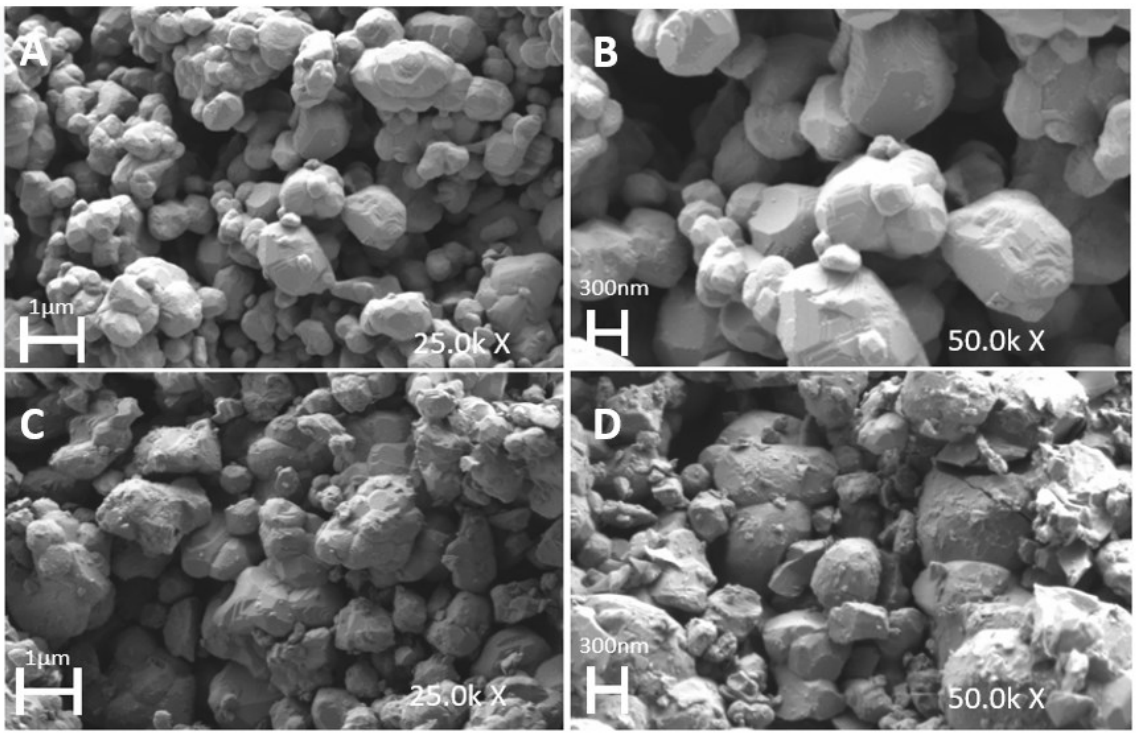

Figure 47 – (A and B) SEM images of non-coated $BaTiO_3$ surface and (C and D) $BaTiO_3$ coated with TiO_2-W for 3 hours.

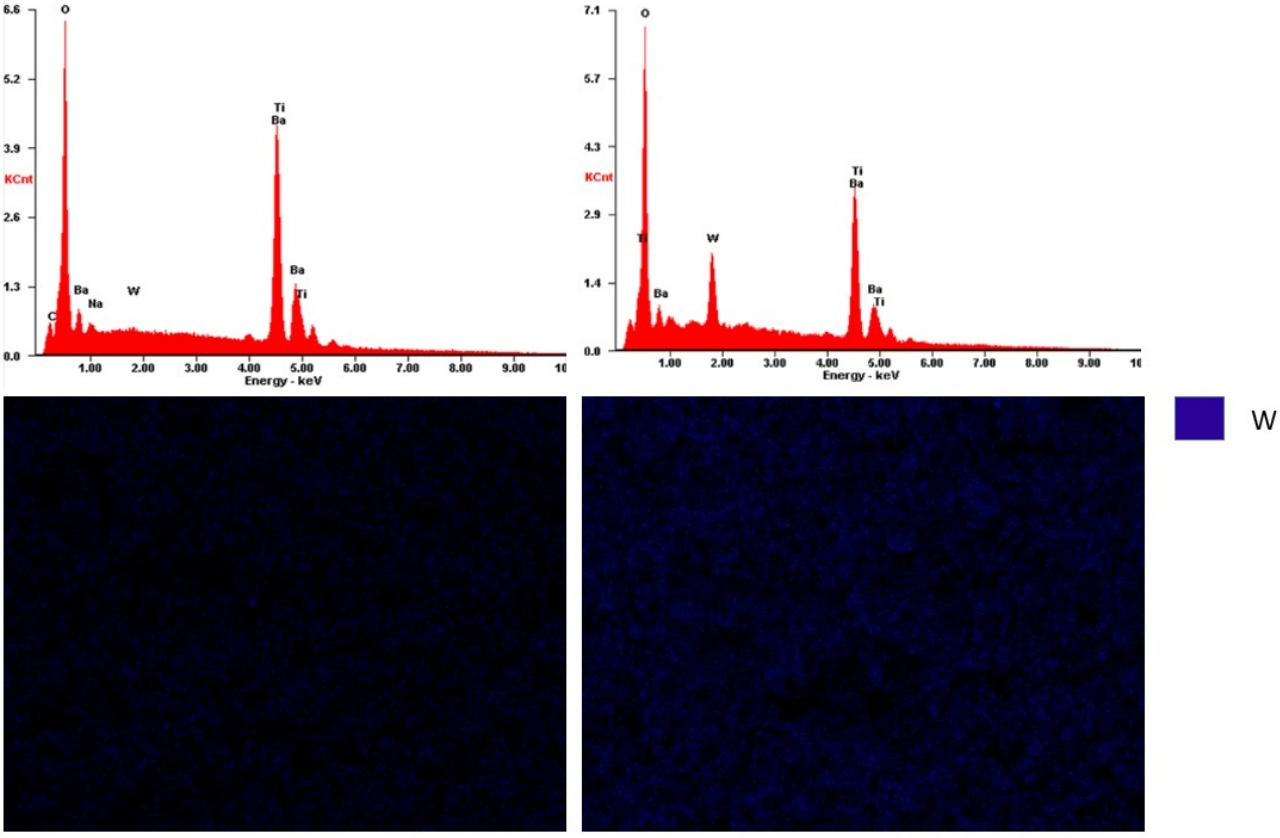

Figure 48 – EDX spectra of $BaTiO_3$ (top left) and $BaTiO_3$ coated with TiO_2-W (top right). EDX mapping of $BaTiO_3$ (bottom left) and $BaTiO_3$ with 3 hour TiO_2-W (bottom right).

3.7.1.2 XPS

XPS spectroscopy of 100µm by 100µm areas was carried out to analyse the stoichiometry of the surface of the $BaTiO_3$ particulates coated with TiO_2 and TiO_2-W and enable an understanding of the role that doped surface coatings could play in non-thermal plasma experiments. Figure 49 shows the XPS spectroscopy of the $BaTiO_3$ particulates coated with TiO_2-W show peaks of W 4f at 35.5 eV and 37.4 eV, W 4d at 248 and W 4p at 458 eV. A reduction in the Ba 3d peaks can also be seen. This also illustrates that the presence of WO_3 is present along with TiO_2 on the $BaTiO_3$ particulates.

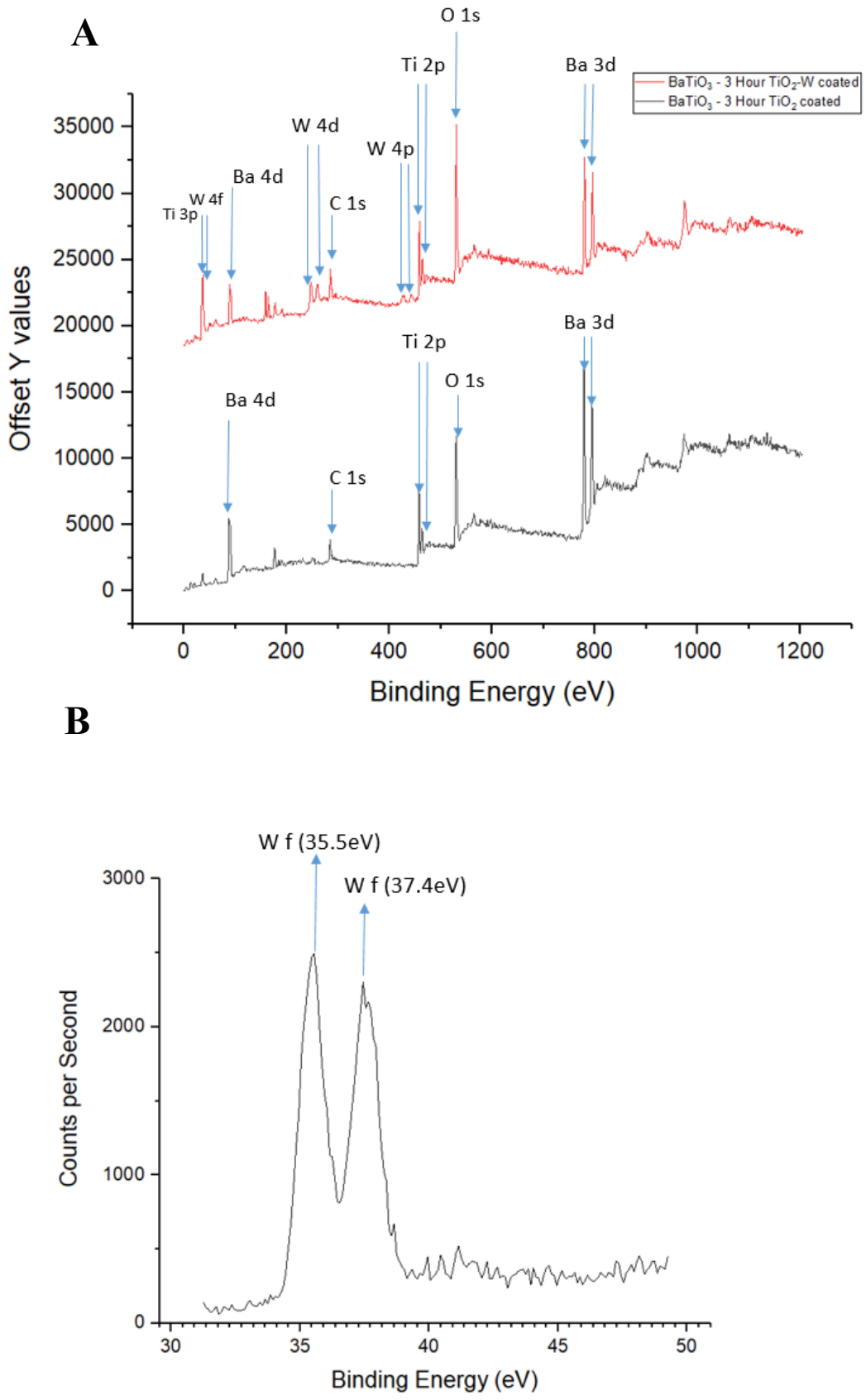

*Figure 49 – **(A)** XPS spectra of glass particulates with 3 hour coating of TiO_2 and $BaTiO_3$ particulates with 3 hour TiO_2-W coating. **(B)** Focussed XPS scan of $BaTiO_3$ particulates with 3 hour TiO_2-W coating showing Wf peaks.*

3.7.2 Photocatalytic Activity

The photocatalytic activity of the TiO_2-W coated $BaTiO_3$ particles increased by 12.5 times compared to uncoated $BaTiO_3$ and by up to 3 times in comparison to the TiO_2 coated $BaTiO_3$ as seen in figure 50. As stated previously, tungsten doping has been used to improve the photocatalytic activity of TiO_2 catalysts. It is thought that using tungsten as a dopant enables the release of up to two electrons for every one dopant atom [80, 187]. This is advantageous as it allows the use of low dopant levels that reduce defect concentrations and hence reduce scattering of charge carriers. Tungsten is an ideal dopant because it is soluble in a TiO_2 matrix since it commonly occurs in the 6^+ oxidation state and in that state has a smaller ionic radius than Ti^{4+} [80, 187]. This can lead to better conductivity and transparency compared to other dopants such as niobium and tantalum.

Furthermore, tungsten doping of TiO_2 has multiple advantages, as it is known to enhance the photocatalytic activity by reducing charge carrier recombination and by increasing light absorption in the visible portion of the spectrum [188]. The effect of doping TiO_2 with tungsten on the bandgap and electron-hole transport can be seen in figure 4.

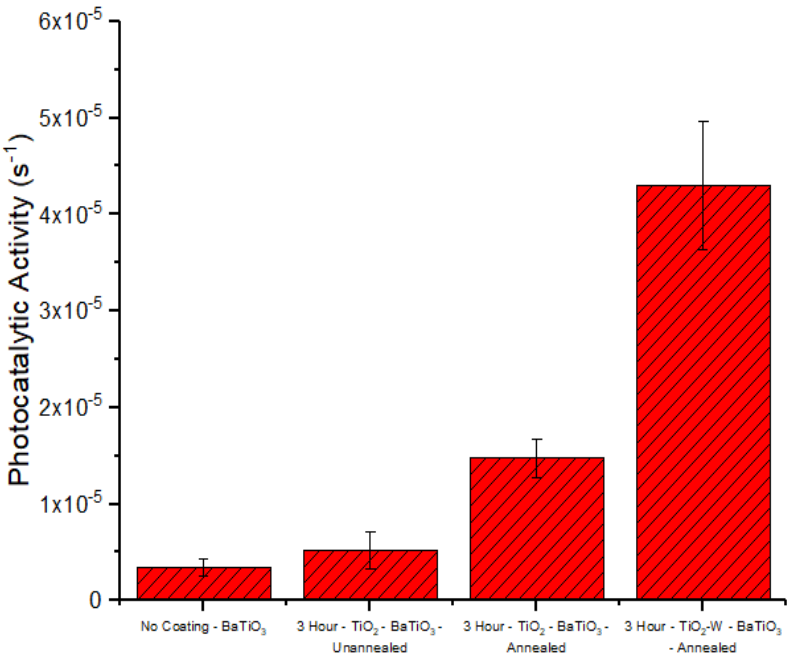

Figure 50 - Photocatalytic activity of $BaTiO_3$, 3 hour TiO_2 coated $BaTiO_3$ unannealed and annealed, 3 hour TiO_2-W coated $BaTiO_3$ particulates using the methylene blue degradation method.

3.7.3. Summary

Coatings of 3 hour TiO_2-W coatings were deposited onto $BaTiO_3$ particulates to investigate the effect of doping on the photocatalytic performance. SEM spectroscopy of non-coated $BaTiO_3$ and $BaTiO_3$ coated with TiO_2-W were analysed and compared. XPS spectroscopy of non-coated $BaTiO_3$ and $BaTiO_3$ coated with TiO_2-W were compared and showed the presence of WO_3. Annealed $BaTiO_3$ coated with TiO_2-W for 3 hours and annealed showed the best photocatalytic activity by up to 3 times compared to $BaTiO_3$ coated with TiO_2 and annealed.

CHAPTER 4 - EFFECT OF PHOTOCATALYST COATED DIELECTRIC PARTICULATES ON OZONE PRODUCTION USING A PACKED BED REACTOR.

Titanium dioxide (TiO_2) films were deposited onto dielectric $BaTiO_3$ particulates for use within a non-thermal packed bed dielectric barrier discharge reactor. Deposition was performed by a novel single stage magnetron sputtering process using two planar unbalanced type II magnetrons in order to produce a high quality photocatalytic thin film with uniform distribution. For these experiments $BaTiO_3$ particulates were coated with TiO_2 for 3 hours. Subsequent annealing of the TiO_2 samples to 500°C for an hour was performed in air in a muffle furnace. Photocatalytic coatings of TiO_2 produced onto the barium titanate ($BaTiO_3$) particulates which were subsequently annealed showed an increase in photocatalytic activity by up to 4 times compared to non-coated $BaTiO_3$. Coated $BaTiO_3$ particulates were placed inside a packed bed dielectric barrier discharge reactor to investigate their effect during the plasma process on the production of ozone from an oxygen-nitrogen gas mix. Oxygen and nitrogen were flowed into the reactor at various flow rates and feed ratios. Feed ratios were altered to investigate their effect on the plasma chemistry with the various packing material. Flow rates tested were in the range of 1 standard litre per minute (SLM) to 3 SLM, which give residence times of 0.011 s and 0.0037 s respectively, in order to investigate the effect of flow rate and specific energy density on the production of ozone. The reactors peak to peak voltage was kept at 8.6 kV, the supplied O_2:N_2 mix of 3:97 was increased to 21:79 in stages of 3 %. Further to this, and in order to gain a further understanding, tests using pure oxygen were also carried out at various specific energy densities for the different packing material, the voltage used was at 9.6 kV to increase the discharge energy within the plasma.

4.1 Ozone Production

It is proposed that an investigation of photocatalytic TiO_2 coatings onto the packing material of a DBD for the production of ozone from oxygen and an O_2:N_2 mix is carried out to study the effects of the photocatalyst on plasma chemistry. Ozone (O_3) is a useful oxidant that sees widespread use in water treatment due to being effective in sterilization. The production of ozone by dielectric barrier discharges is performed at atmospheric pressure and low temperature and requires only air or oxygen, and electricity. The types of dielectric barrier discharge (DBD) reactors employed to produce ozone are packed bed DBDs [53, 189], corona discharge reactors [190, 191], parallel plate reactors [192], and surface dielectric barrier discharges [12], with packed bed reactors, for a given specific energy density, improving energy efficiency up to 12 times. The production of ozone using air flowing through a DBD has issues with regards to the production of harmful nitrogen oxides (N_xO_x). N_xO_x is a serious pollutant and has a huge role in smog and acid rain formation, while also being harmful to inhale. Different types of dielectric barrier discharges have been investigated regarding their effect on N_xO_x formation in air plasma however they are difficult to compare due to differences in structure, geometry and excitation modes among other factors. As a result different discharges provide different reaction pathways for the production of N_xO_x compounds [193]. Plasma catalysis presents a promising approach to reducing N_xO_x production whilst increasing ozone selectivity, however the relatively low temperatures of dielectric barrier discharges can hinder the effectiveness of the catalyst. Photocatalysts, on the other hand, do not require high temperatures to be active, instead they are activated by the absorption of photons of high enough energy and it is hypothesized that the photons emitted by the plasma will activate the photocatalyst. Photocatalysts have been employed in combination with non-thermal plasma in order to increase product yields and increase energy efficiency in a variety of processes [13-15], however the combination of photocatalysts with non-thermal plasma for the production of ozone from air is sparse. Pekárek et al investigated photocatalysts of TiO_2 and zinc oxide in a surface dielectric barrier discharge for the production of ozone from air, it was observed that the concentration of ozone increased compared to when no catalyst was used [12]. TiO_2 catalysts have also been investigated for their effect on N_xO_x reaction pathways and production yields. Jõgi et al implemented TiO_2 catalysts in a coaxial dielectric barrier discharge to investigate the ozone oxidation of NO to NO_2 and N_2O_5. At high temperatures TiO_2 catalyst was found to improve the efficiency of oxidation of NO_2 to N_2O_5 with a proposal that surface species on the TiO_2 were responsible for subsequent reactions [194]. The combination of non-thermal plasma and photocatalysts has received much attention in recent years [13, 195], however there is still a lot of research to be done to further understand the interaction between plasma and catalyst and to confirm whether it is due to the photocatalytic effect. The synergy of combining plasma and catalyst can be beneficial and lead to an increase in desired product yield and energy efficiency [20, 28, 112]. Therefore, it is hypothesised that coating the $BaTiO_3$ with TiO_2 could have a significant effect on the plasma chemistry within the packed bed plasma reactor.

4.2 Thin Film Deposition of Titanium Dioxide Photocatalysts onto Barium Titanate used in Packed Bed Reactor

Thin films of TiO_2 have been coated using two planar unbalanced type II magnetrons onto $BaTiO_3$ particulates. All coatings were deposited in a two target magnetron sputtering rig which was pumped down to a base pressure of 1×10^{-3} Pa. A 300 mm x 100 mm type II unbalanced planar magnetron was used along with a target of titanium of 99.5% purity. The reactive sputtering process was carried out in an argon/oxygen atmosphere. A dual channel Advanced Energy Pinnacle Plus power supply operated in pulsed DC mode was used to power the magnetrons. The flows of oxygen and argon were controlled using mass-flow controllers and fixed to 11.5 sccm and 15 sccm respectively. Table 15 shows the prepared $BaTiO_3$ used in the PBR for ozone production. The process of sputtering the TiO_2 photocatalyst onto the $BaTiO_3$ particulates was carried out using a bespoke oscillating bowl for the uniform coating of the particulates. Heat treatment was performed in an air filled muffle furnace, model Carbolite 3000. TiO_2 thin films were heated to 500°C for an hour to obtain an anatase phase and left to cool to room temperature.

Table 15 – Deposition parameters for the initial magnetron sputtering coating of photocatalysts onto $BaTiO_3$ particulates.

Deposition Time (hr)	Ti Target Power (W)	Frequency (kHz)	Time Pulse (µs)	Oscillating Power (%)	Pre Coating Treatment	Post Coating Treatment
3	1000	150kHz	3.3	70	1100ºC for 4 hours	-
3	1000	150kHz	3.3	70	1100ºC for 4 hours	500ºC for 1 hour

4.2.1 Thin Film Characterisation

Characterisation and analysis of the $BaTiO_3$ particulates coated and used in the non-thermal reactor can be seen in CHAPTER 3 - Deposition of photocatalytic coatings onto particulates for use in a packed bed dielectric barrier discharge, section 3.5. In summary, TiO_2 coated $BaTiO_3$ which was annealed showed an increase of photocatalytic activity by up to 400% compared to uncoated $BaTiO_3$ and up to 283% compared to the unannealed TiO_2 coated $BaTiO_3$.

4.3 Packed Bed Reactor Experimental Conditions.

This section gives a detailed description of the experimental conditions used for the production of ozone using a packed bed plasma reactor. The description of the packed bed reactor used in this work is described in CHAPTER 2 - Methodology. The gases were used as delivered and consisted of oxygen (99.999%) and nitrogen (99.5%).

For experiments using an O_2:N_2 gas mix the peak to peak voltage was kept constant at 8.6 kV, the bead sizes were 1-3 mm, the mass of $BaTiO_3$ packing material was constant at 24 g which corresponded to a packing volume of 12.3 cm^3. The ratio of O_2:N_2 was investigated from 3:97 to 30:70 in increments of 3%. The flow rates of 1SLM and 3SLM were investigated.

For experiments using O_2 the peak to peak voltage was kept constant at 9.6 kV, the bead sizes were 1-3 mm, the mass of $BaTiO_3$ packing material was constant at 24 g which corresponded to a packing volume of 12.3 cm^3. The flow rates of 0.25 SLM, 0.5 SLM, 1 SLM, 2 SLM and 3 SLM were investigated, corresponding to gas residence times of 0.044s, 0.022s, 0.011s, 0.0074s and 0.0037s respectively, were investigated. Figure 51 shows the experimental set-up for the O_2:N_2 experiments.

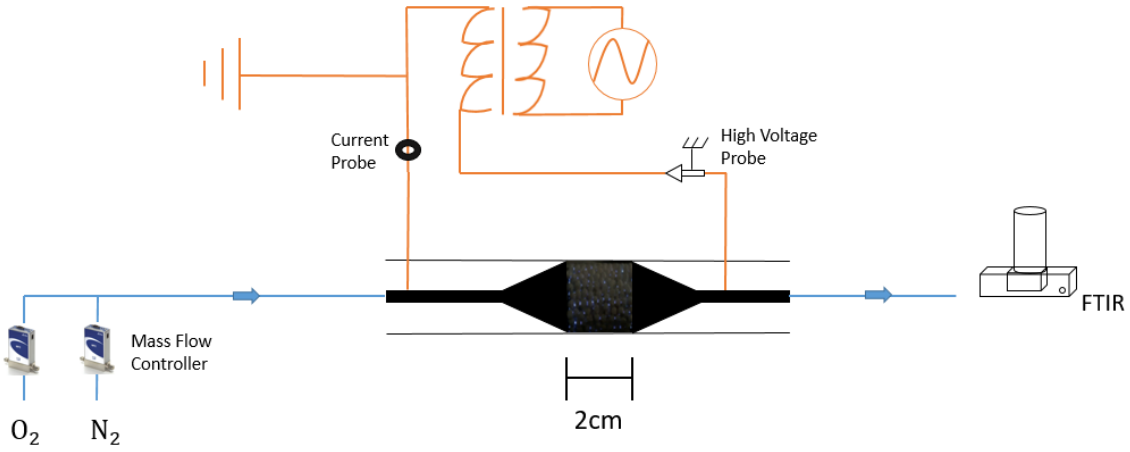

Figure 51 – Schematic of packed bed reactor experimental setup.

Pure nitrogen and oxygen were controlled by mass flow controllers and entered the packed bed reactor. Prior to any experiments nitrogen and oxygen were flowed through the closed system to flush out any impurities within the packed bed reactor and FTIR gas cell, in the case of pure O_2 experiments only O_2 was used to flush out the closed system. The gases were left flowing before any generation of plasma for 10 minutes to ensure the gas flow through the packed bed reactor reached steady state. A background scan on the FTIR was taken before the power supply was switched on and subsequent generation of

plasma. Electrical readings were taken on three separate occasions at 10, 12 and 14 minutes. This was also the case for FTIR readings in order to ensure reliability. Averages were taken and standard error was calculated. The following packing material was used and compared to investigate the effects of the TiO_2 coatings on the plasma chemistry:

- Non-coated $BaTiO_3$.
- $BaTiO_3$ coated with TiO_2 for 3 hours and unannealed.
- $BaTiO_3$ coated with TiO_2 for 3 hours and annealed in air at 500°C for 1 hour.

4.4 Effect of Titanium Dioxide Coatings on Plasma Chemistry

This section contains the results of the aforementioned experiments and describes the effect of the TiO_2 coatings on the plasma chemistry of ozone production. This includes a summary of the electrical measurements of voltage and current, the species present, their concentration and the optical emissions from the plasma.

4.4.1 FTIR analysis

The effect of photocatalytic coatings on plasma chemistry was investigated, both in pure oxygen, and with varying amounts of oxygen mixed with nitrogen. Figure 52 shows a typical FTIR spectra of the outlet gases from an air plasma generated in the packed bed dielectric barrier discharge. This indicates that the main products are NO_2, N_2O_5, N_2O and ozone. In the case of pure oxygen plasma, only ozone was detected. Figure 53 shows an example of the species and their peaks using $BaTiO_3$ coated with TiO_2 for 3 hours and annealed in air at 500°C with a O_2:N_2 ratio of 21:79. The peaks for Ozone are at 717 cm^{-1}, 1089 cm^{-1} and 1152 cm^{-1} [158], NO_2 at 648 cm^{-1}, 1320 cm^{-1}, and 1621 cm^{-1} [159], N_2O at cm^{-1}, 1285 cm^{-1}, and 2224 cm^{-1} [157] N_2O_5 at 1243 cm^{-1}, 1339 cm^{-1}, 1702 cm^{-1}, and 1742 cm^{-1} [160]. From the standard spectra the area under the peaks were calculated using MatLab (see CODE 2 in Appendix) and used in [Eq. 20], along with the calculated area from the measured spectra in order to find the concentration of species produced by the packed bed reactor. The peaks used to calculate the concentration can be seen in table 5.

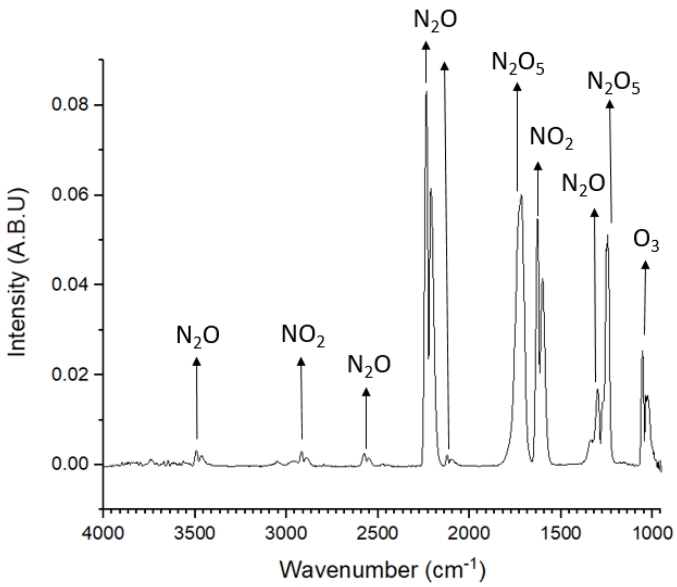

Figure 52 – Example FTIR spectra for ozone production using a packed bed plasma reactor with a peak to peak voltage of 8.6 kV and a frequency of 16 kHz with an inlet gas of 79% nitrogen and 21% oxygen of total flow rate 1 SLM and annealed TiO_2 coated $BaTiO_3$ packing material.

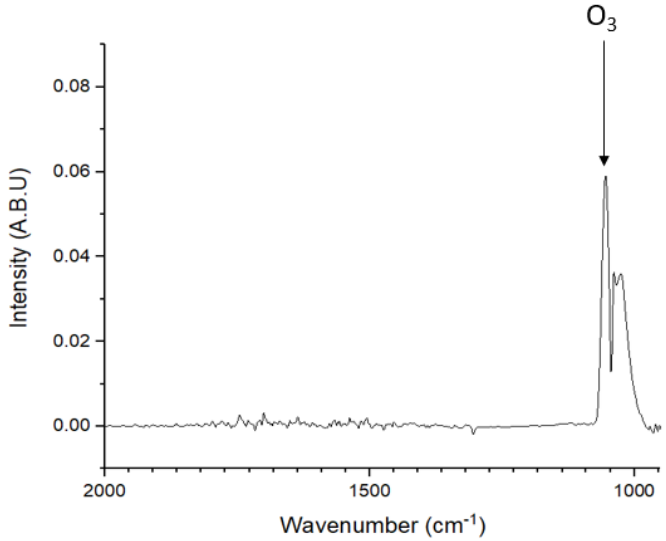

Figure 53 - Example FTIR spectra for ozone production using a packed bed plasma reactor with a peak to peak voltage of 9.6 kV and a frequency of 16kHz with an inlet gas of 100% oxygen of total flow rate 0.25 SLM and annealed TiO_2 coated $BaTiO_3$ packing material.

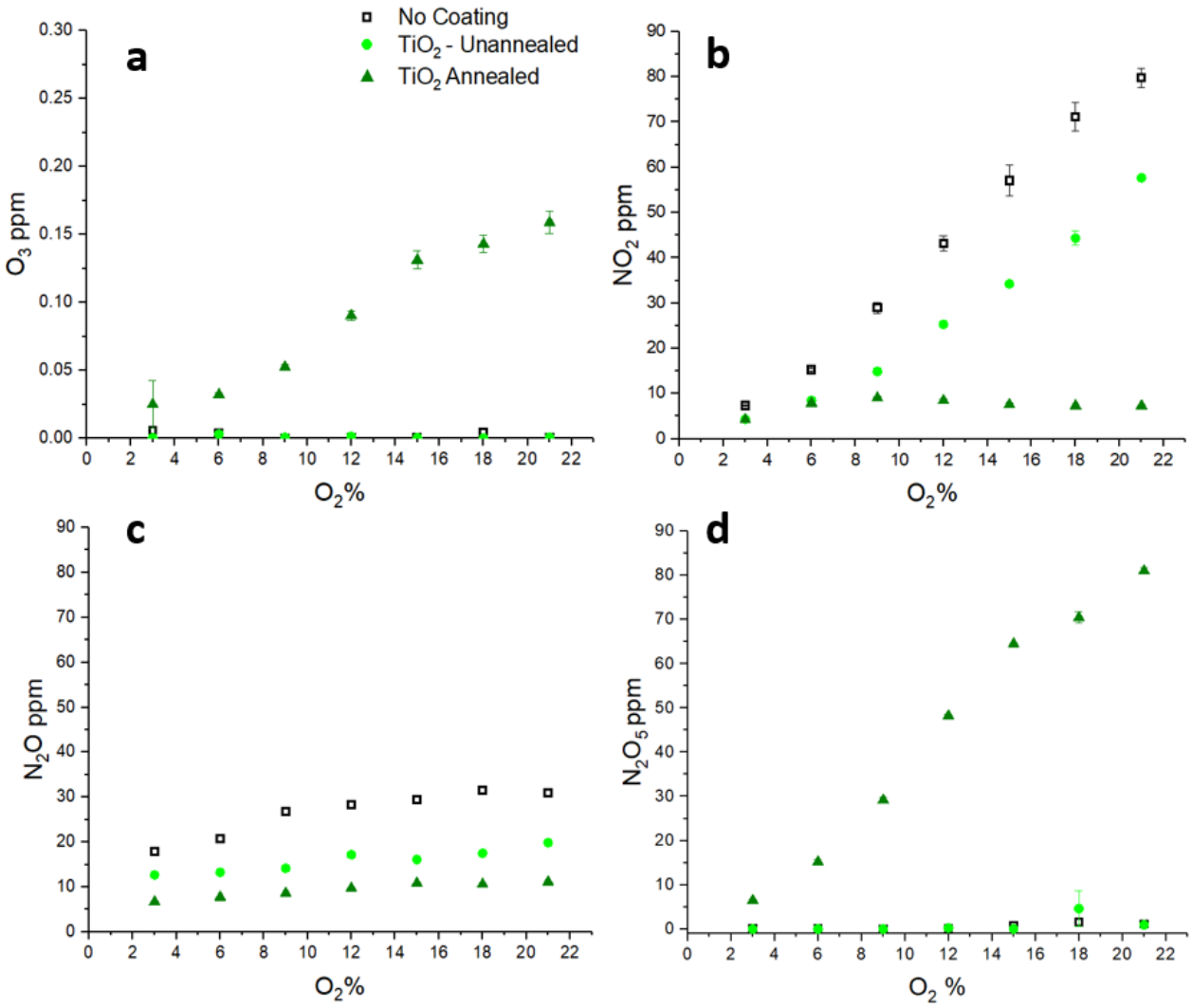

Figure 54 – Effects of oxygen concentration on a) ozone production b) N_2O production, c) NO_2 production and d) N_2O_5 production for uncoated, coated, and coated and annealed $BaTiO_3$ packing material at a residence time of 0.011 seconds, specific energy density of 0.9 kJ/L and a power of 15 watts.

Figure 54 represents the effect of photocatalyst on the formation of products and their concentrations in oxygen-nitrogen plasmas at a residence times from 0.0111 s (1 SLM). In Figure 54-a it can be seen that the annealed TiO_2 produced the highest concentration of ozone. Ozone production with the annealed TiO_2 coated $BaTiO_3$ increased with higher oxygen concentration and was the only packing material to produce ozone at a residence time of 0.0111 s. Uncoated $BaTiO_3$ and unannealed TiO_2 coated $BaTiO_3$ showed minimal generation of ozone. For the annealed TiO_2 it is thought that due to its photocatalytic activity the formation of electron hole pairs could result in increased reactions of electrons with oxygen molecules to form superoxide anions such as O_2^-,O^-, O_3^- or O_2^{--} which cause further reactions within the plasma and produce increased ozone production [196]. Increasing the residence time by decreasing the flow rate lead to a decrease in ozone generation for the non-coated $BaTiO_3$ and the unannealed $BaTiO_3$. The dielectric constant for $BaTiO_3$ can be up to 12,000 [197] in

comparison to TiO_2 which has a dielectric constant up to 100 [198]. This leads to the formation of a strong electric field at the contact points between the particulates, which is thought to cause the decomposition of any ozone that is generated in the plasma. Various studies, as summarized by Chen et al, confirm that particulates with too high dielectric constants can cause the decomposition of ozone, it is theorized that hot spots at the contact points between the particulates cause this decomposition [53]. Yuan et al reported that the higher the SED the increased power density, causing the temperature to increase and resulting in oxygen atoms being increasingly consumed in non-ozone generating reactions and even causing increased ozone destruction due to increased temperature [199]. This is consistent with the non-coated $BaTiO_3$ producing little to no ozone. In the case of the unannealed TiO_2 coated $BaTiO_3$, both the lack of O_2^- production, and the oxygen vacancies present at the surface of the particulates due to an absence of annealing, which act as a sink for the atomic oxygen, reduces the rate of production of ozone in comparison to using photocatalytically active annealed TiO_2-coated $BaTiO_3$. Moreover, the surface of the TiO_2 acts as a sink for atomic nitrogen, as oxygen vacancies have a significant impact on N_2 adsorption, as proved in the case of WO_3 by Sun et al and TiO_2 by Li et al [200, 201] leading to a reduced production of N_2O.

Figure 54-b shows the production of NO_2 with varying oxygen-nitrogen ratio with the different packing material at a residence time of 0.0111 s. Firstly, more NO_2 is produced with increasing oxygen content, this is a result of increased production of active oxygen molecules and atoms in the plasma region leading to increase formation of NO_2 as illustrated in the reaction pathway, in figure 58. Results showed an increase in the formation of NO_2 with the increased residence time when uncoated and unannealed TiO_2-coated beads were used. It is thought that more chemical reactions were taking place when the residence time is increased, leading to further formation of NO_2. The formation of NO_2 relies on reactions with atomic oxygen In the case of unannealed TiO_2, the concentration of NO_2 was less than that with uncoated $BaTiO_3$. This is due to the decreased availability of atomic oxygen due to its oxygen vacancies that could react with NO to form NO_2. The oxygen vacancy effectively leaves a Ti^{3+} ion, which can be thought of as a Ti^{4+} ion with a localised electron which can act as a adsorption site for which can result in an increase in chemical reactivity [202]. Less NO_2 was generated in the presence of photocatalytically active annealed TiO_2. This thought to be due to consuming any produced NO_2 in a followed-up reaction with ozone to produce N_2O_5. In these experiments no NO was observed, it is thought that all the NO produced was used up in the reactions to form NO_2 which can also lead to the formation of other N_xO_x products. Previous research showed little NO production compared to NO_2 in nitrogen and water vapour plasma using a double dielectric DBD [203].

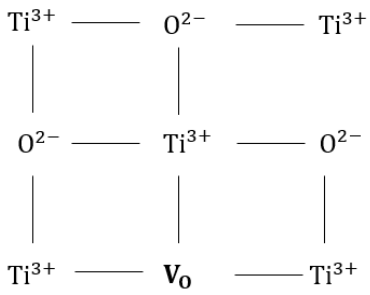

Figure 55 – Representation of an oxygen vacancy in a TiO_2 lattice.

Figure 54-c shows the production of N_2O with the various packing materials and with a residence time of 0.0111 s. Uncoated $BaTiO_3$ produced the highest concentration of N_2O followed by the unannealed TiO_2 coated $BaTiO_3$, annealed TiO_2 coated $BaTiO_3$ produced minimal amounts of N_2O. N_2O is mainly produced via two direct reactions between nitrogen molecules and active oxygen species; and reactions between NO_2 and nitrogen atoms. In these experiments an absence of NO was detected, instead significant presence of N_2O was measured. This could be a result of reactor design and its relatively low gas temperature as DBD's with a low gas temperature produce relatively high N_2O concentrations [193].

Figure 54-d shows the production of N_2O_5 with the previously aforementioned conditions. N_2O_5 is mainly formed via a two-stage reaction scheme with NO_2 reacting with ozone and oxygen atoms to form NO_3, followed by further reactions between NO_3 and NO_2 to form N_2O_5 [204]. Limited formation of N_2O_5 was detected with uncoated $BaTiO_3$ beads as only small concentrations of ozone are generated in this case, and so not enough ozone is formed to complete the reaction to N_2O_5. N_2O_5 was formed in greater concentrations when coated TiO_2 beads were used and it's concentration increased with increasing oxygen concentration, this is a direct result of increased production of active oxygen molecules and atoms in the plasma region leading to increased formation of O_3 which in turn increases the formation of N_2O_5 as explained the reaction scheme pathway in figure 58, which was created from possible reaction pathways from literature [53, 111, 164, 205-209]. Other research also found that in an SBD NO_3, N_2O_5 and O_3 increased together and on the contrary NO and NO_2 increased together [210].

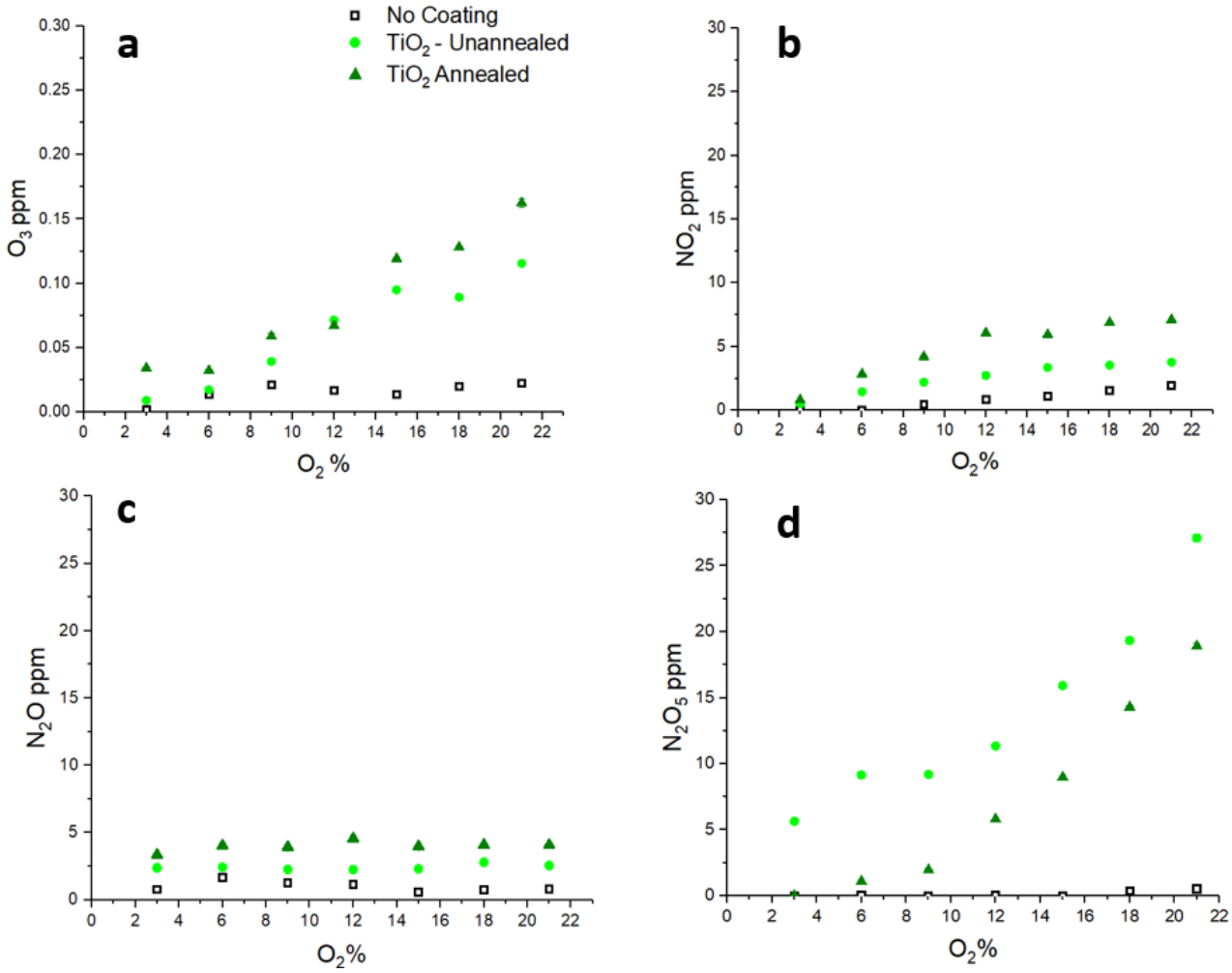

Figure 56 – Effects of oxygen concentration on a) ozone production b) N_2O production, c) NO_2 production and d) N_2O_5 production for uncoated, coated, and coated and annealed $BaTiO_3$ packing material at a residence time of 0.003 seconds, specific energy density of 0.3 kJ/L and a power of 15 watts

Figure 56 shows the effect of increased oxygen content in an oxygen-nitrogen mix with a residence time of 0.0037 s (3SLM). Figure 56-a shows the ozone production at this decreased residence time. It can be seen that no change was observed for the uncoated $BaTiO_3$ in comparison to a residence time of 0.0111 s, it remains the fact that minimal ozone is produced. For the annealed TiO_2 coated $BaTiO_3$ equal amounts of ozone were produced in comparison to the increased residence time of 0.0111 s, the same positive relationship of increased oxygen concentration leading to increased ozone production is apparent. Decreasing the residence time in the case of the unannealed TiO_2 coated leads to less atomic oxygen at the vacancy sites, Alhamid et al studied the effect of flow rate on absorption of catalysts and found that the lower flow rate lead to higher adsorption [211]. Coupled with the lower dielectric constant of the TiO_2 coated $BaTiO_3$, leads to lower decomposition of O_3 once produced, hence an increased concentration of ozone was observed for a lower residence time of 0.003 s.

Figure 56-b, which shows the production of NO_2 shows the annealed TiO_2 coated $BaTiO_3$ produced the most, followed by the unannealed TiO_2 coated $BaTiO_3$ and then the uncoated $BaTiO_3$. The decreased amount of NO_2 for the decreased residence time is accounted for by produced O atoms being exhausted faster to the gas exit, and limiting the amount of reactions taking place [212]. The increased O_3 produced by the TiO_2 coated $BaTiO_3$, regardless of their heat treatment, due to the lower dielectric constant, leads to increased NO_2 production through reactions such as [Eq. 25].

$$O_3 + NO \rightarrow NO_2 + O_2 \quad \text{[Eq. 25]}$$

Figure 56-c, which shows the production of N_2O shows a similar relationship with the NO_2. Such that uncoated $BaTiO_3$ produced the least, whereas TiO_2 coated $BaTiO_3$, regardless of their heat treatment, produced larger amounts. However, it can be stated much less concentrations are present at the lower residence time of 0.003 s compared to 0.011 s. Again, this is due to excited species being exhausted to the exit much sooner. The reason for the increased N_2O levels for the TiO_2 coated $BaTiO_3$ are the less decomposition of ozone due to the reduced electric field and in the case of the annealed TiO_2 coated $BaTiO_3$, increased O radicals due to the photocatalytic effect. N_2O can be produced through by reactions seen in [Eq. 26-30].

$$O_3 + NO \rightarrow NO_2 + O_2 \quad \text{[Eq. 26]}$$

$$O_3 + NO_2 \rightarrow NO_3 + O_2 \quad \text{[Eq. 27]}$$

$$N + NO_2 \rightarrow N_2O + O \quad \text{[Eq. 28]}$$

$$NO_2 + NO_3 \rightarrow NO_2 + NO + O_2 \quad \text{[Eq. 29]}$$

$$NO_3 + NO_3 \rightarrow NO_2 + NO_2 + O_2 \quad \text{[Eq. 30]}$$

Figure 56-d shows the production of N_2O_5 at a residence time of 0.0037s. Similarly, to the higher residence time of 0.0111 s, the uncoated $BaTiO_3$ produced no N_2O_5. On the contrary to the higher residence time, the unannealed TiO_2 coated $BaTiO_3$ produced the most N_2O_5. This follows with the increased O_3 produced. The annealed TiO_2 coated $BaTiO_3$ showed similar levels of N_2O_5 to the unannealed packing material. Again, it can be seen that much lower concentrations are present with the reduced residence time.

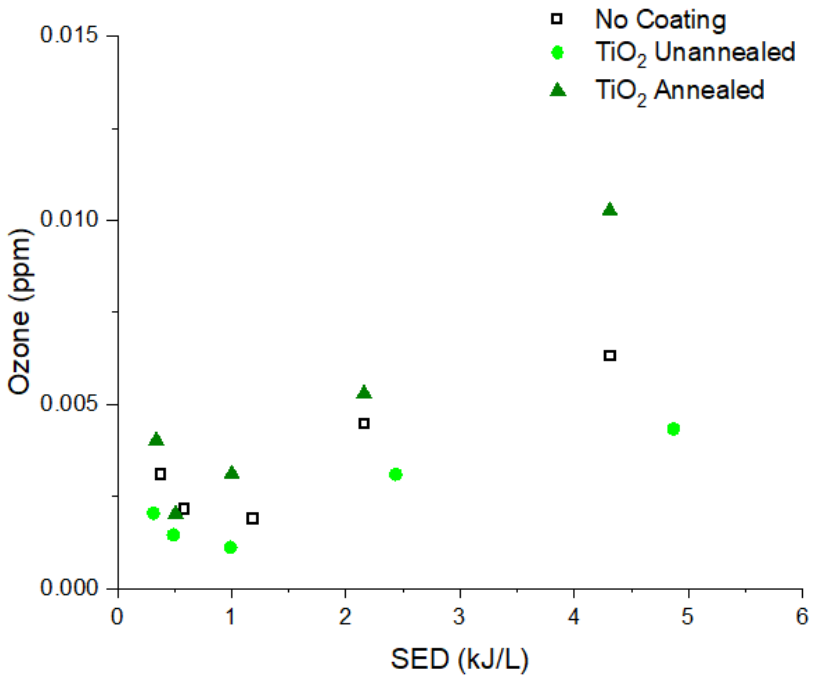

Figure 57 – Ozone production with 100% O_2 against the specific energy density for non-coated particulates, unannealed TiO_2 coated particulates and annealed TiO_2 particulates.

The effect of photocatalytic material on the generation of ozone in pure oxygen plasma is shown in Figure 57. Results using the unannealed TiO_2 coated $BaTiO_3$ show the lowest generation of ozone across the range of investigated SED, whilst the annealed TiO_2 coated $BaTiO_3$ showed the highest generation of ozone across the range of investigated SED. The unannealed TiO_2 coated $BaTiO_3$ is thought to produce the least ozone due to oxygen vacancies present. The non-coated $BaTiO_3$, even with its higher dielectric constant, produces increased ozone in comparison to when the oxygen-nitrogen gas mixture is used. The increased electric field, leading to increased dissociation and excitation of oxygen is beneficial without nitrogen as no unwanted reactions leading to the decomposition of ozone can occur. Ozone is mainly produced in non-thermal plasmas by a two stage reaction scheme with the collision of O_2 and electrons followed by the three body reaction as seen in [Eq. 32] [212]. The increased generation of ozone in the presence of photocatalytically active annealed TiO_2 could be due to the generation of O_2^- [196] which in turn increases the formation of ozone via [Eq. 31-33].

$$O_2 + e^- \rightarrow 2O + e^- \qquad \text{[Eq. 31]}$$

$$O + O_2 + O_2 \rightarrow O_3 + O_2 \qquad \text{[Eq. 32]}$$

$$O_2^- + O \rightarrow O_3 + e^- \qquad \text{[Eq. 33]}$$

A lower concentration of ozone is produced in pure O_2 than in an oxygen-nitrogen gas mixture. This could mean that reaction pathways where nitrogen is involved result in ozone production. Osawa et al demonstrated that excited N_2 can produce O atoms and increase ozone production [213].

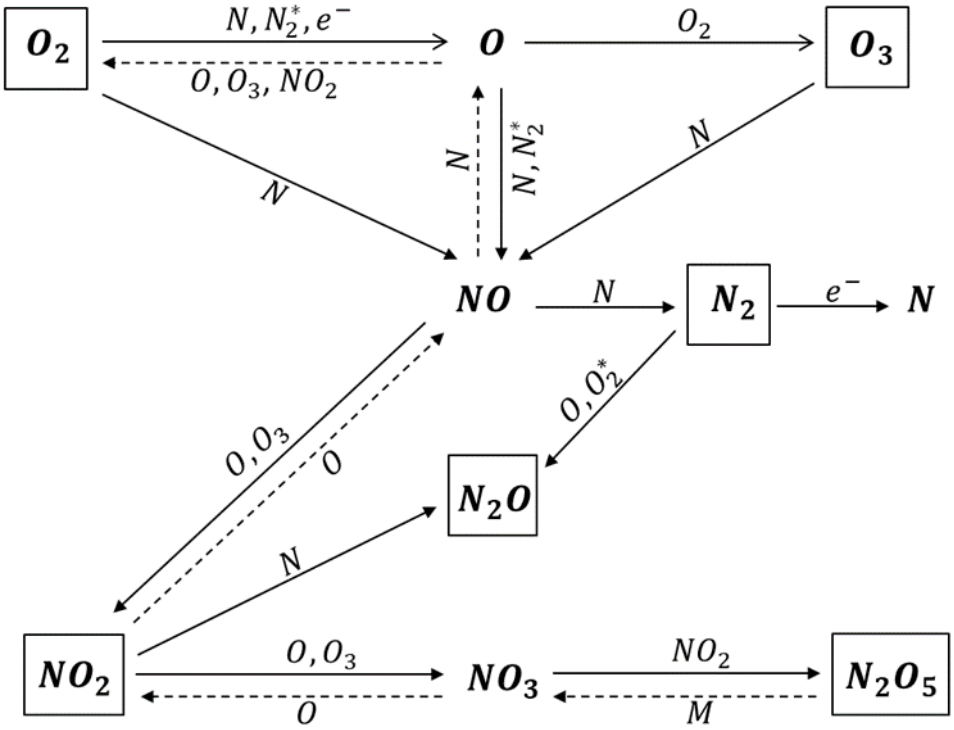

Figure 58 – Reaction pathways for the production of nitrogen and oxygen species using a packed bed dielectric barrier discharge.

4.4.2 Electrical analysis

The instantaneous voltage and current measurements supplied to the PBR were taken to investigate the effect of flow rate on the discharge characteristics and to calculate the power supplied to the PBR. The measurement interval of the voltage and current is 2E-8 s The electrical characteristics taken at 1SLM as seen in figure 59 show larger current pulses in comparison to figure 60 at 3SLM. The same can also be seen in figure 61 at 0.25SLM and figure 62 at 3SLM for pure oxygen. Höft et al studied the effect of gas flow on the breakdown voltage in flowing O_2 and N_2, it was observed that the breakdown voltage increased with a higher gas flow [214]. Therefore, with an increased gas flow rate the number of microdischarges decreases, as seen in figures 59-62, due to an increase in breakdown voltage. This can have a significant effect on the number of reactive species being produced and in turn the concentration of products produced.

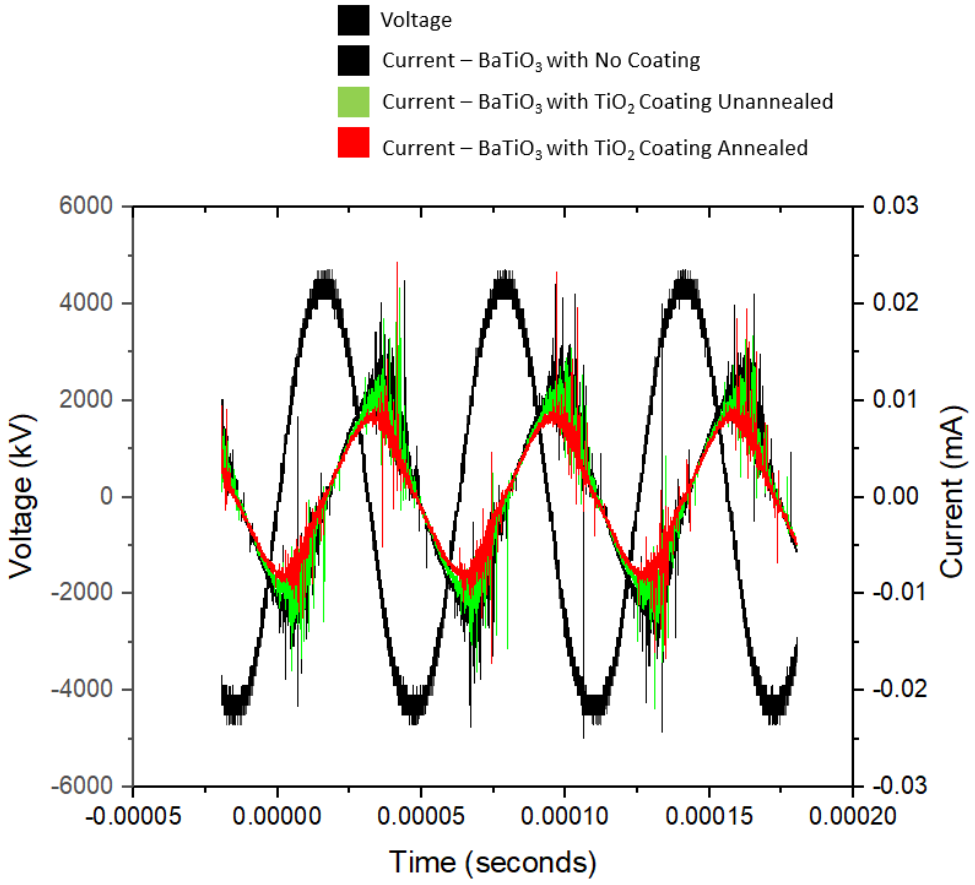

Figure 59 - Electrical characteristics of non-coated $BaTiO_3$, TiO_2 unannealed, TiO_2 annealed at 21% oxygen:79% nitrogen and a residence time of 0.0111 s

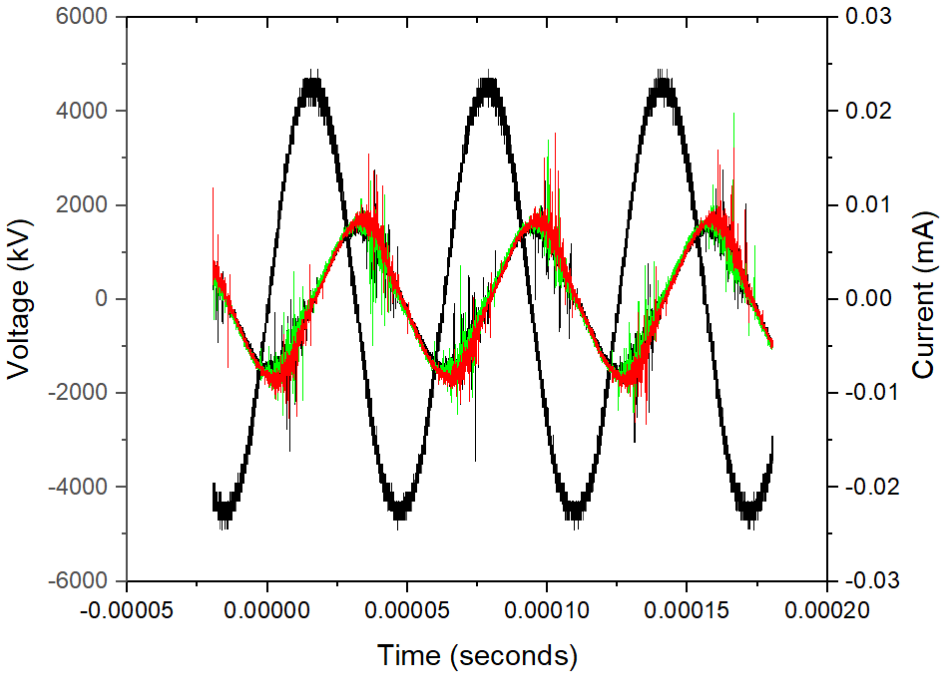

Figure 60 - Electrical characteristics of non-coated $BaTiO_3$, TiO_2 unannealed, TiO_2 annealed at 21% oxygen:79% nitrogen and a residence time of 0.0037 s

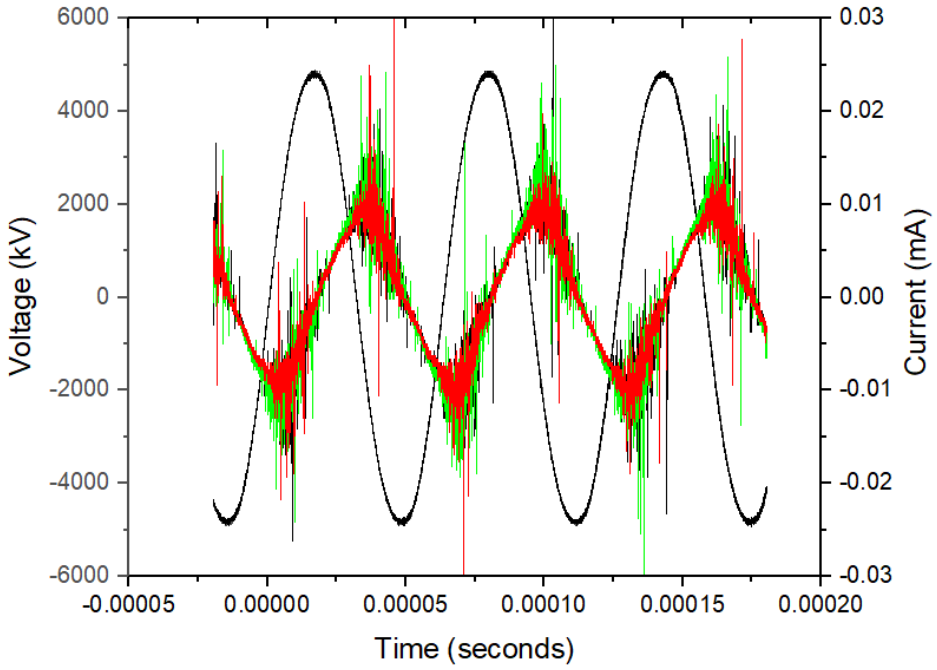

Figure 61 – Electrical characteristics of non-coated $BaTiO_3$, TiO_2 unannealed, TiO_2 annealed with 100% O_2 and a residence time of 0.0444 s.

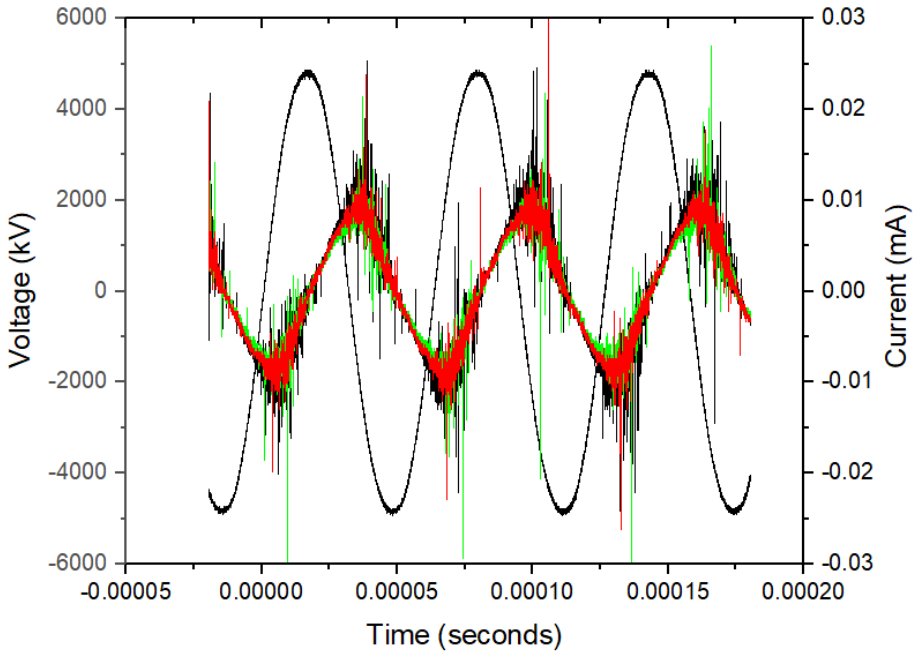

Figure 62 – Electrical characteristics of non-coated $BaTiO_3$, TiO_2 unannealed, TiO_2 annealed with 100% O_2 and a residence time of 0.0037 s.

4.5 Conclusion

Thin films of TiO_2 were deposited onto $BaTiO_3$ particulates via magnetron sputtering using type II unbalanced planar magnetrons, with a deposition time of 3 hours. Raman spectroscopy showed that annealing TiO_2 coated $BaTiO_3$ beads to 500°C produced an anatase phase. TiO_2 coated $BaTiO_3$ particulates, both unannealed and annealed were placed in a PBR DBD to see their effect on ozone generation in an oxygen-nitrogen mix, these particulates were compared with uncoated $BaTiO_3$ Two flow rates (1SLM and 3SLM) of the oxygen-nitrogen mix were used which corresponded to residence times of 0.0111 s and 0.0037 s respectively. The oxygen-nitrogen gas mixtures were varied from 3%:97% to 30%:70%. It was measured that coated $BaTiO_3$ enhanced ozone production by up to 80 times for a residence time of 0.0111 s and up to 10 times for 0.0037 s. Furthermore, the addition of TiO_2 coatings caused a reduction in NO_2 and N_2O as the TiO_2 acts as a recombination site for atomic nitrogen. It was also observed that the TiO_2 coated $BaTiO_3$ increased N_2O_5 production as the increase in O_3 also leads to a decrease in the produced N_2O and NO_2. It was determined that lower flow rates increased the quantity of products produced due to a longer residence time. The ozone production increased when annealed TiO_2 coatings were used due to O_2^- production and a reduction of the electric field at the contact points in the packed bed dielectric barrier discharge reactor. The uncoated $BaTiO_3$ has a higher dielectric constant hence, produces localised hot spots at the contact points causing the decomposition of ozone. The unannealed TiO_2 coated $BaTiO_3$ had vacant oxygen sites, which acted as a sink for atomic oxygen and nitrogen. Therefore, including TiO_2 photocatalysts had a positive effect by increasing ozone production and reducing nitrogen oxides. It also was observed that the annealed TiO_2 had a photocatalytic effect due to its enhanced performance compared to unannealed TiO_2.

CHAPTER 5 – A NON-THERMAL PLASMA REACTOR COMBINED WITH PHOTOCATALYSTS FOR THE DRY REFORMING OF METHANE.

This chapter focuses on the combination of photocatalysts and non-thermal plasma for the dry reforming of methane. Photocatalysts TiO_2 and Tungsten doped TiO_2 coatings (TiO_2-W) coatings were deposited onto dielectric particulates for use within a non-thermal packed bed dielectric barrier discharge reactor to investigate their effects on the dry reforming of methane (DRM). Photocatalytic coatings were deposited by a novel single stage magnetron sputtering process using two planar unbalanced type II magnetrons with a deposition time of 3 hours. TiO_2 coated particulates were annealed to 500°C for an hour in air in a muffle furnace to obtain the most photocatalytically active phase. Subsequent comparison to TiO_2 coated particulates which were not annealed was performed in order to investigate whether annealing the samples had an effect on the plasma chemistry. (TiO_2-W) were prepared and annealed, also to investigate their effect on plasma chemistry. Photocatalytic testing was carried out through the degradation of methylene blue under ultraviolet (UV) which can be seen in detail in Chapter 3. Coated and uncoated $BaTiO_3$ particulates were placed inside a packed bed dielectric barrier discharge reactor to investigate their effect on the DRM. A methane / carbon dioxide /argon mixture was used with a total flow rate of 2 SLM. The CH_4:CO_2 ratios of 1:1.5, 1:3 and 1:6, were investigated to give an understanding of the reaction mechanisms present and to investigate the effect of these by introducing the coated particulates. Finally, experiments were concluded with the gas flow consisting of either methane and argon, or carbon dioxide and argon to further indicate potential reaction mechanisms and the effect of the photocatalyst coatings. It was determined that the best performing CH_4:CO_2 ratio was 1:6 due to increased atomic oxygen, from the degradation of CO_2, which reacts with methane. The best performing catalysts for the DRM were the annealed TiO_2 coated $BaTiO_3$, this was the case for all flow regimes, whereas the worst performing catalysts was the annealed TiO_2-W catalysts.

5.1 Dry Reforming of Methane

As previously mentioned, methane and carbon dioxide are harmful pollutants and a cause of global warming and climate change. The advantage of the DRM process is the use of carbon dioxide, however disadvantages such as the coking of the catalyst and the high energy input means further work is needed to make the process more attractive [215]. Present routes of DRM through catalysis or plasma processes can be seen in figure 63. DRM through the non-thermal plasma routes has many advantages such as low energy input, low temperature, and ease of installation. However, in order to make it more attractive the energy efficiency and yield should be increased. In this investigation photocatalytic TiO_2 and TiO_2-W coatings were deposited onto the packing material $BaTiO_3$ for subsequent use in a PBR for the dry reforming of methane. The dry reforming process was carried out in an argon / carbon dioxide / methane mix to study the effects of the photocatalyst and plasma interaction. Numerous studies have investigated the optimum conditions and utilised catalysts in combination with non-thermal plasma in order to make the process more efficient [27, 52, 96, 97, 99, 104-106, 112, 216-224]. Zeng et al used Al_2O_3 supported metal catalysts in combination with non-thermal plasma for the dry reforming of methane and found an enhancement of the degradation of methane however, they found that the carbon dioxide degradation was not enhanced [99]. Chung et al included $LaFeO_3$ photocatalysts in powder form in a spark discharge reactor to increase syngas production from methane and carbon dioxide [13]. However, little has been done in adding the catalysts, especially photocatalysts, through a physical vapour deposited coating onto high dielectric constant packing material. It is hoped that this technique could enhance conversions due to the activation of the photocatalyst by non-thermal plasma whilst not having a negative impact on the characteristics of the packed bed reactor. Figure 63 shows various technologies for the DRM. The advantage of plasma catalytic DRM is the low temperatures, ease of operation and low energy input.

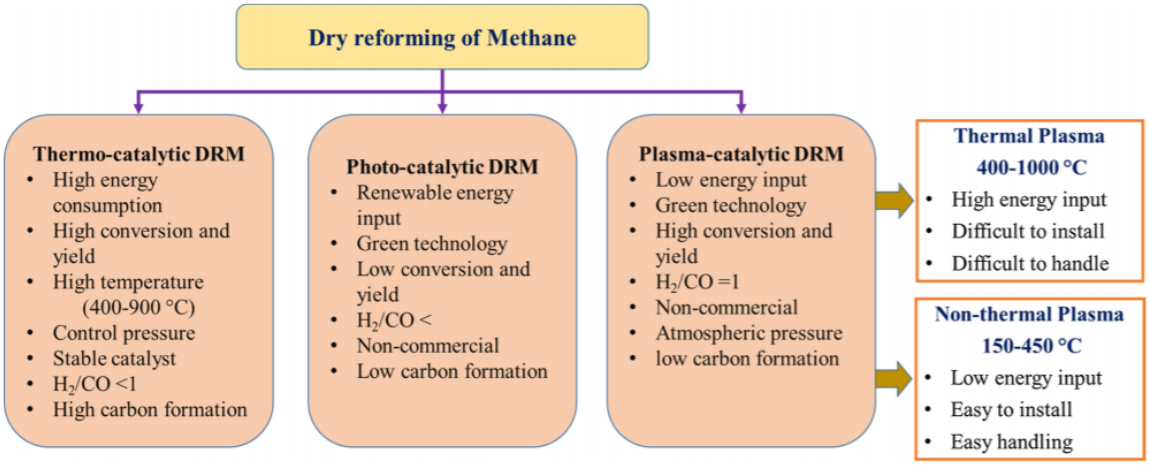

Figure 63 – Technology routes for the dry reforming of methane, taken from Khoja et al [225]

5.2 Thin Film Deposition of Titanium Dioxide and Tungsten doped Titanium Dioxide Photocatalysts onto Barium Titanate Used In Packed Bed Reactor

Thin films of TiO_2 and TiO_2-W have been coated using two planar unbalanced type II magnetrons onto $BaTiO_3$ particulates. All coatings were deposited in a two-target magnetron sputtering rig which was pumped down to a base pressure of 1×10^{-3} Pa. A 300 mm x 100 mm type II unbalanced planar magnetron was used along with a target of titanium of 99.5% purity. The reactive sputtering process was carried out in an argon/oxygen atmosphere. A dual channel Advanced Energy Pinnacle Plus power supply operated in pulsed DC mode was used to power the magnetrons. Table 16 and table 17 show the deposition parameters of the prepared TiO_2 coated $BaTiO_3$ and TiO_2-W coated $BaTiO_3$, respectively. Heat treatment was performed in an air-filled muffle furnace, model Carbolite 3000. TiO_2 thin films were heated to 500°C for an hour to obtain an anatase phase and left to cool to room temperature. TiO_2-W thin films were heated to 600°C for 30mins to obtain an anatase phase and left to cool to room temperature.

Table 16 – Deposition parameters for magnetron sputtering coating of TiO_2 photocatalysts onto $BaTiO_3$ particulates.

Deposition Time (hr)	**Power**	**Frequency (kHz)**	**Time Pulse (µs)**	**Oscillating Power (%)**	**Pre Coating Treatment**	**Post Coating Treatment**
3	1000W	150kHz	3.3	70	1100°C for 4 hours	-
3	1000W	150kHz	3.3	70	1100°C for 4 hours	500°C for 1 hour

Table 17 - Deposition parameters for magnetron sputtering coating of TiO_2-W photocatalysts onto $BaTiO_3$ particulates.

Deposition Time (hr)	**Ti Target Power**	**Ti Target Frequency (kHz)**	**Ti Target Time Pulse (µs)**	**W Target Power**	**W Target Frequency (kHz)**	**W Target Time Pulse (µs)**	**Oscillating Power (%)**	**Pre Coating Treatment**	**Post Coating Treatment**
3	1000W	150kHz	3.3	80W	100	5.0	70	1100°C for 4 hours	600°C for 30mins hour

Characterisation and analysis of the $BaTiO_3$ particulates coated and used in the non-thermal reactor can be seen in CHAPTER 3 - Deposition of photocatalytic coatings onto particulates for use in a packed bed dielectric barrier discharge, section 3.5 and section 3.7.

5.3 Packed Bed Reactor Experimental Conditions

Initial experiments were carried out to investigate the role that photocatalytic coatings have on the degradation of methane and carbon dioxide, the chemical mechanisms involved, the effect of the photocatalytic coatings on the plasma chemistry and the effect of the plasma on the photocatalyst. Prior to the in-depth testing of the photocatalytic coated packing material, initial experiments as seen in figure A1-A3 in the appendix as determined that the optimum frequency of operation was 16 kHz. The frequency was kept constant thereon in. The constant variables for these experiments were the frequency (16 kHz), bead size (2-3 mm), mass of particulates (50 g), packing volume (24.6 cm^3) and total flow rate (2 SLM). The measured variables were the peak to peak voltage (7 - 8.25 kV), the CH_4:CO_2 ratio (1:1.5 to 1:6) and the concentration of the output gases.

Figure 64 shows a schematic of the experimental setup for the DRM. The description of the packed bed reactor used in this work is illustrated in CHAPTER 2 – Methodology.

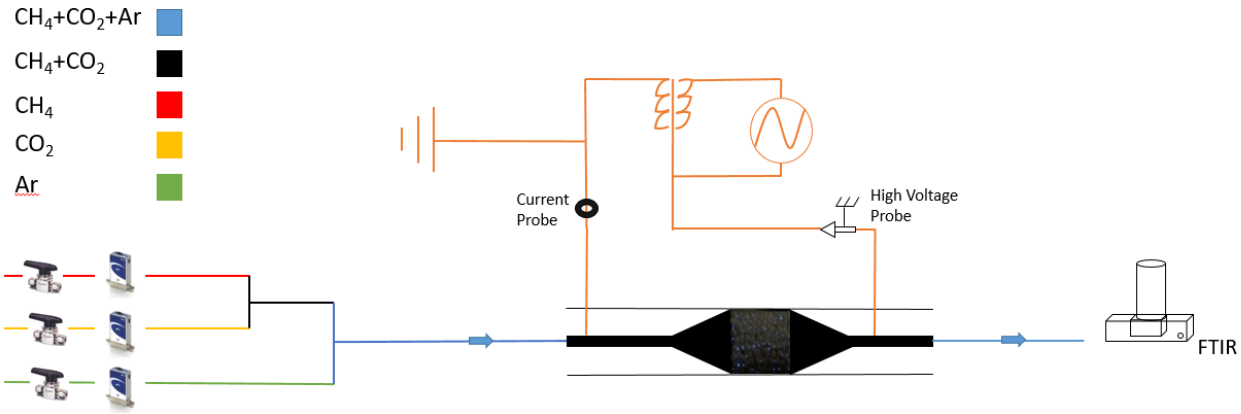

Figure 64 – Schematic of packed bed reactor experimental setup.

Carbon dioxide and methane were mixed with argon and controlled by mass flow controllers before entering the packed bed plasma reactor. Prior to any experiments argon was used to flush out any impurities within the packed bed reactor and FTIR gas cell. The carbon dioxide and methane were then introduced and the system was allowed to reach steady state, which was determined by the intensities present, measured by the FTIR. A background scan on the FTIR was taken before the power supply was switched on and plasma generated. Electrical readings were taken on 3 separate occasions at 10, 12 and 14 minutes after plasma was struck. This was also the case for FTIR readings in order to ensure reliability. Averages were taken and standard error was calculated. The following packing material was used and compared to investigate the effects of the TiO_2 and TiO_2 coatings on the plasma chemistry:

- $BaTiO_3$ with no coating

- $BaTiO_3$ with a 3 hour TiO_2 coating which was not annealed.
- $BaTiO_3$ with a 3 hour TiO_2 coating which was annealed at 500^0C for 1 hour.
- $BaTiO_3$ with a 3 hour TiO_2-W coating which was annealed at 600^0C for 30 minutes.

5.4 Effect of the Photocatalytic Coatings on the Plasma Characteristics

5.4.1 Electrical Measurements

The instantaneous voltage and current measurements were taken to investigate the effect of the coatings on the discharge characteristics such as the intensity or number of microdischarges and breakdown voltage. Figure 65-67 show the electrical characteristic of the different catalysts at CH_4:CO_2 ratio of 1:1.5, 1:3 and 1:6 respectively.

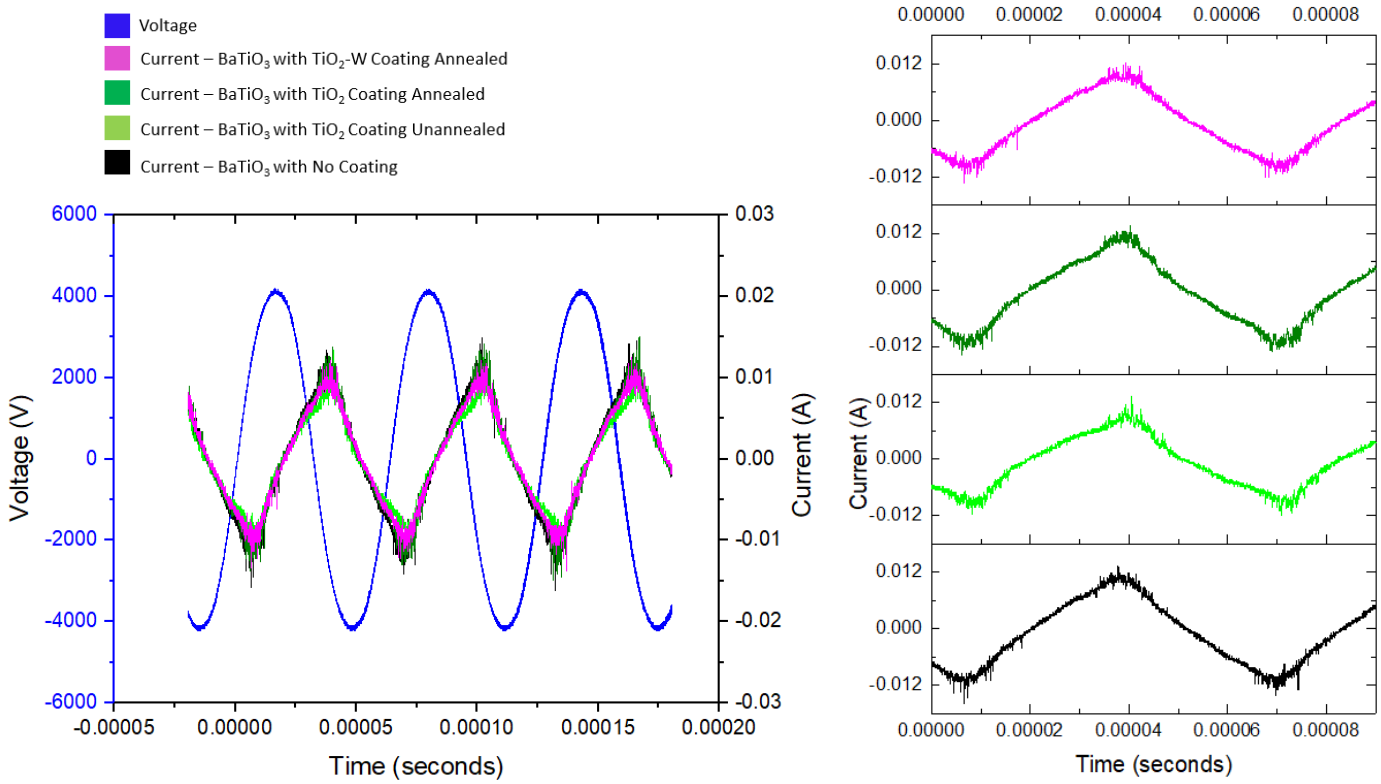

Figure 65 – Electrical characteristics of the different catalyst combinations at 8.25kV peak to peak and a CH_4:CO_2 ratio of 1:1.5.

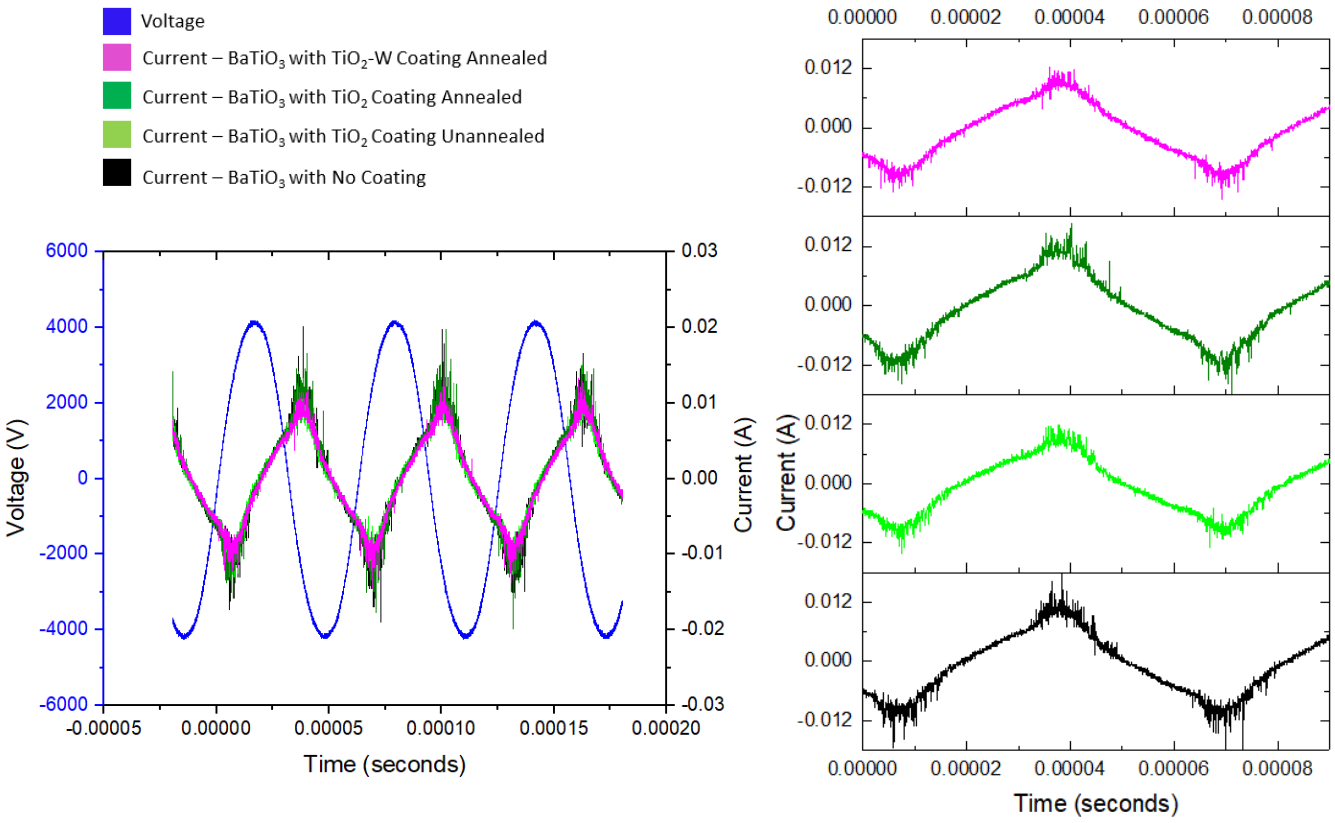

Figure 66 - Electrical characteristics of the different catalyst combinations at 8.25kV peak to peak and a CH_4:CO_2 ratio of 1:3.

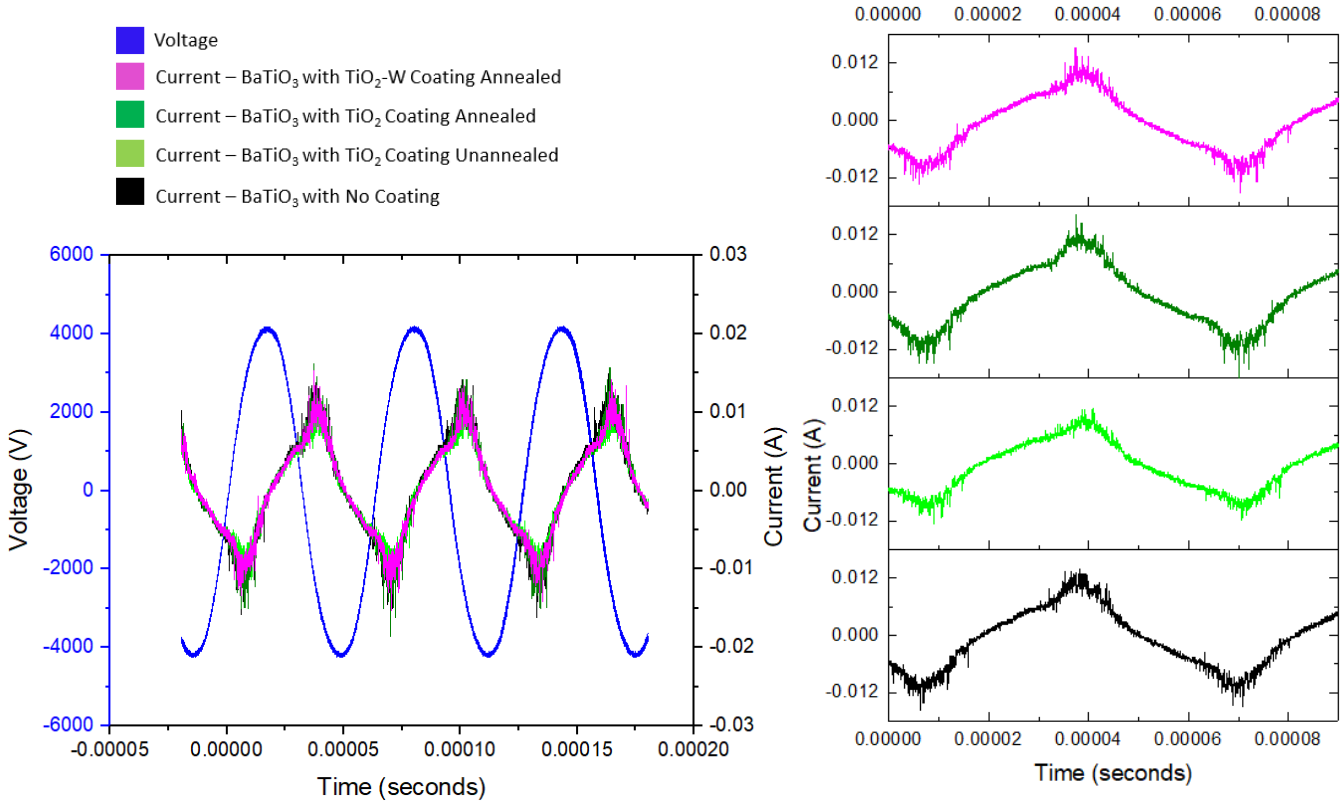

Figure 67 - Electrical characteristics of the different catalyst combinations at 8.25kV peak to peak and a CH_4:CO_2 ratio of 1:6.

Figure 65-67 shows that the maximum current of the filaments is smaller for the $BaTiO_3$ coated with the TiO_2-W catalyst. For example, the maximum current filament for annealed TiO_2 coated $BaTiO_3$ at a feed gas ratio of 1:1.5 was 0.0198 A, compared to 0.0146 A for annealed TiO_2-W coated $BaTiO_3$. The intensity of the microdischarges are lower for the unannealed TiO_2 coated $BaTiO_3$ and the annealed TiO_2-W coated $BaTiO_3$, this was also observed in the measured specific energy density which was calculated from [Eq. 34] and can be seen in section 5.5.

$$\text{SED} = \frac{\text{Power (kW)}}{\text{Flow Rate } (\frac{\text{L}}{\text{s}})} \qquad \text{[Eq. 34]}$$

This can be attributed to a lower dielectric constant of WO_3 which has a static dielectric constant of ~10-20 [11, 226], the static dielectric constant of TiO_2 and $BaTiO_3$ is greater than that of WO_3 which can be up to 100 [198] and 12,000 [197] respectively [227]. The dielectric constant of amorphous TiO_2 and crystalline TiO_2 are comparable according to Prasai et al. [228]. The lower intensity of microdischarges for the TiO_2-W coated $BaTiO_3$ could have a negative impact at specific peak to peak voltages for the dry reforming of methane. Interestingly, figure 66 shows increased intensity of microdischarges in comparison to figure 65 suggesting the gases present have a large impact on the breakdown voltage and hence discharge characteristics.

5.5 Effect of the Photocatalytic Coatings on the Dry Reforming of Methane

This section investigates the effect of photocatalyst coating on the $BaTiO_3$ packing material, the CH_4:CO_2 feed gas ratio and the peak to peak voltage on the dry reforming of methane. The feed gas ratios used were 1:1.5, 1:3 and 1:6, whereas the peak to peak voltage was increased from 7kV to 8.25kV. The measured variables were the species present before and after plasma treatment, their concentrations and the optical emission of the non-thermal plasma. From the FTIR measurements the degradation (%) of methane and carbon dioxide and the production of CO (ppm) were calculated. H_2 molecules cannot be detected using the FTIR due to the absence of a dipole moment.

These characteristics were measured and analysed in order to investigate whether a synergy existed between the use of photocatalyst coated $BaTiO_3$ and the non-thermal plasma.

5.5.1 FTIR Measurements

Figure 68 shows an example FTIR spectrum of the exhaust gas after passing through the plasma reactor. The detected species are methane at 1306 cm^{-1}, 1533 cm^{-1} and 3018 cm^{-1} [157], Carbon dioxide at 667 cm^{-1}, 1340 cm^{-1} and 2350 cm^{-1} [157] and carbon monoxide at 2143 cm^{-1}. From the standard spectra the area under the peaks were calculated using MatLab (see CODE 1 in Appendix) and used in [Eq. 20], along with the calculated area from the measured spectra in order to find the concentration of species produced by the packed bed reactor. The peaks used to calculate the concentration can be seen in table 5. Except for CO_2, where the peaks at wavenumber 3540-3660 cm^{-1} and 3660-3760 cm^{-1} were used. As a consequence of the absorbance of the peak at 2230-2400 cm^{-1} being over an absorbance of 1, hence, would not follow the beer-lambert law, where concentration is proportional to the absorbance.

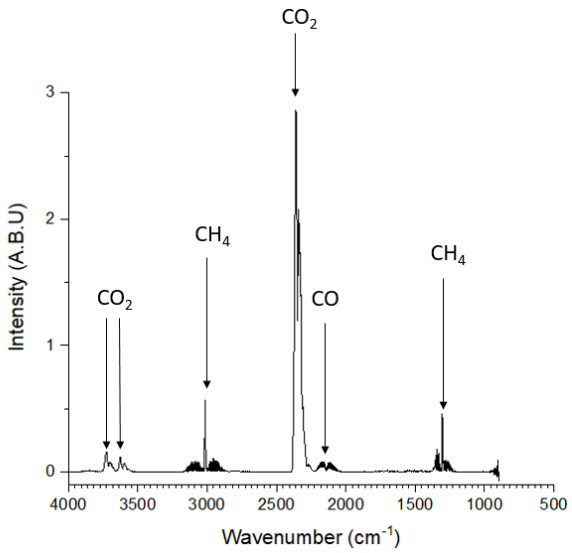

Figure 68 – Example FTIR spectrum of the DRM using TiO_2 coated $BaTiO_3$ annealed to 500°C for an hour. Operational parameters are CH_4:CO_2 1:3, 8.25 kV and 16 kHz.

5.5.2 FTIR Measurements Error

It must be noted that there will exist errors in the measured concentration of species. The error comes from numerous sources. Firstly, there will exist impurities, coming from either the supplied gas or remaining from previous experiments, although every effort was made to reduce this as practically as possible. Most of this will be removed from the spectra by taking a background measurement, although they would still be present. Secondly, error may be present within the concentration calculations due to the use of argon as a carrier gas instead of nitrogen, which was the carrier gas for the standard spectra [224]. Additional error from the difference in resolution of the measurements (1 cm^{-1}) compared to the resolution of the standard spectra (0.5 cm^{-1}) is likely to be a factor. In order to further understand the magnitude of the error, calculations of the concentration based on the flow rate ratio was performed. This assumes the molar concentration is the same as the volumetric concentration. Based on this, the calculated concentration of carbon dioxide and methane is 250ppm and 850 ppm respectively, based on the total flow rate of 2SLM, this gives a 12% error in the concentration of carbon dioxide. Furthermore, the standard error between the measurements was calculated and taken into consideration.

5.5.2 Gas feed ratio of CH_4:CO_2 1:1.5

The dry reforming of methane with a ratio of 1:1.5 to carbon dioxide, diluted in a carrier gas of argon was performed to investigate the effect of different catalytic coatings. Figure 69 and figure 70 shows the methane degradation, CO production and carbon dioxide degradation with a 1:1.5 ratio of CH_4:CO_2. The concentration in ppm in the diluted carrier gas of argon were 500 ppm and 750 ppm of methane and carbon dioxide respectively. Figure 69 shows the methane and carbon dioxide degradation and the carbon monoxide production with varying the applied voltage with a gas feed ratio of 1:1.5. Figure 70 also shows the methane and carbon dioxide degradation and the carbon monoxide production with the measured SED with a gas feed ratio of 1:1.5.

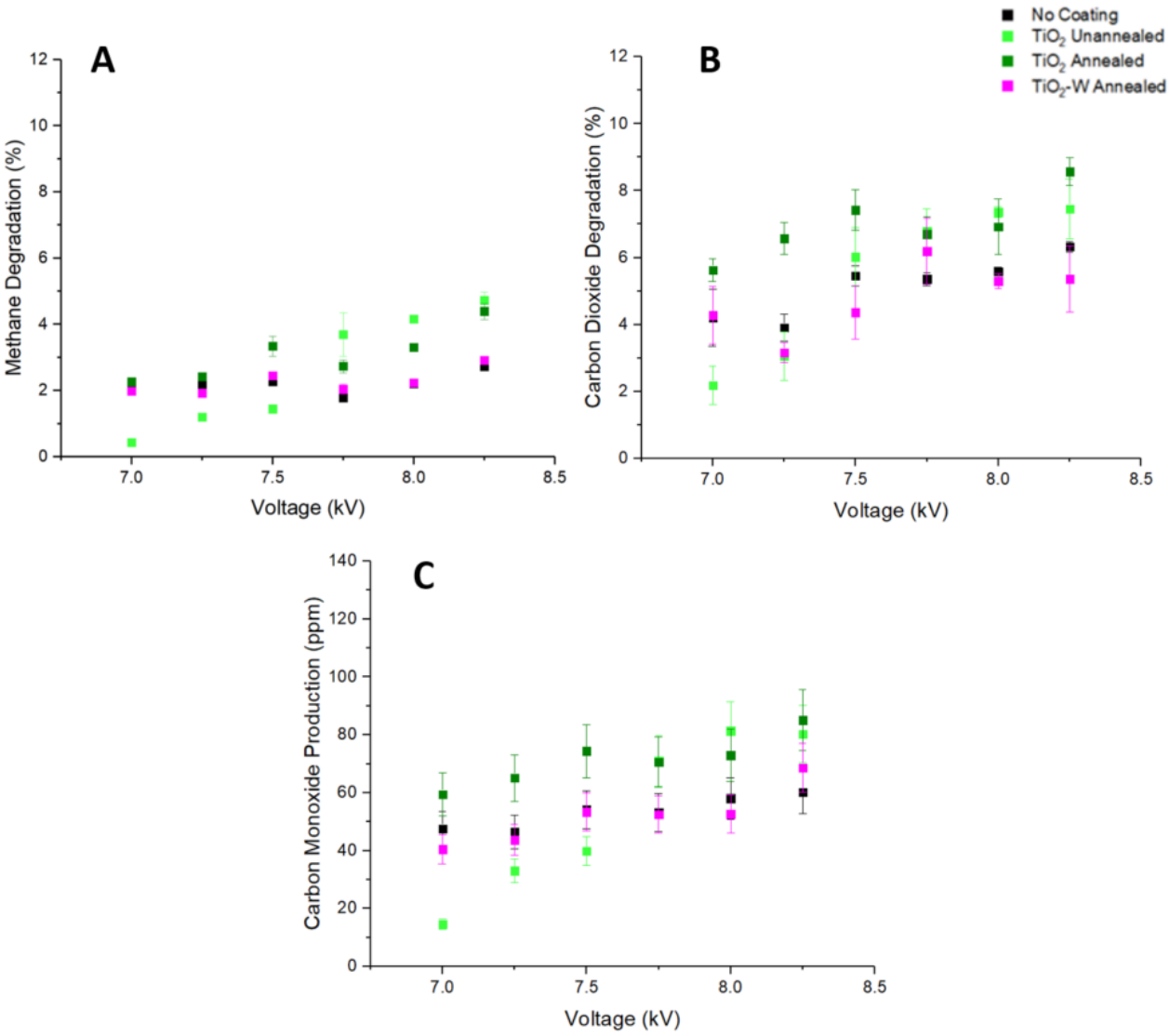

Figure 69 – (A) Methane degradation against applied voltage, (B) carbon dioxide degradation against applied voltage, and (C) carbon monoxide production in ppm against applied voltage with a 1:1.5 CH_4:CO_2 ratio.

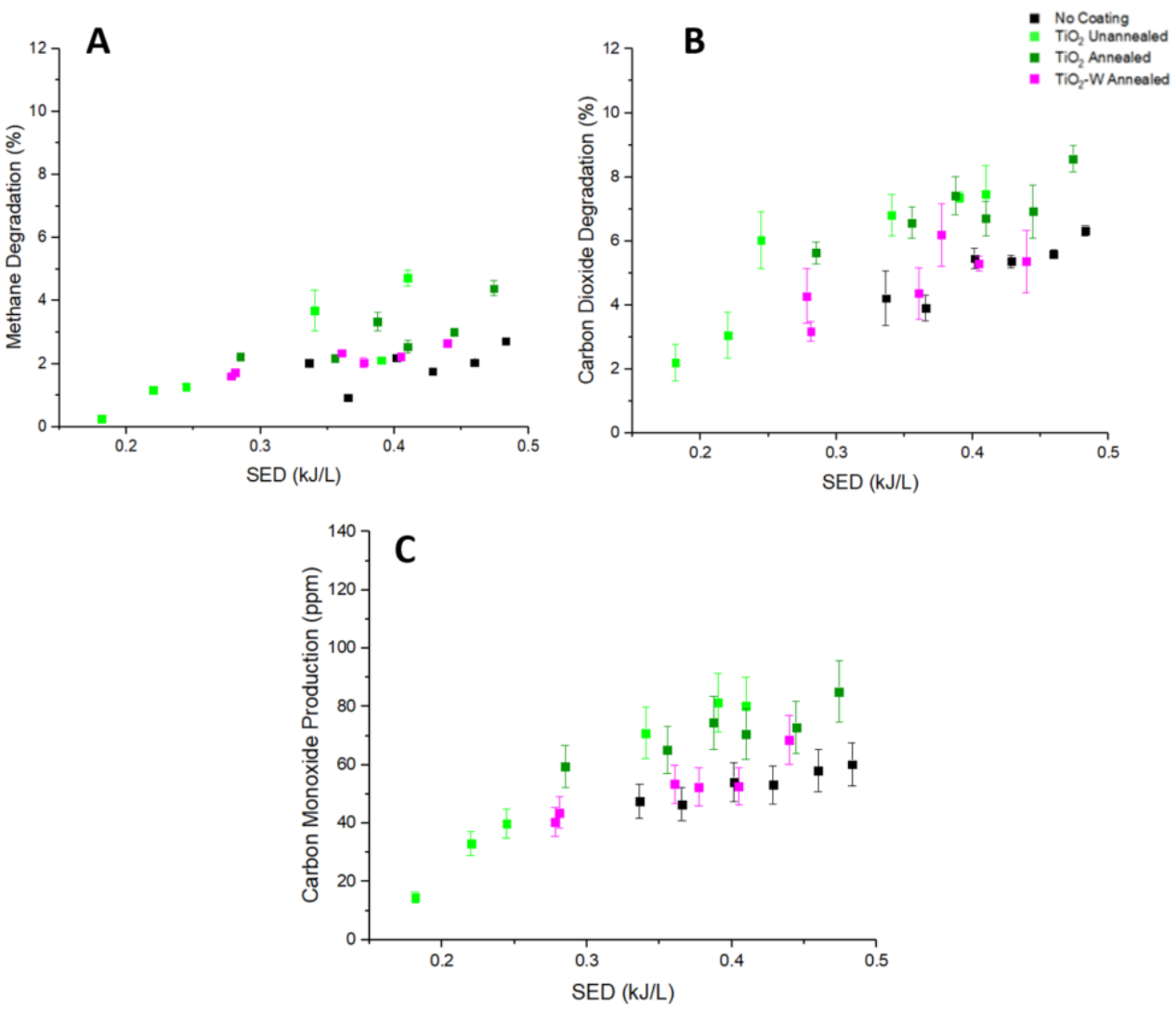

Figure 70 – (A) Methane degradation against SED, (B) carbon dioxide degradation against SED, and (C) carbon monoxide production in ppm against SED with a 1:1.5 CH_4:CO_2 ratio.

Table 18 shows the maximum methane and carbon dioxide degradation and the maximum carbon monoxide production with the various packing material.

Table 18 - Maximum CH_4 and CO_2 degradation and the maximum CO production with a 1:1.5 CH_4:CO_2 ratio

	Maximum CH_4 Degradation (%)	**Maximum CO_2 Degradation (%)**	**Maximum CO production (ppm) (+/- 12%)**
No Coating	2.72	6.32	60.18
TiO_2 Unannealed	4.72	7.46	80.24
TiO_2 Annealed	4.39	8.57	85.12
TiO_2-W Annealed	2.91	6.19	66.05

Figure 69, A and B show that by increasing the applied voltage from 7 kV to 8.25 kV, both the degradation of methane and carbon dioxide was increased. The degradation of methane increased by up to 0.69 %, 4.3 %, 2.13 % and 0.93 % for the non-coated $BaTiO_3$, TiO_2 unannealed coated $BaTiO_3$, TiO_2 annealed $BaTiO_3$ and TiO_2-W annealed $BaTiO_3$ respectively, when increasing the voltage from 7 kV to 8.25 kV. Similar effects of an increase in voltage were also observed for the degradation of carbon dioxide with degradation increasing by 2.11 %, 5.27 %, 2.94 % and 1.91 % for the non-coated $BaTiO_3$, TiO_2 unannealed coated $BaTiO_3$, TiO_2 annealed $BaTiO_3$ and TiO_2-W annealed $BaTiO_3$ respectively. Carbon monoxide production, increased by 21%, 86%, 30% and 41% respectively. It is thought that the number of the microdischarges were increased with increasing the applied voltage. Increasing the voltage does not increase the amount of charge transferred in a microdischarge but increases the amount of microdischarges [229]. An increase in the number of microdischarges increases the number of free electrons leading to a higher probability of electron – molecule collisions. Higher quantities of reactive species due to a higher applied voltage has been reported in other work [104, 230]. An increase in electron collisions could cause a higher degradation of carbon dioxide which follows an increase in CO production as seen in [Eq. 35] [28]. A higher number of electron and molecule collisions also leads to a higher degradation of methane as seen in [Eq. 35-38][99].

$$CO_2 + e \rightarrow e + CO + O \qquad \text{[Eq. 35]}$$

$$CH_4 + e \rightarrow CH_3 + H + e \qquad \text{[Eq. 36]}$$

$$CH_4 + e \rightarrow CH_2 + H_2 + e \qquad \text{[Eq. 37]}$$

$$CH_4 + e \rightarrow CH_3 + H + H_2 + e \qquad \text{[Eq. 38]}$$

Figure 69 shows that an increase in methane concentration had a negative impact on the degradation of carbon dioxide and the production of CO. In comparison to the degradation of carbon dioxide achieved by using a 1:3 ratio of CH_4 and CO_2, which can be seen in figure 71. A maximum degradation of carbon dioxide of 8.57 % was achieved by the TiO_2 annealed particulate packing material, this is 2.68 % less than using a 1:3 ratio. This can be attributed to formation of carbon dioxide via [Eq. 39]. An Increased proportion of methane leads to an increase in OH via reactions with atomic oxygen as seen in [Eq. 40]. This can be attributed to the competing reaction seen in [Eq. 39] where carbon monoxide reacts with the increased amount hydroxyl radicals, due to the excess methane, to produce carbon dioxide [231].

$$CO + OH \rightarrow CO_2 + H \cdot \qquad \text{[Eq. 39]}$$

$$CH_4 + O \rightarrow CH_3 + OH \qquad \text{[Eq. 40]}$$

Due to the reaction [Eq. 39] a decrease in CO production is also observed. For example a reduction by up to 27% for non-coated $BaTiO_3$ can be observed, in comparison to a feed gas ratio of 1:3. Furthermore, an increased concentration of methane in the gas mixture will increase the breakdown voltage of the gas mixture as methane has a higher breakdown voltage in comparison to argon [232]. Therefore, the conversion of methane and carbon dioxide is expected to decrease as the concentration of methane increases. Despite the drop in effectiveness in using a 1:1.5 ratio, in comparison to a feed gas ratio of 1:3 and 1:6, which can be seen in figure 71 and figure 73, it can be clearly seen that the best performing particulates were the unannealed and annealed TiO_2 coated $BaTiO_3$ packing material. Increased oxidation of methane at the anatase TiO_2 could reduce the amount of atomic oxygen consumed in [Eq. 40] leading to reduced formation of carbon dioxide via [Eq. 39] along with increased degradation of carbon dioxide at the conduction band. Increased oxygen vacancies at the unannealed TiO_2 also cause increased degradation of carbon dioxide as mentioned previously, competing with the formation of carbon dioxide in [Eq. 39]. Interestingly, the maximum SED of the unannealed TiO_2 coated $BaTiO_3$ was significantly lower than the annealed TiO_2 coated $BaTiO_3$ and the non-coated $BaTiO_3$, as seen in figure 70. Therefore, the role of the oxygen vacancies play an important role in promoting the degradation of carbon dioxide and methane. Along with an increase in the degradation of methane and carbon dioxide an increase in production of CO was achieved by the unannealed and annealed TiO_2 coated $BaTiO_3$ particulates. The lower dielectric constant of TiO_2-W coated $BaTiO_3$ reduced the intensity and number of microdischarges leading to reduced conversions of methane and carbon dioxide.

5.5.3 Gas feed ratio of CH_4:CO_2 1:3

In order to gain a better understanding and optimise reaction conditions the CH_4:CO_2 ratios in the feed gas were varied. Concentrations of 250 ppm and 750ppm of CH_4 and CO_2 respectively were combined with the argon gas flow using mass flow controllers to achieve a total flow rate of 2 SLM. Figure 71 and figure 72 shows the degradation of methane and carbon dioxide and production of carbon monoxide for the various coated packing material against the applied voltage and measured specific energy density respectively and table 19 shows the maximum degradations of methane and carbon dioxide and production of carbon monoxide.

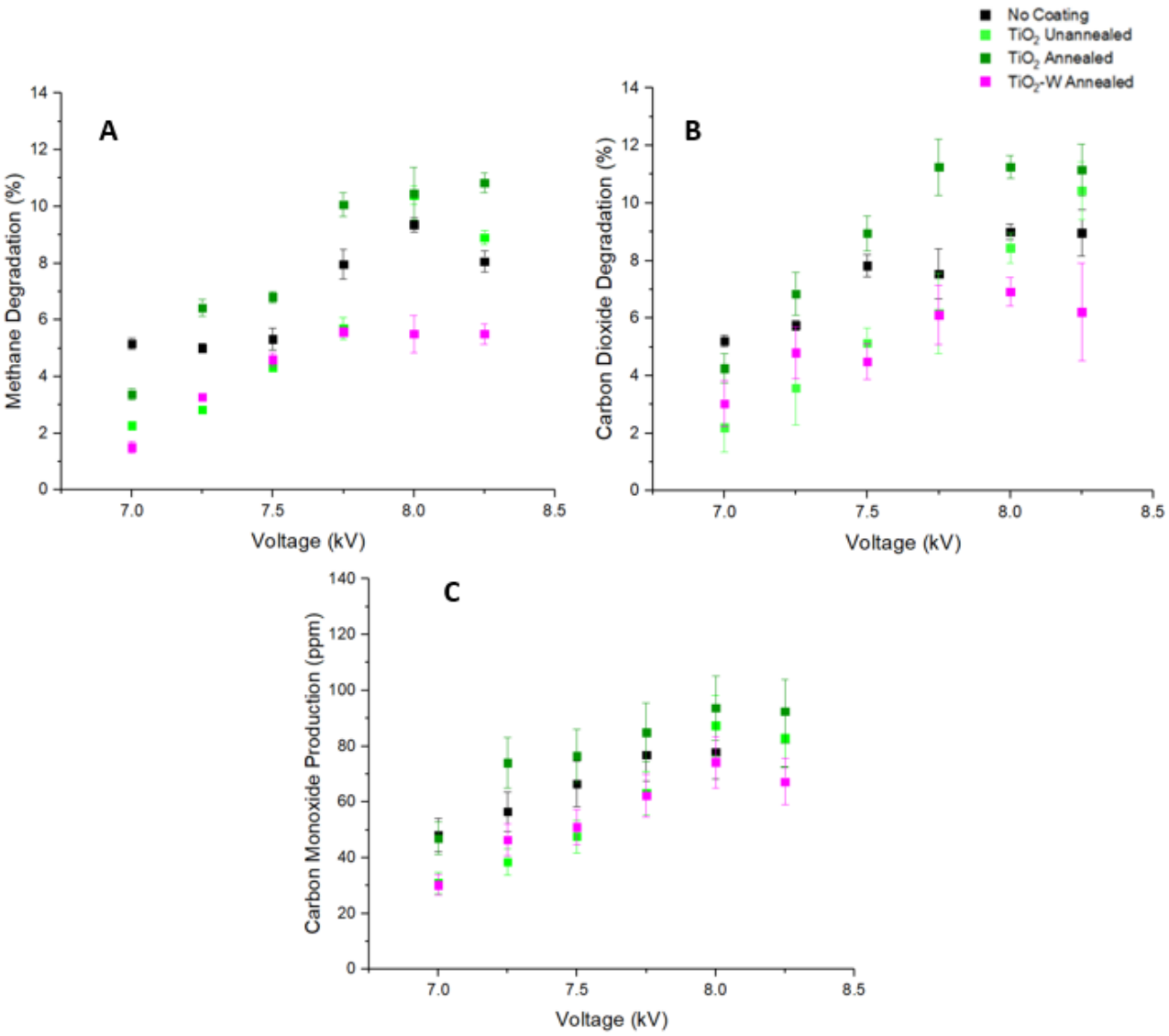

Figure 71 – (A) Methane degradation against applied voltage), (B) carbon dioxide degradation against applied voltage, and (C) carbon monoxide production in ppm against applied voltage

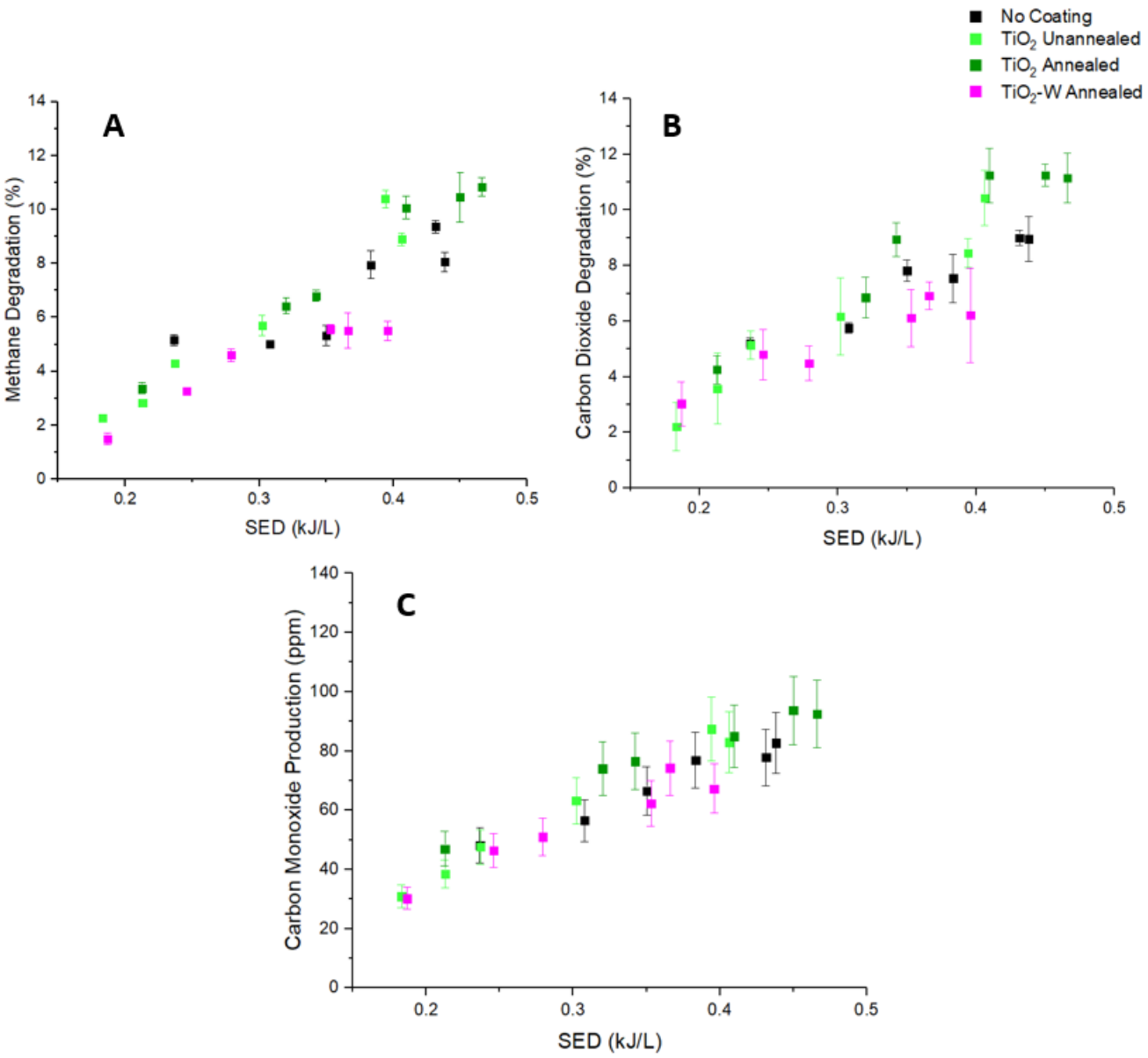

Figure 72 – (A) Methane degradation against specific energy density), (B) carbon dioxide degradation against specific energy density, and (C) carbon monoxide production in ppm against specific energy density.

Table 19 – Maximum CH_4 and CO_2 degradation and the maximum CO production with a 1:3 CH_4:CO_2 ratio.

	Maximum CH_4 Degradation (%)	**Maximum CO_2 Degradation (%)**	**Maximum CO production (ppm) (+/- 12%)**
No Coating	9.36	9	82.67
TiO_2 Unannealed	10.39	10.43	87.41
TiO_2 Annealed	10.83	11.25	93.66
TiO_2-W Annealed	5.56	6.92	74.22

Figure 71, A and B show similar trends that by increasing the applied voltage from 7 kV to 8.25 kV, both the degradation of methane and carbon dioxide was increased. The degradation of methane and carbon dioxide were increased by up to 8.12 % and 8.23% respectively, when increasing the voltage from 7 kV to 8.25 kV. Carbon monoxide production, in ppm, increased by up to 62%. Again it is thought that the number of the microdischarges were increased with increasing the applied voltage [229].

The best performing packing material was the annealed TiO_2 coated $BaTiO_3$, this could be attributed to oxidation and reduction of methane and carbon dioxide by electrons and holes present on the TiO_2 after the activation of the catalyst by the non-thermal plasma. Methane and carbon dioxide could react with the electron from the conductance band of the photocatalyst via [Eq. 36-38]. Alternatively, methane could react with electron hole at valence band and cause oxidation of methane through [Eq. 41] [233]. He *et al.* proved that the anatase (101) facet played a critical role in carbon dioxide adsorption and assisting the electron transfer from the surface of TiO_2 to carbon dioxide in the photoreduction process [234, 235]. Other studies have also confirmed the successful oxidation of methane on TiO_2 photocatalysts with the presence of either carbon dioxide or O_2 through the reaction in [Eq. 42] [236-238].

$$CH_4 + h^+ \rightarrow CH_3 + H^+ \qquad \text{[Eq. 41]}$$

$$CH_4 + 2O_2 \rightarrow CO_2 + 2H_2O \qquad \text{[Eq. 42]}$$

The second best performing is the TiO_2 unannealed coating, after degradation of methylene blue experiments, it was determined that unannealed samples were not photocatalytically active, therefore, it is not possible that electron hole pairs are the reason for the improved performance in comparison to the non-coated $BaTiO_3$. The improved performance of the unannealed TiO_2 coated $BaTiO_3$ could be due to the existence of oxygen vacancies. Due to oxygen vacancies, numerous Ti^{3+} states are present. At the surface, these Ti^{3+} species can reduce adsorbed CO_2 to a bent $CO_2^{\cdot-}$ species, reforming Ti^{4+}, and

again serve as electron trap states for further reduction. Oxygen vacancies can also induce dissociation of CO_2 to adsorbed CO and a healed vacancy [239]. Desorption of any carbon as CO which could aid in the break-up of carbon dioxide and cause an enhancement in break-up of methane as seen in [Eq. 43-46] [240], the desorption of the carbon is discussed further in section 5.6.2 – Coking.

$$CO_2 \rightarrow CO + O \qquad \text{[Eq. 43]}$$

$$CH_4 + O \rightarrow CH_3 + OH \qquad \text{[Eq. 44]}$$

$$CH_4 + O \rightarrow CH_3OH \qquad \text{[Eq. 45]}$$

$$CH_4 + O \rightarrow H_2 + HCHO \qquad \text{[Eq. 46]}$$

The worst performing packing material was the TiO_2-W coated $BaTiO_3$. In figure 72 the effect of a lower breakdown voltage can be seen due to the lower SED values per peak to peak voltage in comparison to the other packing material. It is thought that the addition of tungsten reduced the overall dielectric constant which led to the higher breakdown voltage as the lower the dielectric constant the higher the voltage needed for plasma ignition, as demonstrated in various studies [241, 242]. A higher dielectric constant at the same applied voltage increases the discharge power and electric field strength, this agrees with the calculated SED shown in figure 72. Decreased discharge power would result in reduced conversions, as the higher the dielectric constant of the material the increased intensity, and number of microdischarges [243-245]. Furthermore, the higher the electric field strength, the higher the electron energy [97].

5.5.4 Gas feed ratio of CH_4:CO_2 1:6

Further to varying the ratio of CH_4:CO_2 to 1:1.5, a ratio of 1:6 was investigated with a concentration in ppm of 250 ppm CH_4 and 1500 ppm CO_2. Figure 73 shows the degradation of methane and carbon dioxide and the production of carbon monoxide with applied voltage with a gas feed ratio of 1:6. Figure 74 shows the degradation of methane and carbon dioxide and the production of carbon monoxide with the measured SED with a gas feed ratio of 1:6.

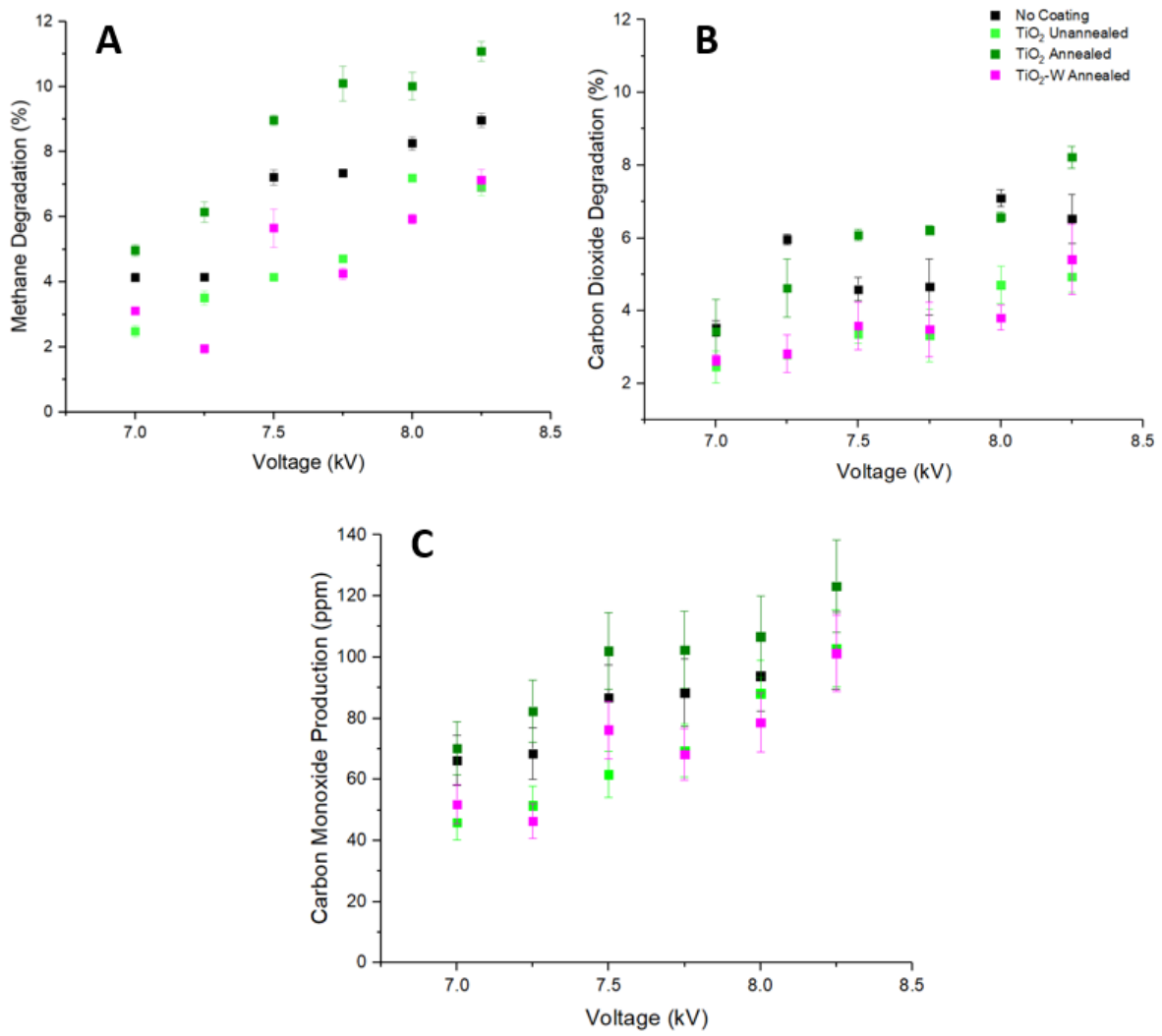

Figure 73 – (A) Methane degradation against applied voltage, (B) carbon dioxide degradation against applied voltage, and (C) carbon monoxide production in ppm against applied voltage with a 1:6 CH_4:CO_2 ratio.

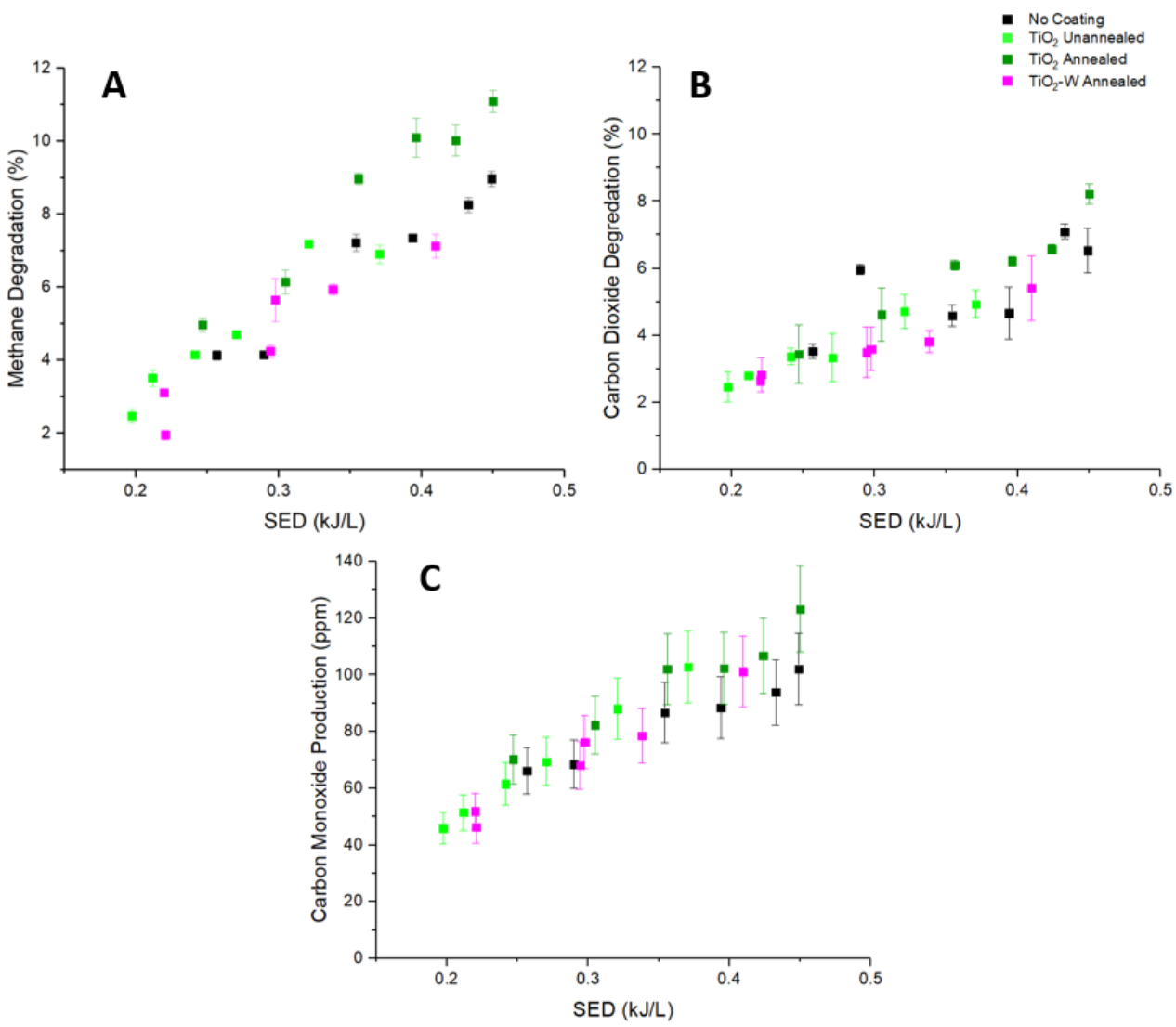

Figure 74 – (A) Methane degradation against SED, (B) carbon dioxide degradation against SED, and (C) carbon monoxide production against SED with a 1:6 CH_4:CO_2 ratio.

Table 20 shows the maximum methane and carbon dioxide degradation and maximum carbon monoxide production with the various packing material

Table 20 - Maximum CH_4 and CO_2 degradation and the maximum CO production with a 1:6 CH_4:CO_2 ratio

	Maximum CH_4 Degradation (%)	**Maximum CO_2 Degradation (%)**	**Maximum CO production (ppm) (+/- 12%)**
No Coating	8.96	7.1	102.09
TiO_2 Unannealed	7.18	4.93	102.85
TiO_2 Annealed	11.08	8.22	123.19
TiO_2-W Annealed	7.12	5.41	101.2

Experiments with a ratio of 1:6 as seen in figure 73 and figure 74, show in an increase of methane degradation of up to 6.69 % compared a ratio of 1:1.15, as seen in figure 69 and figure 70, and up to 1.56% compared to a 1:3 ratio as seen in figure 71 and figure 72. This is despite the fact that carbon dioxide has a higher breakdown voltage than argon and methane and so the degradation of carbon dioxide was expected to decrease. This shows the effect of increased atomic oxygen on the breakdown of methane. The increase in carbon dioxide quantity and ppm dissociation leads to an increase in atomic oxygen species. Atomic oxygen can react with methane, as seen in [Eq. 44-46]. It has been reported in various experimental studies that an increase in the carbon dioxide ratio in the dry reforming of methane leads to an increase in methane degradation [27, 96, 104, 106, 108]. An excess of carbon dioxide within the gas stream produced caused an increased degradation of carbon dioxide by up to 40 ppm, this also follows in an increase in CO produced. Similarly to the previous experiments the TiO_2 annealed $BaTiO_3$ showed a significantly enhanced performance in comparison to all other packing material. This is due to the activation of the anatase phase causing enhanced degradation of carbon dioxide which also leads to increased degradation of methane as explained previously in section 5.5.2.

5.5.5 Gas feed of 100% CO_2 / Argon

The coated packing material was investigated in a gas mixture of carbon dioxide and argon to enable a deeper understanding of the effect on plasma chemistry due to the addition of the photocatalyst coating. The carbon dioxide concentration was the same as previous experiments for the CH_4:CO_2 ratio of 1:3 (750 ppm). A decrease in peak to peak voltage was used due to significant arcing. Figure 75 and figure 76 shows the carbon dioxide degradation and carbon monoxide production against applied voltage and measured SED respectively for the various coated packing material.

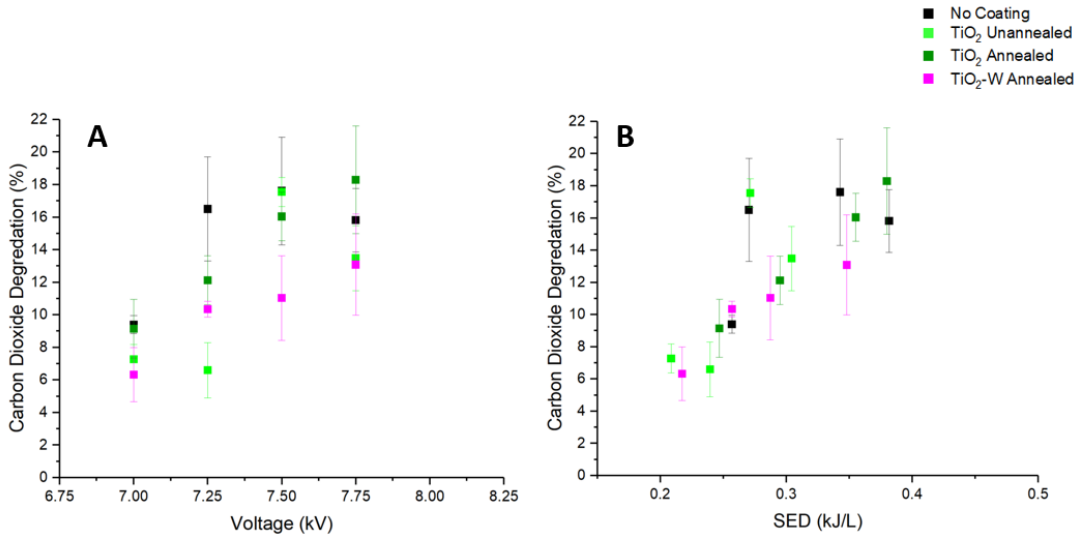

Figure 75 – (A) Carbon dioxide degradation as a function of applied voltage, and (B) carbon dioxide degradation as a function of SED.

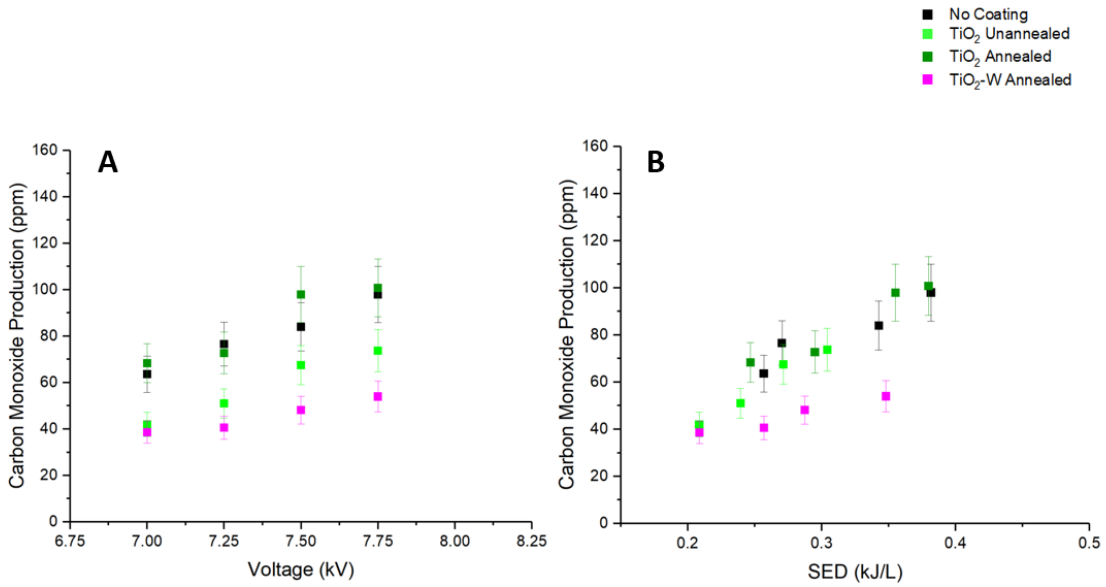

Figure 76 – (A) Carbon monoxide production as a function of applied voltage, (B) carbon monoxide production as a function of SED.

Table 21 – Maximum CO production (ppm) and CO_2 degradation (%) in the reforming of CO_2 in carrier gas argon.

	Maximum CO_2 Degradation (%)	**Maximum CO production (ppm)**
No Coating	17.61	98
TiO_2 Unannealed	17.55	73.73
TiO_2 Annealed	18.3	100.8
TiO_2-W Annealed	13.08	54

Table 21 shows that the dissociation of carbon dioxide is much higher compared to the methane / carbon dioxide /argon gas mixtures. A maximum of 18.3% degradation was achieved when using a carbon dioxide / argon mix compared a maximum of 11.25% in the methane / carbon dioxide / argon gas mixture. A reduced amount of atomic oxygen and energetic electrons available to react and dissociate with carbon dioxide in the methane / carbon dioxide / argon mix due to the competing reactions as seen in [Eq. 36-38, 43-46] could be the reason the same degradation is not seen in the methane / carbon dioxide / argon mix due to their role in reacting and dissociating methane. The lowest degradation was the TiO_2-W coated $BaTiO_3$, again though to be due to the reduced dielectric constant which causes a reduction in the intensity of number of microdischarges. The TiO_2 coated $BaTiO_3$ which was not annealed degraded significantly higher carbon dioxide than the TiO_2-W coated $BaTiO_3$, This could be attributed to the oxygen vacancies which can induce dissociation of carbon dioxide to adsorbed CO and a healed vacancy. However, it can be seen that the maximum carbon dioxide degradation was lower than either uncoated $BaTiO_3$ and annealed TiO_2 coated $BaTiO_3$. This is due to decreased SED for the same applied voltage as seen in figure 75 and figure 76. The non-coated $BaTiO_3$ is the second best performing, most likely due to the increased dielectric constant of the $BaTiO_3$ surface. The best performing is the annealed TiO_2 coated $BaTiO_3$, a photocatalytic effect of the anatase TiO_2 could result in an increased reduction of carbon dioxide due to the electron hole pairs present, further degradation could be caused by an increase in superoxide anions such as O_2^-,O^-, O_3^- or O_2^+ due to the reaction of dissociated carbon dioxide products with the electron hole pairs.

5.5.6 Gas feed of 100% CH_4 / Argon

The degradation of methane in an argon gas mixture was carried out in order to understand the effect of removing carbon dioxide from the gas mixture and to provide further understanding into the effect of the photocatalytic coatings within the packed bed reactor. The methane concentration was the same as previous experiments for the CH_4:CO_2 ratio of 1:3 (250 ppm). A decrease in peak to peak voltage was used due to significant arcing. Figure 77 shows the methane degradation against applied voltage and measured SED with the various coated packing material.

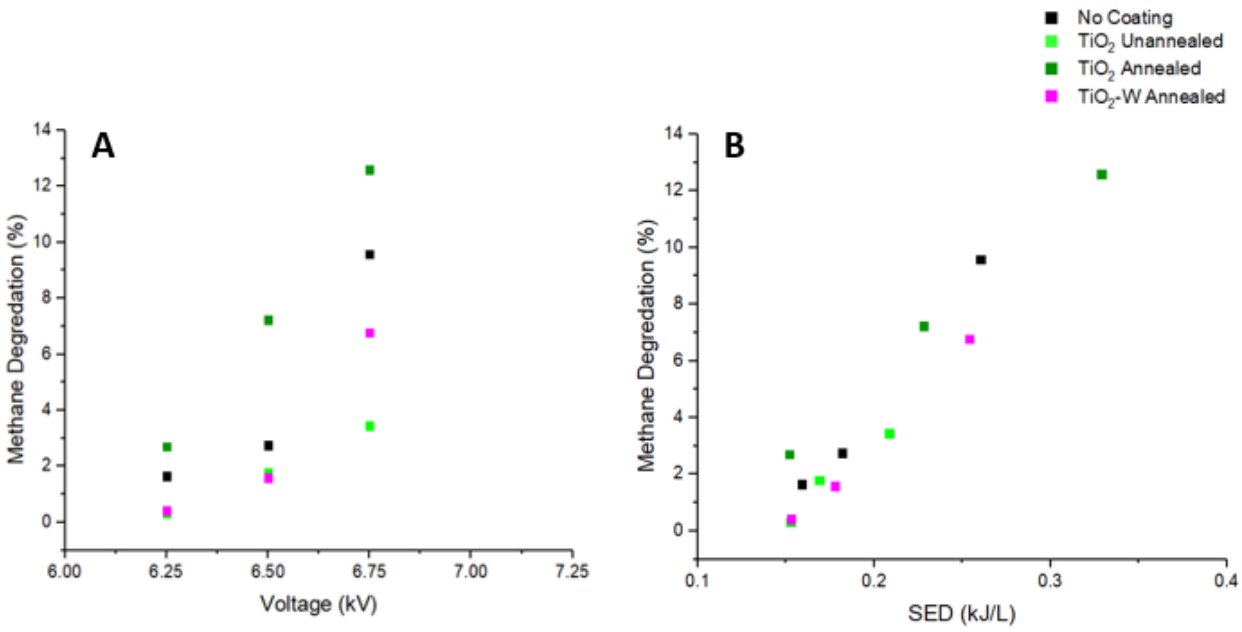

Figure 77 – (A) Methane degradation against applied voltage, (B) methane degradation against SED.

Table 22 – Maximum CH_4 production (ppm) in carrier gas argon.

	Maximum CH_4 degradation (%)
No Coating	9.57
TiO_2 Unannealed	3.45
TiO_2 Annealed	12.59
TiO_2-W Annealed	6.77

The degradation of methane using a methane /argon mix increased slightly from a maximum of 11.08% using a methane / carbon dioxide / argon mix with a ratio of 1:6, to 12.59% with using only methane and argon. This improvement was the case for the annealed TiO_2 coated $BaTiO_3$ and the non-coated $BaTiO_3$, however, the unannealed TiO_2 coated $BaTiO_3$ and the TiO_2-W coated $BaTiO_3$ performed worse with a methane argon mix in comparison to a methane / carbon dioxide / argon mix. The large difference in methane degradation of the unannealed TiO_2 coated $BaTiO_3$ suggest that the CO and atomic oxygen produced at the oxygen vacancies have a significant role in the degradation of methane. Moreover, the SED for the unannealed TiO_2 coated $BaTiO_3$ was significantly lower than the other coated packing material causing significantly decreased dissociation. Carbon dioxide degradation in an argon mix was significantly more than the methane degradation, this is thought to be due to a lower threshold energy for the electron impact dissociations of carbon dioxide (~ 6.4 eV) compared with that of methane (~7.5 eV) [97]. Increased breakup of the methane by the annealed TiO_2 coated is caused by the oxidation of methane with holes at valence band through [Eq. 41].

5.5.7 OES Spectroscopy

OES spectroscopy was measured at maximum peak to peak voltage. This was done in order to determine the generation of photons, their wavelengths produced by the plasma. Figure 78 shows the optical emission spectra graph at 8.25 kV peak to peak voltage.

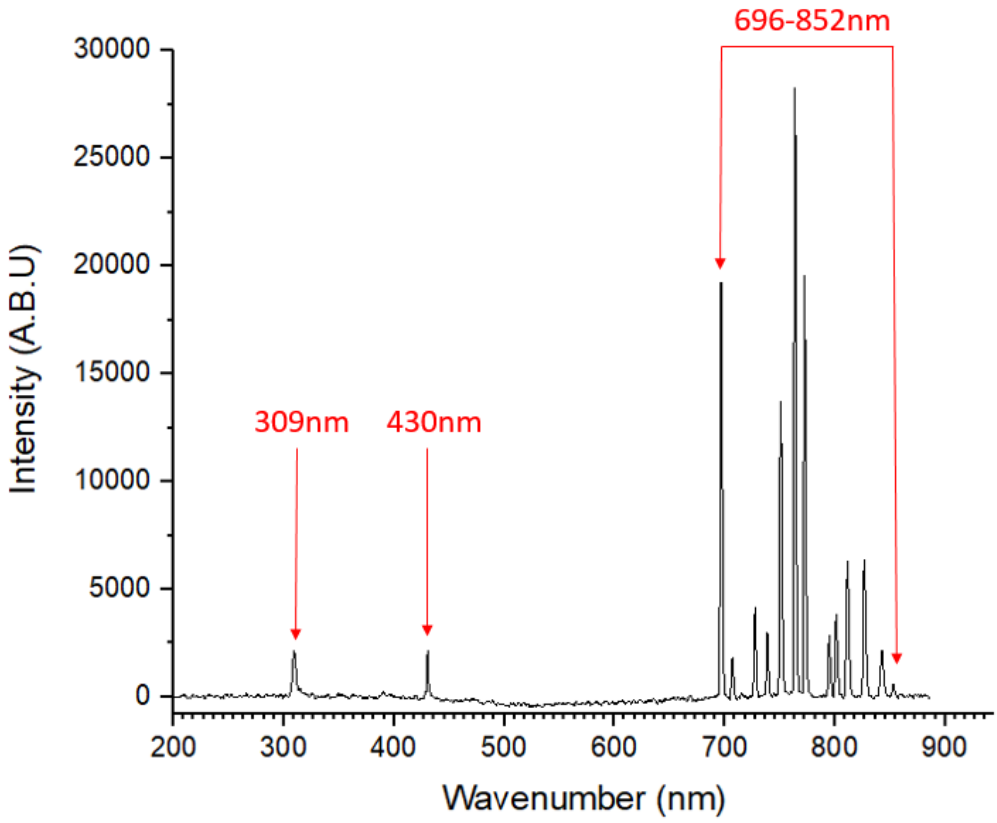

Figure 78 – OES spectra; 8.25kV peak to peak voltage, $BaTiO_3$ coated with TiO_2 packing material, CH_4:CO_2 ratio of 1.

It can clearly be seen that photons in the region of below 315 nm are present indicating photons in the UVA region are produced by the excited species present in the plasma. Other emissions are in the visible light (400-780 nm) and in the infrared region >780 nm. Emissions in the region of 430-852nm are all characteristic of argon emissions, whereas the peak at 309nm in characteristic of OH [246]. The hydroxyl radical can be produced by electron-hole pairs and/or be produced in the plasma via reaction [Eq. 47-50] which includes reaction with water, which can be present in the background as an impurity, it can also be involved in the destruction of methane via [Eq. 50]

$$CH_4 + O \rightarrow CH_3 + OH \qquad \text{[Eq. 47]}$$

$$Ar^* + H_2O \rightarrow OH + H + Ar \qquad \text{[Eq. 48]}$$

$$H_2O + e \rightarrow OH + H + e \qquad \text{[Eq. 49]}$$

$$CH_4 + OH \rightarrow CH_3 + H_2O \qquad [Eq.\ 50]$$

UVA photons have the energy to activate photocatalysts such as TiO_2 and could cause photocatalytic reactions within the non-thermal plasma as their wavelength is below the 387 nm needed to activate TiO_2 [178]. Argon has several photonic emissions within the UVA range, including significant emission lines at 106-155 nm [247, 248], being capable of activating the TiO_2 catalysts. These emission lines could not be detected with our spectrometer, which can only detect emissions down to 190 nm.

5.6 Discussion on Effect of Photocatalytic Coatings

5.6.1 Effect of Coating on Plasma Chemistry.

The introduction of photocatalytic coatings had significant effects on the dry reforming of methane within the packed bed dielectric discharge reactor. Firstly, it can be seen that the introduction of TiO_2-W in most cases negatively impacted the performance of the dry reforming of methane for the same applied voltage and plasma power. A reason for the performance could be due to a negative effect of the W-metal and WO_3 on the overall dielectric constant effecting the plasma properties such as, reduction in electric field and number and intensity of microdischarges. The static dielectric constant of TiO_2 is greater than that of WO_3, the effect of this was observed in the experiments whereby the SED was lower for the same applied voltage when using TiO_2-W coated $BaTiO_3$ compared to TiO_2 coated or non-coated [227]. This indicates a lower breakdown voltage for the TiO_2-W coated $BaTiO_3$ packing material compared to the other coated particulates. A similar effect was observed for the unannealed TiO_2 coated $BaTiO_3$ as seen in the calculated SED. The TiO_2 annealed sample did not affect the SED and no significant differences between itself and the non-coated $BaTiO_3$ were observed. Research into the dielectric constant of TiO_2 thin films conducted by Busani et al and Yang et al show that amorphous TiO_2 thin films have a relatively low dielectric constant compared to TiO_2 thin films which contained anatase and rutile crystallinity [249, 250]. This could account for the increase in performance observed with the annealed TiO_2 coated $BaTiO_3$ compared with the unannealed TiO_2 coated $BaTiO_3$. The two most consistently performing coatings were the non-coated $BaTiO_3$ and the annealed TiO_2 coated $BaTiO_3$. However, in almost all cases the annealed TiO_2 coated $BaTiO_3$ outperformed the non-coated $BaTiO_3$ both for the same applied voltage and the SED. The TiO_2 coated $BaTiO_3$ showed a good degree of photocatalytic activity when testing the activity through the methylene blue degradation method. The annealed TiO_2 is thought to be activated by the UV light produced by the plasma, causing the electron hole pairs to be produced providing reductive and oxidative reaction pathways otherwise not achievable. The quantity of hydrogen produced in this process could not be directly measured,

5.6.2 Coking of Catalysts

$BaTiO_3$ particulates were examined for signs of coking after use within the packed bed reactor. Figure 79 shows the Raman spectra of particulates after their use, it can be seen that the uncoated $BaTiO_3$ showed significantly less coking in comparison to the coated samples. Raman spectroscopy also showed the increase in amorphous substances on the particulates.

Deactivation of catalysts by coke formation, which originates from the methane dissociation and/or carbon dioxide disproportionation, is a serious problem in DRM. Carbon deposition in DRM occurs via two main possible pathways, methane decomposition [Eq. 51] and Boudouard reaction (i.e., CO disproportionation) [Eq. 52] [251].

$$CH_4 \rightarrow C(s) + 2H_2 \qquad \Delta H_{298K} = +75 kJmol^{-1} \qquad \text{[Eq. 51]}$$

$$2CO \rightarrow C(s) + CO_2 \qquad \Delta H_{298K} = -171 kJmol^{-1} \qquad \text{[Eq. 52]}$$

[Eq. 51] is endothermic and favoured at high temperature, whereas [Eq. 52] prefers lower temperature as the reaction is exothermic. Since non-thermal plasma is done at relatively low temperatures the exothermic reaction is more prevalent. Another factor affecting carbon deposition is the surface acidity of catalysts. It was revealed that noble metal catalysts are more resistant to carbon deposition than non-noble metal catalysts [251]. Materials with high Lewis basicity, such as La_2O_3 and CeO_2, can increase the ability of catalysts to chemisorb carbon dioxide, which can react with carbon to form CO, decreasing carbon formation. Carbon formation can be diminished or even suppressed when the active metal is supported on a metal oxide carrier with Lewis basicity. Zheng et al found that carbon deposition was suppressed and was connected to the presence of the active metal oxide, Fe_2O_3 [252]. Therefore it is possible that the TiO_2 coatings aids in the reaction and eventual desorption of the carbon deposits. The same can be said for the TiO_2-W coatings, it is also possible that any WO_3 present could have the same effect.

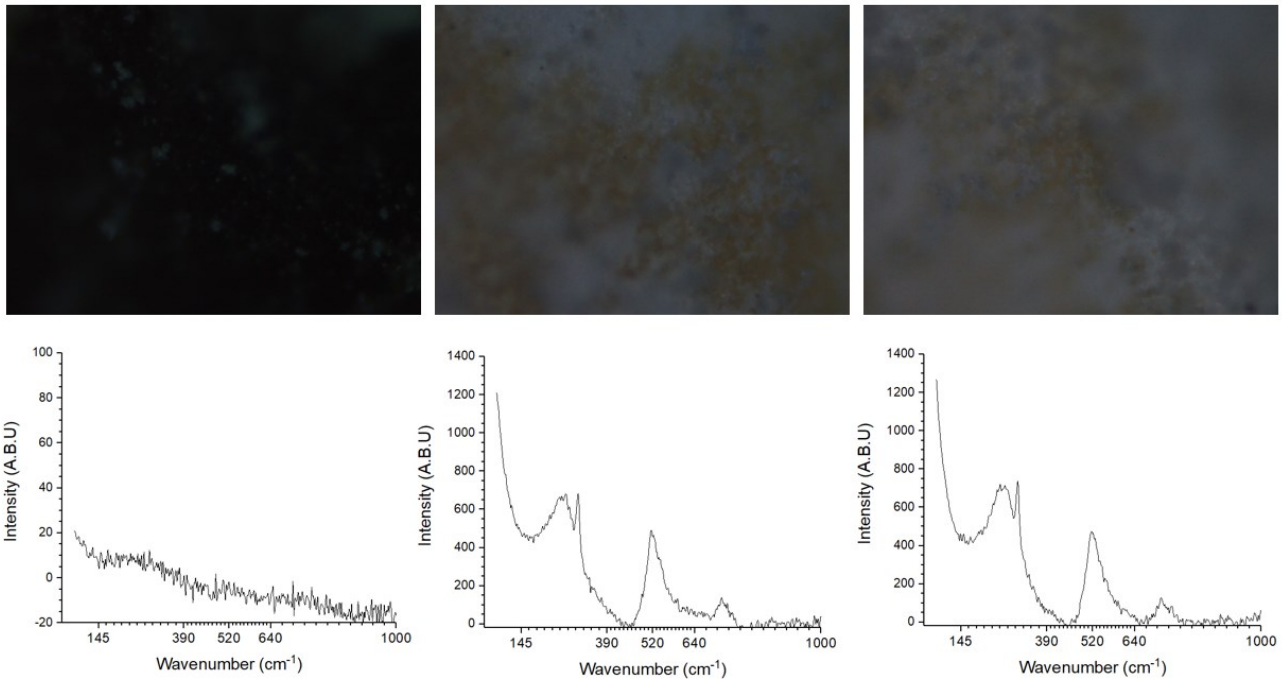

Figure 79 – Raman live image and spectra of coked $BaTiO_3$ after use in the DRM. $BaTiO_3$ no coating (left), $BaTiO_3$ with TiO_2 coating unannealed (middle) and $BaTiO_3$ with TiO_2-W coating (right).

5.7 Energy Efficiency

The energy efficiency was calculated in mmol/kJ to enable comparison to other non-thermal plasma devices in literature. It must be noted that the higher flow rates increases energy efficiency but cause a lower overall degradation compared to other devices.

The energy efficiency was calculated by obtaining the ppm converted per litre and converting to the conversion in mol/s, the method can be seen in CHAPTER 2.

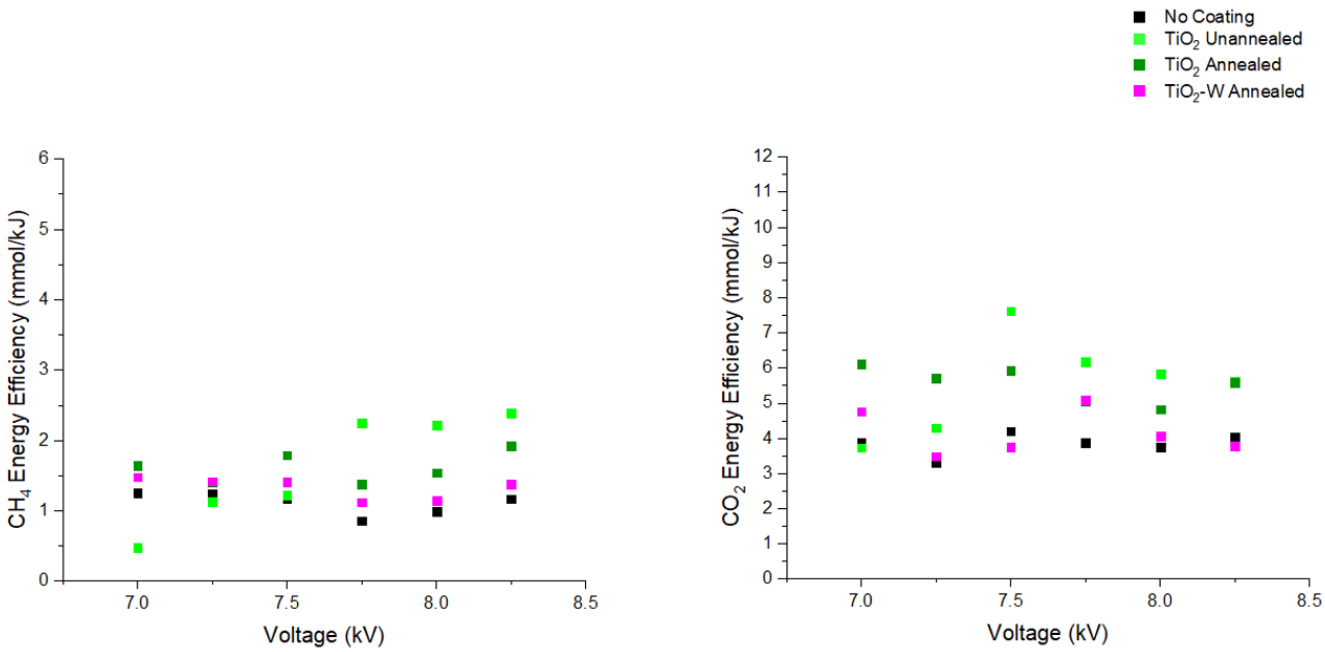

Figure 80 - Energy efficiency of CH_4 conversion (left) and energy efficiency of CO_2 conversion (right) with a 1:1.5 ratio.

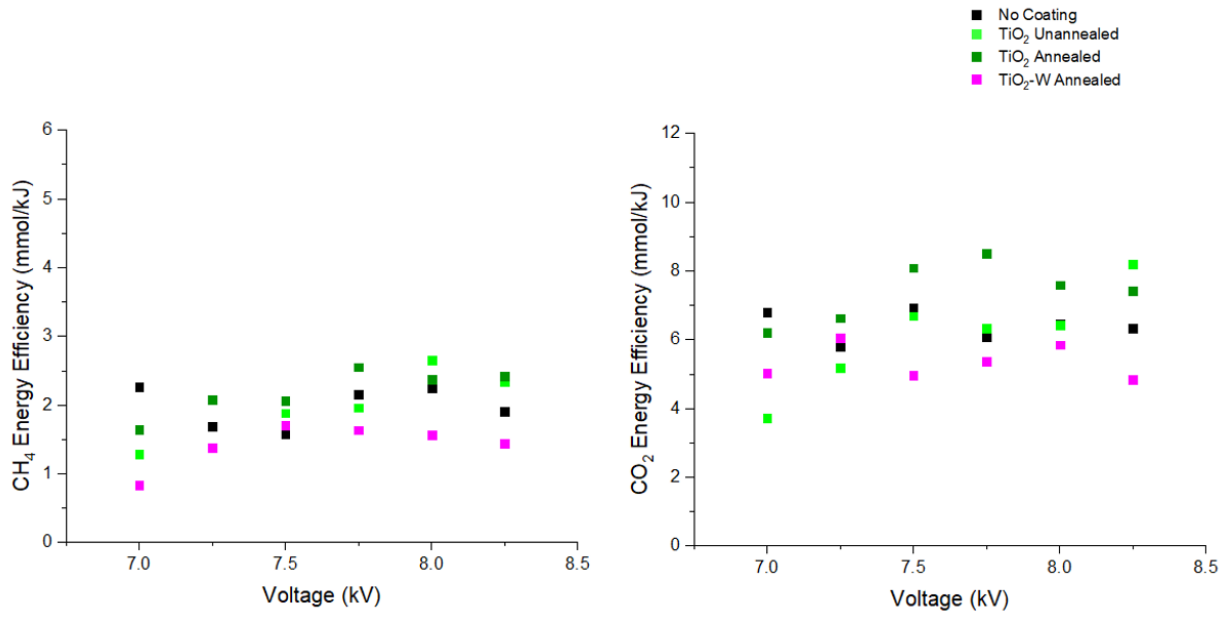

Figure 81 – Energy efficiency of CH_4 conversion (left) and energy efficiency of CO_2 conversion (right) with a 1:3 ratio.

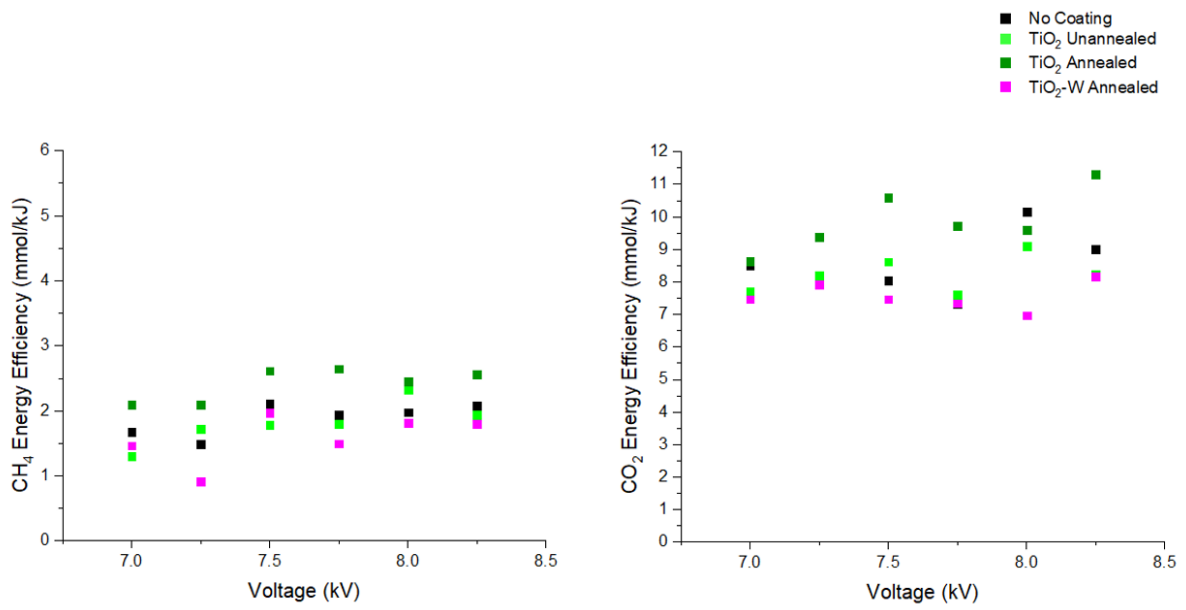

Figure 82 - Energy efficiency of CH_4 conversion (left) and energy efficiency of CO_2 conversion (right) with a 1:6 ratio.

Table 23 – Maximum energy efficiency of the dry reforming of methane and carbon dioxide.

CH_4:CO_2	**Energy Efficiency CH_4 (mmol/kJ)**	**Energy Efficiency CO_2 (mmol/kJ)**	**Total Energy Efficiency (mmol/kJ)**
1:1.5	2.39	7.62	8.85
1:3	2.65	8.59	11.06
1:6	2.64	11.31	13.87

Figures 80-82 show the energy efficiency of methane and carbon dioxide conversion for CH_4:CO_2 ratios of 1:1.5, 1:3 and 1:6. The energy efficiency was generally greatest when using the annealed TiO_2 coated $BaTiO_3$ followed by the unannealed TiO_2 coated $BaTiO_3$, non-coated $BaTiO_3$ and the TiO_2-W coated $BaTiO_3$. The photocatalytic properties of the annealed TiO_2 coated $BaTiO_3$ and the oxygen vacancies of the unannealed TiO_2 coated $BaTiO_3$ are the driving factors in increased energy efficiency. Table 23 shows the maximum energy efficiency achieved for the various gas feed ratios, regardless of packing material. The gas feed ratio of 1:6 achieved the highest energy efficiency due to the increased atomic oxygen which can drive the degradation of methane through [Eq. 44-46]. Although the conversion of carbon dioxide was slightly less for the 1:6 ratio in comparison to the 1:3 ratio, the ppm converted was much greater, therefore, the energy efficiency is significantly greater.

5.8 Conclusion

TiO_2 and TiO_2-W coatings were deposited onto $BaTiO_3$ dielectric particulates for use within a non-thermal packed bed dielectric barrier discharge reactor for the dry reforming of methane. A mixture of methane and carbon dioxide with a carrier gas of argon was used. Various gas ratios of CH_4:CO_2 were investigated to study the effect of the TiO_2 and TiO_2 coatings. Overall it was found that the worst performing catalysts where the $BaTiO_3$ coated with the TiO_2-W annealed, this was attributed to the lower dielectric constant of WO_3. It was found that the annealed TiO_2 coated $BaTiO_3$ enhanced the degradation of carbon dioxide in an argon mix and enhanced the degradation of methane in an argon mix compared to all other catalysts, this is thought to be due to the oxidation and reduction reactions occurring at the anatase TiO_2 sites. The best performing CH_4:CO_2 ratio was 1:6 as this increased the methane degradation as it provided more atomic oxygen which reacts with methane, the energy efficiency was also greater for the 1:6 ratio compared to the other CH_4:CO_2 ratios. The worst performing flow ratio was a ratio of 1:1.5, this achieved the lowest degradations of methane and carbon dioxide and had the lowest energy efficiency. Furthermore, it was observed that by including a coating the formation of coke deposits reduced comparing to uncoated $BaTiO_3$. Although hydrogen could not directly be measured in these experiments, results infer that increased hydrogen was produced with the TiO_2 coated $BaTiO_3$ which was annealed due to maximum CO production with this packing material. Direct measurement of hydrogen with a GCMS could confirm this hypothesis. It is also suggested increasing the residence time could increase the % conversion of methane and carbon dioxide increasing production of hydrogen and carbon monoxide.

CHAPTER 6 – CONCLUSION AND FURTHER WORK

6.1 Conclusion

The primary aim of this work was to investigate the effect of photocatalytic coatings on the packing material in a non-thermal packed bed plasma reactor. Firstly, a non-thermal packed bed reactor (PBR) was designed and manufactured in house and formed the basis to investigate the effects of the combination of photocatalyst coatings and non-thermal plasma.

Secondly, coatings of TiO_2, both unannealed and annealed, and TiO_2-W were deposited onto glass particulates to develop a viable coating method and to investigate their photocatalytic activity before depositing onto $BaTiO_3$ particulates, for use within the PBR. Surface characterisation was carried out using Raman spectroscopy, SEM, XPS and BET surface area analysis. Photocatalytic testing of the prepared coatings were analysed with the methylene blue degradation method under UV light. The TiO_2-W coating was the best performing photocatalyst followed by the annealed TiO_2 coating. The unannealed TiO_2 coating showed no photocatalytic activity, along with the non-coated packing material. Following this, $BaTiO_3$ particulates were coated with TiO_2 and TiO_2-W and showed an increase in photocatalytic activity in comparison to the glass particulates, due to an increased surface area of the $BaTiO_3$. Again the TiO_2-W coating was the best performing followed by the annealed TiO_2 with the unannealed showing no photocatalytic activity. Coatings were characterised with Raman spectroscopy, SEM and XPS.

In order to investigate the role of photocatalysts and their effect on the plasma discharge and chemistry, and determine whether the photocatalytic coatings produced by magnetron sputtering offer a more favourable approach than conventional methods to introducing the catalysts, their effect on nitrogen and oxygen plasma chemistry and on the dry reforming of methane were investigated.

Non-coated $BaTiO_3$ and TiO_2 coated $BaTiO_3$ particulates, both unannealed and annealed were placed in the PBR to investigate their effect on plasma chemistry in an oxygen-nitrogen mix. The presence of TiO_2 on the surface of the packing material affects the plasma chemistry through acting as an atomic oxygen sink, photocatalytic formation of O_2^-, and modification of the dielectric constant of the $BaTiO_3$ particulates. The increase in oxygen species also led to N_2O_5 being formed in the presence of annealed TiO_2, which opens up a potential new route for synthesis of this industrially significant chemical. The findings of this study show that it is possible to tailor the plasma chemistry of nitrogen and oxygen mixtures through the modification of the plasma facing materials and surfaces, optimising yields of ozone and N_2O_5 whilst limiting the formation of harmful by-products.

The effect of TiO_2 and TiO_2-W coatings onto $BaTiO_3$ particulates for use within a non-thermal packed bed dielectric barrier discharge reactor for the dry reforming of methane were investigated for various methane and carbon dioxide feed gas ratios in an argon carrier gas. Annealed TiO_2 coated $BaTiO_3$ significantly increased the degradation of methane and carbon dioxide for all feed gas ratios. This was

attributed to photocatalytic reactions enabled by the plasma. Unannealed TiO_2 increased the performance in some instances due to the presence of oxygen vacancies. Annealed TiO_2-W coated $BaTiO_3$ performed worse in comparison to the non-coated $BaTiO_3$ baseline due to a reduced dielectric constant, resulting in a decreased number of microdischarges. Therefore, it was shown that photocatalytic coatings onto the packing material and in close proximity to the plasma can have a photocatalytic effect and beneficially increase the degradation of both methane and carbon dioxide and production of carbon monoxide, dependent on the photocatalyst. This could lead to a viable route for environmentally sustainable syngas production, which is a useful chemical product.

These studies show that with careful understanding of the plasma-photocatalyst surface interaction, chemical processes could be tailored towards improving the production of desired products and limit the formation of undesired by-products and that photocatalysts produced by magnetron sputtering can enhance the surface interaction between plasma and photocatalysts with minimal disturbance to gas flow.

6.2 Further Work

There are a number of areas which require further work. One of the main areas is the analysis of the products formed in the plasma reactor. The FTIR is not able to detect hydrogen and so analysis using a GCMS would enable further characterisation of the hydrogen production. Secondly, further work on the in situ measurement of the plasma process is recommended. In situ measurements are very important for identifying and quantifying the chemical species formed in the plasma. This information helps in further understanding the mechanism of the chemical reactions taking place in the plasma region. It also helps in optimizing the plasma system and conditions. Another area for further study is to lower the flow rate for the DRM experiments. Increased residence time would help to increase degradation, using a GCMS along with this would be extremely helpful as the FTIR can be overly sensitive.

Other work which could be carried out as a result of the findings in this report is the exploration into different photocatalytic properties such as using other dopants to keep the dielectric constant high and increase photocatalytic efficiency. Finally, scaling up the reactor to increase volumes of syngas produced, the amount of methane and carbon dioxide that can be treated and its energy efficiency is another area of work which could be investigated.

APPENDIX

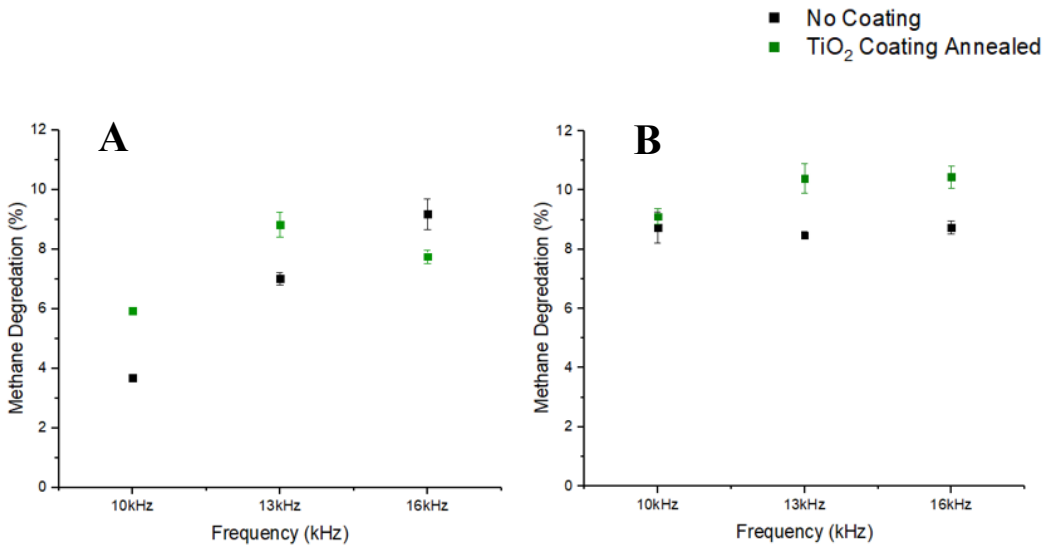

Figure A1 – Methane degradation with respect to frequency. A) Experimental conditions: 7kV, 1SLM flow rate, 240ppm CO_2, 425ppm CH_4, argon carrier gas. B) Experimental conditions: 8kV, 1SLM flow rate, 240ppm CO_2, 425ppm CH_4, argon carrier gas.

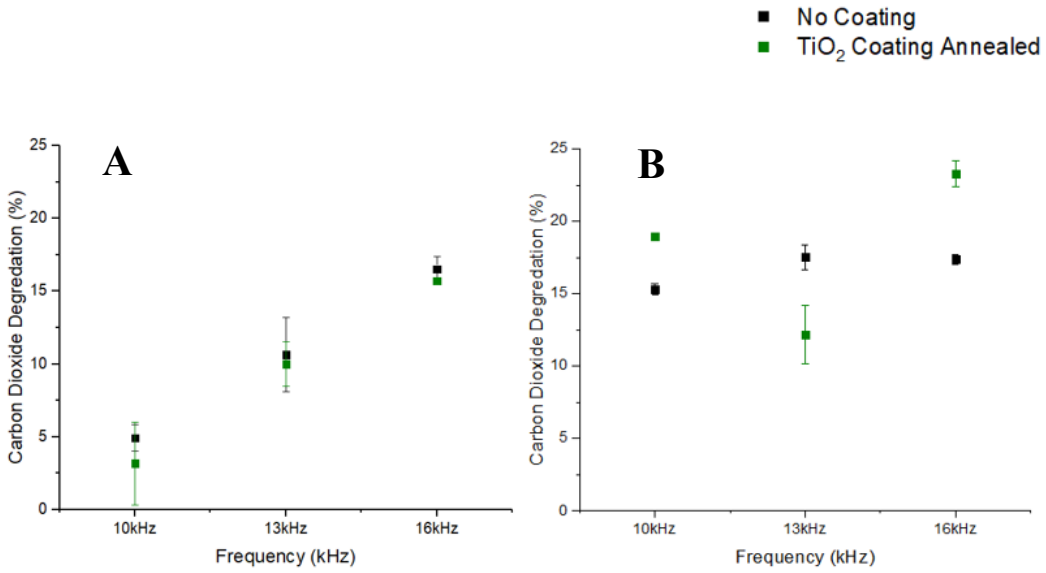

Figure A2 – Carbon dioxide degradation with respect to frequency.A) Experimental conditions: 7kV, 1SLM flow rate, 240ppm CO_2, 425ppm CH_4, argon carrier gas. B) Experimental conditions: 8kV, 1SLM flow rate, 240ppm CO_2, 425ppm CH_4, argon carrier gas.

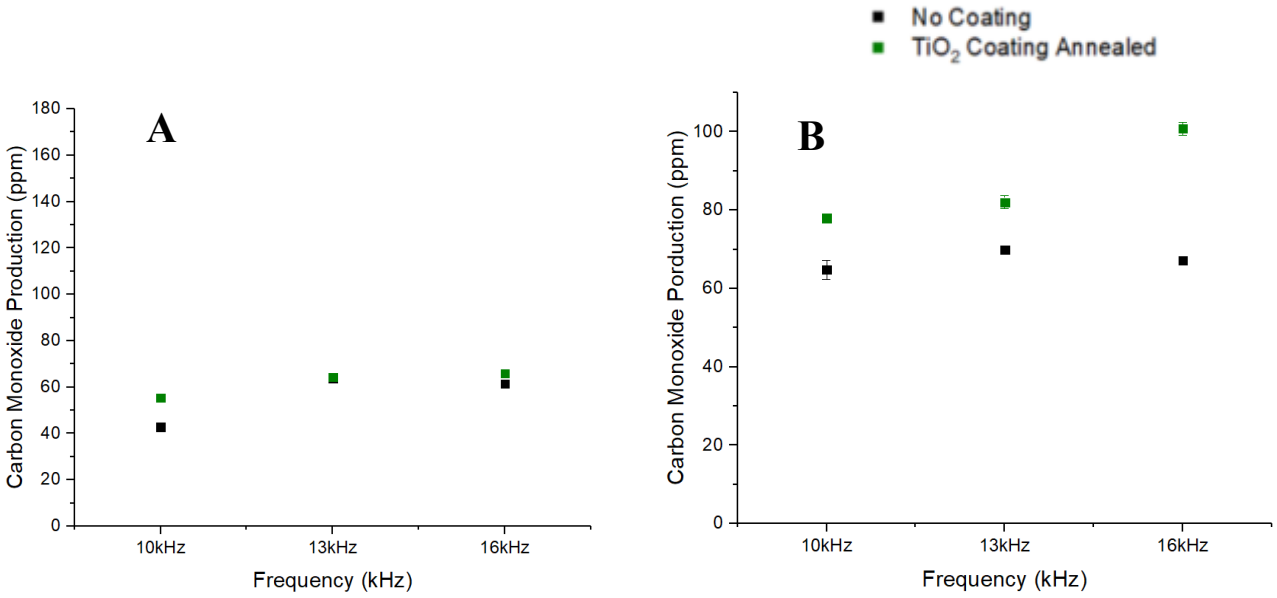

Figure A3 – Carbon monoxide production with respect to frequency. A) Experimental conditions: 7kV, 1SLM flow rate, 240ppm CO_2, 425ppm CH_4, argon carrier gas. B) Experimental conditions: 8kV, 1SLM flow rate, 240ppm CO_2, 425ppm CH_4, argon carrier gas.

CODE 1 – Dry Reforming of Methane Area

```
% Define Inputted Data
sample = Sample4325ByAdministratorDateWednesday;
wave = CreatedasNewDataset;
% Plot Graph
figure()
plot(wave,sample)
xlabel ('Wavenumber');
ylabel ('Absorbance');
set (gca, 'XDir', 'Reverse')
sample(sample<0)=0;
trapz(sample,wave)

% Area Under Graph Between Two Points
idx = wave>=2550 & wave<=3200 ;
wavei=wave(idx);
samplei=sample(idx);
figure()
Methane_1=trapz(wavei,samplei);
area(wavei,samplei)
%%%%%%%%%%%%%%%%%%%%%%%%%%%%%%%%%%%%%%%%%%%%%%%%%%%%%%%%
idx = wave>=1175 & wave<=1400 ;
wavei=wave(idx);
samplei=sample(idx);
figure()
Methane_2=trapz(wavei,samplei);
area(wavei,samplei)
%%%%%%%%%%%%%%%%%%%%%%%%%%%%%%%%%%%%%%%%%%%%%%%%%%%%%%%%
idx = wave>=2010 & wave<=2230 ;
wavei=wave(idx);
```

```
samplei=sample(idx);
figure()
CO=trapz(wavei,samplei);
area(wavei,samplei)
%%%%%%%%%%%%%%%%%%%%%%%%%%%%%%%%%%%%%%%%%%%%%
idx = wave>=2230 & wave<=2400 ;
wavei=wave(idx);
samplei=sample(idx);
figure()
CO2_1=trapz(wavei,samplei);
area(wavei,samplei)
%%%%%%%%%%%%%%%%%%%%%%%%%%%%%%%%%%%%%%%%%%%%%
idx = wave>=3540 & wave<=3660 ;
wavei=wave(idx);
samplei=sample(idx);
figure()
CO2_2=trapz(wavei,samplei);
area(wavei,samplei)
%%%%%%%%%%%%%%%%%%%%%%%%%%%%%%%%%%%%%%%%%%%%%
idx = wave>=3660 & wave<=3760 ;
wavei=wave(idx);
samplei=sample(idx);
figure()
CO2_3=trapz(wavei,samplei);
area(wavei,samplei)
%%%%%%%%%%%%%%%%%%%%%%%%%%%%%%%%%%%%%%%%%%%%%
idx = wave>=3220 & wave<=3360 ;
wavei=wave(idx);
samplei=sample(idx);
figure()
Unknown=trapz(wavei,samplei);
area(wavei,samplei)
%%%%%%%%%%%%%%%%%%%%%%%%%%%%%%%%%%%%%%%%%%%%%%
idx = wave>=3676 & wave<=3733 ;
wavei=wave(idx);
samplei=sample(idx);
figure()
CO2_21=trapz(wavei,samplei);
area(wavei,samplei)
%%%%%%%%%%%%%%%%%%%%%%%%%%%%%%%%%%%%%%%%%%%%%%
idx = wave>=3569 & wave<=3641 ;
wavei=wave(idx);
samplei=sample(idx);
figure()
CO2_31=trapz(wavei,samplei);
area(wavei,samplei)
%%%%%%%%%%%%%%%%%%%%%%%%%%%%%%%%%%%%%%%%%%%%%%
MethaneTotal=Methane_1+Methane_2
CO2Total=CO2_1+CO2_2+CO2_3
CO2=CO2_21+CO2_31;
```

CODE 2 - Ozone/N_xO_x Area

```
sample = Sample2422ByAdministratorDateSunday;
wave = CreatedasNewDataset;

figure()
plot(wave,sample)
xlabel ('Wave');
ylabel ('Sample');
set (gca, 'XDir', 'Reverse')
```

```
sample(sample<0)=0;

trapz(sample,wave)

q = [2263 2149]

trapz(q)

idx = wave>=970 & wave<= 1100;
wavei=wave(idx);
samplei=sample(idx);
figure()
Ozone=trapz(wavei,samplei);
area(wavei,samplei)

%%%%%%%%%%%%%%%%%%%%%%%%%%%%%%%%%%%%%%%%%%%%%%%%%%%%%%%%

idx = wave>=1540 & wave<= 1660;
wavei=wave(idx);
samplei=sample(idx);
figure()
NO2=trapz(wavei,samplei);
area(wavei,samplei)

%%%%%%%%%%%%%%%%%%%%%%%%%%%%%%%%%%%%%%%%%%%%%%%%%%%%%%%%

idx = wave>=1680 & wave<=1760 ;
wavei=wave(idx);
samplei=sample(idx);
figure()
N2O5_1=trapz(wavei,samplei);
area(wavei,samplei)

%%%%%%%%%%%%%%%%%%%%%%%%%%%%%%%%%%%%%%%%%%%%%%%%%%%%%%%%

idx = wave>=2150 & wave<=2260 ;
wavei=wave(idx);
samplei=sample(idx);
figure()
N2O_2=trapz(wavei,samplei);
area(wavei,samplei)

%%%%%%%%%%%%%%%%%%%%%%%%%%%%%%%%%%%%%%%%%%%%%%%%%%%%%%%%

 idx = wave>=2520 & wave<= 2600;
wavei=wave(idx);
samplei=sample(idx);
figure()
N2O_3=trapz(wavei,samplei);
area(wavei,samplei)

%%%%%%%%%%%%%%%%%%%%%%%%%%%%%%%%%%%%%%%%%%%%%%%%%%%%%%%%

idx = wave>=3420 & wave<= 3500;
wavei=wave(idx);
samplei=sample(idx);
figure()
N2O_4=trapz(wavei,samplei);
```

```
area(wavei,samplei)

%%%%%%%%%%%%%%%%%%%%%%%%%%%%%%%%%%%%%%%%%%%%%

N2O=N2O_2+N2O_3+N2O_4
N2O5=N2O5_1
%%%%%%%%%%%%%%%%%%%%%%%%%%%%%%%%%%%%%%%%%%%%%
%%%%%%%%%%%%%%%%%%%%%%%%%%%%%%%%%%%%%%%%%%
NOX=NO2+N2O+N2O5
```

CODE 3 - Electrical Data (Power)

```
% Define Variables
Voltage = V;
Current = A;
Time = VerticalUnits;


figure()


% Plot Graph
plot(Time,Voltage)
xlabel ('Time');
ylabel ('Voltage');


yyaxis right
plot(Time,Current)
ylabel ('Current');


% Find Power
mV=meanabs(V)
mI=meanabs(A)


P=sqrt((mV^2*mI^2))
```

OES of O_2:N_2 Plasma

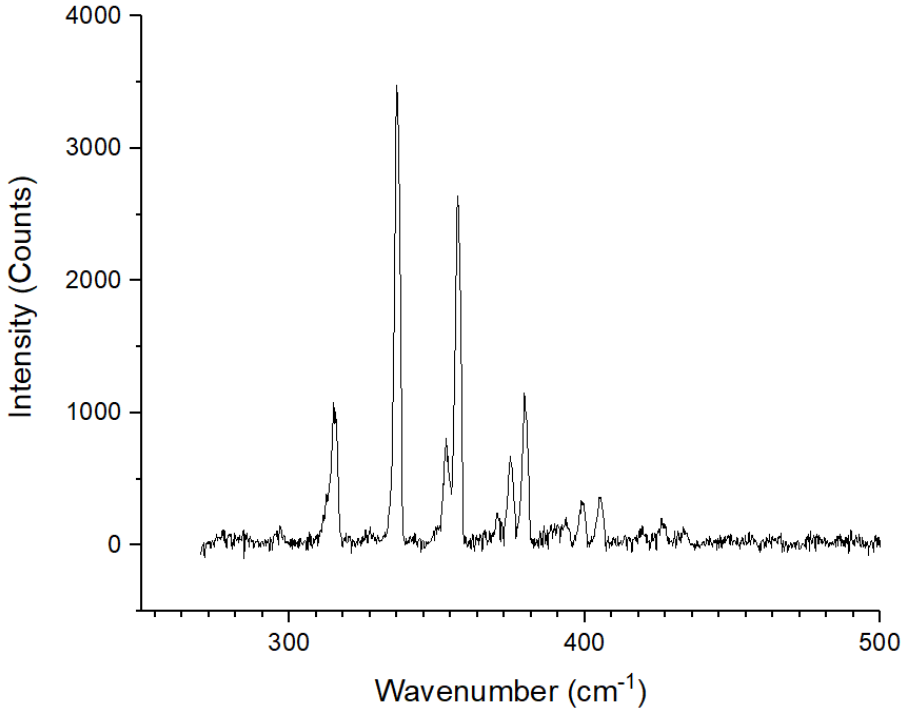

Figure 83 – Example Optical emission spectra graph at 10kV peak to peak voltage with a gas mixture of O_2/N_2 with annealed TiO_2 coated $BaTiO_3$ particulates.

OES of Ar:CH_4:CO_2

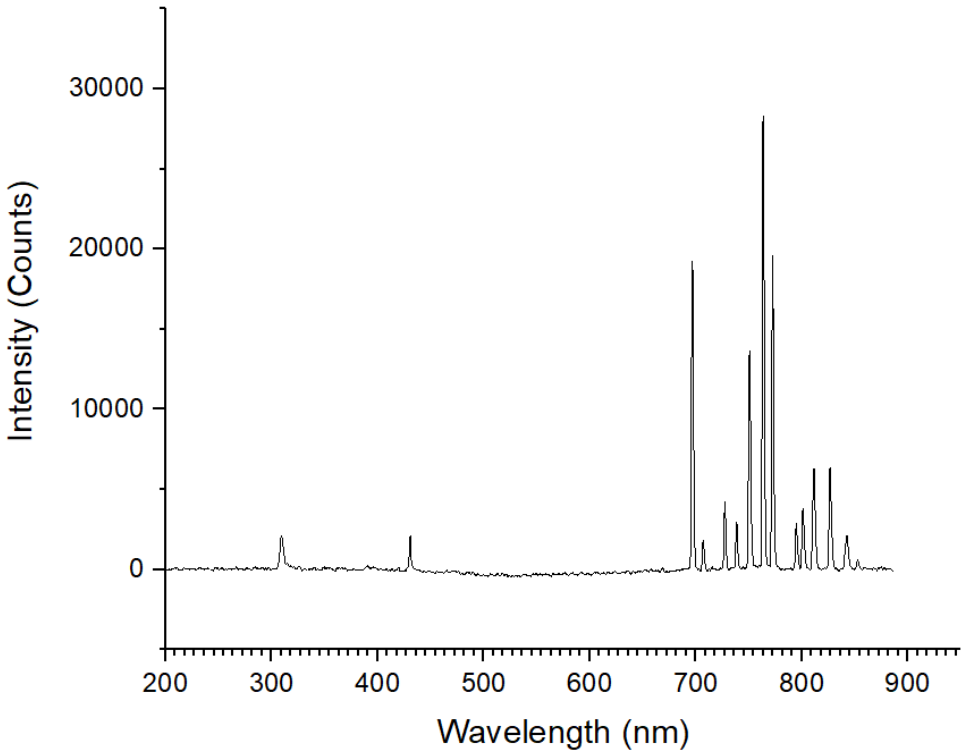

Figure 84 - Example Optical emission spectra graph at 8.25kV peak to peak voltage with a gas mixture of CH_4:CO_2 with a ratio of 1 using annealed TiO_2 coated $BaTiO_3$ particulates.

REFERENCES

1. Nations, U., *2015 Energy Statistics Yearbook*, U. Nations, Editor. 2015, United Nations: https://unstats.un.org/unsd/energy/yearbook/default.htm.
2. Department for Business, E.a.I.S. *UK Energy Statistics, Q1 2017*. 2017.
3. Agency, I.E. *Energy Snapshot*. 2017; Available from: https://www.iea.org/newsroom/energysnapshots/global-carbon-dioxide-emissions-1980-2016.html.
4. Laboratory, E.S.R. *Trends in Atmospheric Carbon Dioxide*. 2017; Available from: https://www.esrl.noaa.gov/gmd/ccgg/trends/.
5. NOAA. *Trends in Atmospheric Carbon Dioxide*. Available from: https://www.esrl.noaa.gov/gmd/ccgg/trends/mlo.html.
6. Agency, E.E., *Trends in atmospheric concentrations of CO2, CH4 and N2O*. 2018.
7. Change, U.N.F.o.C. *Paris Agreement*. 2017; 1]. Available from: http://unfccc.int/paris_agreement/items/9485.php.
8. Sharaf, O.Z. and M.F. Orhan, *An overview of fuel cell technology: Fundamentals and applications.* Renewable and Sustainable Energy Reviews, 2014. **32**: p. 810-853.
9. Barbir, F., *Chapter One - Introduction*, in *PEM Fuel Cells (Second Edition)*. 2013, Academic Press: Boston. p. 1-16.
10. Hagos, F.Y., A.R.A. Aziz, and S.A. Sulaiman, *Trends of Syngas as a Fuel in Internal Combustion Engines.* Advances in Mechanical Engineering, 2014. **6**: p. 401587.
11. Kim, H.-H., et al., *A multidisciplinary approach to understand the interactions of nonthermal plasma and catalyst: A review.* Catalysis Today, 2015. **256, Part 1**: p. 13-22.
12. Pekárek, S., J. Mikeš, and J. Krýsa, *Comparative study of TiO2 and ZnO photocatalysts for the enhancement of ozone generation by surface dielectric barrier discharge in air.* Applied Catalysis A: General, 2015. **502**: p. 122-128.
13. Chung, W.-C., Y.-E. Lee, and M.-B. Chang, *Syngas production via plasma photocatalytic reforming of methane with carbon dioxide.* International Journal of Hydrogen Energy, 2018.
14. Nasonova, A. and K.-S. Kim, *Effects of TiO2 coating on zeolite particles for NO and SO2 removal by dielectric barrier discharge process.* Catalysis Today, 2013. **211**: p. 90-95.
15. Ghorbani Shahna, F., et al., *Chlorobenzene degeradation by non-thermal plasma combined with EG-TiO2/ZnO as a photocatalyst: Effect of photocatalyst on CO2 selectivity and byproducts reduction.* Journal of Hazardous Materials, 2017. **324**: p. 544-553.
16. Hu, J., et al., *Degradation of benzene by bipolar pulsed series surface/packed-bed discharge reactor over MnO2–TiO2/zeolite catalyst.* Chemical Engineering Journal, 2016. **293**: p. 216-224.
17. Jiang, N., et al., *Plasma-catalytic degradation of benzene over Ag–Ce bimetallic oxide catalysts using hybrid surface/packed-bed discharge plasmas.* Applied Catalysis B: Environmental, 2016. **184**: p. 355-363.
18. Li, Y., et al., *Post plasma-catalysis for VOCs degradation over different phase structure MnO2 catalysts.* Chemical Engineering Journal, 2014. **241**: p. 251-258.

19. Zhu, X., et al., *Post-plasma catalytic removal of methanol over Mn–Ce catalysts in an atmospheric dielectric barrier discharge.* Applied Catalysis B: Environmental, 2016. **183**: p. 124-132.

20. Lu, N., et al., *Diagnostics of Plasma Behavior and TiO2 Properties Based on DBD/TiO2 Hybrid System.* Plasma Chemistry and Plasma Processing, 2018. **38**(6): p. 1239-1258.

21. Henderson, P.S., et al., *Investigation into the properties of titanium based films deposited using pulsed magnetron sputtering.* Surface and Coatings Technology, 2003. **174-175**: p. 779-783.

22. Ratova, M., *Enhanced Properties of Photocatalytic Titania Thin Films via Doping During Magnetron Sputtering*. 2013, Manchester Metropolitan University.

23. Ratova, M., *Enhanced Properties of Photocatalytic Titania Thin Films Via Doping During Magnetron Sputter Deposition*. 2013: Manchester Metropolitan University.

24. Ratova, M., G.T. West, and P.J. Kelly, *Photocatalytic visible-light active bismuth tungstate coatings deposited by reactive magnetron sputtering.* Vacuum, 2015. **115**(Supplement C): p. 66-69.

25. Iervolino, G., et al., *Enhanced photocatalytic hydrogen production from glucose aqueous matrices on Ru-doped LaFeO3.* Applied Catalysis B: Environmental, 2017. **207**: p. 182-194.

26. Speight, J.G., *Chapter 8 - Hydrocarbons from Synthesis Gas*, in *Handbook of Industrial Hydrocarbon Processes*, J.G. Speight, Editor. 2011, Gulf Professional Publishing: Boston. p. 281-323.

27. Nguyen, H.H. and K.-S. Kim, *Combination of plasmas and catalytic reactions for CO2 reforming of CH4 by dielectric barrier discharge process.* Catalysis Today, 2015. **256, Part 1**: p. 88-95.

28. Mei, D., et al., *Plasma-photocatalytic conversion of CO2 at low temperatures: Understanding the synergistic effect of plasma-catalysis.* Applied Catalysis B: Environmental, 2016. **182**: p. 525-532.

29. Pen˜a, M.A., J.P. Gómez, and J.L.G. Fierro, *New catalytic routes for syngas and hydrogen production.* Applied Catalysis A: General, 1996. **144**(1): p. 7-57.

30. Mozetič, M., et al., *Chapter 2 - Introduction to Plasma and Plasma Diagnostics*, in *Non-Thermal Plasma Technology for Polymeric Materials*, S. Thomas, et al., Editors. 2019, Elsevier. p. 23-65.

31. Keidar, M. and I.I. Beilis, *Chapter 1 - Plasma Concepts*, in *Plasma Engineering (Second Edition)*, M. Keidar and I.I. Beilis, Editors. 2018, Academic Press. p. 3-100.

32. Samal, S., *Thermal plasma technology: The prospective future in material processing.* Journal of Cleaner Production, 2017. **142**: p. 3131-3150.

33. Napartovich, A.P., *Overview of Atmospheric Pressure Discharges Producing Nonthermal Plasma.* Plasmas and Polymers, 2001. **6**(1): p. 1-14.

34. Gallagher, M.J. and A. Fridman, *Chapter 8 - Plasma Reforming for H2-Rich Synthesis Gas*, in *Fuel Cells: Technologies for Fuel Processing*, D. Shekhawat, J.J. Spivey, and D.A. Berry, Editors. 2011, Elsevier: Amsterdam. p. 223-259.

35. Xiao, D., *Fundamental Theory of Townsend Discharge*, in *Gas Discharge and Gas Insulation*, D. Xiao, Editor. 2016, Springer Berlin Heidelberg: Berlin, Heidelberg. p. 47-88.

36. Loeb, L.B., *Fundamental Processes of Electrical Discharge in Gases*. 1939: John Wiley & Sons.

37. Raether, H., *Die Entwicklung der Elektronenlawine in den Funkenkanal.* Zeitschrift für Physik, 1939. **112**(7): p. 464-489.

38. Meek, J.M., *A Theory of Spark Discharge.* Physical Review, 1940. **57**(8): p. 722-728.

39. Xiao, D., *Fundamental Theory of Streamer and Leader Discharge*, in *Gas Discharge and Gas Insulation*, D. Xiao, Editor. 2016, Springer Berlin Heidelberg: Berlin, Heidelberg. p. 89-121.

40. Tiwari, S., et al., *Microwave Plasma-Enhanced and Microwave Heated Chemical Reactions.* Plasma Chemistry and Plasma Processing, 2020. **40**(1): p. 1-23.

41. Smulders, E., E.J.M. Heesch, and S. van Paasen, *Pulsed Power Corona Discharges for Air Pollution Control.* Plasma Science, IEEE Transactions on, 1998. **26**: p. 1476-1484.

42. Abahazem, A., et al., *Electric and Spectroscopic Studies of Pulsed Corona Discharges in Nitrogen at Atmospheric Pressure.* Journal of Analytical Sciences, Methods and Instrumentation, 2017. **7**.

43. Fridman, A. *Physics and applications of the Gliding Arc discharge*. in *The 31st IEEE International Conference on Plasma Science, 2004. ICOPS 2004. IEEE Conference Record - Abstracts.* 2004.

44. Fridman, A., et al., *Gliding arc gas discharge.* Progress in Energy and Combustion Science, 1999. **25**(2): p. 211-231.

45. Štefečka., M., et al., *Experimental study of atmospheric pressure surface discharge in helium.* Science and Technology of Advanced Materials, 2001. **2**(3-4): p. 587.

46. Kogelschatz, U., *Dielectric-barrier discharges: Their History, Discharge Physics, and Industrial Applications.* Plasma Chemistry and Plasma Processing, 2003. **23**(1): p. 1-46.

47. Kostov, K.G., et al., *Bacterial sterilization by a dielectric barrier discharge (DBD) in air.* Surface and Coatings Technology, 2010. **204**(18): p. 2954-2959.

48. Sawtell, D., A. Martin Philip, and W. Sheel David, *Enhanced AP-PE-CVD Process Understanding and Control by Application of Integrated Optical, Electrical and Modelling Diagnostics.* Plasma Processes and Polymers, 2009. **6**(1): p. S637-S642.

49. Quoc An, H.T., et al., *Application of atmospheric non thermal plasma-catalysis hybrid system for air pollution control: Toluene removal.* Catalysis Today, 2011. **176**(1): p. 474-477.

50. Kostov, K.G., et al., *Characteristics of dielectric barrier discharge reactor for material treatment.* Brazilian Journal of Physics, 2009. **39**: p. 322-325.

51. Xu, X., *Dielectric barrier discharge — properties and applications.* Thin Solid Films, 2001. **390**(1–2): p. 237-242.

52. Montoro-Damas, A.M., et al., *Plasma reforming of methane in a tunable ferroelectric packed-bed dielectric barrier discharge reactor.* Journal of Power Sources, 2015. **296**: p. 268-275.

53. Chen, H.L., et al., *Review of packed-bed plasma reactor for ozone generation and air pollution control.* Industrial and Engineering Chemistry Research, 2008. **47**(7): p. 2122-2130.

54. Butterworth, T., R. Elder, and R. Allen, *Effects of particle size on CO2 reduction and discharge characteristics in a packed bed plasma reactor.* Chemical Engineering Journal, 2016. **293**: p. 55-67.

55. Ergun, S. and A.A. Orning, *Fluid Flow through Randomly Packed Columns and Fluidized Beds.* Industrial & Engineering Chemistry, 1949. **41**(6): p. 1179-1184.

56. Chang, J.S., et al. *The effects of barium titanate pellet shapes on the gas discharge characteristics of ferroelectric packed bed reactors*.

57. Manley, T.C., *The electrical characteristics of the ozonator discharge.* Trans. Electrochem. Soc., 1943. **84**: p. 83-96.

58. Ranade, V.V. and S.S. Joshi, *Chapter 1 - Catalysis and Catalytic Processes*, in *Industrial Catalytic Processes for Fine and Specialty Chemicals*, S.S. Joshi and V.V. Ranade, Editors. 2016, Elsevier: Amsterdam. p. 1-14.

59. Biswas, J. and I.E. Maxwell, *Recent process- and catalyst-related developments in fluid catalytic cracking.* Applied Catalysis, 1990. **63**(1): p. 197-258.

60. Hill, J.W. and R.H. Petrucci, *General Chemistry: An Integrated Approach*. 2002: Prentice Hall.

61. Wang, W., et al., *Photocatalysis in Environment, Energy, and Sustainability.* International Journal of Photoenergy, 2016. **2016**: p. 5436847.

62. Michal, R., S. Sfaelou, and P. Lianos, *Photocatalysis for renewable energy production using PhotoFuelCells.* Molecules (Basel, Switzerland), 2014. **19**(12): p. 19732-19750.

63. Preethi, V. and S. Kanmani, *Photocatalytic hydrogen production.* Materials Science in Semiconductor Processing, 2013. **16**(3): p. 561-575.

64. Sharma, A. and B.-K. Lee, *Photocatalytic reduction of carbon dioxide to methanol using nickel-loaded TiO2 supported on activated carbon fiber.* Catalysis Today, 2017. **298**: p. 158-167.

65. Liu, J.-Y., X.-Q. Gong, and A.N. Alexandrova, *Mechanism of CO2 Photocatalytic Reduction to Methane and Methanol on Defected Anatase TiO2 (101): A Density Functional Theory Study.* The Journal of Physical Chemistry C, 2019. **123**(6): p. 3505-3511.

66. Qin, G., et al., *Photocatalytic reduction of carbon dioxide to formic acid, formaldehyde, and methanol using dye-sensitized TiO2 film.* Applied Catalysis B: Environmental, 2013. **129**: p. 599–605.

67. Yu, X., et al., *Selective photocatalytic conversion of methane into carbon monoxide over zinc-heteropolyacid-titania nanocomposites.* Nature Communications, 2019. **10**(1): p. 700.

68. Neatu, S., J. Maciá-Agulló, and H. Garcia, *Solar Light Photocatalytic CO2 Reduction: General Considerations and Selected Bench-Mark Photocatalysts.* International journal of molecular sciences, 2014. **15**: p. 5246-62.

69. Baloyi, J.o.M.a.J., *Modified Titanium Dioxide for Photocatalytic Applications*. 2018: Photocatalysts - Applications and Attributes.

70. Fujishima, A. and K. Honda, *Electrochemical Photolysis of Water at a Semiconductor Electrode.* Nature, 1972. **238**(5358): p. 37-38.

71. Macwan, D.P., P.N. Dave, and S. Chaturvedi, *A review	 on nano-TiO2 sol–gel type syntheses and its applications.* Journal of Materials Science, 2011. **46**(11): p. 3669-3686.

72. Hou, Y.-Q., et al., *Influence of annealing temperature on the properties of titanium oxide thin film.* Applied Surface Science, 2003. **218**(1–4): p. 98-106.

73. Martin, N., et al., *Microstructure modification of amorphous titanium oxide thin films during annealing treatment.* Thin Solid Films, 1997. **300**(1): p. 113-121.

74. Luttrell, T., et al., *Why is anatase a better photocatalyst than rutile? - Model studies on epitaxial TiO2 films.* Scientific Reports, 2014. **4**: p. 4043.

75. Chen, X., et al., *Increasing Solar Absorption for Photocatalysis with Black Hydrogenated Titanium Dioxide Nanocrystals.* Science, 2011. **331**(6018): p. 746.

76. Pylnev, M., W.-H. Chang, and M.-S. Wong, *Shell of black titania prepared by sputtering TiO2 target in H2 + Ar plasma.* Applied Surface Science, 2018. **462**: p. 285-290.

77. Fei Huang, A.Y., Hui Zhao, *Influences of Doping on Photocatalytic Properties of TiO2 Photocatalyst.* Semiconductor Photocatalysis - Materials, Mechanisms and Applications, 2016.

78. Zaleska-Medynska, A., *Doped-TiO2: a review.* Recent Patents on Engineering, 2008. **2**: p. 157-164.

79. Yalçın, Y., M. Kılıç, and Z. Cinar, *The Role of Non-Metal Doping in TiO2 Photocatalysis.* Journal of Advanced Oxidation Technologies, 2010. **13**: p. 281-296.

80. Chen, D.-m., et al., *W-doped anatase TiO2 transparent conductive oxide films: Theory and experiment.* Journal of Applied Physics, 2010. **107**(6): p. 063707.

81. Choi, J., H. Park, and M.R. Hoffmann, *Effects of Single Metal-Ion Doping on the Visible-Light Photoreactivity of TiO2.* The Journal of Physical Chemistry C, 2010. **114**(2): p. 783-792.

82. Hagos, T.T., *Current State Of Doped-Tio 2 Photocatalysts And Synthesis Methods To Prepare Tio 2 Films: A Re- view.* 2019.

83. Diwald, O., et al., *Photochemical Activity of Nitrogen-Doped Rutile TiO2(110) in Visible Light.* The Journal of Physical Chemistry B, 2004. **108**(19): p. 6004-6008.

84. Chen, L.-C., et al., *Characterization and photoreactivity of N-, S-, and C-doped ZnO under UV and visible light illumination.* Journal of Photochemistry and Photobiology A: Chemistry, 2008. **199**(2): p. 170-178.

85. Basavarajappa, P.S., et al., *Recent progress in metal-doped TiO2, non-metal doped/codoped TiO2 and TiO2 nanostructured hybrids for enhanced photocatalysis.* International Journal of Hydrogen Energy, 2019.

86. Chen, T.-T., et al., *The exceptional photo-catalytic activity of ZnO/RGO composite via metal and oxygen vacancies.* Applied Catalysis B: Environmental, 2013. **142-143**(Supplement C): p. 442-449.

87. Patil, A.B., K.R. Patil, and S.K. Pardeshi, *Ecofriendly synthesis and solar photocatalytic activity of S-doped ZnO.* Journal of Hazardous Materials, 2010. **183**(1): p. 315-323.

88. Ihara, T., et al., *Visible-light-active titanium oxide photocatalyst realized by an oxygen-deficient structure and by nitrogen doping.* Applied Catalysis B: Environmental, 2003. **42**(4): p. 403-409.

89. Lee, K.M., et al., *Recent developments of zinc oxide based photocatalyst in water treatment technology: A review.* Water Research, 2016. **88**(Supplement C): p. 428-448.

90. Arabi, K., et al., *Syngas production by plasma treatments of alcohols, bio-oils and wood.* Journal of Physics: Conference Series, 2012. **406**: p. 012026.

91. Snoeckx, R. and A. Bogaerts, *Plasma technology – a novel solution for CO2 conversion?* Chemical Society Reviews, 2017. **46**(19): p. 5805-5863.

92. Feng, X., et al., *Synergistic effects and mechanism of a non-thermal plasma catalysis system in volatile organic compound removal: a review.* Catalysis Science & Technology, 2018. **8**(4): p. 936-954.

93. Aymen Amine Assadi, A.B., Cédric Vallet, Dominique Wolbert, *Use of DBD plasma, photocatalysis, and combined DBD plasma/photocatalysis in a continuous annular reactor for isovaleraldehyde elimination - Synergetic effect and byproducts identification. The Chemical Engineering Journal*, 2014.

94. Kameshima, S., et al., *Pulsed dry methane reforming in plasma-enhanced catalytic reaction.* Catalysis Today, 2015. **256, Part 1**: p. 67-75.

95. Rahimpour, M.R., et al., *Combination of non-thermal plasma and heterogeneous catalysis for methane and hexadecane co-cracking: Effect of voltage and catalyst configuration.* Chemical Engineering Journal, 2013. **219**: p. 245-253.

96. Chung, W.-C., et al., *Dry Reforming of Methane with Dielectric Barrier Discharge and Ferroelectric Packed-Bed Reactors.* Energy & Fuels, 2014. **28**(12): p. 7621-7631.

97. Gallon, H., *Dry Reforming of Methane Using Non-Thermal Plasma-Catalysis*, in *Department of Chemistry*. 2011, The University of Manchester: The University of Manchester.

98. Abedi, K., et al., *Decomposition of chlorinated volatile organic compounds (CVOCs) using NTP coupled with TiO2/GAC, ZnO/GAC, and TiO2–ZnO/GAC in a plasma-assisted catalysis system.* Journal of Electrostatics, 2015. **73**(Supplement C): p. 80-88.

99. Zeng, Y., et al., *Plasma-catalytic dry reforming of methane over γ-Al2O3 supported metal catalysts.* Catalysis Today, 2015. **256, Part 1**: p. 80-87.

100. Jiang, J.-C., *A first-principles study on effects of electric field on heterogeneous catalysis*. 2019: 9 th World Congress on Chemistry and Medicinal Chemistry.

101. Welborn, V.V., L. Ruiz Pestana, and T. Head-Gordon, *Computational optimization of electric fields for better catalysis design.* Nature Catalysis, 2018. **1**(9): p. 649-655.

102. Wallis, A.E., J.C. Whitehead, and K. Zhang, *Plasma-assisted catalysis for the destruction of CFC-12 in atmospheric pressure gas streams using TiO2.* Catalysis Letters, 2007. **113**(1): p. 29-33.

103. Fakeeha, A., et al., *Effect of changing CH4 /CO2 ratio on hydrogen production by dry reforming reaction*. Vol. 1. 2006. 245-256.

104. Mei, D.H., S.Y. Liu, and X. Tu, *CO2 reforming with methane for syngas production using a dielectric barrier discharge plasma coupled with Ni/γ-Al2O3 catalysts: Process optimization through response surface methodology.* Journal of CO2 Utilization, 2017. **21**: p. 314-326.

105. Bo, Z., et al., *Plasma assisted dry methane reforming using gliding arc gas discharge: Effect of feed gases proportion.* International Journal of Hydrogen Energy, 2008. **33**(20): p. 5545-5553.

106. Khoja, A.H., M. Tahir, and N.A.S. Amin, *Dry reforming of methane using different dielectric materials and DBD plasma reactor configurations.* Energy Conversion and Management, 2017. **144**: p. 262-274.

107. Kundu, S.K., et al., *Experimental investigation of alumina and quartz as dielectrics for a cylindrical double dielectric barrier discharge reactor in argon diluted methane plasma.* Chemical Engineering Journal, 2012. **180**: p. 178-189.

108. Yap, D., J.-M. Tatibouët, and C. Batiot-Dupeyrat, *Catalyst assisted by non-thermal plasma in dry reforming of methane at low temperature.* Catalysis Today, 2018. **299**: p. 263-271.

109. Pu, Y.-K., et al., *Tuning effect of inert gas mixing on electron energy distribution function in inductively coupled discharges.* Plasma Physics and Controlled Fusion, 2005. **48**(1): p. 61-70.

110. S. Jo[1] , D.H.L., W.S. Kang[1] , Y.-H. Song[1], *Effect of noble gas for methane decomposition in DBD reactor*, in *21st International Symposium on Plasma Chemistry (ISPC 21)*. 2013: Cairns Convention Centre, Queensland, Australia.

111. Fridman, A., *Plasma Chemistry*. 2008, Cambridge: Cambridge University Press.

112. Tu, X., et al., *Dry reforming of methane over a Ni/Al2O3 catalyst in a coaxial dielectric barrier discharge reactor*. Vol. 44. 2011. 274007.

113. Mei, D., et al., *Plasma-assisted conversion of CO2in a dielectric barrier discharge reactor: understanding the effect of packing materials.* Plasma Sources Science and Technology, 2014. **24**(1): p. 015011.

114. Kim, H., et al., *Mechanical and electrical properties of NbMoTaW refractory high-entropy alloy thin films.* International Journal of Refractory Metals and Hard Materials, 2019. **80**: p. 286-291.

115. Smestad, G., et al., *Photoactive thin film semiconducting iron pyrite prepared by sulfurization of iron oxides.* Solar Energy Materials, 1990. **20**(3): p. 149-165.

116. Roberts, E.W., *Thin solid lubricant films in space.* Tribology International, 1990. **23**(2): p. 95-104.

117. Ratova, M., et al., *Visible light active photocatalytic C-doped titanium dioxide films deposited via reactive pulsed DC magnetron co-sputtering: Properties and photocatalytic activity.* Vacuum, 2018. **149**: p. 214-224.

118. Visinescu, C.M., et al., *Photocatalytic degradation of acetone by Ni-doped titania thin films prepared by dc reactive sputtering.* Applied Catalysis B: Environmental, 2005. **60**(3): p. 155-162.

119. Marek, M., et al., *Ultra-thin polyimide film as a gas-separation layer for composite membranes.* Polymer, 1996. **37**(12): p. 2577-2579.

120. Ratova, M., G. T. West, and P. J. Kelly, *Optimization Studies of Photocatalytic Tungsten-Doped Titania Coatings Deposited by Reactive Magnetron Co-Sputtering*. Vol. 3. 2013. 194.

121. Yao, M., et al., *Photocatalytic activities of Ion doped TiO2 thin films when prepared on different substrates.* Thin Solid Films, 2009. **517**(21): p. 5994-5999.

122. Zhao, Y.-X., et al., *Photocatalytic properties of TiO2 films prepared by bipolar pulsed magnetron sputtering.* Surface and Coatings Technology.

123. Purica, M., et al., *Optical and structural investigation of ZnO thin films prepared by chemical vapor deposition (CVD).* Thin Solid Films, 2002. **403-404**: p. 485-488.

124. A.M. Torres-Huerta, M.A.D.C.a.A.B.L.O., *Applications of CVD to Produce Thin Films for Solid-State Devices*, in *Chemical Vapor Deposition - Recent Advances and Applications in Optical, Solar Cells and Solid State Devices*. 2016.

125. Hammond, M.S., *Chemical vapor deposition: Thermal and plasma deposition of electronic materials. By S. Sivaram, Van Nostrand Reinhold, New York 1995, ix, 292 pp., hardcover, $49.00, ISBN 0-442-01079-6.* Chemical Vapor Deposition, 1996. **2**(5): p. 210-210.

126. Li, D., et al., *Nanostructure and photocatalytic properties of TiO2 films deposited at low temperature by pulsed PECVD.* Applied Surface Science, 2019. **466**: p. 63-69.

127. Guillard, C., et al., *Physical properties and photocatalytic efficiencies of TiO2 films prepared by PECVD and sol–gel methods.* Materials Research Bulletin, 2004. **39**(10): p. 1445-1458.

128. Robabeh Bashiri, N.M.M.a.C.F.K., *Advancement of Sol-Gel–Prepared TiO2 Photocatalyst*, in *Recent Applications in Sol-Gel Synthesis*. 2017.

129. Akpan, U.G. and B.H. Hameed, *The advancements in sol–gel method of doped-TiO2 photocatalysts.* Applied Catalysis A: General, 2010. **375**(1): p. 1-11.

130. Tseng, T.-K., et al., *A Review of Photocatalysts Prepared by Sol-Gel Method for VOCs Removal.* International journal of molecular sciences, 2010. **11**: p. 2336-61.

131. Aydın, C., et al., *Controlling of crystal size and optical band gap of CdO nanopowder semiconductors by low and high Fe contents.* Journal of Electroceramics, 2012. **29**(2): p. 155-162.

132. Coaters, S.o.V., *Educational Guide to Vacuum Deposition Technology*. 1996.

133. Thornton, J.A., *High rate sputtering techniques.* Thin Solid Films, 1981. **80**(1): p. 1-11.

134. Materials, S.A. *An Overview of Magnetron Sputtering*. 2021 [cited 2020 16/01/2021]; Available from: https://www.sputtertargets.net/blog/an-overview-of-magnetron-sputtering.html.

135. Musil, J., et al., *Reactive magnetron sputtering of thin films: present status and trends.* Thin Solid Films, 2005. **475**(1–2): p. 208-218.

136. Ratova, M., et al., *Reactive magnetron sputtering deposition of bismuth tungstate onto titania nanoparticles for enhancing visible light photocatalytic activity.* Applied Surface Science, 2017. **392**(Supplement C): p. 590-597.

137. Ratova, M., et al., *Reactive Magnetron Sputter Deposition of Bismuth Tungstate Coatings for Water Treatment Applications under Natural Sunlight.* Catalysts, 2017. **7**(10).

138. Mosquera, A.A., et al., *Effect of silver on the phase transition and wettability of titanium oxide films.* Scientific Reports, 2016. **6**(1): p. 32171.

139. Alonso Frank, M., *Functionalization of Steels and other Metallic Materials with Hydrophobic Layers - Influence on Wetting and Corrosion Resistance*. 2017.

140. Joining, C.C.f.W.a. *Microscopy*. Available from: https://sites.ualberta.ca/~ccwj/teaching/microscopy/.

141. Prize, T.N. *The Nobel Prize in Physics 1930*. [cited 2020 28/03/2020]; Available from: https://www.nobelprize.org/prizes/physics/1930/summary/.

142. Krishnan, R.S. and R.K. Shankar, *Raman effect: History of the discovery.* Journal of Raman Spectroscopy, 1981. **10**(1): p. 1-8.

143. Materials, A. *XPS Surface Area Analysis*. 2021; Available from: https://www.andersonmaterials.com/xps/.

144. Stojilovic, N., *Why Can't We See Hydrogen in X-ray Photoelectron Spectroscopy?* Journal of Chemical Education, 2012. **89**(10): p. 1331-1332.

145. Ambroz, F., et al., *Evaluation of the BET Theory for the Characterization of Meso and Microporous MOFs.* Small Methods, 2018. **2**(11): p. 1800173.

146. Andronic, L., et al., *Photocatalytic activity of cadmium doped TiO2 films for photocatalytic degradation of dyes.* Chemical Engineering Journal, 2009. **152**(1): p. 64-71.

147. Dariani, R.S., et al., *Photocatalytic reaction and degradation of methylene blue on TiO2 nano-sized particles.* Optik - International Journal for Light and Electron Optics, 2016. **127**(18): p. 7143-7154.

148. Houas, A., et al., *Photocatalytic degradation pathway of methylene blue in water.* Applied Catalysis B: Environmental, 2001. **31**(2): p. 145-157.

149. Saepurahman, M.A. Abdullah, and F.K. Chong, *Dual-effects of adsorption and photodegradation of methylene blue by tungsten-loaded titanium dioxide.* Chemical Engineering Journal, 2010. **158**(3): p. 418-425.

150. ISO, *Fine ceramics (advanced ceramics, advanced technical ceramics) — Determination of photocatalytic activity of surfaces in an aqueous medium by degradation of methylene blue*. 2017.

151. Mills, A., C. Hill, and P.K.J. Robertson, *Overview of the current ISO tests for photocatalytic materials.* Journal of Photochemistry and Photobiology A: Chemistry, 2012. **237**: p. 7-23.

152. Grao, M., et al., *Crystalline TiO_2 supported on stainless steel mesh deposited in a one step process via pulsed DC magnetron sputtering for wastewater treatment applications.* Journal of Materials Research and Technology, 2020. **9**(3): p. 5761-5773.

153. Sung Soo RYU, S.C.P., Sang Pyo Lee, Dong Sook Sinn, Sang Kyun Lee, Dang Hyok Yoon., *Method for manufacturing dielectric ceramic powder, and multilayer ceramic capacitor obtained by using the ceramic powder*. 2005.

154. Holub, M., *On the measurement of plasma power in atmospheric pressure DBD plasma reactors.* International Journal of Applied Electromagnetics and Mechanics, 2012. **39**: p. 81-87.

155. Larkin, P.J., *Chapter 1 - Introduction: Infrared and Raman Spectroscopy*, in *Infrared and Raman Spectroscopy (Second Edition)*, P.J. Larkin, Editor. 2018, Elsevier. p. 1-5.

156. Corporation, T., *Introduction to Fourier Transform Infrared Spectroscopy*. 2001.

157. Shimanouchi, T., et al., *Tables of molecular vibrational frequencies.* Journal of Physical and Chemical Reference Data, 1978. **7**(4): p. 1323-1444.

158. Lee, T.J. and G.E. Scuseria, *The vibrational frequencies of ozone.* The Journal of Chemical Physics, 1990. **93**(1): p. 489-494.

159. Ross, W.L., *The infrared absorption spectra of nitrogen dioxide*. 1950: University of British Columbia.

160. Bencivenni, L., et al., *Infrared spectrum and theoretical study of the dinitrogen pentoxide molecule (N2O5) in solid argon.* The Journal of Chemical Physics, 1996. **104**(20): p. 7836-7846.

161. SOCIETY, C., *Ozone standard spectra*, in *COBLENTZ NO. 10565*. 2018: DOW CHEMICAL COMPANY.

162. Sharpe, S.W., et al., *Gas-Phase Databases for Quantitative Infrared Spectroscopy.* Applied Spectroscopy, 2004. **58**(12): p. 1452-1461.

163. Coblentz Society, I., *Evaluated Infrared Reference Spectra*, N.I.o.S.a.T. Eds. P.J. Linstrom and W.G. Mallard, Gaithersburg MD, 20899, Editor. August 14, 2019: **NIST Chemistry WebBook, NIST Standard Reference Database Number 69**.

164. Fitzsimmons, C., J. Shawcross, and J. Whitehead, *Plasma-assisted synthesis of N2O5 from NO2 in air at atmospheric pressure using a dielectric pellet bed reactor.* Journal of Physics D: Applied Physics, 1999. **32**: p. 1136.

165. Vlček, J., A.D. Pajdarová, and J. Musil, *Pulsed dc Magnetron Discharges and their Utilization in Plasma Surface Engineering.* Contributions to Plasma Physics, 2004. **44**(5-6): p. 426-436.

166. Al-Homoudi, I.A., et al., *Fabrication of Anatase TiO2 Thin Film Using Pulsed DC Magnetron Sputtering.* MRS Proceedings, 2004. **848**: p. FF3.20.

167. Berg, S. and T. Nyberg, *Fundamental understanding and modeling of reactive sputtering processes.* Thin Solid Films, 2005. **476**(2): p. 215-230.

168. Ohsaka, T., F. Izumi, and Y. Fujiki, *Raman spectrum of anatase, TiO2.* Journal of Raman Spectroscopy, 1978. **7**(6): p. 321-324.

169. Colomban, P. and A. Slodczyk, *Raman intensity: An important tool to study the structure and phase transitions of amorphous/crystalline materials.* Optical Materials, 2009. **31**(12): p. 1759-1763.

170. Ranfang Zuo , G.D., Weiwei Zhang , Lianhua Liu , Yanming Liu , Lefu Mei , and Zhaohui Li, *Photocatalytic Degradation of Methylene Blue Using TiO 2 Impregnated Diatomite.* Advances in Materials Science and Engineering, 2014.

171. Vasiljevic, Z.Z., et al., *Photocatalytic degradation of methylene blue under natural sunlight using iron titanate nanoparticles prepared by a modified sol–gel method.* Royal Society Open Science. **7**(9): p. 200708.

172. Diebold, U. and T.E. Madey, *TiO2 by XPS.* Surface Science Spectra, 1996. **4**(3): p. 227-231.

173. NIST. *NIST XPS search query for Ti*. 2012 [cited 2019; Available from: https://srdata.nist.gov/xps/EngElmSrchQuery.aspx?EType=PE&CSOpt=Retri_ex_dat&Elm=Ti.

174. Scientific, T.F. *Titanium*. 2013-2019 [cited 2019; Available from: https://xpssimplified.com/elements/titanium.php.

175. Kelly, P., et al., *The distribution of ion energies at the substrate in an asymmetric bi-polar pulsed DC magnetron discharge.* Plasma Sources Science and Technology, 2002. **11**.

176. Kelly, P.J., et al., *The Influence of Pulse Frequency and Duty on the Deposition Rate in Pulsed Magnetron Sputtering.* Plasma Processes and Polymers, 2007. **4**(3): p. 246-252.

177. Ratova, M., et al., *Pulsed DC magnetron sputtering deposition of crystalline photocatalytic titania coatings at elevated process pressures.* Materials Science in Semiconductor Processing, 2017. **71**: p. 188-196.

178. Eufinger, K., *Effect of deposition conditions and doping on the structure, optical properties and photocatalytic activity of d.c. magnetron sputtered TiO 2 thin films.* 2007.

179. Ki, S.J., et al., *Facile preparation of tungsten oxide doped TiO2 photocatalysts using liquid phase plasma process for enhanced degradation of diethyl phthalate.* Chemical Engineering Journal, 2019. **377**: p. 120087.

180. Sathasivam, S., et al., *Tungsten Doped TiO2 with Enhanced Photocatalytic and Optoelectrical Properties via Aerosol Assisted Chemical Vapor Deposition.* Scientific Reports, 2015. **5**: p. 10952.

181. Ullah, I., et al., *Tuning the band gap of TiO2 by tungsten doping for efficient UV and visible photodegradation of Congo red dye.* Spectrochimica Acta Part A: Molecular and Biomolecular Spectroscopy, 2018. **204**: p. 150-157.

182. Manciu, F., et al., *Spectroscopic analysis of tungsten oxide thin films.* Journal of Materials Research, 2010. **25**: p. 2401-2406.

183. Daniel, M.F., et al., *Infrared and Raman study of WO3 tungsten trioxides and WO3, xH2O tungsten trioxide tydrates.* Journal of Solid State Chemistry, 1987. **67**(2): p. 235-247.

184. Horsley, J.A., et al., *Structure of surface tungsten oxide species in the tungsten trioxide/alumina supported oxide system from x-ray absorption near-edge spectroscopy and Raman spectroscopy.* The Journal of Physical Chemistry, 1987. **91**(15): p. 4014-4020.

185. McGuire, G.E., G.K. Schweitzer, and T.A. Carlson, *Core electron binding energies in some Group IIIA, VB, and VIB compounds.* Inorganic Chemistry, 1973. **12**(10): p. 2450-2453.

186. [cited 2019 18th April]; Available from: https://xpssimplified.com/elements/tungsten.php.

187. Couselo, N., et al., *Tungsten-Doped TiO2 vs Pure TiO2 Photocatalysts: Effects on Photobleaching Kinetics and Mechanism.* The Journal of Physical Chemistry C, 2008. **112**(4): p. 1094-1100.

188. Kafizas, A. and I.P. Parkin, *Combinatorial Atmospheric Pressure Chemical Vapor Deposition (cAPCVD): A Route to Functional Property Optimization.* Journal of the American Chemical Society, 2011. **133**(50): p. 20458-20467.

189. Xu, S., J.C. Whitehead, and P.A. Martin, *CO2 conversion in a non-thermal, barium titanate packed bed plasma reactor: The effect of dilution by Ar and N2.* Chemical Engineering Journal, 2017. **327**: p. 764-773.

190. Mennad, B., et al., *Effect of the anode material on ozone generation in corona discharges.* Vacuum, 2014. **104**: p. 29-32.

191. Jung, J.-S. and J.-D. Moon, *Corona discharge and ozone generation characteristics of a wire-plate discharge system with a glass-fiber layer.* Journal of Electrostatics, 2008. **66**(5): p. 335-341.

192. Wei, L.S., et al., *Experimental and theoretical study of ozone generation in pulsed positive dielectric barrier discharge.* Vacuum, 2014. **104**: p. 61-64.

193. Pei, X., et al., *Reducing energy cost of NOx production in air plasmas.* Chemical Engineering Journal, 2019. **362**: p. 217-228.

194. Jõgi, I., et al., *Oxidation of NO by ozone in the presence of TiO2 catalyst.* Fuel, 2016. **173**: p. 45-51.

195. Karuppiah, J., et al., *Nonthermal plasma assisted photocatalytic oxidation of dilute benzene.* Journal of Chemical Sciences, 2012. **124**(4): p. 841-845.

196. Yanallah, K., et al., *Experimental investigation and numerical modelling of positive corona discharge: ozone generation.* Journal of Physics D: Applied Physics, 2009. **42**(6): p. 065202.

197. Zhao, X., et al., *Preparation and properties of BaTiO3 ceramics from the fine ceramic powder.* Ceramics International, 2015. **41**: p. S111-S116.

198. Wypych, A., et al., *Dielectric Properties and Characterisation of Titanium Dioxide Obtained by Different Chemistry Methods.* Journal of Nanomaterials, 2014. **2014**: p. 124814.

199. Yuan, D., et al., *Ozone production in parallel multichannel dielectric barrier discharge from oxygen and air: The influence of gas pressure.* Journal of Physics D Applied Physics, 2016. **49**: p. 455203.

200. Sun, Z., et al., *Oxygen vacancy enables electrochemical N2 fixation over WO3 with tailored structure.* Nano Energy, 2019. **62**: p. 869-875.

201. Li, C., et al., *Promoted Fixation of Molecular Nitrogen with Surface Oxygen Vacancies on Plasmon-Enhanced TiO2 Photoelectrodes.* Angewandte Chemie International Edition, 2018. **57**(19): p. 5278-5282.

202. Thompson, T. and J. T. Yates, *TiO2-based Photocatalysis: Surface Defects, Oxygen and Charge Transfer*. Vol. 35. 2005. 197-210.

203. Abd-Allah, Z., et al., *Mass Spectrometric Observations of the Ionic Species in a Double Dielectric Barrier Discharge Operating in Nitrogen.* Plasma Processes and Polymers, 2015. **13**: p. n/a-n/a.

204. Tang, X., et al., *Nitrogen Fixation and NO Conversion using Dielectric Barrier Discharge Reactor: Identification and Evolution of Products.* Plasma Chemistry and Plasma Processing, 2018. **38**(3): p. 485-501.

205. Penetrante, B.M., et al., *Identification of mechanisms for decomposition of air pollutants by non-thermal plasma processing.* Plasma Sources Science and Technology, 1997. **6**(3): p. 251-259.

206. Gentile, A.C. and M.J. Kushner, *Reaction chemistry and optimization of plasma remediation of NxOy from gas streams.* Journal of Applied Physics, 1995. **78**(3): p. 2074-2085.

207. Gal, A., M. Kurahashi, and M. Kuzumoto, *An energy-consumption and byproduct-generation analysis of the discharge nonthermal plasma-chemical NO-reduction process.* Journal of Physics D: Applied Physics, 1999. **32**(10): p. 1163-1168.

208. Herron, J.T. and D.S. Green, *Chemical Kinetics Database and Predictive Schemes for Nonthermal Humid Air Plasma Chemistry. Part II. Neutral Species Reactions.* Plasma Chemistry and Plasma Processing, 2001. **21**(3): p. 459-481.

209. Vervloessem, E., et al., *Plasma-Based N2 Fixation into NOx: Insights from Modeling toward Optimum Yields and Energy Costs in a Gliding Arc Plasmatron.* ACS Sustainable Chemistry & Engineering, 2020. **8**(26): p. 9711-9720.

210. Park, S., W. Choe, and C. Jo, *Interplay among ozone and nitrogen oxides in air plasmas: Rapid change in plasma chemistry.* Chemical Engineering Journal, 2018. **352**: p. 1014-1021.

211. Alhamid, M., et al., *Effect of Methane Gas Flow Rate on Adsorption Capacity and Temperature Distribution of Activated.* International Journal of Technology, 2015. **6**: p. 584.

212. Sung, T.L., et al., *Effect of pulse power characteristics and gas flow rate on ozone production in a cylindrical dielectric barrier discharge ozonizer.* Vacuum, 2013. **90**(Supplement C): p. 65-69.

213. Osawa, N., et al., *Effect of nitrogen addition to ozone generation characteristics by diffuse and filamentary dielectric barrier discharges at atmospheric pressure.* EPJ Applied Physics, 2017. **78**.

214. Höft, H., M. Becker, and M. Kettlitz, *Impact of gas flow rate on breakdown of filamentary dielectric barrier discharges.* Physics of Plasmas, 2016. **23**: p. 033504.

215. Aouad, S., et al., *A Review on the Dry Reforming Processes for Hydrogen Production: Catalytic Materials and Technologies*. 2018. p. 60-128.

216. Yap, D., J.-M. Tatibouët, and C. Batiot-Dupeyrat, *Catalyst assisted by non-thermal plasma in dry reforming of methane at low temperature.* Catalysis Today, 2017.

217. Kumar, N., et al., *Dry reforming of methane with isotopic gas mixture over Ni-based pyrochlore catalyst.* International Journal of Hydrogen Energy, 2019.

218. Wang, H., et al., *Influence of tubular reactor structure and operating conditions on dry reforming of methane.* Chemical Engineering Research and Design, 2018. **139**: p. 39-51.

219. Nozaki, T. and K. Okazaki, *Non-thermal plasma catalysis of methane: Principles, energy efficiency, and applications.* Catalysis Today, 2013. **211**: p. 29-38.

220. Chung, W.-C., I.Y. Tsao, and M.-B. Chang, *Novel plasma photocatalysis process for syngas generation via dry reforming of methane.* Energy Conversion and Management, 2018. **164**: p. 417-428.

221. Bromberg, L., et al., *Plasma catalytic reforming of methane.* International Journal of Hydrogen Energy, 1999. **24**(12): p. 1131-1137.

222. Tu, X. and J.C. Whitehead, *Plasma-catalytic dry reforming of methane in an atmospheric dielectric barrier discharge: Understanding the synergistic effect at low temperature.* Applied Catalysis B: Environmental, 2012. **125**(Supplement C): p. 439-448.

223. Allah, Z.A. and J.C. Whitehead, *Plasma-catalytic dry reforming of methane in an atmospheric pressure AC gliding arc discharge.* Catalysis Today, 2015. **256, Part 1**: p. 76-79.

224. Chung, W.-C. and M.-B. Chang, *Review of catalysis and plasma performance on dry reforming of CH4 and possible synergistic effects.* Renewable and Sustainable Energy Reviews, 2016. **62**: p. 13-31.

225. Khoja, A.H., M. Tahir, and N.A.S. Amin, *Recent developments in non-thermal catalytic DBD plasma reactor for dry reforming of methane.* Energy Conversion and Management, 2019. **183**: p. 529-560.

226. Korotcenkov, G., *Metal Oxides for Solid-State Gas Sensors: What Determines Our Choice?* Materials Science and Engineering: B, 2007. **139**: p. 1-23.

227. Raju, G.G., *Dielectrics in Electric Fields*. Power engineering. 2003: Taylor & Francis.

228. Prasai, B., et al., *Properties of amorphous and crystalline titanium dioxide from first principles.* Journal of Materials Science, 2012. **47**: p. 7515-7521.

229. Brandenburg, R., *Dielectric barrier discharges: progress on plasma sources and on the understanding of regimes and single filaments.* Plasma Sources Science and Technology, 2017. **26**(5): p. 053001.

230. Zhang, K., et al., *A Study on CO2 Decomposition to CO and O2 by the Combination of Catalysis and Dielectric-Barrier Discharges at Low Temperatures and Ambient Pressure.* Industrial & Engineering Chemistry Research, 2017. **56**(12): p. 3204-3216.

231. Yao, S.L., et al., *Plasma Reforming and Coupling of Methane with Carbon Dioxide.* Energy & Fuels, 2001. **15**(5): p. 1295-1299.

232. Marić, D., et al., *Gas breakdown and secondary electron yields.* The European Physical Journal D, 2014. **68**(6): p. 155.

233. Chang, e.C.C.a.M.B., *CO2 Reforming with CH4 via Plasma Catalysis System*, in *Carbon Dioxide Chemistry, Capture and Oil Recovery*. 2018.

234. He, H., P. Zapol, and L.A. Curtiss, *A Theoretical Study of CO2 Anions on Anatase (101) Surface.* The Journal of Physical Chemistry C, 2010. **114**(49): p. 21474-21481.

235. He, H., P. Zapol, and L.A. Curtiss, *Computational screening of dopants for photocatalytic two-electron reduction of CO2 on anatase (101) surfaces.* Energy & Environmental Science, 2012. **5**(3): p. 6196-6205.

236. Thampi, K.R., J. Kiwi, and M. Grätzel, *Room temperature photo-activation of methane on TiO2 supported molybdena.* Catalysis Letters, 1988. **1**(5): p. 109-116.

237. Kleinschmidt, O. and D. Hesse, *Kinetics of the photocatalytic total oxidation of different alkanes and alkenes on TiO2 powder.* The Canadian Journal of Chemical Engineering, 2002. **80**(1): p. 71-78.

238. Graetzel, M., K.R. Thampi, and J. Kiwi, *Methane oxidation at room temperature and atmospheric pressure activated by light via polytungstate dispersed on titania.* The Journal of Physical Chemistry, 1989. **93**(10): p. 4128-4132.

239. Lee, J., D.C. Sorescu, and X. Deng, *Electron-Induced Dissociation of CO2 on TiO2(110).* Journal of the American Chemical Society, 2011. **133**(26): p. 10066-10069.

240. Lin, C.L. and W.B. DeMore, *Reactions of atomic oxygen (1D) with methane and ethane.* The Journal of Physical Chemistry, 1973. **77**(7): p. 863-869.

241. Van Laer, K. and A. Bogaerts, *How bead size and dielectric constant affect the plasma behaviour in a packed bed plasma reactor: a modelling study.* Plasma Sources Science and Technology, 2017. **26**(8): p. 085007.

242. Taheraslani, M. and H. Gardeniers, *Coupling of CH4 to C2 Hydrocarbons in a Packed Bed DBD Plasma Reactor: The Effect of Dielectric Constant and Porosity of the Packing.* Energies, 2020. **13**(2).

243. Butterworth, T.D., *The Effects of Particle Size on CO2 reduction in Packed Bed Dielectric Barrier Discharge Plasma Reactors*. 2015, University of Sheffield.

244. Li, R., et al., *Influence of dielectric barrier materials to the behavior of dielectric barrier discharge plasma for CO2 decomposition.* Solid State Ionics, 2004. **172**(1): p. 235-238.

245. Li, R., et al., *Plasma catalysis for CO2 decomposition by using different dielectric materials.* Fuel Processing Technology, 2006. **87**(7): p. 617-622.

246. Knust, S., et al., *Surface modification of ZnMgAl-coated steel by dielectric-barrier discharge plasma.* RSC Advances, 2019. **9**(60): p. 35077-35088.

247. Jaritz, M., et al., *The effect of UV radiation from oxygen and argon plasma on the adhesion of organosilicon coatings on polypropylene.* Journal of Physics D: Applied Physics, 2016. **50**(1): p. 015201.

248. Golda, J., et al., *Vacuum ultraviolet spectroscopy of cold atmospheric pressure plasma jets.* Plasma Processes and Polymers, 2020. **17**(6): p. 1900216.

249. Busani, T. and R.A.B. Devine, *Dielectric and infrared properties of TiO2films containing anatase and rutile.* Semiconductor Science and Technology, 2005. **20**(8): p. 870-875.

250. Yang, W., et al., *An investigation of annealing on the dielectric performance of TiO2thin films.* Semiconductor Science and Technology, 2006. **21**(12): p. 1573-1579.

251. Cai, X. and Y. Hu, *Advances in catalytic conversion of methane and carbon dioxide to highly valuable products.* Energy Science & Engineering, 2019. **7**: p. 4-29.

252. Zheng, Y., et al., *H2 production from partial oxidation of CH4 by Fe2O3-supported Ni-based catalysts in a plasma-assisted packed bed reactor.* Proceedings of the Combustion Institute, 2019. **37**(4): p. 5481-5488.